TECHNISCHE UNIVERSITÄT WIEN

Dissertation

Assessment of Various Processing Schemes and Solution Strategies to Improve the Performance of GNSS Tropospheric Tomography

Carried out in order to obtain the academic degree "Doctor of Technical Sciences" under the supervision of

Ao.Univ.Prof. Dipl.-Ing. Dr.techn. Robert Weber

E120-4

Department of Geodesy and Geoinformation

Higher Geodesy Group

Submitted to Technical University of Vienna

Faculty of Mathematics and Geoinformation

by

Zohreh Adavi

Matr.-Nr.: 11901848

Vienna, Jun 2022

Dissertation

Assessment of Various Processing Schemes and Solution Strategies to Improve the Performance of GNSS Tropospheric Tomography

ausgeführt zum Zwecke der Erlangung des akademischen Grades eines Doktors der technischen Wissenschaften unter der Leitung von

Ao.Univ.Prof. Dipl.-Ing. Dr.techn. Robert Weber

E120-4

Department für Geodäsie und Geoinformation

Forschungsgruppe Höhere Geodäsie

eingereicht an der Technischen Universität Wien

Fakultät für Mathematik und Geoinformation

Von

Zohreh Adavi

Matr.-Nr.: 11901848

Wien, Jun 2022

REVIEWER

Prof. Dr. rer. nat. Jens Wickert
Institut für Geodäsie und Geoinformationstechnik
Technische Universität Berlin, Deutschland

Prof. Dr. Witold Rohm
Institute of Geodesy and Geoinformatics
Wroclaw University of Environmental and Life Sciences, Wroclaw, Poland

Acknowledgments

First, I would say my gratitude to my divine God, who has always been with me no matter how much wrong I was. The second thanks go to my family because of their endless understanding and support even though miles of distance are between us. I am warmly grateful for having an inspiring sister who always had time for me no matter how busy she was and tried to help me in the best way she could. Lots of thanks also go to my loyal Babak, who showed me how love could be amazing, who has faith in me and gives me tons of energy to find my best version every day.

I would like to say my deepest thanks to Robert, who was not only my supervisor but also my Papa during these years. He was always patient with me and provided a very calm and friendly research environment, which helped me follow my thoughts and ideas. He was always available for discussion, and to be honest, each time with his comments and feedback, a new door opened towards the endless science for me. Finally, I want to acknowledge Witold, who has always supported me in different ways and inspired me since I was an MSc student. I am forever indebted to him.

To my devoted parents, compassionate brothers, supportive sister & my beloved Babak

"What we know is a drop, what we don't know is an ocean."

Isaac Newton

Abstract

In recent years, the Global Navigation Satellite System (GNSS) has turned out to be a valuable tool for remotely sensing the atmosphere. In this context, GNSS tomography evolved to an extremely promising technique to reconstruct the spatio-temporal structure of the troposphere. Therefore, this method can offer a permanent monitoring service for water vapour and wet refractivity fields at low cost and a reasonable spatial resolution compared to conventional observations, like radiosonde and radio occultation profiles. However, there are still some challenges and open questions in GNSS tomography which extremely affect the quality of the reconstructed field. Hence, the main objective of this dissertation is to investigate different strategies to solve some of them.

The economic issue to deploy multi-frequency receivers with a sufficient spatial resolution of a few tens of kilometers is one of the challenges for GNSS tomography. Therefore, the feasibility of using single-frequency observations in GNSS tomography as an alternative approach is investigated. Another challenge of GNSS tomography relates to different parameterization methods for computing the design matrix. Therefore, the effect of the straight-line method versus the ray-tracing method as well as the impact of considering the topography in the tomography model is studied for computing the design matrix. Further attention is given to multi-GNSS observations in GNSS tomography due to improving observation geometry compared to a sole GPS/ GLONASS system scenario. Therefore, by focusing on GALILEO's effect, the impact of different constellations is investigated to retrieve a wet refractivity field. GNSS tomography is also suffering from the insufficient spatial coverage of GNSS signals in the voxels within the given time window. Hence, the design matrix is sparse, and the observation equation system of the tomography model is mixed-determined. Thus, physical meaningful constraints as well as external data sources should be applied. In this dissertation, the new dataset from the Geostationary Operational Environmental Satellite (GOES) sounder supplements the system of observation equations and consequently, the tomographic solution leads to an improved reconstructed wet refractivity field. Besides, this method is a kind of discrete ill-posed problem. So, all singular values of the structure matrix (A) in the tomography problem decay gradually to zero without any noticeable gap in the spectrum. Hence, slight changes in the measurements can lead to extremely unstable parameter solutions. In consequence, the regularization method should be applied to stabilize the inversion process and ensure a stable and unique solution for the tomography problem. The algebraic reconstruction techniques (ART) and the Total Variation (TV) method are examined to reconstruct a regularized solution with acceptable accuracy. Moreover, the TV method can also reconstruct a promising wet refractivity field without any initial field in a shorter time span. Thereby, retrieving the wet refractivity field using this method is also investigated. A further attempt is given to analyse the quality of the reconstructed field in GNSS tomography. To the author' best knowledge for the first time in GNSS tropospheric tomography, the spread of the resolution matrix is employed to assess the quality of the

retrieved wet refractivity solution without a need to use reference observations and calculate statistical measures like RMS and Bias in this method.

Kurzfassung

In den letzten Jahren hat sich das Globale Navigationssatellitensystem (GNSS) als ein wertvolles Instrument für die Fernerkundung der Atmosphäre erwiesen. In diesem Zusammenhang hat sich die GNSS-Tomographie zu einer äußerst vielversprechenden Technik entwickelt, um die räumlich-zeitliche Struktur der Troposphäre zu rekonstruieren. Daher kann diese Methode eine ausgezeichnete Alternative zur Überwachung von Wasserdampf und feuchten Refraktionsfeldern zu geringen Kosten und einer angemessenen räumlichen Auflösung im Vergleich zu konventionellen Beobachtungen, wie Radiosonden- und Radio-Okkultationsprofilen, bieten. Es gibt jedoch noch einige Herausforderungen und offene Fragen bei der GNSS-Tomographie, welche die Qualität des rekonstruierten Feldes stark beeinflussen. Daher besteht das Hauptziel dieser Dissertation darin, verschiedene Strategien zur Lösung einer Vielzahl dieser Probleme zu untersuchen.

Eine der Herausforderungen für die GNSS-Tomographie ist die wirtschaftliche Frage der Bereitstellung von Mehrfrequenzempfängern mit einer ausreichenden räumlichen Auflösung von einigen zehn Kilometern. Daher wird die Machbarkeit der Verwendung von Einzelfrequenzbeobachtungen in der GNSS-Tomographie als alternativer Ansatz untersucht. Eine weitere Herausforderung in der GNSS-Tomographie hängt von den verschiedenen Parametrisierungsmethoden zur Berechnung der Entwurfsmatrix ab. Daher werden die Auswirkungen der geometrisch geradlinigen Signalausbreitung Methode gegenüber der Ray-Tracing-Methode sowie die Auswirkungen der Berücksichtigung der Topographie im Tomographiemodell für die Berechnung der Entwurfsmatrix untersucht. Ein weiteres Augenmerk wird auf Multi-GNSS-Beobachtungen in der GNSS-Tomographie gelegt, da sich die Beobachtungsgeometrie im Vergleich zu einem GPS/GLONASS- Szenario verbessert. Daher wird der Einfluss verschiedener Konstellationen untersucht, um das feuchte Refraktionsfeld zu erhalten, wobei der Schwerpunkt auf der Hinzunahme von GALILEO liegt. Die GNSS-Tomographie leidet auch unter der unzureichenden räumlichen Abdeckung der GNSS-Signale in den Voxeln innerhalb des gegebenen Zeitfensters. Daher ist die Entwurfsmatrix spärlich besetzt, und das Beobachtungsgleichungssystem des Tomographiemodells ist gemischt-determiniert. Daher sollten sowohl physikalisch sinnvolle Einschränkungen als auch externe Datenquellen verwendet werden. In dieser Dissertation ergänzt der neue Datensatz des Geostationären Operationellen Umweltsatelliten (GOES) das System der Beobachtungsgleichungen, und folglich führt die tomographische Lösung zu einem verbesserten rekonstruierten feuchten Refraktionsfeld.

Außerdem handelt es sich bei der Troposphären-Tomographie um eine Art diskretes ungelöstes Problem. So zerfallen alle Singulärwerte der Strukturmatrix ($\boldsymbol{A}$) allmählich auf Null, ohne dass es zu einer merklichen Lücke im Spektrum kommt. Daher können geringfügige Änderungen in den Messungen zu extrem instabilen Parameterlösungen führen. Infolgedessen sollte die Regularisierungsmethode angewandt werden, um den Inversionsprozess zu stabilisieren und damit eine stabile und eindeutige Lösung für das Tomographieproblem zu gewährleisten. Die algebraischen

Rekonstruktionstechniken (ART) und die Methode der totalen Variation (TV) werden untersucht, um eine regularisierte Lösung mit akzeptabler Genauigkeit zu generieren. Darüber hinaus kann die TV-Methode auch das vielversprechende feuchte Refraktionsfeld ohne initiales Referenzfeld in einer kürzeren Zeitspanne rekonstruieren. Ein weiterer Versuch wird unternommen, um die Qualität des rekonstruierten Feldes in der GNSS-Tomographie zu analysieren. In dieser Dissertation wird nach bestem Wissen des Autors zum ersten Mal in der GNSS-Troposphären-Tomographie die Spreizung (spread) der Auflösungsmatrix verwendet, um die Qualität der abgerufenen Lösung für die feuchte Refraktivität zu bewerten, ohne dass Referenzbeobachtungen verwendet und statistische Maße wie RMS und Bias in dieser Methode berechnet werden müssen.

Contents

Chapter 1

1 Introduction

One of the most variable components in the Earth's atmosphere is water vapour , which has a remarkable role in the formation of clouds, rain, snow, and air pollution (Troller, 2004;Yao et al., 2016). Hence, improving the accuracy of the estimated water vapour could lead to more accurate predictions of severe weather conditions and precipitation, as well as enhancing the comprehension of the world's climate change by meteorologists (Brenot et al., 2014;Lutz, 2008;Manning et al., 2012;Norquist and Chang, 1994;Zhang, 1999). Various techniques like Lidar (Bock et al., 2001;Braun and Rocken, 2003;Tarniewicz et al., 2002), radiosonde, water vapour radiometer (Braun et al., 2003;Dodson et al., 1996), ground sensors (Herschke, 2002;Lutz, 2008;Troller, 2004), and radio occultation (Andrisaniand and Francesco, 2020;Turk et al., 2019;Wickert et al., 2002) have been applied to measure the spatio-temporal behaviour of this parameter. However, these methods have some disadvantages and limitations such as high cost or poor spatial-temporal resolution (Bai, 2004;Kačmařík and Rapant, 2012;Troller, 2004). Instead, Global Navigation Satellite Systems (GNSS) could help to overcome these drawbacks due to the continuous scans of the troposphere at a low cost with a reasonable precision and finer spatio-temporal resolution in comparison to the common techniques (Bevis et al., 1992;Dick et al., 2001;Douša, 2004;Hurter et al., 2012;Priego et al., 2017;Rocken et al., 1995;Wickert et al., 2021).

In the coming years, the number of available measurements from dense GNSS networks and new satellite constellations like GALILEO (Europe), Beidou (China), QZSS (Japan) or IRNSS (India) will dramatically increase (Sá, 2018). Analysing the signals of GNSS satellites provides tropospheric products such as Zenith Total Delay (ZTD), Slant Tropospheric Delay (STD), and Integrated Water Vapour (IWV) which can apply in atmospheric studies and particularly for meteorology and climatology. Nevertheless, all of the derived products from GNSS only monitor the behaviour of the troposphere in the zenith or slant directions of a satellite to a receiver without capturing spatial variability of the water vapour. To resolve this issue, the tomography technique, which integrates slant observations over a time span from a GNSS network, has been being investigated purposefully by different researchers to model the wet part of the troposphere in the high spatial and temporal domain. GNSS tomography is an all-weather condition emerging remote sensing method in the field of meteorology. Water vapour or the wet refractivity distribution in the troposphere can be assimilated in forecasting and nowcasting models. In this technique, the area of interest is divided into 3D elements (Voxel) in vertical and horizontal directions and then the measurements of the Slant Wet Delay (SWD) are integrated in the desired time period in order to reconstruct the behaviour of the wet refractivity in this time window (Rohm and Bosy, 2011;Troller, 2004). Over the past few years, the potential of using GNSS to specify the four dimensional (4D) wet refractivity and water vapour fields using Tomography has been evaluated in various studies (Adavi and Weber, 2019;Bender et al., 2011;Brenot et al., 2020;Ding et al., 2017;Flores, 1999;Gradinarsky and Jarlemark, 2004;Lutz, 2008;Manning, 2013;Möller, 2017;Nilsson et al., 2004;Perler, 2011;Rohm and Bosy, 2009;Rothacher et al., 1996).

1.1 Objectives and Contributions

The intent of this dissertation is to improve a 4D ground-based GNSS tomography technique in order to better understand the tropospheric structure which is essential for water vapour monitoring and nowcasting applications. The research of this thesis was motivated by analyzing and improving different features of the tomography model by taking into account current developments of tropospheric tomography infrastructures like parameterization and solving methodology. In this context, the following objectives and contributions have been considered:

1. Assessment of the GNSS tomography in different scale regions by considering topography and different parameterization methods
2. Feasibility of GOES-R products as a constraint in order to enhance the GNSS tomography solution
3. Evaluation of regularization techniques in GNSS tropospheric tomography based on single- and dual-frequency observations
4. Investigation of the impact of the GALILEO constellation in combination with GPS and GLONASS constellations to estimate the tropospheric delay and solve the ill-posed inverse problem to retrieve the wet refractivity field
5. Optimizing the temporal resolution of the tomography model by applying the Total Variation (TV) regularization method
6. Defining a new method to analyse the quality of the tomography solution using the concept of spread of the resolution matrix

1.2 Thesis outline

Aside of the introduction, this thesis consists of six chapters, which are demonstrated in brief as follows:

Chapter 2 gives an overview of the physical foundation of the troposphere with a focus on the characteristic of the GNSS signal propagation in this part of the atmosphere. The fundamental models to derive the tropospheric delays from the GNSS signals as well as tropospheric refractivity are explained in this chapter.

Chapter 3 provides the concept of GNSS tropospheric tomography and describes the mathematical basis for the solution as well as highlights the solving strategies for the tomography problem. Moreover, a literature review covering the remarkable research activities in this field is also reported in this chapter.

Chapter 4 presents the outline for special case studies which cover parts of two different continents, namely Europe and America. In addition, meteorological datasets like synoptic measurements and numerical weather models are described in this chapter. All these case studies together with the meteorological dataset provide a good foundation for Chapter 5 in order to investigate GNSS tropospheric tomography solutions.

Chapter 5 investigates the accuracy of the reconstructed tomography field by considering single frequency measurements in comparison to dual-frequency measurements, new datasets as a constraint, applying different parameterization methods, using different GNSS constellations, and performing a direct regularization method named Total Variation (TV) compared to iterative regularization methods. Moreover, a new proxy for the validation of the GNSS tomography model, namely 'spread', is also studied in this chapter.

Chapter 6 depicts the main conclusions from this work and also provides an outlook on possible future work which can be implemented in the GNSS tomography in order to enhance the accuracy of the reconstructed wet refractivity field.

1.3 PhD Presentation

The provided results and datasets in this dissertation are partly based on the published/under-review journal papers, which are listed as follows:

1. Adavi, Z., and Weber, R.: Evaluation of Virtual Reference Station Constraints for GNSS Tropospheric Tomography in Austria Region, Adv. Geosci., 50, 39-48, 10.5194/adgeo-50-39-2019, 2019.
2. Adavi, Z., Rohm, W., and Weber, R.: Analyzing Different Parameterization Methods in GNSS Tomography Using the COST Benchmark Dataset, IEEE Journal of Selected Topics in Applied Earth Observations and Remote Sensing, 13, 6155-6163, 0.1109/JSTARS.2020.3027909, 2020.
3. Adavi, Z., and Weber, R.: Application of the Total Variation Method in near real-time GNSS Tropospheric Tomography [under review], International Association of Geodesy Symposia,, 2022.
4. Adavi, Z., Weber, R., and Glaner, M. F.: Assessment of regularization techniques in GNSS tropospheric tomography based on single- and dual-frequency observations, GPS Solutions, 26, https://doi.org/10.1007/s10291-021-01202-2, 2022a.
5. Adavi, Z., Weber, R., and Rohm, W.: Pre-analysis of GNSS tomography Solution using the concept of Spread of Model Resolution Matrix, Journal of Geodesy, 10.1007/s00190-022-01620-1, 2022b.

Chapter 2

2 Physical Foundation and Propagation Characteristic of the Troposphere

The earth's atmosphere can be classified using the well-known features named: ionization, temperature, and propagation (Seeber, 1993). By considering the propagation of the radio waves in the atmosphere, two layers can be characterized: troposphere and ionosphere. The ionosphere is the upper part of the atmosphere which is a dispersive medium relative to the radio waves. Therefore, the propagation delay in this layer is frequency-dependent and in consequence, it can be eliminated using a linear combination of dual-frequency observables. The lower layer of the Earth's atmosphere is the troposphere which is a non-dispersive medium with respect to micro-waves signals. This layer of the atmosphere is also called the neutral atmosphere which is basically regarding the feature of the temperature profile.

The propagated GNSS signals are remarkably affected by the troposphere along the entire path to the GNSS receiver. As the troposphere is non-dispersive for micro waves frequencies, therefore, the tropospheric effects on the signal cannot be eliminated with multi-frequency observations. The troposphere could physically influence the signal in two ways: (1) delaying of the propagated rays because of the non-vacuum nature of the troposphere, and (2) bending the GNSS signals.

The fundamental knowledge about the troposphere and also the basic models of tropospheric delays and refractivity are presented in this chapter. Moreover, an overview of the current techniques to derive tropospheric features like wet refractivity and water vapour is provided here.

2.1 State of the Troposphere

The term troposphere was created in 1908 by Teisserenc de Bort and literally implies the sphere of turning, as the vertical motions (rising and descending air currents) in this layer are with respect to the vertical gradient of temperature(Lutgens et al., 2018). In fact, as shown in Fig 2. 1, different layers of the atmosphere and particularly the troposphere, can be determined as function of temperature relative to the height. According to this figure, the troposphere is the layer between the sea level $\approx 0\ meter$ and the upper atmosphere, where the temperature reduces linearly by increasing height with the gradient of about $-6.5\ K/km$ (Wallace and Hobbs, 2006). The actual value of this temperature gradient depends on the season, height, and also geographical location(Mendes, 1999). Moreover, the upper boundary of the troposphere is the first temperature minimum which is a function of the latitude and seasons. In general, the maximum value of the tropospheric height occurs at the equator and summertime, and its minimum value shows up in the Polar Regions and wintertime (Dowling and Showman, 2007;Hall et al., 2011).

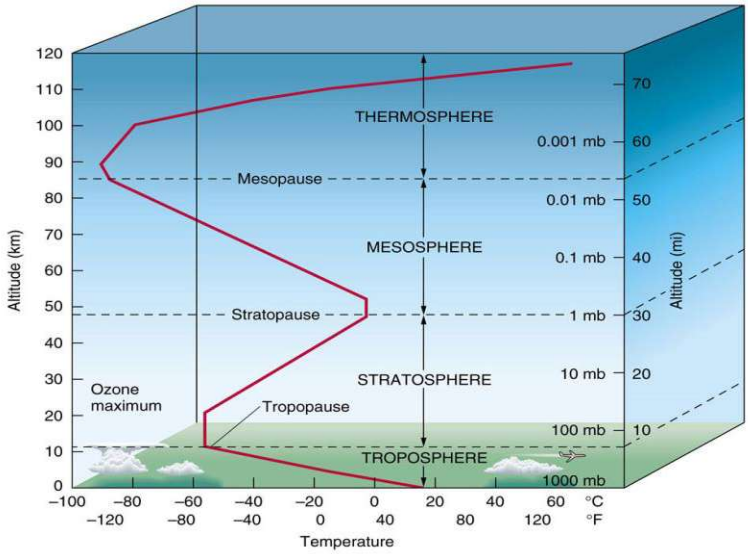

Fig 2. 1. Typical atmospheric temperature profile of the earth, taken from (Talkshop, 2014)

This lowermost layer of the atmosphere is in the main focus of meteorologists and climatologists due to the occurrence of all important weather phenomena in this layer (Lutgens et al., 2018). All violent storms, precipitation, rain, snow, hurricanes, and almost all clouds happen in this layer of the atmosphere (Hoyle, 2005;Lutgens et al., 2018;Möller, 2017). Troposphere encompasses about 80% of the total mass of the atmosphere and also nearly all the aerosols and water vapour (Fleagle and Businger, 1980;Wallace and Hobbs, 2006). According to the composition of the troposphere, this layer can be subdivided into two constituents named dry air (mixture of nitrogen, oxygen and organ as the major constituents) and water vapour (Lutz, 2008;Mendes, 1999;Zhang, 1999). Using the ideal gas law and the hydrostatic equation, dry air gases and water vapour are modelled in hydrostatic equilibrium (Kleijer, 2004;Zhang, 1999).

For the ideal (perfect) gases, the equation of state is defined as follows (Kleijer, 2004):

$$\alpha\, P = R_m\, T \tag{2.1}$$

with

α : Specific volume $[m^3\, kg^{-1}]$

P : Pressure $[N\, m^{-2}]$

R_m : Specific gas constant $[J\, kg^{-1}\, K^{-1}]$

T : Temperature $[K]$

The specific volume α is formulated as:

$$\alpha \doteq \frac{1}{\rho} \doteq \frac{V}{m} \tag{2.2}$$

where ρ $[kg\, m^{-3}]$, V $[m^3]$ and m $[kg]$ are density, volume , and mass, respectively. Applying Eqs. (2.1) and (2.2), the equation of state, for both water vapour and dry air are obtained as detailed:

$$e = \rho_v R_v T \tag{2.3}$$

$$P_d = P - e = \rho_d R_d T \tag{2.4}$$

whereby:

P_d : Partial pressure of dry air $[N\ m^{-2}]$

e : Partial pressure of water vapour $[N\ m^{-2}]$

R_d : Specific gas constant of dry air $[J\ kg^{-1}\ K^{-1}]$

R_v : Specific gas constant of water vapour $[J\ kg^{-1}\ K^{-1}]$

Here, $R_d = 287.06 \pm 0.01\ [J\ kg^{-1}\ K^{-1}]$, and $R_v = 461.525 \pm 0.003\ [J\ kg^{-1}\ K^{-1}]$.

The specific humidity $q\ [g/kg]$ depicts another way to express the humidity as follows (Kleijer, 2004;Möller, 2017):

$$q = \frac{\rho_v}{\rho} = \frac{0.622\ e}{P - 0.378\ e} \tag{2.5}$$

In addition, by applying the equation of state for moisture, we end up with the following equation:

$$P = \rho_m R_m T \tag{2.6}$$

where $\rho_m\ [kg\ m^{-3}]$ is the density of moisture air. As $\rho_m = \rho_d + \rho_v$, R_m can be defined as below:

$$R_m = R_d (1 + 0.61\ w) \tag{2.7}$$

Here $w\ [-]$ denotes a mixing ratio. If we introduce Eq. (2.7) in Eq. (2.6), we obtain:

$$P = \rho_m R_d T_v \tag{2.8}$$

where $T_v\ [K]$ is the virtual temperature as defined below:

$$T_v \doteq (1 + 0.61\ w)\ T \tag{2.9}$$

In a closed system, when the number of water molecules leaving the surface equals the number of returning molecules, the air reaches an equilibrium called saturation (Kleijer, 2004;Lutgens et al., 2018). The saturation vapour pressure is an empirical function of temperature and given as (Kleijer, 2004;Schüler, 2001):

$$e_{sat} = 6.112\ exp\left[\frac{17.62\ t}{243.12 + t}\right] \tag{2.10}$$

where t is temperature in [℃]. Using this parameter, the relative humidity ($RH\ [-]$) can be expressed as:

$$RH \approx \frac{e}{e_{sat}} \tag{2.11}$$

Therefore, the troposphere is a function of temperature T, air pressure P, and water vapour pressure e. Fig 2. 2 shows the profiles of these parameters with respect to the height. According to this figure, the dry part of the troposphere is more easily predictable because the air pressure and temperature have stable quantities. In the wet part of the troposphere, the water vapour pressure between the earth's surface up to about 10 km height is variable over time and also location. Therefore, this part of the atmosphere cannot be modelled straightforwardly.

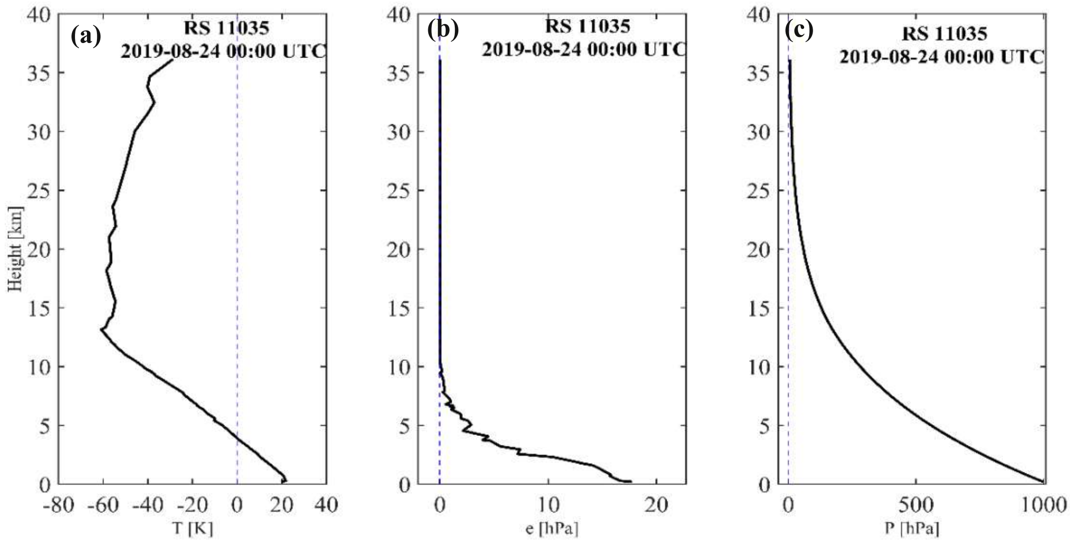

Fig 2. 2. Profiles of temperature T (a) , partial water vapour pressure e (b) and air pressure (c) on August 24th, 2019 at 00:00 UTC for RS11035 located at the Vienna airport

2.2 The Water Vapour Distribution in the Troposphere

Water can emerge in three physical states in the troposphere: ice crystals, liquid droplets, and water vapour. The most variable form of the water is vapour. This parameter is highly variable both temporally and spatially, and therefore remains challenging to modelling. Almost all water vapour is placed up to about 2 km above the surface and only less than 5% of this quantity could be discovered above 5 km (Kleijer, 2004;Shangguan, 2014;Treuhaft and Lanyi, 1987).

Water vapour is a key parameter in the water cycle of the earth. As shown in Fig 2. 3, the evapotranspiration of water sources on the earth is the reason for producing water vapour(Guerova, 2003;Lutgens et al., 2018).

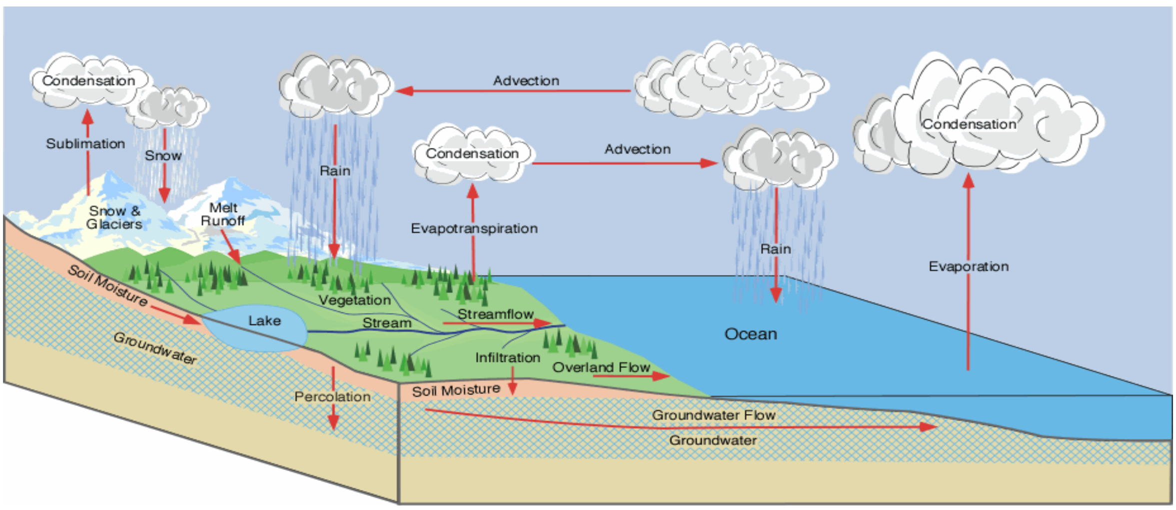

Fig 2. 3. Water cycle of the water vapour (Guerova, 2003)

The evapotranspiration contains sublimation from snow, transpiration from vegetation evaporation, and ice surfaces and ocean and lakes (Guerova, 2003). Therefore, the water cycle happens as condensation and precipitation in the form of snow or rain and emanating again by transpiration, sublimation, and evaporation (Guerova, 2003;Lutgens et al., 2018;Troller, 2004). In this content, water vapour plays an essential role in the climatological studies over long and short periods as well as numerical weather prediction (Guerova, 2003). Hence, observing the tropospheric water vapour to produce a time series along with its spatial distribution is of essential importance for the climate and atmosphere studies (Troller, 2004). Responding to this demand, some techniques and instruments have been developed to directly determine the tropospheric water vapour. Table 2. 1 demonstrates some of these techniques and instruments. In this table, the limitations and advantages of different techniques are presented.

Table 2. 1. Key characteristics of different techniques and instrument to measure the water vapour (table adapted from (Champollion et al., 2005;Heublein, 2019;Sá, 2018)

Technique/Instrument	Observations Conditions	Horizontal Resolution	Cost	Time Resolution
Radiosonde	All	Low	High	Low
Ground Sensor	Clear Sky	High	High	Low
Airborne	Clear Sky	Low	High	Low
Spaceborne (Satellite Image)	Clear Sky	High	High	Low
Solar Spectrometer	Clear Sky	Low	High	Low
Water Vapour Radiometer	Clear Sky	Low	High	Low
Radio Occultation	All	Low	High	Low
GNSS (IWV)	All	High	Low	High
GNSS Tomography	All	High	Low	High

According to Table 2. 1, GNSS tomography could provide 4D spatio-temporal information of water vapour in all-weather conditions with an almost reasonable resolution which is also beneficial concerning time and cost aspects in comparison to other techniques. Therefore, the main focus of the thesis is on GNSS tomography. Moreover, the different aspects and progress of this method will be discussed here.

2.3 Interactions of GNSS radio waves and the Troposphere

The troposphere influences the GNSS signals due to the interaction between the radio waves and this part of the atmosphere. The effect of the troposphere on the GNSS rays causes the variability of the refractive index and therefore this parameter plays an essential role in the propagation of radio waves within the troposphere. On one hand, as the refractivity index is larger than unity, the velocity of the ray's propagation speed is decreased when approaching the earth's surface (slowing). On the other hand, the trajectory of the radio signal deviates from the straight line due to the continuous variation of the refractive index (bending). The combination of these two impacts on GNSS signals is called propagation delay or tropospheric refraction (d_{trp}). Fig 2. 4 presents the bending of the path of a radio wave due to refractivity index variations.

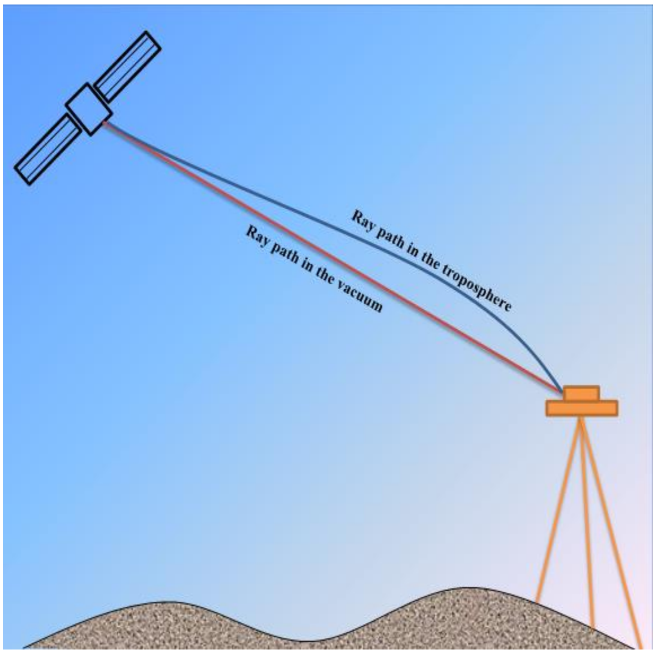

Fig 2. 4. GNSS signal Propagation through the atmosphere

The tropospheric refraction can be computed as follows (Hoyle, 2005;Mendes, 1999;Troller, 2004):

$$d_{trp} = \underbrace{\int_{rec}^{sat} [n(s) - 1]\ ds}_{slowing} + \underbrace{[S - G]}_{bending} \tag{2.12}$$

where S and G are the curved path and the geometric path, respectively. ds is a differential element of length (s) along the ray trajectory between satellite (sat) and receiver (rec). The second term in Eq. (2.12), sometimes called geometric delay, is only considerable for radio waves with low observation angles below 10°. Moreover, for a horizontally stratified troposphere, this geometric delay vanishes in the zenith direction (Mendes, 1999). Hence, Eq. (2.12) could be simplified to:

$$d_{trp} = \int_{rec}^{sat} [n(s) - 1]\ ds \tag{2.13}$$

As the refractive index is very close to one, it is frequently replaced with a parameter that is easier to work called refractivity ($N\ [ppm]$):

$$N \equiv 10^6\ (n - 1) \tag{2.14}$$

Therefore, Eq. (2.13) can be reformulated as noted below:

$$STD = 10^{-6} \int_{rec}^{sat} N\ ds \tag{2.15}$$

where $STD\ (= d_{trp})$ is the abbreviation of Slant Total Delay. According to Eq. (2.15), the STD is dependent on the refractivity along a satellite to receiver path. This parameter is mainly specified by three meteorological parameters: temperature, pressure and water vapour pressure:

$$N = \underbrace{\left[k_2\left(\frac{e}{T}\right) + k_3\left(\frac{e}{T^2}\right)\right]}_{N_w} + \underbrace{k_1\left(\frac{p_d}{T}\right)}_{N_h} \tag{2.16}$$

Therefore, the refractivity can be separated into a wet (N_w) and hydrostatic component (N_h):

$$N = N_w + N_h \tag{2.17}$$

In Eq. (2.16), k_2 and k_3 are the factors of the wet contribution in the total wet refractivity and k_1 relates to the dry part of the troposphere. These factors were re-computed over the decades and one of the most commonly used parameter sets has been published by (Rüeger, 2002):

$k_1 = 77.689\ ^2 \pm 0.0094\ [K/hpa]$
$k_2 = 71.2952 \pm 1.3\quad [K/hpa]$
$k_3 = 375463\ \pm 760\quad [K/hpa]$

Fig 2. 5 demonstrates the variation of wet refractivity and dry refractivity. According to this figure, the wet part of refractivity is almost negligible above 10 km but has a considerable amount in the lowest 5 km. However, the dry part of refractivity shows a smooth behaviour with height and it contributes significantly from ground up to 35 km.

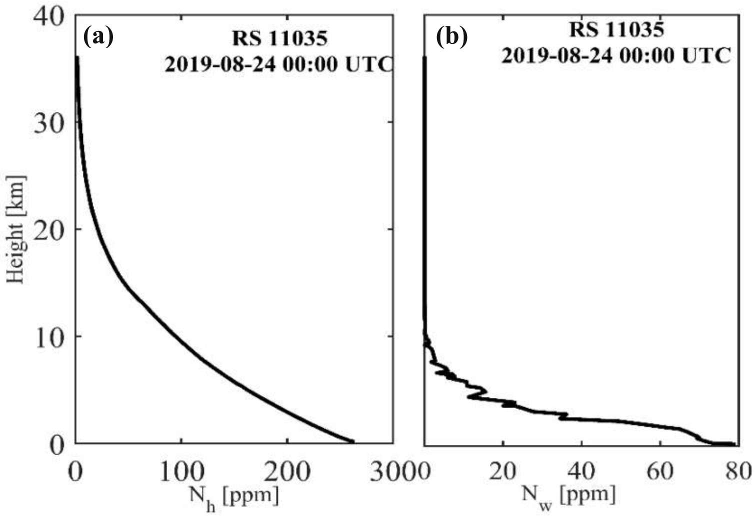

Fig 2. 5. Profiles of hydrostatic refractivity (a) and wet refractivity (b) on August 24th, 2019 at 00:00 UTC for RS11035 located at the Vienna airport

Substituting Eq. (2.17) in Eq. (2.15) gives:

$$STD = \underbrace{10^{-6} \int_{sat}^{rec} N_h ds}_{SHD} + \underbrace{10^{-6} \int_{sat}^{rec} N_w ds}_{SWD} \tag{2.18}$$

or symbolically can be written as follows:

$$STD = SHD + SWD \tag{2.19}$$

whereby Slant Wet Delay (SWD) and Slant Hydrostatic Delay (SHD) are the delays caused by the dry and wet part of the troposphere along the signal path.

2.4 Modelling the Path Delay of GNSS Signals

When modelling the path delays of GNSS signals, two different aspects have to be considered:

- Error source: Adverting effects on the performance of GNSS satellites reduces the accuracy of GNSS positioning.
- Information source: Propagation of the radio waves in the troposphere can provide some valuable information about random disturbances and also characteristics in this medium.

Therefore, the tropospheric impact on a GNSS signal should be identified and modelled. However, computing the path delay using the integrals defined in Eq. (2.18) requires the determination of the refractivity along the ray trajectory. This technique is time-consuming and typically not applicable. Therefore, several models have been established which compute the path delay using just a few parameters. In the following, we describe models for the path delay in the zenith direction. Moreover, the mapping function and tropospheric gradients are described here, as well.

2.4.1 Hydrostatic Delay Model

The hydrostatic component of the propagation delay in zenith direction is around 2.2 meters at sea level. Assuming a Zenith Total Delay (ZTD) of roughly 2.4 meters, then this part of the delay accounts for almost 90% of the total delay and refers to Zenith Hydrostatic Delay (ZHD).

ZHD can be obtained accurately using meteorological surface measurements like pressure or/and temperature which depends on the hydrostatic model. The various hydrostatic models differ mainly due to the assumptions made regarding the vertical hydrostatic refractivity profile. However, most of these models have no remarkable difference as they are just using different refractivity constants. Therefore, only two well-known strategies to model this part of the delay are described in this section.

•Saastamoinen

The hydrostatic component of the ZTD can be estimated with accuracy from millimetre to sub-millimetre, using the Saastamoinen model if precise measurements of surface pressure (P_s) are available. This model is most commonly used in the geodetic techniques and reads as follows (Saastamoinen, 1973):

$$ZHD\ [m] = \frac{(0.0022768)\ P_S[hPa]}{1-0.0026\ \cos 2\varphi - 0.00028\ H_S} \tag{2.20}$$

where, $\varphi\ [deg]$ and $H_s[km]$ are the latitude and orthometric height, respectively.

• Hopfield

Another most commonly used model for the hydrostatic delay is the Hopfield model. This model implies the assumption of quartically expression of dry refractivity (Hopfield, 1969;Mendes, 1999). The ZHD of the Hopfield model reads as noted below (Hopfield, 1969;Schüler, 2001):

$$ZHD\ [m] = \left(\left(\frac{0.62291}{T_S[K]}\right) + 0.0023081\right) P_S[hPa] \tag{2.21}$$

where $T_s\ [K]$ is the surface temperature.

2.4.2 Wet Delay Model

The wet component of the total delay is much smaller than the ZHD and therefore it forms solely 10% of the total delay. Moreover, modelling of this parameter from meteorological surface measurements is extremely difficult due to the strong variation in time and space. In fact, Radiosonde (RS) ascents were analysed for the definition of most models of the wet part. Here, we only present the wet components of the tropospheric total delay of the models mentioned before.

•Saastamoinen

This model was proposed by Saastamoinen (1973) and it has two important assumptions: (1) linear decrease of temperature with height, and (2) a decrease of the water vapour pressure with height. Based on that, the Saastamoinen model of ZWD reads as follows (Mendes, 1999;Saastamoinen, 1973):

$$ZWD\,[m] = 0.0022768\left(\frac{1255}{T_s[K]} + 0.05\right) e_s[hpa] \tag{2.22}$$

where e_s is the surface water vapour pressure.

• Hopfield

Hopfield used a similar procedure as before. She derived the wet zenith delay based on the quartic atmospheric profile, which defines the wet component of refractivity (N_w) as a fourth-degree function of height above the geoid(Hopfield, 1969, 1971, 1972;Schüler et al., 2001):

$$ZWD\,[m] = \left[555.7 + 1.792\,.\,10^{-4}\,.\,exp\left(\frac{t_s[°C]}{22.90}\right)\right].\frac{e_s[hpa]}{T_s^2\,[K^2]} \tag{2.23}$$

It should be noted that the accuracy of these models is not better than a few centimetres (Ghoddousi-Fard, 2009). Therefore, this parameter is generally considered as unknown in GNSS data processing due to the difficulty to estimate high accurate ZWD from the wet models. Then, using the estimated ZTD from the processing of the measurements and computed ZHD from hydrostatic models like Saastamoinen, ZWD can be calculated:

$$ZWD = ZTD - ZHD \tag{2.24}$$

2.4.3 Horizontal Gradient

Up to now, the troposphere was assumed to be azimuthal symmetric and horizontally layered. This assumption is appropriate for most applications. However, azimuthal asymmetry can cause significant errors in geodetic measurements. For example, this is one of the largest error sources in raytracing, mainly for low elevation angles (Kleijer, 2004). A most common way to deal with these asymmetries is to estimate horizontal gradients, which denote approximately the partial derivative of the ZWD with respect to the latitude and longitude (Dach et al., 2015;Zus et al., 2019). In the year 1973, Saastamoinen calculated theoretically the maximum magnitude of the horizontal gradient of 2 cm at 10° which was comparable to a zenith delay error of fewer than 4 mm (Saastamoinen, 1973). Therefore, it is essential to account for this error source for low elevation angles. The most common way to model these asymmetries is horizontal gradients estimation (Dach et al., 2015;Mendes, 1999). One method to represent the azimuthal asymmetry is to consider a tilted troposphere (see Fig 2. 6).

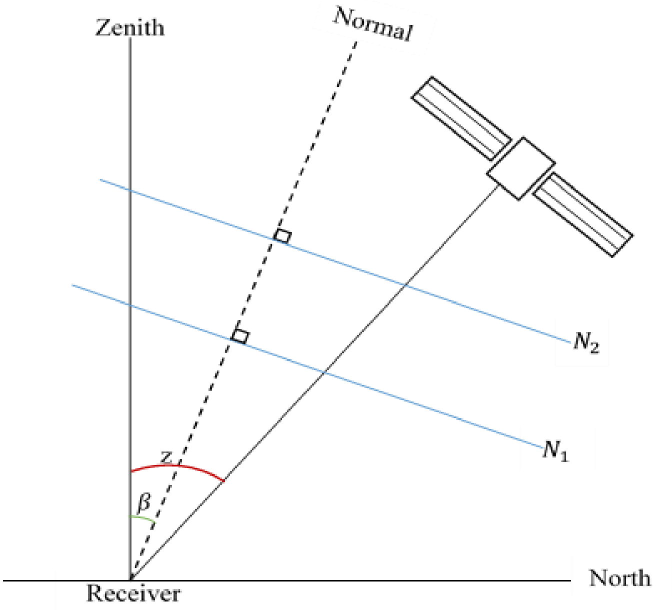

Fig 2. 6. Tropospheric layers of refractivity N_1 and N_2 tilted by the angle β, where β is the small angle between the geometric zenith direction and tropospheric normal direction

Having assume β is small ($\cos\beta \cong 1$), we can write (Meindl et al., 2004;Mendes, 1999;Zhang et al., 2021):

$$\tilde{z} = z + \delta z = z + \beta \cos(\alpha - \alpha_0) \tag{2.25}$$

$$= z + \beta \cos\alpha_0 \cos\alpha + \beta \sin\alpha_0 \cos\alpha$$

where $\tilde{z}$ represents the zenith angle with respect to the normal direction, and α_0 denotes the azimuth of the tropospheric normal direction with respect to the geometric zenith direction. Moreover, z and α are the zenith and azimuth angles of the signal, respectively. With definition of $x = \beta\cos\alpha_0$ and $y = \beta \sin\alpha_0$, Eq. (2.25) can be stated as follows (Meindl et al., 2004;Mendes, 1999):

$$\tilde{z} - z = \delta z = x\cos\alpha + y\cos\alpha \tag{2.26}$$

and then by using Taylor series, the following expression can be defined for the gradient delay in a tilted tropospheric layer (Kleijer, 2004;Dach et al., 2015;Meindl et al., 2004):

$$STD_\alpha \approx \underbrace{MF_\alpha(z)\ \tan z}_{Mapping\ \ function} \left(\underbrace{\vec{G}.[\cos\alpha\ \sin\alpha]}_{Gradient\ delay} \right) \tag{2.27}$$

where $\vec{G} \doteq [G_N; G_E]$ is a gradient vector in the opposite direction of the projected normal (Kleijer, 2004) where G_N and G_E are the north and east components of that. Accordingly, the second part of Eq. (2.27) can be defined as listed below (Kleijer, 2004;Mendes, 1999):

$$G(\alpha) \doteq \vec{G}.[\cos\alpha\ \sin\alpha] = G_N\cos\alpha + G_E \sin\alpha \tag{2.28}$$

Therefore, the gradient delay due to the azimuthal asymmetry is composed of a north and an east component.

An azimuthal mapping function due to the tilted troposphere was proposed by (Chen and Herring, 1997):

$$MF_\alpha(z) = \frac{1}{\cos z\ \cot z + 0.0032} \tag{2.29}$$

2.4.4 Mapping Functions

In order to map a tropospheric delay in zenith direction to a slant delay at different elevation angles (ε), mapping functions are applied. According to Fig 2. 7, the simple approximation of the mapping function is the inverse of the sine function of the elevation angle ε:

$$MF(\varepsilon) = \frac{1}{\sin\varepsilon} \tag{2.30}$$

which is acceptable for elevation angles above ~15° (Skone, 2003). Therefore, ZTD can be transformed to STD using a mapping function as follows:

$$STD = MF(\varepsilon)\, ZTD \tag{2.31}$$

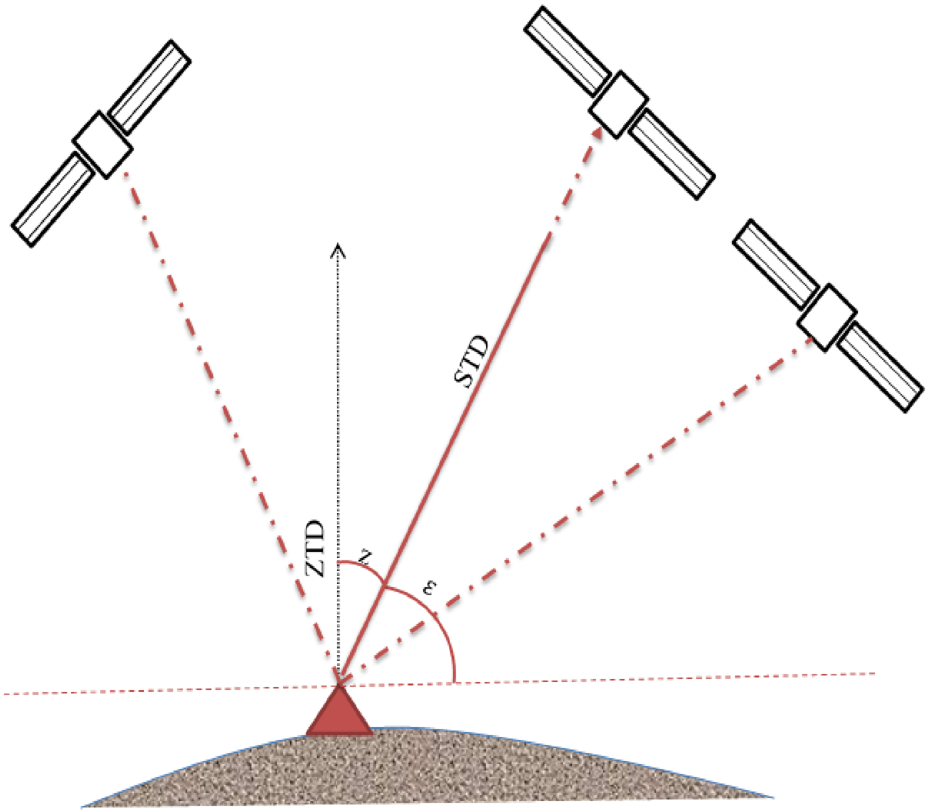

Fig 2. 7. Map ZTD to STD at the specific elevation angle

In the past 25 years, a number of researchers have developed more accurate mapping functions (Böhm et al., 2006a;Böhm and Schuh, 2004a;Davis et al., 1985;Ifadis, 1992;Landskron and Böhm, 2018;Marini, 1972;Niell, 1996). Eq. (2.32) shows the conventional form of mapping functions for the dry and wet part of the delay with three coefficients a, b and c, for a given elevation angle ε (Herring, 1992;Marini, 1972;Niell, 1996, 2001):

$$MF(\varepsilon) = \frac{1+\frac{a}{1+\frac{b}{1+c}}}{\sin\varepsilon+\frac{a}{\sin\varepsilon+\frac{b}{c+\sin\varepsilon}}} \tag{2.32}$$

The three coefficients a, b and c differ for the wet and dry part due to the different thickness of both parts of the troposphere (Mendes, 1999). Table 2. 2 displays a list of input parameters required for the hydrostatic mapping function and the wet mapping function of three different mapping functions (Böhm and Schuh, 2004b):

Table 2. 2. Input parameters for NMF, IMF and VMF mapping functions

Name / Type	Niell Mapping Function (NMF)	Isobaric Mapping Function (IMF)	Vienna Mapping Function (VMF)
Hyd.	DoY, h, φ	z_{200}, h, φ	h, a_h $(, b_h, c_h)$
Wet.	φ	$smfw_3, h$	a_w $(, b_w, c_w)$

In Table 2. 2, z_{200} is the height of the $200\ hPa$ level and $smfw_3$ is computed using a Numerical Weather Model (NWM) at each grid point by the following formula (Niell, 2003):

$$smwf_3 = \frac{losw}{zwd} \tag{2.33}$$

with

$$losw = 0.5\ \sum_{i=2}^{N}[N_w(h_i) + N_w(h_{i-1})]\,.\big(s(h_i) - s(h_{i-1})\big) \tag{2.34}$$

$$ZWD = 0.5\ \sum_{i=2}^{N}[N_w(h_i) + N_w(h_{i-1})]\,.(h_i - h_{i-1}) \tag{2.35}$$

whereby N_w is the wet refractivity and s is the distance along the geometric signal path at an elevation of 3.3°. Moreover, h_i denotes the height of the i^{th} pressure level.

The coefficients of the VMF function are calculated optimally based on direct ray-tracing through the European Centre for Medium-range Weather Forecasts (ECMWF) model data (Böhm and Schuh, 2004a;Böhm et al., 2006b). For the hydrostatic VMF, the coefficients b_h and c_h are extracted from the dry part of the IMF as follows (Böhm and Schuh, 2004a;Niell, 1996):

$$b_h = 0.002905 \tag{2.36}$$

$$c_h = c_0 + \left[\left(\cos\left(\frac{DoY-28}{365}\,.2\pi + \psi\right) + 1\right).\frac{c_{11}}{2} + c_{10}\right].(1 - \cos\varphi) \tag{2.37}$$

and the coefficients b_w and c_w of the wet VMF, are taken from the non-hydrostatic part of the NMF as shown below (Böhm and Schuh, 2004a;Niell, 2001):

$$b_w = 0.00146 \tag{2.38}$$

$$c_w = 0.04391 \tag{2.39}$$

The coefficients a_h, a_w can be calculated by inverting Eq. (2.32) with b and c fixed as above (Böhm and Schuh, 2004a). All mentioned coefficients are computed every six hours and therefore this mapping function is available in near real-time.

In this thesis, the VMF1 mapping function is applied to compute STD by Eq. (2.40) due to:

- ✓ Applying a mapping function based on the numerical weather model (IMF and VMF) is more reasonable than other choices (NMF) because of better repeatability of station height and baseline lengths
- ✓ Improving VMF due to the exploitation of this mapping function with the full information of the NWM

$$STD = VMF1_h(\varepsilon).ZHD + VMF1_w(\varepsilon).ZWD + MF_\alpha(\varepsilon).[G_N\cos\alpha + G_E\sin\alpha] \tag{2.40}$$

Moreover, the Slant Hydrostatic Delay (SHD) and the Slant Wet delay (SWD) can be calculated as follows:

$$SHD = VMF1_h(\varepsilon).ZHD + MF_\alpha(\varepsilon).\left[G_{N_h}\cos\alpha + G_{E_h}\sin\alpha\right] \quad (2.41)$$

$$SWD = VMF1_w(\varepsilon).ZWD + MF_\alpha(\varepsilon).\left[G_{N_w}\cos\alpha + G_{E_w}\sin\alpha\right] \quad (2.42)$$

where G_{N_h} and G_{E_h} are the hydrostatic horizontal gradients and G_{N_w} and G_{E_w} are the wet horizontal gradients.

Chapter 3

3 GNSS Tropospheric Tomography

Due to the development of GNSS (more satellites, more signals and more stations), some researchers have been focusing on employing the slant measurements to determine the three-dimensional (3D) behaviour of water vapour. This kind of 3D field reconstruction from combined measurements is denoted as tomography, an approach that has been mostly applied in medicine for imaging the human body, like Magnetic Resonance Imaging (MRI). GNSS tomography is a promising and developing method to determine the spatio-temporal behaviour of the water vapour of the troposphere using the tropospheric slant wet delay (SWD) along the lines-of-sight to each satellite. Therefore, the principle input data for GNSS tomography is the GNSS ray path and the tropospheric signal delay. Using these observations, the most important but highly variable key element of the troposphere, water vapour, can be modelled in terms of temporal variation and spatial distribution. In addition, increasing the length of the derived delay time series allows to apply GNSS tomography results for long term meteorology studies.

For modelling wet refractivity field (N_w) using the tomographic technique, the troposphere is discretized to a finite number of 3D elements, named voxels. Then, GNSS signals passing through each voxel are used to retrieve the spatial and temporal behaviour of the wet refractivity.

In the following sections, some important studies and notable progress in GNSS tomography are explained. Then, the most significant features in the tomography techniques like defining the equation system and tomography model are described. After that, the mathematical basis for the tomography solution as well as the solving strategy is investigated. Finally, the statistical evaluation of the reconstructed wet refractivity field is discussed.

3.1 State of the Art in GNSS Tomography

Over the past two decades, several methods have been developed in order to determine the 3D structure of the tropospheric wet refractivity. According to that, the most significant features of the GNSS tomography can be divided into four parts: the datasets and constraints used to solve the tomography problem (observations), selection of optimal dimensions of voxels and the design of the tomography model (parameterization), how to formulate and regularize the tomographic problem (inversion), and evaluation. Therefore, in the following, the most important studies regarding these features are presented separately.

3.1.1 Constraints and Additional Data Sources

As GNSS signals cannot cover all the model elements in GNSS topography, therefore some constraints and additional data sources should be utilized in order to achieve the solution for all voxels. In this regard, both Flores et al. (2000a) and Gradinarsky and Jarlemark (2004) used horizontal and vertical smoothing constraints as well as a boundary constraint to ensure zero refractivity above a certain height. Braun and Rocken (2003) used a single-frequency GPS Network together with Raman LIDAR observations to estimate four-dimensional (4D) images of water vapour density. In the year 2004 and in the following years the work of the French group within the framework of the ESCOMPTE program (Kačmařík and Rapant, 2012;Cros et al., 2004), Champollion et al. (2005)

applied the standard atmosphere as a vertical constraint for mid-latitudes. Moreover, they proposed using surface meteorological observations for the reconstruction of wet refractivity in the lowest layer. Another research group in China applied the output of a numerical weather model (NWM) as a priori knowledge for wet refractivity reconstruction using the GNSS tomography technique (Song et al., 2006). Besides, they defined horizontal smoothing constraints by considering a certain degree of correlation between adjacent cell elements based on the Gaussian weighted mean using controllable width. In the year 2006, the average results of all radiosonde profiles over a certain time of interest used as a priori information in the GNSS tropospheric tomography (Bi et al., 2006). Rohm and Bosy (2011) extracted a set of parameters for the observation equation system of the tomography problem using the analysis of airflow. In year 2013, Rohm proposed an unconstrained method for GNSS tomography using the combination of successive epochs of data (Rohm et al., 2013).

Xia et al. (2013) suggested applying water vapour profiles above 2 km from radio occultation into the observation equation system to overcome the issue of an ill-posed structure matrix in the tomography problem. In the year 2014, Adavi and Mashhadi-Hossainali applied the Virtual Reference Stations (VRS) as an additional synthetic observation to estimate a unique wet refractivity field of the tropospheric tomography model (Adavi and Mashhadi-Hossainali, 2014).

Some researchers used the estimated Integrated Water Vapour (IWV) values from interferometric synthetic aperture radar (InSAR) to improve the efficiency of the tomography solution (Benevides et al., 2015b;Douša, 2004;Hurter et al., 2012). In the following, Benevides et al. (2015a) applied high-resolution water vapour from a moderate-resolution imaging spectroradiometer (MODIS) to improve the accuracy of the reconstructed tomography field. In the year 2018, Radiosonde and Atmospheric Infrared Sounder (AIRS) were used to initialize and update a 3-D tropospheric wet refractivity field. Jaberi Shafei and Mashhadi-Hossainali (2020) used reflected signals from an air-borne reflectometry mission as an additional constraint in the tropospheric tomography to achieve a unique solution. Based on their results, the accuracy of the reconstructed field is sufficient, however the reflectometry data should be checked during severe weather conditions before the reconstruction step.

3.1.2 Voxel Design

In order to model the wet refractivity in the troposphere, this layer should be spatially divided into a number of voxels. It is assumed that the wet refractivity amount in each voxel will stay constant during the study time period. Therefore, voxel design is one of the effective parameters to optimize the modelling of wet refractivity. In this respect, during the past two decades, some researchers have proposed several methods for the voxel design in the GNSS tomography. In the year 2000, Seko et al. introduced a moving cell method to improve the distribution of the path-crossed voxels impartially. In their method, all cell elements moved with the same speed of the precipitation system for a suitable period. In that case, all voxels translated at the speed of the precipitation system, and therefore due to the movement of cell elements, and due to changes of the GPS station geometry, the path lengths in each voxel are time-dependent (Seko et al., 2000). The moving cell method to design the tomography time-dependent model was further improved by Priego et al. (2017) and Noguchi et al. (2004) for local-scale phenomena up to a time resolution of 10 min. In their work, the whole tomography model moved with the speed of the horizontal wind velocity. Nevertheless, in this method the effect of vertical wind cannot be resolved due to the complex and unpredictable inherent of the wind velocity. In the year 2004, Troller defined open voxels for each horizontal layer to prevent leaving rays from the model boundaries (Troller, 2004). By doing this, all signals are crossing voxels from the upper to the lower layers of the tomography model.

Bi et al. (2006), Bender and Raabe (2007) and Ghafari Razin and Voosoghi (2020) showed that the spatial resolution of the tomography model is very sensitive to the density of the GNSS network and the number of available GNSS satellites and stations. They suggested to define the horizontal resolution of the tomography model based on the distance between neighbouring stations to increase the number of crossed voxels by signal rays. In the year 2013, Manning proposed to use an exponential model to define the vertical resolution instead of using a lower number of levels as well as equidistant spacing as it leads to better results (Manning, 2013). Adavi and Mashhadi-Hossainali (2014) used the model space resolution matrix to define the optimum horizontal resolution for the tomography model due to the dependency of this matrix to the property of the design matrix of the tomography problem. According to their results, the optimum spatial resolution can be achieved when the resolution matrix is close to identity. Chen and Liu (2014) proposed a technique to improve the model elements distribution in both vertical and horizontal directions and subsequently enhanced the tomography reconstruction. In their method, the optimum resolution is defined according to finding the maximum number of ray-crossing of voxels in both longitude and latitude directions. In the vertical direction, the optimal vertical resolution and the maximum height of the tomography model are obtained based on the computed water vapour from radiosonde data. In the year 2016, Yao and Zhao recommended a novel, optimized method of voxel division for the tropospheric tomography. In this method, the vertical boundary is defined like Chen and Liu (2014) based on the derived water vapour for a long time period (Yao and Zhao, 2016). In the horizontal domain, the concept of non-uniform symmetrical division of horizontal voxels is considered to increase the total number of voxels crossed by rays.

Zhao et al. (2020) proposed an innovative method using Adaptive Node Parameterization (ANP) using a combination of three meshing techniques to dynamically adjust both the boundary of the tomographic region and the position of nodes at each tomographic epoch. The three meshing methods are boundary extraction, Delaunay triangulation, and force-displacement algorithm. Based on their research, this method could improve the performance of the tomography solution. In the year 2020, Wang et al. proposed 'The High Flexibility GNSS Tomography (HFGT)' method to define the GNSS tomography model to adapt the size of the GNSS network (Wang et al., 2020). In this method, the tomography region and its spatial division at each tomography window is defined based on the distribution of the GNSS signals in real time.

3.1.3 Solving Methodology and Regularization

Since the year 2000, a number of methods have been developed to reconstruct the tropospheric structure using the GNSS tomography, which mainly focuses on the regularization techniques and solving methodology. In this regard, in 2000, Hirahara successfully conducted a 4D tropospheric tomography experiment based on the damped least-square method due to the singularity of the observation equation system of the tomography problem (Hirahara, 2000). Braun and Rocken (2003) and Braun (2004) used the extended sequential batch filter to overcome the sensitivity of the GNSS tomography model as well as updating the tomography solution. In years 2006 and 2007, Nilsson et al. presented a new troposphere tomography method to retrieve the 3D behaviour of the wet refractivity field directly from the raw GPS phase data (Nilsson and Gradinarsky, 2006;Nilsson et al., 2007). This method improves the accuracy of the wet refractivity in comparison to the regular GNSS tomography which applies SWD observations affected by a number of error sources. Rohm and Bosy (2009) applied the Moore–Penrose pseudo inverse to invert the observation equation system of the tomography model. In the proposed method, no additional constraint is required and therefore the actual state of the wet refractivity field is reflected by the tomography reconstruction. In the year 2011, Perler et al. presented new parameterized methods to reconstruct a 4D water vapour field that improve the quality of retrieved images. They applied trilinear and spline functions in ellipsoidal coordinates to retrieve the tomography model. Therefore, discretization impacts are minimized without considerably increasing the number of unknown parameters (Perler et al., 2011). Bender et al. (2011) implemented several members from algebraic reconstruction techniques (ART) to reconstruct the wet part of the troposphere. According to their result, the multiplicative techniques (MART) could estimate the tomography solution with higher accuracy in least processing time in comparison to other iterative techniques of the ART family.

In the year 2013, Rohm et al. proposed the new GNSS tomography model named TOMO2 (Rohm et al., 2013) . TOMO2 applies a robust Kalman filtering technique to solve the unconstrained tomography model. Besides, according to their study, the real SWD dataset is influenced by noise and outliers, and therefore advanced processing is required beyond the ordinary Kalman filter for real GNNS data. They also achieved a better conditioned model matrix by removing the linearly dependent parameters and observations. Xia et al. (2013) presented a combined iterative and non-iterative reconstruction algorithm (CRA) using GPS observations and COSMIC profiles. In this method, first, a generalized inverse solution of water vapour density is calculated using the NIRT (non-iterative reconstruction technique) by considering COSMIC radio occultation profiles as vertical smoothing constraints. Then, the estimates from the NIRT steps are applied in the IRT (iterative reconstruction technique). They proposed a new iterative algorithm named improved algebraic reconstruction technique (IART) which can remarkably improve the computational efficiency by reducing the number of iterations. In the year 2015, Adavi and Mashhadi-Hossainali used a hybrid regularization method to compute a reconstructed tomography solution. This method is combined of the Least-Square QR (LSQR) and the Tikhonov regularization techniques and benefits from the advantage that both the non-iterative and iterative techniques are independent of an initial field (Adavi and Mashhadi-Hossainali, 2015). Guo et al. (2016) proposed for GPS troposphere tomography an optimal weighting method to determine the optimal weights for three types of equations, namely the observation equation, the horizontal constraint equation, and the vertical constraint equation. According to the obtained results, the accuracy of the reconstructed tomography model using the proposed method under various weather conditions is significantly better than the conventional equal weighting scheme and constant weighting methods. In the year 2019, Yoa et al. presented an improved pixel-based tropospheric tomography model. This model uses the layered optimal polynomial coefficients which are extracted from the European Centre for Medium-Range Weather Forecasts (ECMWF) to reconstruct the 3D water vapour distribution in the troposphere (Yao et al., 2019). The proposed method is much more efficient and convenient in equations form compared to the traditional method. Ghafari Razin and Voosoghi (2020) used artificial neural networks (ANNs) to model the wet refractivity of the troposphere. In their method, the objective function is calculated using the squared difference between SWD from GNSS (SWDGPS) and SWD from ANN (SWDANN). Then, the ANN network is trained by a hybrid PSO (particle swarm optimization) -BP (backpropagation) algorithm to obtain the minimum of the objective function as well as optimize the network weights. Using the calculated objective function, the wet refractivity can be reconstructed with the high accuracy. Haji Aghajany et al. (2020) proposed a new tropospheric tomography based on the B-spline function which discretizes vertically some of the model layers whereas the Wet Vapour Density (WVD) B- spline function is applied horizontally. This method efficiently reduces the number of unknown parameters due to estimation of coefficients of the WVD function in each layer. Consequently, it can overcome the rank deficiency of the tropospheric tomography problem. In 2020, Zhao et al. recommended a method to consider the signals leaving the side face of the tomography model to improve the stability of the tomography solution using the combination of GNSS observations with data derived from the empirical Global Pressure and Temperature 2 wet model (Zhao et al., 2020).

3.2 Tomography Problem Formulation

The word "tomography" stems from the Ancient Greek words tomo "section/layer" and grafëin "write/record". Tomography is a general technique to determine the characteristics or inner structure of some objects, e.g. the Earth's atmosphere or the human body, based on integrated measurements over the time span in different directions and different locations. This method has numerous applications in medicine, earth science, material science, archeology and acoustics. The fundamental mathematics behind the tomography was formed by Radon (1986) which is also known as Radon transform. The mathematical basis of tomography is now used as the integral geometry, where the object is retrieved from measurements existing in the form of integrals over manifolds of less dimensionality (Kunitsyn and Tereshchenko, 2003).

Tomography is an important and informative inverse problem (Aster et al., 2005) and therefore, it can be considered as a subset of inverse theory. This method is distinguished by a specific form of the data kernel that includes measurements made along signals (Menke, 2012). The tomography model is a function of two or more variables that can be related to the measurements by the following equation (Aster et al., 2005;Menke, 2012):

$$d_i = \int_{C_i}^{4} [m(x(s), y(s))]\, ds \tag{3.1}$$

Here, m and d are the model function and measurements along the ray path. Moreover, C_i is a curved ray with arc length s. There are several factors that limit a continues formulation of the tomography model (Eq. (3.1)) in reality. First, the Dirac delta function is not square-integrable which causes some issues like no integrable singularities at the intersection points of rays (Menke, 2012). Second, in 3D cases, rays may not cross at all, and therefore all the s will be zero (Menke, 2012). All of these issues can be solved by replacing rays with tubes of finite cross-sectional width (Menke, 2012). As this approximation corresponds to a smoothing of the model function $m(x(s), y(s))$, a discretization of the continuous problem (Eq. (3.1)) by dividing it into subregions with constant m and adequate size to guarantee a reasonable number of rays (more than one), often satisfies demands in this respect (Menke, 2012).

The discrete form of Eq. (3.1) can then be noted as (Aster et al., 2005;Menke, 2012;Natterer, 1986):

$$d_i = \sum_j G_{ij} m_j \tag{3.2}$$

where $i = 1{:}n$ and $j = 1{:}m$ are the number of rays and subregions. Moreover, G_{ij} is the length of the i^{th} ray in the j^{th} subregions.

In this work, the outlier aims to reconstruct the 3D wet refractivity field based on the discretized form of the tomography model (Eq. (3.2)), named the voxel-based tomography, using the rays containing the information of tropospheric delays at different elevation angles. Therefore, a tomography model needs to be designed in order to retrieve the 3D image of wet refractivity using the integrated rays over the intended resolution time which are emitted from GNSS satellites and received at GNSS sites. Fig 3.1 shows the required steps to derive the wet refractivity distribution using GNSS observations in the GNSS tomography. In the following parts, the tropospheric tomographic reconstruction of wet refractivity using the voxel-based method according to the mentioned phases in Fig 3. 1 is presented.

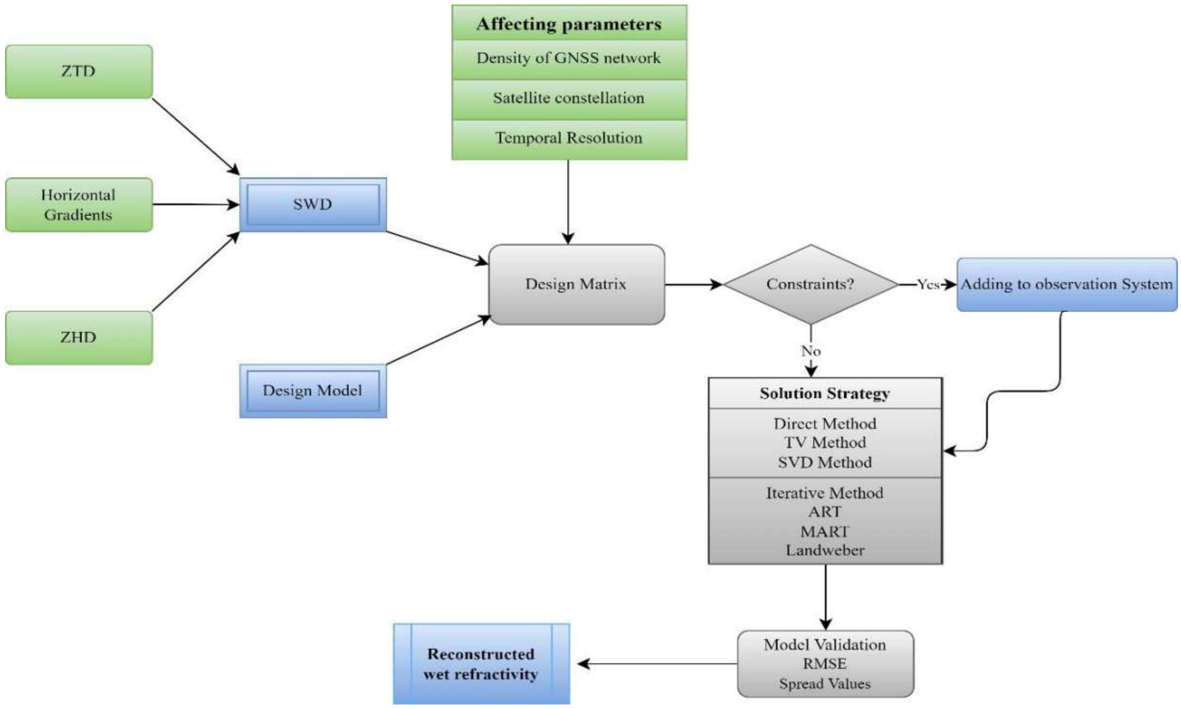

Fig 3. 1. Design of Tomography Model

3.2.1 Equation System of the Tomography within a Discretised Refractivity Field

In order to reconstruct the wet refractivity (N_w) [unit: ppm] structure, the wet part of the troposphere is discretized to 3D voxels. Then, the spatiotemporal behaviour of the wet part of the refractivity is retrieved by analysing the impact of the wet part of the troposphere on GNSS signals with an assumption that N_w is constant in the individual model elements. For this purpose, a large number of $SWDs$ [unit: mm] are integrated in the GNSS tomography according to Eq. (3.3) (Flores et al., 2000a;Heublein, 2019):

$$SWD_i = 10^{-6} \cdot \sum_{j=1}^{m} N_{w_j} \cdot d_{ij} \tag{3.3}$$

whereby, d_{ij} is the length of the i^{th} signal inside the j^{th} model element [unit: km] (see Fig 3. 2). According to Eq. (3.3), the total slant wet delay observation of each satellite (SWD_i) can be defined as a summation over voxels intersected by the GNSS signals.

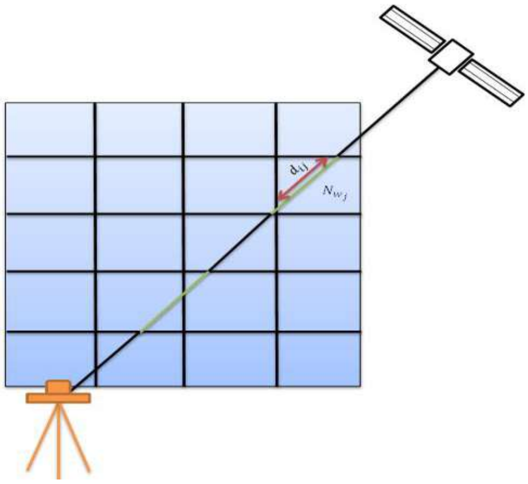

Fig 3. 2. Principle of the GNSS Tomography, ray path within the discretized wet troposphere above the GNSS network

We can reformulate Eq. (3.3) in matrix notation as follows (Flores et al., 2000b):

$$\boldsymbol{SWD} = \boldsymbol{A}\,\boldsymbol{N_w} \tag{3.4}$$

Here, $\boldsymbol{SWD}$ is the observation vector of length m where m is calculated from the number of GNSS stations and visible satellites in the defined time window of the tomography model. $\boldsymbol{N_w}$ represents the refractivity field vector of length n where n $(L_1 \times L_2 \times L_3)$ is the number of voxels in the tomography model. Consequently, $\boldsymbol{A}$ is a $m \times n$ matrix with the responsibility of mapping the unknown space onto the measurement space. $\boldsymbol{A}$ is called a design matrix with the following definition (Rohm and Bosy, 2009):

$$\boldsymbol{A} = \begin{bmatrix} d_{11} & 0 & 0 & 0 & \cdots & d_{1n} \\ d_{21} & d_{22} & d_{23} & 0 & \cdots & d_{2n} \\ \vdots & \vdots & \vdots & \vdots & \ddots & \vdots \\ d_{m1} & d_{m2} & 0 & d_{m4} & \cdots & d_{mn} \end{bmatrix} \tag{3.5}$$

According to Eq. 3.5, the coefficients of the design matrix $\boldsymbol{A}$ can be defined as follows:

$$A_{ij} = \begin{cases} d_{ij} & if\ ray\ i\ cross\ voxel\ j \\ 0 & otherwise \end{cases} \tag{3.6}$$

As shown in Eq. (3.4), matrix $\boldsymbol{A}$ is a mapping matrix governed by the resolution of the tomography model, the satellite constellation, the distribution of the GNSS receivers as well as the tomography window (Bender et al., 2011;Lutz, 2008;Troller, 2004). Due to insufficient spatial coverage of the voxels by GNSS rays within the tomography window, some of the voxels are intersected by a small number or a plenty number of signals and others are not passed at all. Therefore, the design matrix $\boldsymbol{A}$ is a sparse matrix , and Eq. (3.4) is mixed-determined (Menke, 2012). Hence, the exact solution of the tomography problem cannot be estimated directly through Eq. (3.4) since the inversion of the design matrix is incalculable. In other words, the model null space of the design matrix is non-trivial, which causes the partly ill-conditioned tomographic inversion system. In order to reconstruct the wet refractivity field using Eq. (3.4), some constraints or external data sources should be added to the tomography problem as well as some inversion techniques must be applied which are discussed in more details in Section 3.3 and Section 3.4.

3.2.2 Tomographic Voxel Model

The 3D tomography model is defined by dividing the wet part of troposphere into finite volume pixels, named voxels, to reconstruct the spatio-temporal behaviour of the wet refractivity (see Fig 3. 3). This model is designed over the GNSS network and therefore it highly depends on the orography of the study area as well as distances between GNSS stations. Moreover, the horizontal and vertical resolution of the voxels should be determined based on the GNSS network characteristics. In this regards, here we use the exponential layer function to define the vertical spacing between the layers of the tomography model (Manning, 2013;Möller, 2017;Perler, 2011)

$$dh(i) = dh(0)\, q_h^i \tag{3.7}$$

where $dh(i)$ is the height difference of the successive layers and $dh(0)$ is the height difference between the first two layers. Moreover, q_h^i is the growth factor (see (Perler, 2011) for more details). To take into account the topography of the investigated area the height of the grid point should be computed based on the elevation model of the case study area. Therefore, an appropriate interpolation method like nearest-neighbour interpolation or biharmonic spline interpolation is used according to the orography of the case study and density of the elevation model. In addition, to ensure that the contribution of low elevation rays (tracked mostly by reference sites at the border of our model area) which leave the tomographic model via lateral surfaces is accounted for correctly, the tomography area was extended by a sparse outer voxels model. The horizontal size of these boundary zones is chosen 5° in this research. Details of this design phase are provided in chapter 5.

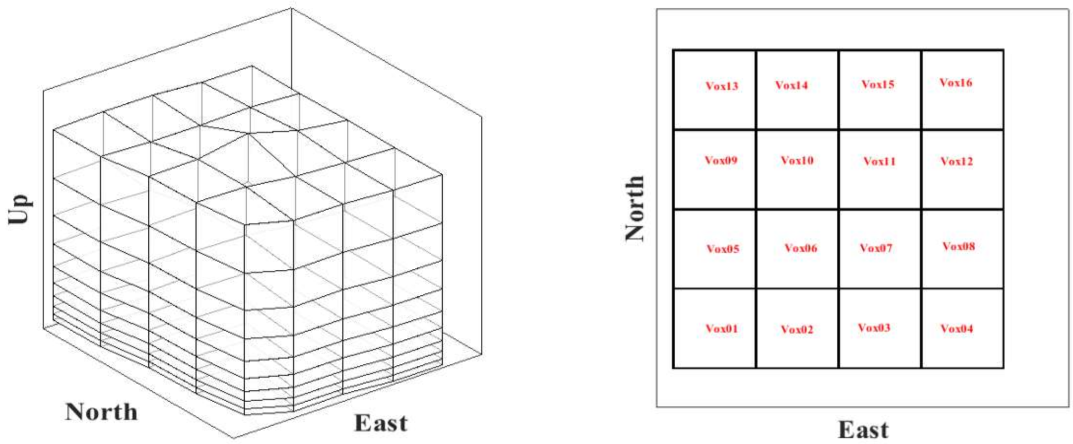

(a) (b)

Fig 3. 3. Schematic representation of the tomography model (a) and voxel numbering within the first layer of the tomography model (b)

The horizontal resolution is determined by means of the concept of the model resolution matrix ($\boldsymbol{R_m}$) which was firstly used by Adavi and Mashhadi-Hossainali (2014). This matrix is given by:

$$\boldsymbol{R_m} = \boldsymbol{A}^{\dagger}\boldsymbol{A} \tag{3.8}$$

where $\boldsymbol{A}^{\dagger}$ is a generalized inverse of $\boldsymbol{A}$ (Eq. (3.4)) and both matrices can be defined using the singular value decomposition theorem as follows (Aster et al., 2005):

$$\boldsymbol{A} = \boldsymbol{U}\,\boldsymbol{S}\,\boldsymbol{V} = \boldsymbol{U}_p \boldsymbol{S}_p \boldsymbol{V}_p^T \tag{3.9}$$

$$\boldsymbol{A}^{\dagger} = \boldsymbol{V}_{\mathrm{p}} \boldsymbol{S}_{\mathrm{p}}^{-1} \boldsymbol{U}_{\mathrm{p}}^{\mathrm{T}} \tag{3.10}$$

where $\boldsymbol{U}$ $[m \times m]$ is an orthogonal matrix of eigenvectors ($\boldsymbol{u}^{(i)}$) that spans the data space ($\mathcal{R}_{\mathrm{m}}$) (Menke, 2012):

$$\boldsymbol{U} = [\boldsymbol{u}^{(1)} \quad \boldsymbol{u}^{(2)} \quad \boldsymbol{u}^{(3)} \quad \dots \quad \boldsymbol{u}^{(m)}] \tag{3.11}$$

Moreover, $\boldsymbol{V}$ $[n \times n]$ is an orthogonal matrix of eigenvectors ($\boldsymbol{v}^{(\mathrm{i})}$) that spans the model space ($\mathcal{R}_{\mathrm{n}}$) (Menke, 2012):

$$\boldsymbol{V} = [\boldsymbol{v}^{(1)} \quad \boldsymbol{v}^{(2)} \quad \boldsymbol{v}^{(3)} \quad \dots \quad \boldsymbol{v}^{(n)}] \tag{3.12}$$

and $\boldsymbol{S}$ $[m \times n]$ is a diagonal eigenvalue matrix which contains nonnegative diagonal elements called singular values which are generally arranged in decreasing size $[s_1 \geq s_2 \geq \cdots \geq s_{p=min(m,n)}]$. Here, p is the number of non-zero singular values. Therefore, $\boldsymbol{S}$ can be partitioned as noted below:

$$\boldsymbol{S} = \begin{bmatrix} \boldsymbol{S}_p & \boldsymbol{0} \\ \boldsymbol{0} & \boldsymbol{0} \end{bmatrix} \tag{3.13}$$

and consequently, $\boldsymbol{U}_{\mathrm{p}}$ and $\boldsymbol{V}_p$ are the first p columns of $\boldsymbol{U}$ and $\boldsymbol{V}$, respectively.

Substitution of Eq. (3.9) and Eq. (3.10) into Eq. (3.8) gives:

$$\boldsymbol{R_m} = \boldsymbol{V}_p \boldsymbol{S}_p^{-1} \boldsymbol{U}_p^T\, \boldsymbol{U}_p \boldsymbol{S}_p \boldsymbol{V}_p^T = \boldsymbol{V}_p \boldsymbol{V}_p^T \tag{3.14}$$

According to Eq. (3.14), if $rank(\boldsymbol{A}) = p = n$, $\boldsymbol{R_m}$ is an identity matrix, and all model parameters will be perfectly retrieved. If the model null space of matrix $\boldsymbol{A}$ is non-trivial ($Null(\boldsymbol{A}) \neq \{0\}$) then $\boldsymbol{R_m}$ is not an identity matrix, which is demonstrating how the resolved model parameters smear out the true model parameters. Therefore, the model resolution matrix characterizes whether the model parameters can be predicted well. This matrix can be used as an important tool for the experimental design due to the independence from the actual measurements and dependency on the a priori field and the data kernel ($\boldsymbol{A}$) (Menke, 2012). Thereby, with the assumption of knowing the vertical resolution, the optimum horizontal resolution of the tomography model can be obtained by means of the resolution matrix. Further investigation is presented in Chapter 5.

3.2.3 Ray-tracing of Signal Path

In order to create the design matrix of the tomographic inversion system Eq. (3.4), the distances within each voxel should be calculated by means of ray-tracing. In recent years, different ray-tracing algorithms have been established in the VLBI or GNSS community to estimate different parameters like slant tropospheric delay or the structure matrix of the tomography equation system (Haase et al., 2003;Haji Aghajany and Amerian, 2017;Hobiger et al., 2008;Hofmeister, 2016;Möller and Landskron, 2019;Nafisi et al., 2012). Here, the straight-line strategy and the Eikonal ray-tracing as two popular ray-tracing methods to solve the GNSS tomography problem are investigated.

3.2.3.1 Straight-Line Geometry

To determine the intersection point of GNSS signals and voxels faces using the straight line ray-tracing the corresponding procedures should be applied:

a. The Earth-Centered, Earth-Fixed (ECEF) coordinates of all GNSS stations and all satellites (from SP3 or the navigation file) within the tomography window are transformed into the local NEU-system (NEU) using the following formula (Cai et al., 2011;Grewal et al., 2007;Siegfried, 2009):

$$\begin{bmatrix} E \\ N \\ U \end{bmatrix} = \begin{bmatrix} -\sin\lambda_r & \cos\lambda_r & 0 \\ -\sin\varphi_r\cos\lambda_r & -\sin\varphi_r\sin\lambda_r & \cos\varphi_r \\ \cos\varphi_r\cos\lambda_r & \cos\varphi_r\sin\lambda_r & \sin\varphi_r \end{bmatrix} \begin{bmatrix} X - X_r \\ Y - Y_r \\ Z - Z_r \end{bmatrix} \tag{3.15}$$

where (X_r, Y_r, Z_r) and $(\varphi_r, \lambda_r, h_r)$ are the Cartesian and geodetic coordinates of the ENU origin in the ECEF and $(X, \mathrm{Y}, \mathrm{Z})$ are the satellite or station coordinates. In this thesis, the middle point of the study area has been chosen as the origin.

b. The line equation between GNSS station (sta) and satellite (sat) is calculated in the NEU as follows:

$$l_a + l_d\, par = 0; \quad par \subseteq [0\ 1] \tag{3.16}$$

with

$$l_d = [E_{sta} - E_{sat};\ N_{sta} - N_{sat};\ U_{sta} - U_{sat}] \tag{3.17}$$

$$l_a = [E_{sta};\ N_{sta};\ U_{sta}] \tag{3.18}$$

c. par is computed as noted below:

$$par = \frac{[(P_1 - P_0) \times (P_2 - P_0)] \times [l_a - P_0]}{-l_d \,.\, [P_0 \times (P_2 - P_0)]} \tag{3.19}$$

where P_0, P_1 and P_2 are arbitrary points in intended voxel corners, defined by a triangle on the voxel face.

d. The intersection points between each GNSS line-of-sight and the voxels planes (see Fig 3. 4) are calculated by substituting par in Eq. (3.16). Only points that are situated in the intended voxel are selected.

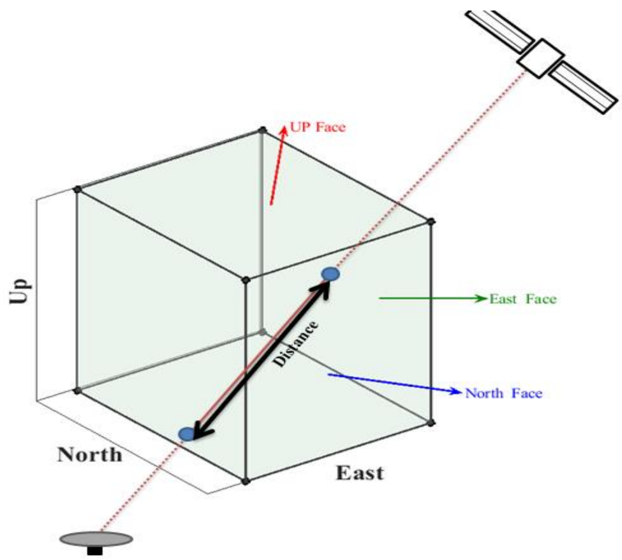

Fig 3. 4. Schematic representation of voxel faces and intersection points of ray path on it

e. Finally, the Euclidean distance between inside intersection points is calculated to populate the design matrix.

3.2.3.2 Eikonal Ray-Tracing Method

Variation of refractivity through the path trajectory causes some deviation from the straight line. The schematic representation of the real path in the tomography model is shown in Fig 3. 5. Therefore, to reconstruct the accurate ray path, ray-tracing over a Numerical weather model could be used. The Eikonal equation is the fundamental method for ray-tracing which can determine the real path trajectory and also the optical path length between satellite and receiver. This equation is valid under the assumption of geometric optic approximation and considering the microwave propagation as a ray. (Möller, 2017). According to these assumptions, the propagation path of the electromagnetic ray can be determined by solving the Eikonal equation (Born and Wolf, 1999;Hobiger et al., 2008;Hofmeister, 2016;Nilsson et al., 2013):

$$\|\nabla L\| = N(\boldsymbol{r}) \tag{3.20}$$

whereby L and ∇L represent the optical path length and the components of ray directions, respectively. Moreover, N is the refractive index of the troposphere at position $\boldsymbol{r}$.

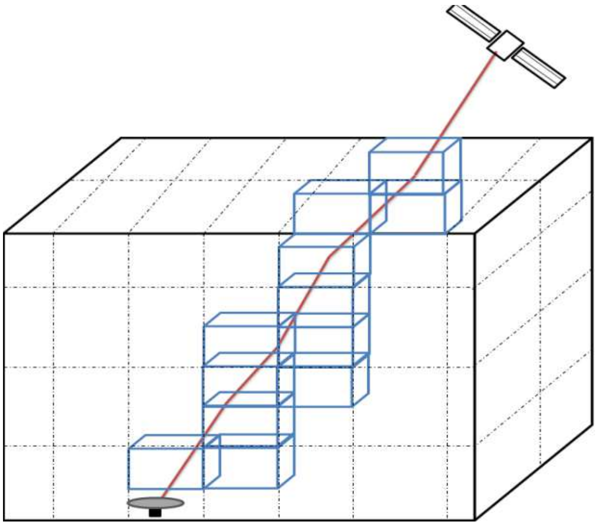

Fig 3. 5. Geometric illustration of bended path trajectory in tomography model

Eq. (3.20) is a partial differential equation of the first order for $N(\boldsymbol{r})$ and it can be denoted in many other different forms as well. In the general form, the Hamiltonian conical formalism is applied (Born and Wolf, 1999;Cerveny, 2005;Hofmeister, 2016;Nafisi et al., 2012;Nilsson et al., 2013):

$$H(\boldsymbol{r}, \nabla L) \doteq \frac{1}{\alpha}\left\{(\nabla L \,.\, \nabla L)^{\frac{\alpha}{2}} - N(\boldsymbol{r})^{\alpha}\right\} = 0 \tag{3.21a}$$

$$\frac{d\boldsymbol{r}_i}{du} = \frac{\partial H}{\partial \nabla L_i} \tag{3.21b}$$

$$\frac{d\nabla L_i}{du} = -\frac{\partial H}{\partial \boldsymbol{r}_i} \tag{3.21c}$$

$$\frac{dL_i}{du} = \nabla L_i \,.\, \frac{\partial H}{\partial \nabla L_i} \tag{3.21d}$$

where $H(\boldsymbol{r}, \nabla L)$ represents the Hamiltonian function and α is a real number that defines the type of parameter of interest u (Nilsson et al., 2013). In Table 3. 1, different possible cases for α are demonstrated (Cerveny, 2005;Hofmeister, 2016;Nafisi et al., 2012).

Table 3. 1. Different options to set a type of the intended parameter in the Hamiltonian Formalism (Cerveny, 2005;Nafisi et al., 2012)

$\boldsymbol{\alpha}$	$\boldsymbol{du}$	$\boldsymbol{u}$
0	dt	Travel time along the ray $[t]$
1	ds	Arc length along the ray $[s]$
2	$d\sigma$	Natural variable along the ray $[\sigma]$

According to Table 3. 1 by setting $\alpha = 1$, the length of the ray can be determined. In addition, any coordinate system could be generally used for solving Eq. (3.20). However, as noted by Alkhalifah and Fomel (2001), the spherical coordinate system is more appropriate than the Cartesian coordinate system, due to be the most natural orthogonal system to solve the Eikonal equation in a point source case. Moreover, this coordinate system commonly meets the demands of ray tracing in the atmosphere. Hence, the spherical coordinate system is applied here to solve the Eikonal ray-tracer (Hofmeister, 2016). Consequently, Eq. (3.21) can be rewritten as follow:

$$H(r,\theta,\lambda) \doteq \left[L_r + \frac{1}{r^2}L_\theta + \frac{1}{r^2(\sin\theta)^2}L_\lambda\right] - N(r,\theta,\lambda,t) = 0 \tag{3.22}$$

whereby r is a radial distance, θ $[0,\pi]$ and λ $[0,2\pi]$ are the co-latitude, and the longitude, respectively. $L_r = \partial L/\partial r$, $L_\theta = \partial L/\partial\theta$, and $L_\lambda = \partial L/\partial\lambda$ represent the components of the ray directions (Nafisi et al., 2012). Moreover, t is a time parameter which defines the temporal variability of the refractivity. According to that, the first six equations in a spherical coordinate system can be defined by substituting Eq. (3.22) into Eq. (3.21b) and Eq. (3.21c) (Hobiger et al., 2008;Hofmeister, 2016;Nafisi et al., 2012):

$$\frac{dr}{ds} = \frac{1}{\omega}\,L_r \tag{3.23a}$$

$$\frac{d\theta}{ds} = \frac{1}{\omega}\frac{L_\theta}{r^2} \tag{3.23b}$$

$$\frac{d\lambda}{ds} = \frac{1}{\omega}\frac{L_\lambda}{r^2(\sin\theta)^2} \tag{3.23c}$$

$$\frac{dL_r}{ds} = \frac{\partial N(r,\theta,\lambda,t)}{\partial r} + \frac{1}{\omega r}\left[\frac{L_\theta^2}{r^2} + \frac{L_\lambda^2}{r^2(\sin\theta)^2}\right] \tag{3.23d}$$

$$\frac{dL_\theta}{ds} = \frac{\partial N(r,\theta,\lambda,t)}{\partial\theta} + \frac{1}{\omega}\left[\frac{L_\lambda^2}{r^2(\sin\theta)^3}\right] \tag{3.23e}$$

$$\frac{dL_\lambda}{ds} = \frac{\partial N(r,\theta,\lambda,t)}{\partial\lambda} \tag{3.23f}$$

with the auxiliary parameter ω , as obtained below (Nafisi et al., 2012):

$$\omega = \left[L_r^2 + \frac{1}{r^2}L_\theta^2 + \frac{1}{r^2(\sin\theta)^2}L_\lambda^2\ \right] = N(r,\theta,\lambda,t) \tag{3.24}$$

By solving Eq. (3.23a) to Eq. (3.23f) simultaneously, the positions of all points along the ray trajectory can be specified (Hofmeister, 2016;Nafisi et al., 2012). In this work, the Runge-Kutta technique as a known and standard approach to solve these equations is used (Nafisi et al., 2012). For this purpose, the differential equation system (Eq. (3.23)) can be written in vector form:

$$\frac{d\boldsymbol{Y}}{ds} = \vec{F}(s, \boldsymbol{Y}) \tag{3.25}$$

where $\vec{F}$ denotes the system equation of Eq. (3.23) and Y is defined as:

$$\boldsymbol{Y} = [r, \theta, \lambda, L_r, L_\theta, L_\lambda]^T \tag{3.26}$$

Therefore, to solve Eq. (3.25), the initial conditions of vector $\boldsymbol{Y}$ are required. For this purpose, $(r, \theta, \lambda, N_0, z_0, \alpha_0)$ extracted from the GNSS station at the starting point is considered as the initial guess ($\boldsymbol{Y}_0$) (Cerveny, 2005;Nafisi et al., 2012;Gegout et al., 2014):

$$\boldsymbol{Y}_0 = \begin{bmatrix} r_0 \\ \theta_0 \\ \lambda_0 \\ N_0 \cos z_0 \\ N_0\, r_0 \sin z_0 \cos \alpha_0 \\ N_0\, r_0 \sin z_0 \sin \alpha_0 \sin \theta_0 \end{bmatrix} \tag{3.27}$$

Moreover, in order to calculate the Eikonal equation in the 3D case, it is essential to know the gradient components of the refractive index with respect to the spherical coordinate system (Hobiger et al., 2008;Nafisi et al., 2012):

$$\nabla N_r = \frac{\partial N(r,\theta,\lambda,t)}{\partial r} \tag{3.28a}$$

$$\nabla N_\theta = \frac{\partial N(r,\theta,\lambda,t)}{\partial \theta} \tag{3.28b}$$

$$\nabla N_\lambda = \frac{\partial N(r,\theta,\lambda,t)}{\partial \lambda} \tag{3.28c}$$

The quantities in Eq. (3.28) can be extracted from the Numerical weather model (See Appendix A for more details) (Hobiger et al., 2008;Nafisi et al., 2012). Therefore, this strategy needs plenty of time for the preparation of initial values and then computing the ray propagation in the troposphere. In contrast to this, the 2D Eikonal ray-tracing can significantly reduce the computation burden due to limiting the ray path to a vertical plane with comparable results (Hobiger et al., 2008;Nafisi et al., 2012). Accordingly, in 2D mode, the horizontal gradient of refractivity $[\nabla N_\theta, \nabla N_\lambda]$ is eliminated and consequently the six partial equations (3.23a) to (3.23f) are reduced to the four equations shown below:

$$\frac{dr}{ds} = \frac{1}{\omega} L_r \tag{3.29a}$$

$$\frac{d\theta}{ds} = \frac{1}{\omega} \frac{L_\theta}{r^2} \tag{3.29b}$$

$$\frac{dL_r}{ds} = \frac{\partial N(r,\theta,\lambda,t)}{\partial r} + \frac{1}{\omega r}\left[\frac{L_\theta^2}{r^2} + \frac{L_\lambda^2}{r^2(\sin\theta)^2}\right] \tag{3.29c}$$

$$\frac{dL_\theta}{ds} = \frac{1}{\omega}\left[\frac{L_\lambda^2}{r^2(\sin\theta)^3}\right] \tag{3.29d}$$

In order to solve the differential equation system (Eq. (3.29)) in 2D-mode, the Runge-Kutta technique can be applied (Gegout et al., 2014;Nafisi et al., 2012).

The accuracy of the tomography solutions using different parameterization techniques, namely Eikonal and straight-line, is assessed against radiosonde measurements in Section 5.3.4. Moreover, the efficiency of the spherical coordinate system and variation of ray direction to estimate intersection points with the voxel faces is investigated in this section by neglecting bending effect (setting $N = 1$) and solving the equation system of (3.29).

3.2.4 Applied Constraints

Due to the inadequate geometric distribution of GNSS stations with respect to the satellite constellation, the number of slant delays within the integration period is limited. Therefore, it is usually not possible to collect enough measurements in each voxel. In fact, there are three different scenarios for the model' parameters:

1) Overdetermined: Voxel with a lot of rays (Fig 3. 6 (a)),

2) Underdetermined: Voxel without any ray or voxels with equal distance rays which, therefore, cannot individually be resolved (Fig 3. 6 (b)),

3) Mixed-determined: Combination of case (1) and case (2) (Fig 3. 6 (c)).

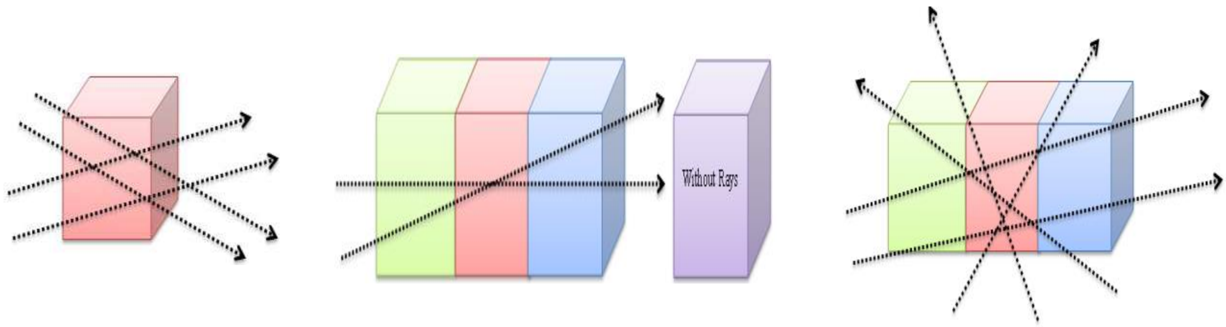

(a) **(b)** **(c)**

Fig 3. 6. Three different scenarios for the parameters of the tomography model, (a) overdetermined, (b) underdetermined, and (c) mixed-determined

According to these scenarios and due to the slow change of the satellites geometry in GNSS tomography during the integration time, the whole equation system of the tomography problem (Eq. (3.4)) is mixed-determined (Menke, 2012). Hence, the model null space of the design matrix is non-trivial which causes the partly ill-conditioned tomographic inversion system. Therefore, some constraints as pseudo-observations are added to the equation system of the tomographic problem in order to strengthen the design matrix ($\boldsymbol{A}$) and obtain an optimal solution.

a) Horizontal Constraint

For a regional area, a certain model element can be represented by the adjacent voxels due to the stability of the atmospheric water vapour (Rius et al., 1997). As a result, the following relative horizontal constraints can be defined in each height layer with l voxels (Flores et al., 2000b;Rohm and Bosy, 2011):

$$w_{1,k}N_{w_1} + w_{2,k}N_{w_2} + \cdots + w_{i-1,k}N_{w_{i-1}} - N_{w_k} + w_{i+1,k}N_{w_{i+1}} + \cdots + w_{l,k}N_{w_l} = 0 \tag{3.30}$$

where k refers to voxels in this layer. According to Eq. (3.30), each wet refractivity (N_{w_k}) is the weighted mean of its neighbors at the same layer. The horizontal coefficients or simply weight of the i^{th} voxel (w_i) can be calculated based on the inverse distance as follows (Heublein, 2019;Zhao et al., 2019):

$$w_{i,k} = \begin{cases} \frac{\frac{1}{d_{i,k}}}{\sum_{i=1}^{l} \frac{1}{d_{i,k}}} & if\ i \neq k \\ -1 & if\ \ i = k \end{cases} \tag{3.31}$$

Here, $d_{i,k}$ is a distance between the center of voxel k and the center of adjacent voxel (i) of the intended height layer. Therefore, the equation system of the horizontal constraint can be expressed as below:

$$\mathbf{0} = \boldsymbol{H}\, \boldsymbol{N_w} \tag{3.32}$$

$\boldsymbol{H}$ is the coefficient matrix of horizontal constraints.

b) Vertical Constraint

The vertical constraint can be defined using the approximation of the refractivity profile by an exponential decay with height as follows (Davis et al., 1993;Elósegui et al., 1998;Flores et al., 2000a)

In addition, vertical constraints are added to Eq. (3.4) with the purpose to determine the characteristic of the wet refractivity field in this direction. Here, an exponential law according to (Davis et al., 1993) has been applied which is defined as follows (Elósegui et al., 1998;Yang et al., 2018):

$$N_{w_k}\,(h_k) - e^{(h_{k+l}-h_k)/H}\, N_{w_{k+l}}\,(h_{k+l}) = 0 \tag{3.33}$$

whereby h_k and h_{k+l} stands for the height of voxel k and voxel $k + l$, respectively. H represents the water vapour scale height, which varies between 1 to 2 km (Elósegui et al., 1998;Kleijer, 2004;Yang et al., 2018). Eq. (3.32) can be presented in matrix form by considering $\boldsymbol{V}$ as a coefficient matrix:

$$\mathbf{0} = \boldsymbol{V}\, \boldsymbol{N_w} \tag{3.34}$$

c) priori Information

An a priori constraint can be applied in order to impose the reconstructed wet refractivity field to a given value in a specific voxel or layer (Troller, 2004). Generally, this constraint can be extracted from some external dataset like radiosonde or radio occultation. Moreover, as the amount of water vapour is negligible in the uppermost layers, the wet refractivity is constrained to zero in these layers. Consequently, the prior constraint gives as:

$$N_{w_{0_k}} = 1.\, N_w \tag{3.35}$$

where $N_{w_{0_k}}$ is an a priori value for the kth voxel. Therefore, the equation system of a priori information can be written as:

$$\boldsymbol{N_{w_0}} = \boldsymbol{B}\, \boldsymbol{N_w} \tag{3.36}$$

By substituting all possible types of constraint equations into Eq. (3.4), the extended tomography model can be expressed as follows:

$$\begin{bmatrix} \boldsymbol{SWD} \\ \boldsymbol{0} \\ \boldsymbol{0} \\ \boldsymbol{N_{w_0}} \end{bmatrix} = \begin{bmatrix} \boldsymbol{A} \\ \boldsymbol{H} \\ \boldsymbol{V} \\ \boldsymbol{B} \end{bmatrix} \boldsymbol{N_w} \tag{3.37}$$

3.3 Mathematical Basis for the Inverse Problem Solution

The tomography model (Eq. (3.1)) belongs to the group of the Fredholm integral equations of the first kind (IFK) (Aster et al., 2005;Menke, 2012). This kind of problem is inherently ill-posed. Therefore, due to the nature of IFK obtaining a useful solution is difficult. In this work, the discrete form of the IFK integral (Eq. (3.4)) is used. Thus, increasing the number of unknowns implies a more and more badly conditioned matrix $\boldsymbol{A}$ (Aster et al., 2005). Problems like this are called discrete ill–posed problems as the singular values of its design matrix decays gradually towards zero without any noticeable gap between non-zero and zero singular values (Aster et al., 2005;Hansen, 1998;Menke, 2012). Fig 3. 7 shows an example for the singular values in the tomography problem which slowly decay to zero. As a result a small change in the measurements can lead to an enormous change in the parameters of the model and therefore an inverse solution is extremely unstable (Aster et al., 2005).

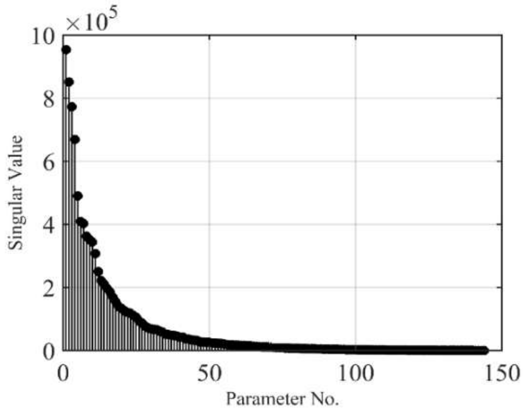

Fig 3. 7. Singular values of the tomography model for 144 voxels

In order to measure the sensitivity of the inverse solution to perturbations of the data and the design matrix, the 2-norm condition number is used (Aster et al., 2005;Hansen, 1998):

$$cond(\boldsymbol{A}) = \|\boldsymbol{A}\|_2 \|\boldsymbol{A}^{\dagger}\|_2 = \frac{s_1}{s_p} \tag{3.38}$$

Therefore, the condition number is a ratio between the largest (s_1) and smallest (s_p) singular values of the design matrix ($\boldsymbol{A}$). This parameter can also apply to determine the instability of the solution (Aster et al., 2005). According to Eq. (3.38), the condition number shows how inaccurate the estimated solution might be due to errors on the right hand side of the equation. Therefore, the tomography equation system (Eq. (3.4)) is ill-conditioned and in consequence as said before it is ill-posed as well. In order to stabilize the inversion process and produce a stable unique solution, regularization methods should be used at the cost of limiting us to a smoothed model (Aster et al., 2005;Hansen, 1998). According to this, the most prominent strategies to regularize the tomography model are presented in the next section.

3.4 Solving Methodology for the Inverse Problem

The purpose of this section is to summarize important strategies to solve the equation system of the tomography model (Eq. (3.4)). As mentioned before, the main characteristic of this problem is that all singular values of the design matrix ($\boldsymbol{A}$) decay gradually to zero without no obvious gap in the spectrum. Therefore, the regularization technique should be applied in order to reconstruct the wet refractivity field using the Tomography model. Table 3. 2 demonstrates various regularization methods which are involved in this work to retrieve the wet refractivity structure. According to this table, two different classes of regularization methods are used to produce a stable inverse solution: (1) direct regularization algorithm (Total Variation (TV) method), and (2) iterative regularization Algebraic Reconstruction Techniques (ART) and its variants Multiplicative Algebraic Reconstruction Technique (MART) and Landweber.

Table 3. 2. Various regularization methods to reconstruct the wet refractivity field in this research (Adavi et al., 2022a)

Regularization Method	Regularization Parameter	Initial Field
Landweber	$\lambda \in (0,1]$	AROME/TV Outputs
MART	$\lambda \in (0,2]$	
ART	$\lambda \in (0, 2/s_{max}^2]$	
TV	$\lambda, \beta \in [2^4, 2^{13}]$	NONE

Therefore, in this section, some of the ART techniques (ART, MART and Landweber) are detailed. These methods have been particularly developed for the tomography reconstruction problems and are mostly applicable to such approaches (Aster et al., 2005;Landweber, 1951). Then, the TV regularization technique is described. This method was first proposed by Rudin et al. (1992) for image denoising problems. TV is a nonlinear technique that effectively preserves discontinuities in the model and resists noise (Aster et al., 2005;Karl, 2005;Lee et al., 2007;Vogel and Oman, 1996).

3.4.1 Iterative Techniques

Iterative methods are mainly defined based on the coefficient matrix $\boldsymbol{A}$ and prior information which produce a sequence of regularized solutions $[\boldsymbol{N}_w^1, \boldsymbol{N}_w^2, \cdots, \boldsymbol{N}_w^k]$ in each step ($k = 1,2,\ldots$) by performing very simple algebraic operations such as multiplication and summation between matrices (Hansen, 1998). After a sequence of iterations, the estimated solution approaches some other undesired solutions which increase the norm of the error vector. Therefore, due to noise the sequence of the solutions converges to the contaminated solution in later stages. Often, this phenomena is referred to as semi-convergence (Hansen, 1998;Natterer, 1986). Therefore, selecting the appropriate k is quite important in the iterative methods as it plays the role of the regularization parameter. There are a lot of strategies to obtain an optimum number of iterations k such as Discrepancy Principal (DP), the L-Curve method, Flattest Slope (FS) and Generalized Cross Validation (GCV) (Golub and Matt, 1996;Hansen, 1998;Wu, 2003). Nevertheless, the most reasonable stopping rule strategy is to find a minimum inconsistency between the reconstructed value and the a priori information (Nikazad, 2007). In this work, we apply this method to select the appropriate regularization parameter due to access to the radiosonde observations.

This kind of technique is quite applicable in a large problem with the considerable sparsity in the design matrix $\boldsymbol{A}$ (Aster et al., 2005) as there is no need to invert the coefficient matrix $\boldsymbol{A}$ during the reconstruction procedure (Bender et al., 2011). Due to that, these techniques have been chosen as the most popular and successful methodologies to reconstruct the behaviour of water vapour in the troposphere and also the structure of the total electron content of the ionosphere in recent decades (Adavi and Mashhadi-Hossainali, 2014;Bender et al., 2011;Adavi and Mashhadi-Hossainali, 2015;Kak and Slaney, 1999;Stolle et al., 2006;Xia et al., 2013;Zhao et al., 2018). The main form of the iterative regularization technique is represented as below (Kaltenbacher et al., 2008):

$$\boldsymbol{N}_w^{k+1} = \boldsymbol{N}_w^k + G_k(\boldsymbol{N}_w^k, \boldsymbol{SWD}) \tag{3.39}$$

whereby G_k and k are a correction term and iteration number, respectively. G_k can be defined differently according to the desired methodology. This algorithm is a kind of closed-loop process and it starts with an initial guess for the unknown parameters field (Lohvithee, 2019), which could be estimated from the NWM model. Then, to correct the estimated wet refractivity field for the next iteration, the inconsistency between the estimated wet refractivity field and the initial field is computed (Bender et al., 2011;Gordon, 1974;Lohvithee, 2019). Fig 3.8 demonstrates the idea behind the iterative techniques. As shown in this figure, the iterative algorithm begins with an initial solution and then the next solution is calculated by using the projection of the first solution onto the hyperplane in n-dimensional space (line in 2D) defined by the first equation of the system of observation equations. This process is repeated for all of the hyperplanes defined by the observation equations system. Finally, if $\boldsymbol{d} = \boldsymbol{A}\,\boldsymbol{m}$ has a unique solution, the algorithm converges and otherwise, it will fail (Aster et al., 2005). In the following, very popular iterative techniques to obtain an approximate solution of the tropospheric tomography problem are defined.

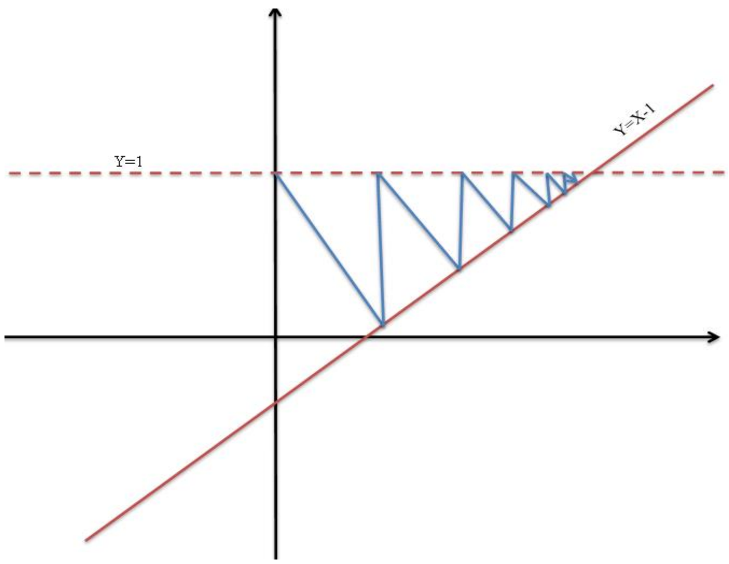

Fig 3. 8. An example of an iterative algorithm applied to a system of two equations (Figure adopted from Aster et al. (2005))

Algebraic Reconstruction Technique (ART) - This algorithm has been especially developed for the tomographic reconstruction problems (Aster et al., 2005). Moreover, ART is one of the most popular and frequently used algorithms among the different types of iterative methods (Gordon et al., 1970). In this method, the solution is updated via sweeps over the rows $\boldsymbol{A}^{i}$ of the design matrix $\boldsymbol{A}$ and therefore, there is no need to invert a large sparse matrix $\boldsymbol{A}$. Based on this, ART can be formulated as below (Gordon, 1974;Kak and Slaney, 1999) :

$$\boldsymbol{N}_{\boldsymbol{w}}^{k+1} = \boldsymbol{N}_{\boldsymbol{w}}^{k} + \lambda \frac{\boldsymbol{SWD}_i - \langle \boldsymbol{A}^i, \boldsymbol{N}_{\boldsymbol{w}}^{k} \rangle}{\langle \boldsymbol{A}^i, \boldsymbol{A}^i \rangle} \boldsymbol{A}^i \tag{3.40}$$

where i is the row number. The ART method covers two loops: The inner loop (index i) processes observation by observation. The outer loop (index k) is started after applying all $SWDs$ in Eq. (3.40) (Bender et al., 2011;Xiaoying et al., 2014b). λ is a regularization parameter from $(0,1]$ and provides the weight of the correction term with respect to the initial wet refractivity field (Bender et al., 2011;Turonova, 2011).

Multiplicative Algebraic Reconstruction Technique (MART)- In this technique, the successive estimate value of the corresponding voxel is corrected by multiplication with G_k which corresponds to the second factor in Eq. (3.39) (Subbarao et al., 1997). In principle, this increases the convergence speed compared to additive techniques like ART (Bender et al., 2011;Subbarao et al., 1997). This method can be accomplished using(Subbarao et al., 1997):

$$\boldsymbol{N}_{\boldsymbol{w}j}^{k+1} = \boldsymbol{N}_{\boldsymbol{w}j}^{k} \cdot \lambda \left(\frac{\boldsymbol{SWD}_i}{\langle \boldsymbol{A}^i, \boldsymbol{N}_{\boldsymbol{w}}^{k} \rangle} \right)^{\frac{\lambda \boldsymbol{A}_j^i}{\langle \boldsymbol{A}^i, \boldsymbol{A}^i \rangle}} \tag{3.41}$$

where j is the column number of the voxel. In this method, the regularization parameter λ is defined within the range of $(0,2]$ (Bender et al., 2011).

Landweber- Landweber is one of the classical iterative regularization techniques and belongs to the Simultaneous Iterative Reconstruction Technique (SIRT) family (Hansen, 1998;Kaltenbacher et al., 2008). To retrieve the wet refractivity field using this technique, as shown in Eq. (3.42), all rows of the coefficient matrix $\boldsymbol{A}$ are used in one iteration. This implies that the system of observation equations is solved simultaneously. The wet refractivity field in iteration $k+1$ can be retrieved according to (Landweber, 1951):

$$\boldsymbol{N}_{\boldsymbol{w}}^{k+1} = \boldsymbol{N}_{\boldsymbol{w}}^{k} + \lambda_k \boldsymbol{A}^T (\boldsymbol{SWD} - \boldsymbol{A}\boldsymbol{N}_{\boldsymbol{w}}^{k}) \tag{3.42}$$

whereby λ_k is a relaxation parameter which can be optimally determined in a range of $0 < \lambda_k < 2/s_{max}^2$ (Aster et al., 2005;Elfving et al., 2010;Hansen, 1998). However, this strategy, named optimal choice, needs beforehand knowledge of the real solution (Elfving et al., 2010). Other strategies to determine the relaxation parameter λ_k are line search, ψ_1-based relaxation strategy, ψ_2-based relaxation strategy, and modified ψ_1 and ψ_2 strategies (Aster et al., 2005;Elfving et al., 2010;Hansen, 1998). In this work, the modified ψ_2-based relaxation strategy is used that takes advantage of better damping of the noise propagation and also faster convergence (Elfving et al., 2012;Elfving et al., 2010).

The relaxation parameter in the modified ψ_2-based relaxation strategy is defined as below (Elfving et al., 2010):

$$\lambda_k = \begin{cases} \frac{\sqrt{2}}{s_{max}^2} & for\ k = 0,1 \\ \tau_k \frac{2}{s_{max}^2} (1 - \xi_k) & for\ k \geq 2 \end{cases} \tag{3.43}$$

where $\xi_k \in (0,1)$ is the unique root in (Elfving et al., 2010):

$$g_{k-1}(\xi_k) = \left[(2k-1)(\xi_k)^{k-1}\right] - \frac{1-(\xi_k)^{k-1}}{1-\xi_k} = 0 \tag{3.44}$$

Moreover, $\tau_k \in (0,(1-\xi_k)^{-1})$ is normally chosen as a constant value $\tau_k = \tau$. If $\tau > 1$ then the convergence is accelerated (Elfving et al., 2010).

3.4.2 Total Variation Method

The TV regularization method has been used in different kinds of inverse problems such as Computer Tomography (CT) reconstruction with low signal-to-noise ratio with promising results (Defrise et al., 2011;Persson et al., 2001;Sidky et al., 2006;Tang et al., 2009). In recent years, the TV method has also been applied in ionospheric tomography (IED) as well.

The objective function in the TV regularization method is given as (Jensen et al., 2012;Lohvithee, 2019;Persson et al., 2001;Rudin et al., 1992):

$$J(\boldsymbol{N_w}) = \text{argmin}\left(\tau\|\boldsymbol{N_w}\|_{TV} + \frac{1}{2}\,\|\,\boldsymbol{A}\,\boldsymbol{N_w} - \boldsymbol{SWD}\|_2^2\right) \tag{3.45}$$

whereby, $\tau > 0$ is the regularization parameter and the TV norm ($\|\boldsymbol{N_w}\|_{TV}$) in Eq. (3.45) can be calculated as follows (Persson et al., 2001):

$$\|\boldsymbol{N_w}\|_{TV} = \left\|\vec{D}\,\boldsymbol{N_w}\right\|_1 = \sum_{i,j,k}\left\|D_{i,j,k}\,N_{w_{i,j,k}}\right\| \tag{3.46}$$

where $D_{i,j,k}\,N_{w_{i,j,k}}$ is the discrete gradient of N_w at voxel *i, j, k*. Here, the augmented Lagrangian algorithm for TV minimization is used (Li, 2009):

$$\mathcal{L}_A(w_{i,j,k}, N_w) = \sum_{i,j,k}\left(\|w_{i,j,k}\| - \mathcal{V}_{i,j,k}^T\left(D_{i,j,k}\boldsymbol{N_w} - w_{i,j,k}\right) + \frac{\beta_{i,j,k}}{2}\,\|D_{i,j,k}\boldsymbol{N_w} - w_{i,j,k}\|_2^2\right) - \lambda^T(\boldsymbol{A}\,\boldsymbol{N_w} - \boldsymbol{SWD}) + \frac{\mu}{2}\,\|\boldsymbol{A}\,\boldsymbol{N_w} - \boldsymbol{SWD}\|_2^2 \tag{3.47}$$

where w_i can be obtained as shown below(Li, 2009):

$$w_i = max\left\{\left\|D_{i,j,k}\boldsymbol{N_w} - \frac{\upsilon_{i,j,k}}{\beta_{i,j,k}}\right\| - \frac{1}{\beta_{i,j,k}}, 0\right\}\frac{(D_{i,j,k}N_w - \upsilon_{i,j,k}/\beta_{i,j,k})}{\|D_{i,j,k}N_w - \upsilon_{i,j,k}/\beta_{i,j,k}\|} \tag{3.48}$$

$\upsilon_{i,j,k}$ and λ are continuously updated during the minimization of Eq. (3.47) in each iteration step (Li, 2009;Li et al., 2010):

$$\tilde{\upsilon}_{i,j,k}{}^{iter+1} = \upsilon_{i,j,k}{}^{iter} - \beta_{i,j,k}\left(D_{i,j,k}\boldsymbol{N_w}^* - w_{i,j,k}{}^*\right) \quad for\ all\ i,j,k \tag{3.49a}$$

$$\tilde{\lambda}^{iter+1} = \lambda^{iter} - \mu\,(\boldsymbol{A}\,\boldsymbol{N_w}^* - \boldsymbol{SWD}) \tag{3.49b}$$

In Eq. (3.49a) and Eq. (3.49b), $\boldsymbol{N_w}^*$ and $w_{i,j,k}{}^*$ indicate approximate values for Eq. (3.47) (Li, 2009). Moreover, the barrier parameter μ should be defined based on the sparsity level of the true solution and the noise level in the observation (Li et al., 2010). However, the determination of the noise level without accessing the exact solution is challenging. According to experience, μ varies from 2^4 to 2^{13}, and the best value is chosen subject to the RMSE of the recovered field (Li, 2009;Li et al., 2010). The value of $\beta_{i,j,k}$ should also been chosen between 2^4 and 2^{13} (Li et al., 2010).

In Section 5.1.5, various regularization method, including ART methods and TV, are used to retrieve the wet refractivity field. Then, the discrepancy of the reconstructed profiles and derived profiles from radiosonde observations are investigated. Section 5.1.6 studies the accuracy of the reconstructed wet refractivity field using the TV method in different temporal resolutions compared to radiosonde observations.

3.5 Statistical Evaluation of Tomography Solution

One of the challenges in the GNSS tomography is the quality assessment of the reconstructed solution. In recent years, a lot of efforts have been done by different researchers in order to evaluate the reliability of the estimated tomography solution using independent sources such as radiosonde measurements, Numerical Weather Models (NWM), and Water vapour Radiometer (WVR) (Bastin et al., 2007;Brenot et al., 2018;Brenot et al., 2014;Champollion et al., 2009;Elgered et al., 1991;Gradinarsky and Jarlemark, 2004;Hanna et al., 2019;Nilsson et al., 2007;Notarpietro et al., 2011;Troller, 2004;Van Baelen et al., 2011)

Here, two different strategies to evaluate the quality of GNSS tomography model parameters are defined. First, some statistical measures like Root Mean Square Error (RMSE), Bias, standard deviation (Std), Relative Error (RE), and Mean Absolute Error (MAE) are described. Then, the concept of spread to analyse the quality of the reconstructed tomography field is investigated.

3.5.1 Statistical Tools

The accuracy of the reconstructed tomography model is normally evaluated using different statistical tools, named RMSE, Mean Bias, Std, MAE, and RE (Jia et al., 2021;Rohm and Bosy, 2009;Shangguan et al., 2011;Xiaoying et al., 2014a;Zhang et al., 2017;Zhao et al., 2019). These statistics tools can be calculated by the following equations (Guerova, 2003;Jia et al., 2021;Xiaoying et al., 2014a;Zhao et al., 2019):

$$Bias = \frac{1}{n_l} \sum_{i=1}^{n_l} \left(\boldsymbol{N}_{\boldsymbol{w}_{tomo_i}} - \boldsymbol{N}_{\boldsymbol{w}_{ref_i}} \right) \quad (3.50)$$

$$RMSE = \sqrt{\frac{1}{n_l} \sum_{i=1}^{n_l} \left(\boldsymbol{N}_{\boldsymbol{w}_{tomo_i}} - \boldsymbol{N}_{\boldsymbol{w}_{ref_i}} \right)^2} \quad (3.51)$$

$$Std = \sqrt{RMSE^2 - Bias^2} \quad (3.52)$$

$$MAE = \frac{1}{n_l} \sum_{i=1}^{n_l} \left| \boldsymbol{N}_{\boldsymbol{w}_{tomo_i}} - \boldsymbol{N}_{\boldsymbol{w}_{ref_i}} \right| \quad (3.53)$$

$$RE = \frac{\left| N_{w_{tomo}} - N_{w_{ref}} \right|}{N_{w_{ref}}} \quad (3.54)$$

Here, n_l is the number of height levels and $\boldsymbol{N}_{\boldsymbol{w}_{tomo}}$ and $\boldsymbol{N}_{\boldsymbol{w}_{ref}}$ are the computed wet refractivity field from the tomography model and from the reference observation data like radiosonde profiles. In this study, we consider only voxels along the vertical profile of the radiosonde ascend that are intersected by the radiosonde at different height levels.

In addition, the quartiles and interquartile range (IQR) can be applied to assess the obtained results. To do so, the result is divided into four equal parts, namely first quartile (Q_1), second quartile (Q_2), and third quartile (Q_3) where Q_2 is equivalent to the median of the result (Moore et al., 2013). IQR is defined as the difference between Q_3 and Q_1 (Moore et al., 2013).

3.5.2 Spread of Resolution Matrix

One of the fundamental challenges in the tomography technique is to appraise the quality of the reconstructed model parameters. According to the solution quality, we can identify the regions, which are fairly-well resolved or unresolved. One of the well-known tools to deal with inversion problems, e.g. seismology, is the spread of the model resolution matrix in order to evaluate the quality of the estimated solution. This quantity measures the quality of the model parameters by considering the goodness of data, model resolution matrix and covariance matrix. The main concept behind this value is the model resolution matrix $\boldsymbol{R_m}$, which contains valuable information about the design matrix and observation quality. The model resolution matrix $\boldsymbol{R_m}$ is one of the valuable mathematical tools to analyse the quality of the solution of inverse problems (Aster et al., 2005;Menke, 2012). Fig 3. 9 shows an instance for the diagonal elements of the model resolution matrix in the first layer of the arbitrary tomography model. According to this figure, Voxel 15 is empty, and Voxel 16 is crossed by a few signals, and therefore they are poorly resolved by GNSS measurements.

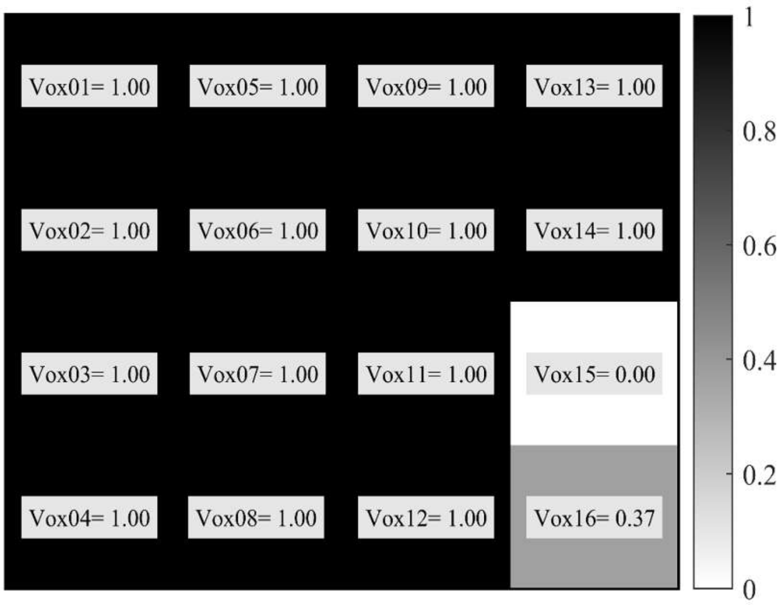

Fig 3. 9. An example of the model resolution matrix with different resolving for the model parameters

However, in Eq. (3.8), the resolution matrix merely depends on rays' distribution without counting the quality of the initial field and measurement covariance matrix ($\boldsymbol{C_{obs}}$). Hence, to identify the model resolution matrix, we imagine the true model solution, named $\boldsymbol{N_w^{true}}$, and the estimated solution, named $\boldsymbol{N_w^{est}}$. The true model parameters are determined by Eq. (3.4) ($\boldsymbol{SWD}^{obs} = \boldsymbol{A}\,\boldsymbol{N}_w^{true}$). In practice, the data sources contain some error sources and therefore the solution of Eq. (3.4) can be calculated as below:

$$\boldsymbol{N}_w^{est} - \boldsymbol{N}_{\boldsymbol{w}_0} = \boldsymbol{C}_{\boldsymbol{m}}\,\boldsymbol{A}^T\boldsymbol{B}^{-1}\left[\boldsymbol{A}\,\boldsymbol{N}_w^{true} - \boldsymbol{A}\,\boldsymbol{N}_{\boldsymbol{w}_0}\right] \tag{3.55}$$

with

$$\boldsymbol{B} = \boldsymbol{A}\,\boldsymbol{C}_{\boldsymbol{m}}\boldsymbol{A}^T + \boldsymbol{C}_{\boldsymbol{obs}} \tag{3.56}$$

whereby $\boldsymbol{N}_{\boldsymbol{w}_0}$ is an a priori wet refractivity field and could be extracted from the numerical weather model and $\boldsymbol{B}^{-1}$ is the inverse of $\boldsymbol{B}$ and can be calculated using Eq. (3.10). In this research, $\boldsymbol{C}_{\boldsymbol{m}}$ is a $n \times n$ diagonal matrix and can be expressed as (Brenot et al., 2018;Champollion, 2005):

$$\boldsymbol{C}_{\boldsymbol{m}} = diag\,(\delta_m\,\boldsymbol{N}_{\boldsymbol{w}_0}) \tag{3.57}$$

where δ_m is a damping coefficient and defined within the range of (0 1).

By simplifying Eq. (3.55), we obtain (Brenot et al., 2018;Menke, 2012;Tarantola, 2005):

$$\boldsymbol{N}_w^{est} - \boldsymbol{N}_{\boldsymbol{w}_0} = [\boldsymbol{C}_{\boldsymbol{m}}\,\boldsymbol{A}^T\boldsymbol{B}^{-1}\boldsymbol{A}\,]\,(\boldsymbol{N}_w^{true} - \boldsymbol{N}_{\boldsymbol{w}_0}) \tag{3.58}$$

Eq. (3.58) defines how closely the estimated model parameters fit a true model. Therefore, according to Eq. (3.58), the model resolution matrix $\boldsymbol{R}_{\boldsymbol{m}}$ is given by Eq. (3.59) as follows (Aster et al., 2005;Menke, 2012):

$$\boldsymbol{R}_{\boldsymbol{m}} = \boldsymbol{C}_{\boldsymbol{m}}\,\boldsymbol{A}^T\boldsymbol{B}^{-1}\boldsymbol{A} \tag{3.59}$$

According to Eq. (3.59), if the null space of the design matrix is trivial $\mathcal{N}(\boldsymbol{A}) = \{\boldsymbol{0}\}$ and, in other words, if the resolution matrix is identity ($\boldsymbol{R}_{\boldsymbol{m}} = \boldsymbol{I}$), then, all voxels will be recovered exactly with high accuracy. Moreover, it reflects valuable information on the reconstruction quality of each inversion parameter (Menke, 2012). Based on that, large diagonal elements with small off-diagonal elements indicate the desired parameter could be adequately resolved by the current geometry and quality of observation data. Large off-diagonal elements lead to a low quality of the determined parameters.

Therefore, Menke (2012) applied the spread of the diagonal and off-diagonal elements of the resolution matrix to measure the goodness of the resolution in inverse problems is as follows:

$$Spread\;(\boldsymbol{R}_{\boldsymbol{m}}) = \textstyle\sum_{i=1}^{M}\sum_{j=1}^{M}\left[R_{m_{ij}} - \delta_{ij}\right]^2 \tag{3.60}$$

where δ_{ij} are the elements of the identity matrix $\boldsymbol{I}$. Eq. (3.60) is sometimes called the Dirichlet spread function. However, the Dirichlet spread function is not a proper measure of the goodness of resolution because the off-diagonal elements of this matrix are all weighted equally, despite whether they are close or far from the main diagonal (Menke, 2012). Therefore, a weighting factor W_{ij} can be added to solve this issue. Consequently, Eq. (3.60) is rewritten as follows (Menke, 2012;Miller and Routh, 2007;Toomey and Foulger, 1989):

$$BGH\!:\;Spread\,(R_{m_i}) = \textstyle\sum_{j=1}^{M} W_{ij}\left[R_{m_{ij}} - \delta_{ij}\right]^2 \tag{3.61}$$

Here, W_{ij} is the physical distance between elements in [km]. The new spread function is frequently called the Backus-Gilbert (BG) spread function (Kaltenbacher et al., 2008;Piretzidis and Sideris, 2016). In this research, W_{ij} is calculated based on the Gaussian inverse distance (GID) between voxels in the same layer, namely horizontally, and therefore W_{ij} is zero for voxels in different layers. From now on, the BGH abbreviation is used for the BG spread due to considering GID for every horizontal layer. According to Eq. (3.61), a well-resolved parameter corresponds to a smaller spread of the corresponding row of the model resolution matrix, whereas a poorly resolved parameter corresponds to a larger one.

Another way to define the spread is as follow (Maercklin, 2004;Michelini and McEvilly, 1991):

$$Mich\text{:}\;\; Spread\ (R_{m_i}) = log\left[\|R_{m_i}\|^{-1} \sum_{j=1}^{M} \left(\frac{R_{m_{ij}}}{\|R_{m_i}\|}\right)^2 D_{ji}\right] \tag{3.62}$$

where $\|R_{m_i}\|$ is the L_2 norm for the i^{th} row of the resolution matrix R_m.This definition for the spread is known as Michelini spread function (Mich). In Eq. (3.62), D_{ji} is the spatial distance between the i^{th} and j^{th} model parameters. Here, in contrast to BGH, the spread value is negative and a larger negative value corresponds to a well-resolved parameter. Section 5.3.5 assesses the spread of the resolution matrix as a prior quality indicator for the reconstructed wet refractivity field.

Chapter 4

4 Outline of Study Areas and Datasets

In the first section of this chapter, four field campaigns to analyse the impact of different features in the GNSS tomography solution are presented. Two of the campaign areas are located in Austria, one of them covers most of the western parts of the Czech Republic and East Germany and the last one is part of the USA CORS GNSS network. In section 2, the meteorological ground measurement network is defined. The pressure measurements of this network are spatially interpolated to the location of GNSS stations in order to estimate the hydrostatic part of the tropospheric delay. Moreover, radiosonde observations are also presented in this part. This type of observation is applied as a gold reference to assess the accuracy of the reconstructed wet refractivity field in the respective campaign areas. In the last part of this section, the GOES-R sounder products are introduced as constraints in the system of observation equations in order to improve the tomography solution. In section 3, the types of numerical weather models which are applied in this work are defined. Two of these models, named AROME and ALADIN, only cover the region of Europe, and one of them, called ERA5, as a global model, could apply to the different parts of the world.

4.1 Study Areas

In this section, four different datasets are presented, which will be used to evaluate the accuracy of the reconstructed wet refractivity field by means of different strategies like regularization techniques, parameterization methods, and observations of multiple GNSS constellations. In the first part, two different GNSS networks in the Austria region are introduced. Then, the COST benchmark dataset is detailed, which contains real and simulated measurements. Finally, the CORS GNSS network located in the part of the USA is defined.

4.1.1 Austria

In Austria, several regional Real-Time Kinematic (RTK) reference networks are operated. Here, data of two of these networks, labelled EVN and EPOSA are investigated. In the first part, the EPOSA (Echtzeit Positionierung Austria) GNSS network is introduced. Then, the EVN (Energie Versorgung Niederösterreich) GNSS network which is placed in Lower Austria is stated.

4.1.1.1 EPOSA Network

EPOSA is the GNSS network operated by Energie Burgenland AG, ÖBB Infrastruktur AG, and Wiener Netze GmbH which consists of thirty-eight permanent GNSS stations covering the whole Austrian territory. Therefore, this network has considerable potential for tropospheric tomography modelling and other meteorological studies.

In this work, GPS+ GLONASS observations of only twenty-one permanent GNSS reference stations of the EPOSA network are, mostly located in the eastern part of Austria, considered due to the availability of their observations for the time of interest, DoYs 232-245 in August 2019. Rinex files of the GNSS sites include phase and code observations with a rate of 15 seconds for GPS, and GLONASS satellites. Therefore, the area of interest extends from 13.40° to 17° in longitude, and 46.5° to 48.5° in latitude according to the location of selected GNSS permanent stations. Fig 4. 1 demonstrates the distribution of the multi GNSS stations as well as the location of the radiosonde station RS11035.

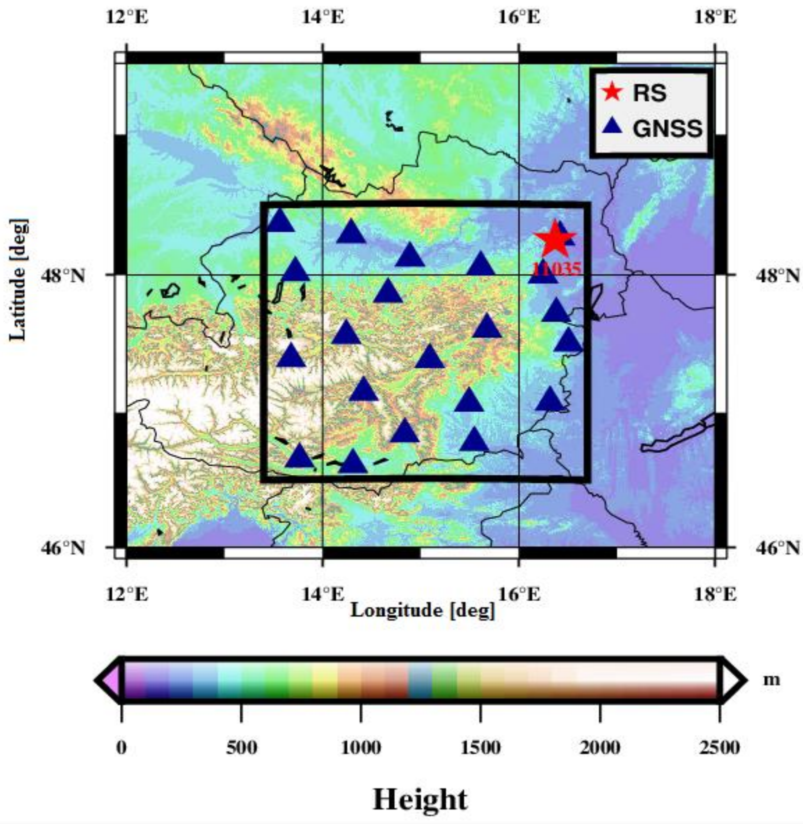

Fig 4. 1. GNSS network of the EPOSA in the eastern part of Austria (Adavi et al., 2022a)

In this network, the heights of the GNSS sites vary from 220 m to 860 m. The mean interstation distance is about 60 km. In the next chapter, the feasibility of using single-frequency observations in comparison to the dual frequency observations and the impact of different regularization methods are analysed using this dataset.

4.1.1.2 EVN Network

EVN is the GNSS network utilized by the Austrian power supply company Energie Versorgung Niederösterreich which consists of twelve permanent reference GNSS stations located across the area of Lower Austria. Rinex files of reference stations include phase and code observations with a rate of 15 seconds for GPS, GLONASS, and GALILEO satellites.

In this campaign, the spans DoYs 100-109 in April and DoYs 233-244 in August 2019 are considered to analyse the impact of GALILEO on the accuracy of the reconstructed tomography field. More details about these items could be found in the next chapter. Fig 4. 2 shows the location of the ten stations that are used in this study and also the place of the radiosonde station for evaluation of the tomography solution. The heights of the GNSS sites vary from 218 m to 860 m and the distances between stations range from 32 km to 151 km.

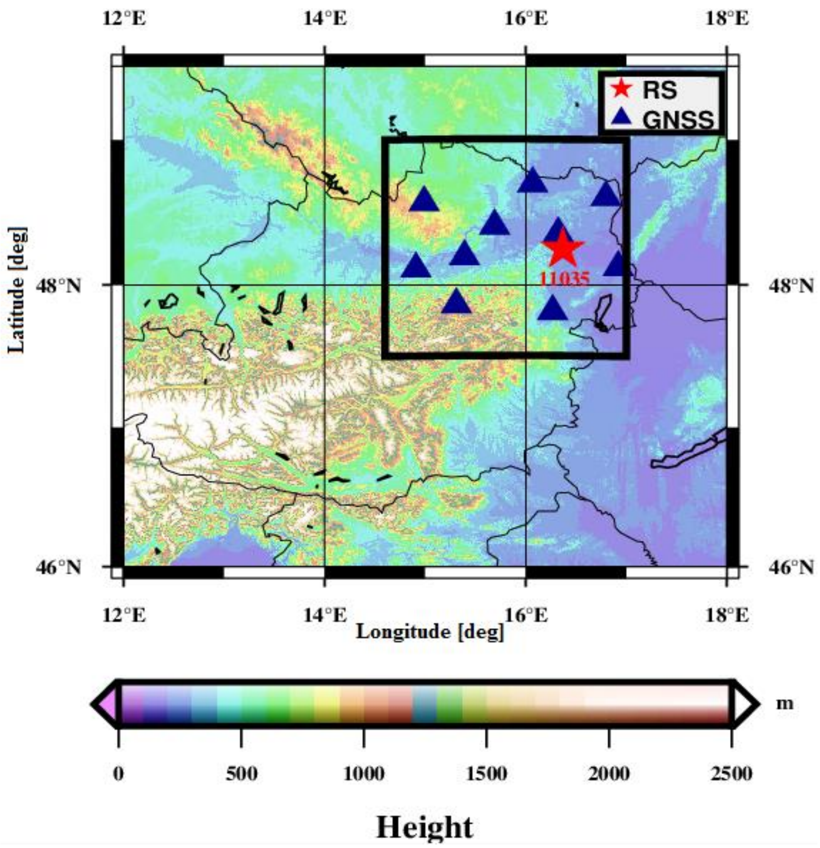

Fig 4. 2. GNSS network of the EVN in the lower part of Austria

4.1.2 COST Action

The EU COST Action ES2016 aimed to improve: (a) the quality of precise point positioning using the advanced GNSS techniques, (b) severe weather forecasting, and (c) climate monitoring (Douša et al., 2016;Jones et al., 2018). The campaign delivered tropospheric ZTDs with a time resolution of 1 hour and horizontal gradients with 6 hours' time resolution as well as ALADIN numerical weather model data and products (Douša et al., 2016). This dataset covers the strong precipitation period in June 2013 leading to atypical floods. This allows to study the troposphere dynamics and content during such crisis.

In this work, the area ranging from 10.15˚ to 14˚ in longitude, and 49˚ to 52˚ in latitude located in the central part of Europe is visited. This campaign contains 72 stations, which are located mostly in East Germany and western parts of the Czech Republic. The height difference between these stations is about 815 m and the average distance is about 48 km in the GNSS network. Spatial distribution of GNSS stations and the location of radiosonde stations used for this study are shown in Fig 4. 3.

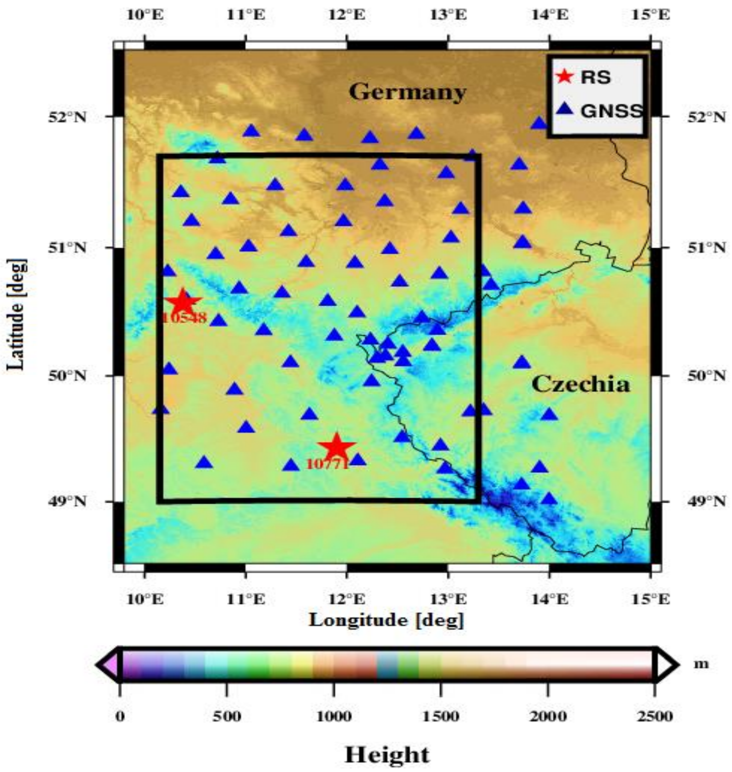

Fig 4. 3. GNSS network of the COST Action in the central Europe

Here, the time span 160-176 in the year 2013 is considered in order to investigate the impact of ray-tracing methods on the accuracy of the tomography solution in comparison to straight-line methods. Moreover, analysis of the spread of the resolution matrix as a proxy for the quality of the GNSS tomography is performed in this campaign due to the availability of the synthetic data in this campaign as well as huge precipitation on some days within the period of interest. Table 4. 1 shows an overview of the applied datasets in the area of interest.

Table 4. 1. Applied dataset and time period in the GNSS network of the COST Action

Dataset	Period	Data
GNSS	160-176	SWD, NWP model
Synthetic	149-165	Synthetic SWD, NWP model

4.1.3 USA CORS Network

The Continuously Operating Reference Stations (CORS) network covers more than 1900 stations in the United States, Canada, Mexico, Central and South America, the Caribbean, and Iraq (Snay and Soler, 2008). The network is designed by NOAA/National Geodetic Survey (NGS) for multi-purpose like positioning, navigation, meteorology, and geophysics applications using GNSS data containing code and carrier phase measurements. Moreover, more than 200 organizations, various governments, academic, and private organizations, contribute to this program in order to share data with NGS. These data are analysed and distributed free of charge for numerous geodetic researches and applications (Snay and Soler, 2008;CORS, 2022;SOPAC, 2022).

In this thesis, only 72 GNSS stations of this network are utilized, which cover a territory mostly located in North America ranging from 38.4° to 42.8 ° in latitude, 87.2 ° W to 83 ° W in longitude. Fig 4. 4 presents the area of interest in this study with the distribution of GNSS receivers and the location of the radiosonde station. The minimum and maximum geodetic heights in this network are 128 m and 337 m, respectively and therefore the area is almost flat without any considerable height differences between stations. In addition, interstation distances vary from 4 km to 480 km in this campaign.

The CORS campaign is used in order to analyse in Section 5.4 the efficiency of GOES-R sounders as a new constraint to improve the accuracy of the reconstructed wet refractivity field.

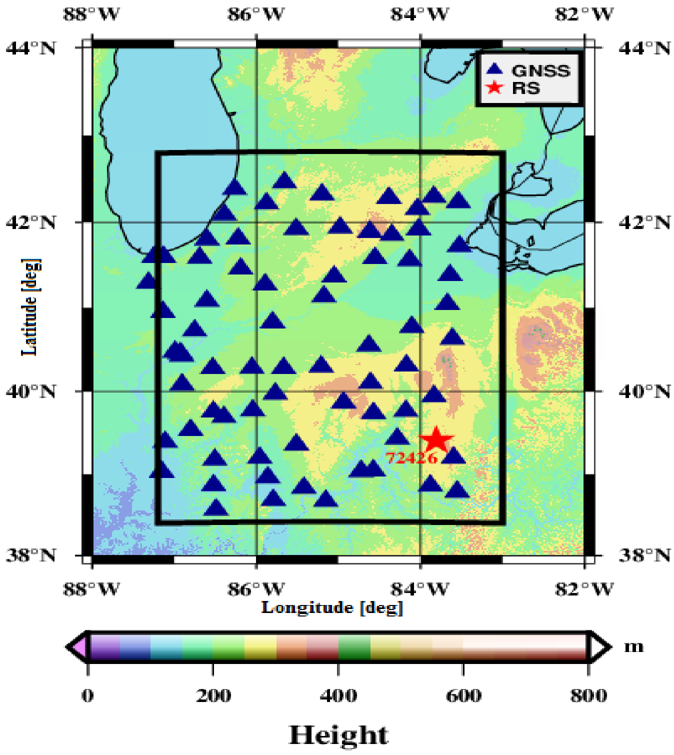

Fig 4. 4. The area of interest in the CORS network

4.2 Meteorological Observations

In this part, the most important meteorological dataset which is used to compute required inputs for the GNSS tomography is described. This data can be divided into three different categories. In the first category, the surface meteorological observations like pressure and temperature are presented. These types of measurements are applied to estimate the hydrostatic part of the tropospheric delay and then the most important input, SWD, could be calculated using Eq. (2.40). Here, only the TAWES network is introduced which is responsible for providing meteorological measurements throughout Austria. The COST campaign contains SWD data for both synthetic and real datasets. For the CORS campaign, the Global Pressure Temperature 3 (GPT3) model was used to estimate the pressure as the surface meteorological measurements which was not available for this network. The GPT3 is an empirical model on a 5° × 5° and 1° × 1° global grid including various meteorological parameters such as pressure, temperature, and specific humidity (Landskron, 2017;Landskron and Böhm, 2018). All meteorological parameters were obtained from monthly average pressure levels data of the ECMWF Re-Analysis product (ERA-Interim) (Landskron, 2017). The GPT3 empirical model can be employed with reasonable accuracy when there is no access to the meteorological measurements (Park et al., 2018;Yuan et al., 2020). Here, a Matlab program established at TU Wien was used to calculate the GPT3 outputs, particularly pressure. To do so, only the station location (φ, λ, h), the date and the GPT3 model with spatial resolution 1° × 1° were used. Please refer to (Landskron, 2017;VMF Data Server, 2022) for more details. The second category belongs to the data which has the role of enhancing the model accuracy. In this work, the GOES-R meteorological products for the first time are applied in the tomography model in order to achieve a unique solution with reasonable accuracy. The last category contains some external data which is used as a reference model to compare with the retrieved wet refractivity field. Here, radiosonde observations are utilized as a reference model for the validation of the tomography solution. In the following, all mentioned data categories in the tropospheric tomography of this work are presented in separate sections.

4.2.1 Surface Meteorological Data

TAWES is the national meteorological network of Austria which is operated by the Zentralanstalt für Meteorologie und Geodynamik (ZAMG). This network is one of the most dense synoptic networks in the world comprising more than 250 semi-automatic weather stations. Fig 4. 5 demonstrates the distribution of the synoptic stations throughout Austria.

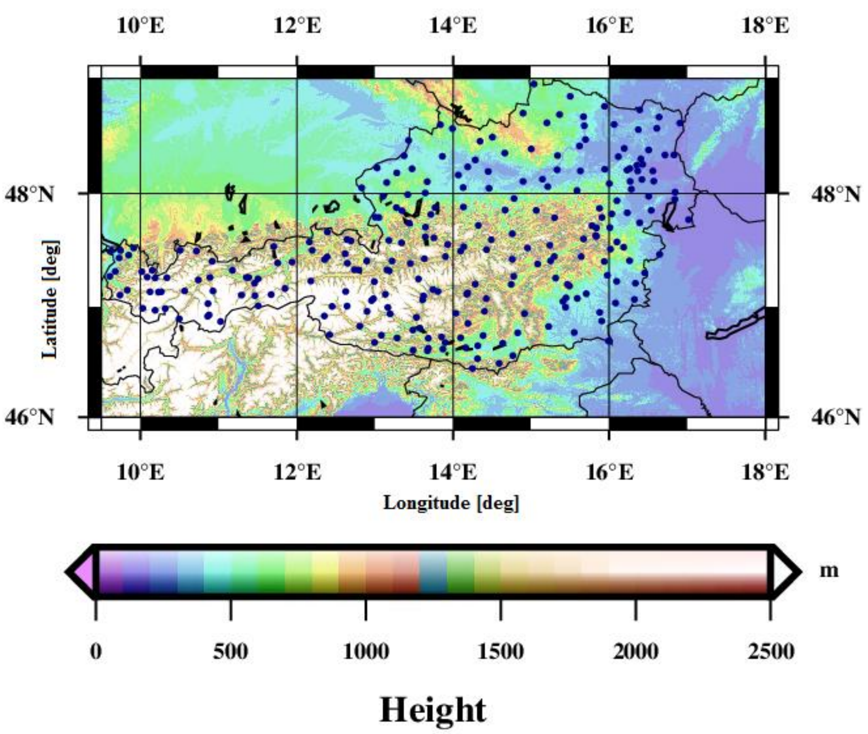

Fig 4. 5. Distribution of TAWES stations in Austria

The TAWES stations measure meteorological parameters such as pressure, temperature, wind speed, wind direction, and relative humidity with a rate of 10 minutes. Fig 4. 6 reports the time series of relative humidity (*RH*), temperature (*T*), and pressure (*P*) for one of the TAWES stations located at $(48.11°, 13.67°, 660.92\, m)$ on DoY 243 September 1st, 2017. These measurements could be interpolated to the GNSS receiver sites using appropriate methods such as polynomial, inverse distance weighting (IDW), and Kriging according to the type of parameters, the distance between synoptic stations and the receiver station, and the topography of the area of interest (see for e.g. (Al-Shaery et al., 2011;Stahel et al., 2006)).

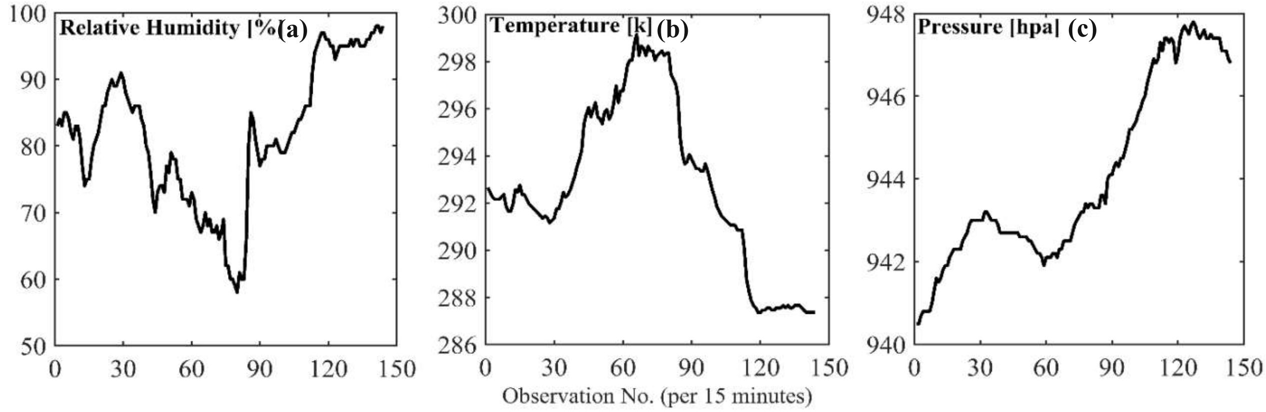

Fig 4. 6. Time series of relative humidity *RH* (a), Temperature *T*, and air pressure *P* on DoY 243 in year 2017 located at $(\mathbf{48.11°, 13.67°, 660.92}\ \boldsymbol{m})$ in the TAWES network

In this work, only the pressure parameter at the location of the GNSS receiver is required to feed the Saastamoinen model to compute *ZHD*. Therefore, the polynomial method is applied to estimate the pressure at the desired position (φ, λ, h) with an error of less than $\pm 1\ hpa$ (Stahel et al., 2006):

$$\hat{P} = a_0 + a_1\lambda + a_2\varphi + a_3\ h \tag{4.1}$$

where $\hat{P}$ is the fitted pressure, a_0 is the intercept of the fitted line, and a_1, a_2, and a_3 refer to the slope coefficients. These coefficients are estimated by applying the least square method to the TAWES pressures located with an average distance of 40 km from the intended GNSS stations. By substituting derived coefficients, the pressure at the GNSS station is computed using Eq. (4.1).

4.2.2 Radiosonde Observations

The radiosonde is acknowledged as a highly accurate standard technique to measure the meteorological parameters of the atmosphere since 1950 (Sá, 2018). The radiosonde is a balloon-borne instrument package that measures different parameters such as temperature ($\sigma_T = \pm 0.5°C$), pressure ($\sigma_P = \pm 1hpa - \pm 2hpa$), relative humidity ($\sigma_{RH} = \pm 5\%$), and geopotential height and transmits them to a ground receiver using radio waves (Heublein, 2019;Manning, 2013). Moreover, measurements of wind speed and wind direction are also acquired due to the tracking of the radiosonde in the flight via GPS (NWS, 2022). The radiosonde profiles associated to the radiosonde station are accessible at 00:00 UTC and 12:00 UTC and can be freely downloaded via NOAA (NOAA, 2022) or Wyoming weather Web (UMYO, 2022). Fig 4. 7 shows the radiosonde ascending a few minutes after launching the balloon.

Fig 4. 7. Radiosonde ascending a few minutes after launch (TWV, 2022)

In order to validate the tomography solution in the area of interest, radiosonde station measurements are used. Table 4. 2 lists the utilized radiosonde stations with their geodetic coordinates. For this purpose, the retrieved wet refractivity field is interpolated to the RS location in each layer using the Inverse Distance Weighting (IDW) method (Wong, 2017) and assuming a strict vertical noise of the radiosonde when passing the different layers.

Table 4. 2. Radiosonde stations in different campaigns

Campaign	Radiosonde Station	Location	Available
Austria (EVN/EPOSA)	11035	16.37E, 48.25N, 200	NOAA/ Wyoming weather Web
COST	10548	10.38E, 50.57N, 450	
	10771	11.90E, 49.43N, 419	
CORS	72426	83.94W, 39.25N, 317	

4.2.3 GEOS-R Data

The Geostationary Operational Environmental Satellite-R Series (GOES-R) is the latest generation of geostationary satellites operated by the National Oceanic and Atmospheric Administration (NOAA) of the United States (US). The first two of the GOES-R series named GOES-16 and GOES-17 were launched in November 2016 and March 2018, respectively (Schmit et al., 2019). GOES-16 is located at $75°W$ (GOES-East) and GOES-17 is operated at $135°W$ about 36000 km above the Earth's equator. Fig 4. 8 illustrates the geographical coverage region of the GOES-16 and GOES-17 satellites.

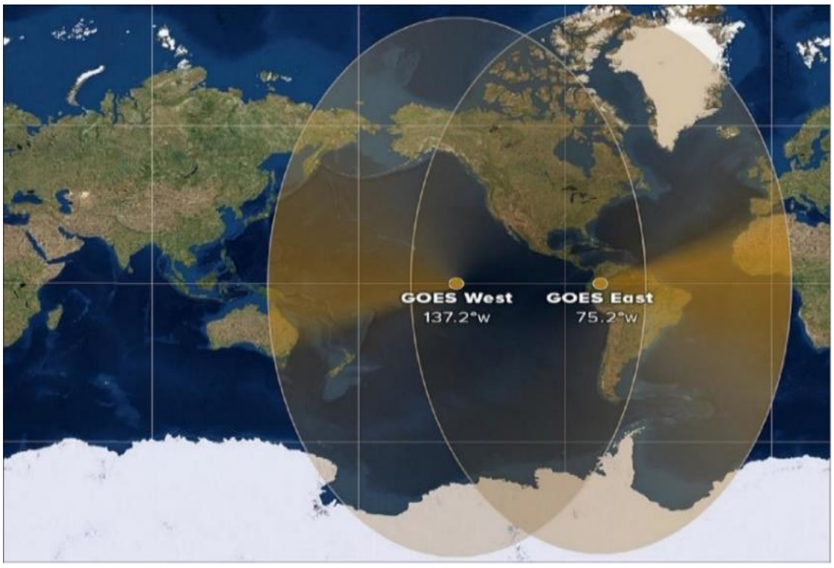

Fig 4. 8. Geographical coverage area of the GOES-16 and GOES-17 (eoPortal Directory, 2022)

The main instrument on-board in the GOES-R series is the Advanced Baseline Imager (ABI) in order to observe the Earth's weather (Schmit et al., 2017;Schmit et al., 2005). Therefore, these satellites could provide continuous and valid environmental data for weather analysis, forecasts, and monitoring (Yu and Wu, 2012). The ABI sounder includes two channels in the visible part of the electromagnetic spectrum, four channels in the near-infrared and ten channels in the infrared and therefore this sounder views the Earth with 16 spectral bands (Schmit et al., 2018). The ABI sounder has a four times finer spatial resolution (0.5–2 km) and more than five times faster coverage rate (30 sec to 10 min) in comparison to the previous generation of GEOS imagers (Schmit et al., 2019;Schmit et al., 2018). The ABI sounder provides the Legacy Atmospheric Profile (LAP) products over each 5 × 5 ABI pixels box region with clear-sky IR channel radiances as follows (Schmit et al., 2019;Yu and Wu, 2012):

- Legacy atmospheric vertical moisture profile (LVM)
- Legacy atmospheric vertical temperature profile (LVT)
- Total precipitable water (TPW)
- Layered precipitable water (LPW)
- Derived atmospheric stability indices (DSI)

These products could be generated in three different coverages: Full Disk (FD), continental United States (CONUS), and Mesoscale. Table 4. 3 describes some properties of these products.

Table 4. 3. Coverage Regions of ABI products (Carlomusto, 2019)

Coverage region	Description
FD	Near hemispheric earth region centered at the longitude of the sensing satellite
CONUS	An approximately 3000 km x 5000 km region intended to cover the continental United States within the constraints of viewing angle from the sensing satellite
Mesoscale	An approximately 1000 km x 1000 km dynamically centered region in the instrument's field of regard. The particular coverage region associated with a mesoscale product is operator- selected to support high-rate temporal analysis of environmental conditions in regions of interest

A full explanation of the LAP products can be discovered in the volume 5 of GOES-R Series Product Definition and User's Guide (PUG) (Carlomusto, 2019).

In this work, only LVM and LVT products of GOES-16 are used in order to compute the wet refractivity field as an initial field to improve the quality of the tomography solution. Table 4. 4 summarizes the performance requirements of those profile (Carlomusto, 2019;Schmit et al., 2017).

Table 4. 4. LVM and LVT profiles performance requirements

LAP Products	Range	Geographic Range	Measurement Accuracy	Mapping Accuracy
LVM	0 to 100 %	FD, CONUS and Mesoscale	Surface to 500 hPa: 18% 500 to 300 hPa: 18% 300 to 100 hPa: 20%	5 km
LVT	180 to 320 K	FD, CONUS and Mesoscale	1 K below 400 hPa and above boundary layer	5 km

The temperature and moisture profiles include values at 101 standard pressure levels in the atmosphere between 0.005 and 1100 hPa (Carlomusto, 2019). Fig 4. 9 shows an example of LVM (*RH*) and LVT (*T*) products for an arbitrary point in the area scanned by GOES-16 on the 1st of August 2019 at noontime.

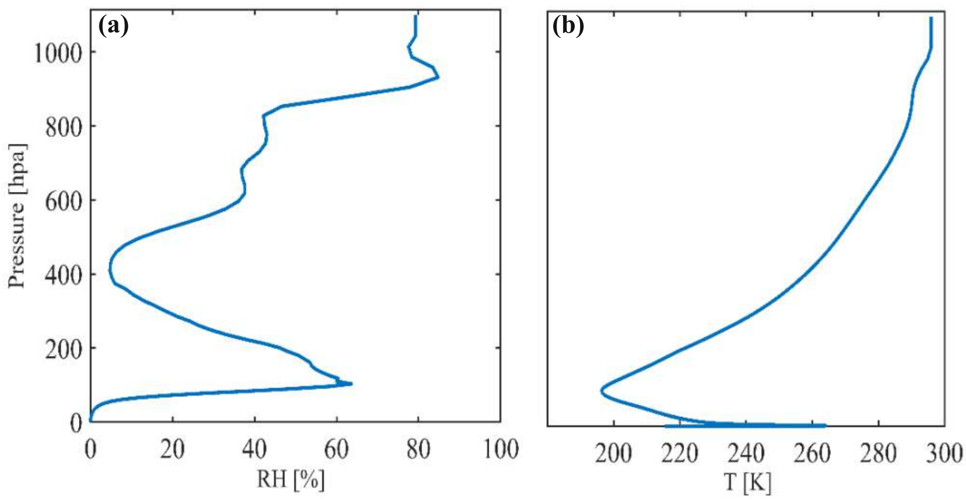

Fig 4. 9. Legacy vertical profile of relative humidity *RH* (a), Temperature *T* of GOES16 on August 1, 2019

Due to existing some gaps in this dataset, the natural neighbour interpolation method has been employed to produce missing data values. This method is a fast, reliable and robust technique which is closely associated with the Delaunay triangulation and the Voronoi diagram (Ledoux and Gold, 2005). Therefore, Eq. (4.2) is used in order to estimate RH or T at the desired location as follows (Ledoux and Gold, 2005;Sibson, 1980):

$$\hat{z} = \sum_{i=1}^{N} w_i \; z_i \tag{4.2}$$

where $\hat{z}$ is the estimated value at the query location, and z_i is the known value at each point located in the Voronoi polygon. n is the number of neighbor polygons, and w_i denotes the weight of each polygon and can be calculated as below (Ledoux and Gold, 2005;Sibson, 1980):

$$w_i = \frac{Vol_i}{Vol_{total}} \tag{4.3}$$

Here, Vol_i and Vol_{total} are the volume of polygon i and the total volume of n neighbor polygons. Accordingly, w_i is always between 0 and 1.

4.3 Numerical Weather Model

Numerical weather prediction models (NWPM) play an important role in meteorology and climate change studies in recent decades due to the appearance of a variety new meteorological measurements and strong processing techniques (Yang et al., 2013;Stensrud, 2009). These models could generate either short-term weather forecasts or long-term climate predications using a series of mathematical models (Yang et al., 2013). NWPM models acquire observations of meteo sensors like ground meteorological stations, radiosonde weather balloons, commercial aircraft and remote sensing weather satellites. Then, the state of weather is predicted at any future epoch by processing these measurements with computer models containing atmosphere and oceans models (Stensrud, 2009;Yang et al., 2013). Therefore, the final outcome of the NWPM contains meteorological parameters such as air pressure, wind, temperature, humidity, cloudiness, precipitation, evaporation, and soil moisture to describe the weather system in time. The basic mathematical equations for NWPM models that could estimate the most important characteristics of the atmosphere behaviour rely on (Pu and Kalnay, 2019;Stensrud, 2009):

- Newton's second law (density, pressure, wind)
- Conservation of mass (density, wind)
- Conservation of energy (temperature, wind)
- Equation of state (density, pressure, temperature)

These equations are also known as primitive equations. In consequence, the future state of the weather system can be predicted at the instant time t by knowing the evaluation laws of the atmospheric state at the instant time t_0 (Alves et al., 2016). Fig 4. 10 shows NWPM outputs displaying the temperature, pressure levels, and wind at the initial state time and also six hours later for the COST campaign on the 29th of May 2018.

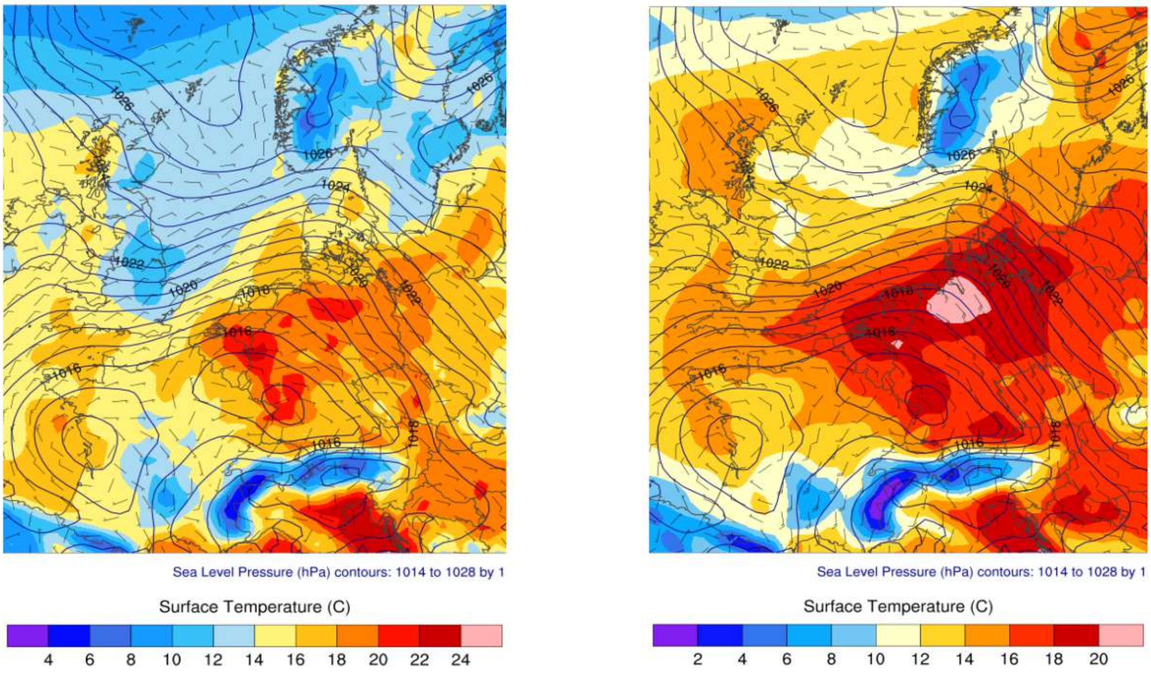

(a) (b)

Fig 4. 10. Surface temperature, pressure levels and wind at (a) 00:00 UTC, and (b) 06:00 UTC

The NWMP models can be different in terms of horizontal and vertical resolution, temporal resolution, and coverage (global or regional). Most regional NWPM models and some global models apply finite difference methods in all spatial dimensions to solve the NWPM equations system (Collins, 2013). For the rest of the models such as global medium range forecasting models and global climate models, finite difference methods and spectral methods are used in the vertical direction and horizontal directions, respectively (Collins, 2013;Jang and Hong, 2016). Table 4. 5 summarizes the most important NWM models with their significant characteristics.

Table 4. 5. Well-known NWM models with their main characteristics

NWM	Horiz. Res	Vert. Res	Temp. Res	Converge	Format	Tem. Coverage
ERA Interim	0.125-3	37 levels (1000-1 hpa)	00,06,12,18	global	NetCdf, grib	1979-2019 Aug
ERA5	0.25	37 levels (1000-1 hpa)	Hourly	global	NetCdf, grib	1979-present
AROME	0.028×0.018	23 levels (1000-100 hpa)	Hourly	Regional (Europe)	grib	2008-present
ALADIN	0.042	87 model levels (1023-1 hpa)	00, 06, 12, 18	Regional (Europe)	grib	1997-present

These models could provide accurate weather parameters at discrete grid points for any certain time. However, appropriate spatio-temporal interpolation methods are demanded in order to find meteorological parameters at a specific single point. In this work, the following steps are applied to compute the meteorological parameters of the desired point at the time of interest:

a) Horizontal Interpolation

The horizontal interpolation is required to estimate the meteorological parameters at the location of the grid points of the tomography model or an arbitrary integration point. In this work, the bilinear interpolation method is applied (Hobiger et al., 2008;Schüler, 2001).

b) Vertical Interpolation

The vertical interpolation is carried out to determine the weather parameters at the actual height, which is essential for the wet refractivity computation. It is much more suitable to use separate interpolation methods for temperature, water vapour pressure, and air pressure due to the nonlinearity of these parameters for computation of refractivity (see Eq. (2.16)) (Hobiger et al., 2008;Nafisi et al., 2012). Therefore, a simple linear interpolation method could be applied in order to determine temperature at the specific height level (Hobiger et al., 2008;Nafisi et al., 2012;Schüler, 2001). In the case of air pressure and water vapour pressure, a logarithmic interpolation is performed to gain values of these parameters at the desired vertical level (Hobiger et al., 2008;Nafisi et al., 2012;Schüler, 2001).

c) Temporal Interpolation

As the GNSS observations, as well as the tomography model, have different temporal resolution in comparison to the NWM products, the temporal interpolation method is required for each observation epoch. The weighted average is the most applied method to estimate the meteorological parameters at the time of interest (Nafisi et al., 2012). Hence, this method is applied to calculate the wet refractivity using Eq. (2.16) at the tomography epoch.

By considering these points, different numerical weather models are used in the investigated campaigns in order to estimate the initial field for the GNSS tomography model. Table 4. 6 demonstrates the models applied within the different campaigns.

Table 4. 6. Applied numerical weather models in different campaigns

campaign	NWM
EPOSA/EVN	AROME/ERA5
COST	ALADIN
CORS	ERA5

Chapter 5

5 Analysis of GNSS Tomography Features for different Campaigns

This chapter aims to analyse important features of GNSS tomography in four different case studies, which have been described in chapter 4. In Section 1, the feasibility of using single-frequency (SF) observations compared to dual-frequency (DF) observations is investigated. Moreover, the ART techniques and the TV method are assessed in this section. The impact of different GNSS constellations in the tropospheric tomography are examined in Section 2. Analysis of the topography effect as well as ray-tracing methods in the GNSS tomography are studied in Section 3. Moreover, the spread of the resolution matrix as a proxy for GNSS tomography quality is analysed in this section. Finally, the feasibility of using GOES-R as an initial field is discussed in Section 4.

5.1. EPOSA Network: Evaluation of Regularization Methods in GNSS Tomography based on Single- and Dual-Frequency Observations and Feasibility of Near-real Time Tomography

The resolution of the reconstructed wet refractivity is highly dependent on the GNSS network density. Consequently, an existing dense GNSS network is one of the essential pre-requirements in this approach. However, the use of DF receivers is not economically practicable in this regard, as these receivers are remarkably expensive. As an alternative, SF receivers can be considered to achieve a sufficient spatial resolution for GNSS meteorology (Bai, 2004;Deng et al., 2009;Krietemeyer et al., 2018). Therefore, in this section, the potential of SF observations in comparison to DF observations is examined for reconstructing the wet refractivity field in the EPOSA GNSS network with twenty-one stations. To quantify the ionospheric delay in the SF processing in Precise Point Positioning (PPP) mode, the Satellite-specific and Epoch-differenced Ionospheric Delay (SEID) model is used (Deng et al., 2009). Aside from the impact of SF and DF observations on the accuracy of ZTD and the wet refractivity field, a second essential component in GNSS tomography is investigated in this section. This second element concerns the effect of various regularization techniques, including ART methods and TV, by considering SF and DF observations.

Another challenge in GNSS tomography is the dependency of the accuracy of the retrieved wet refractivity structure on the quality of the a priori field using some of the solution strategies like ART methods. Therefore, the retrieved tomography field may be very similar to the a priori field instead to reflect the real physical conditions if the chosen regularization parameter was not suitable. Another challenging task in the GNSS tomography is to reconstruct a reasonable near-real-time solution, especially when the number of rays is low and the area covered by the voxel model is large. Here, the TV method is used to retrieve a regularized solution without any initial field in a shorter time span.

Therefore, first, the designed tomography model for the EPOSA network is defined. Then, the estimation of the ZTD using SF observations in PPP mode and DF observations in double-difference mode are described. In the first strategy, SF observations are processed using PPP in goGPS software. In the second strategy, DF observations are processed in double-difference mode with the Bernese software. The accuracy of the estimated ZTD using SF and DF modes is discussed in comparison to ZTD derived from the NWM model. In this study, the AROME (Applications of Research to Operations at MEsoscale) model, which is one of the regional NWM models in Europe, is employed. After that, the reconstructed wet refractivity field using different regularization methods on two different observation types (SF and DF) are compared to radiosonde observations. Finally, the obtained results using the TV and Landweber method in different temporal resolutions compared to radiosonde observations are investigated.

5.1.1 Tomography Model Configuration

For parameterization above the area of interest, we need to select an optimum size of the model elements. Here, the model space resolution matrix ($\boldsymbol{R_m}$) concept (Adavi and Mashhadi-Hossainali, 2014;Adavi and Weber, 2019) was applied to select an optimal horizontal resolution of the tomography model between 40 km and 70 km (see Fig 5. 1). As described in Section 3.2.2, an optimal resolution is obtained when the resolution matrix is close to identity (Aster et al., 2005). This means the well-resolved and poor-resolved model elements are close to 1 and 0, respectively. According to Fig 5.1, when the number of poorly resolved model elements (shaded voxels) by GNSS signals is decreased, resolution matrices have converged to the identity matrix (see Fig 5. 1 (d)). However, as the refractivity is considered as a constant value in each voxel, the model elements should not be too large. Hence, 60 km was selected as the optimum horizontal resolution. In the vertical direction, an exponential layer function was applied (see Eq. (3.7)). Nine vertical layers are employed in this study.

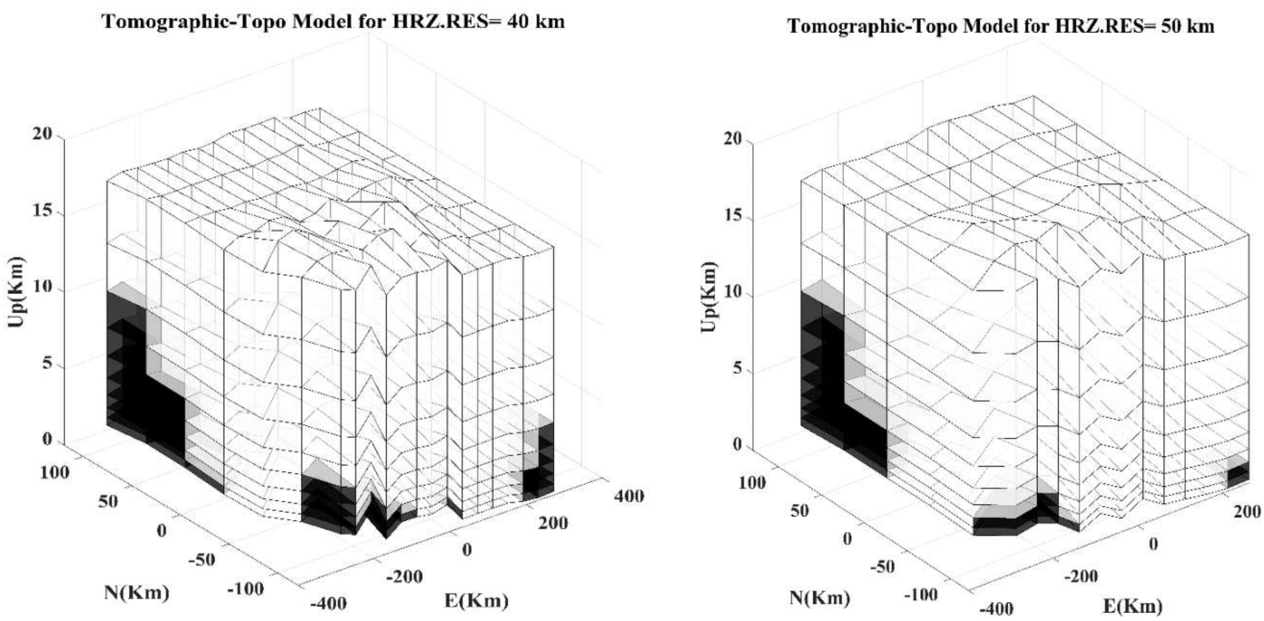

(a) (b)

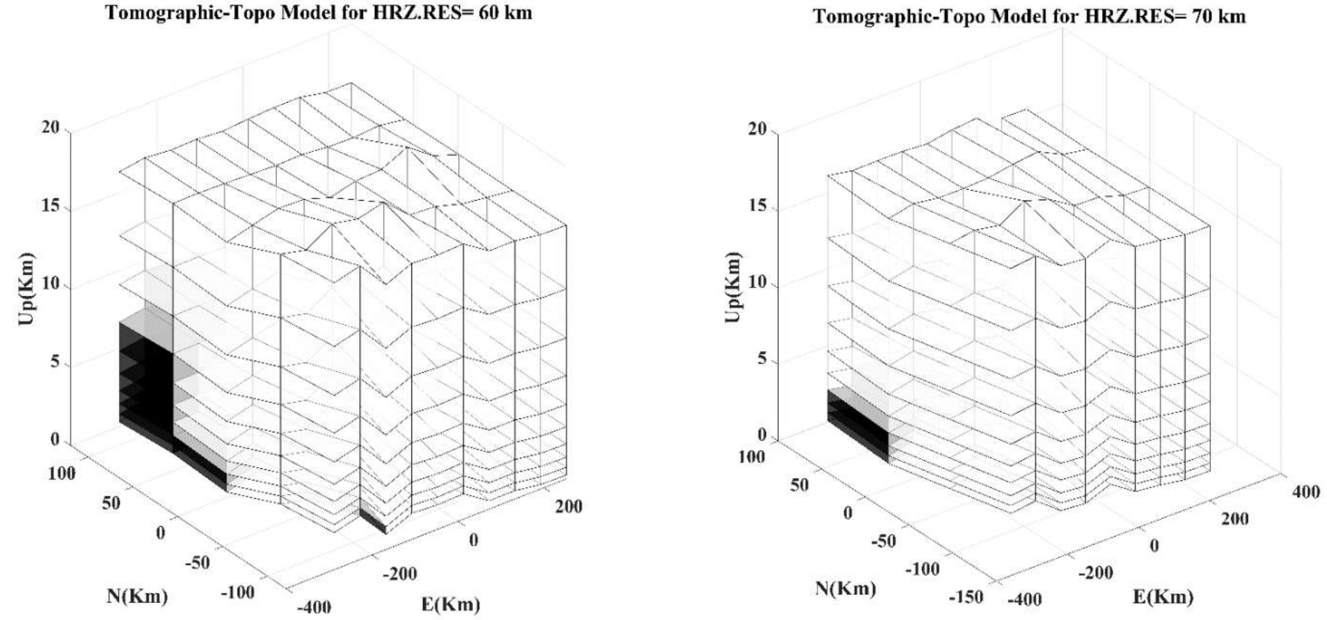

(c) (d)

Fig 5. 1. The tomography model for the horizontal resolutions of (a) 40 km, (b) 50 km, (c) 60 km and (d) 70 km (Adavi and Weber, 2019)

5.1.2 GNSS Data Processing

This section introduces two different strategies for estimating the ZTD. In the first strategy, the undifferenced PPP mode is applied for tropospheric modelling in the goGPS software using SF observation data (Herrera et al., 2016). The ZTD is derived by processing dual-frequency (DF) observations with the Bernese GNSS software in the second one.

5.1.2.1 PPP Strategy using SEID Algorithm

The ionospheric delay is one of the major error sources in GNSS based positioning. For that reason, the ionospheric-free linear combination (IF LC) built of dual-frequency observations is normally used in PPP. Unfortunately, cheap SF receivers do not track observations on a second frequency. In addition, the accuracy of the ionospheric model should be a few tens of TECU in order to achieve promising results using SF observations. This quality can neither be provided at the moment by well-known broadcast models like Klobuchar or NeQuick nor by IGS-GIMs. To overcome these difficulties Deng et al. (2009) developed a technique that derives a synthetic second frequency from multi-frequency receivers located close to the SF receiver using the geometry-free linear combination. They call this approach the Satellite-specific and Epoch-differenced Ionospheric Delay (SEID) model (see Fig 5. 2). Hence, with the generated synthetic second frequency, it is possible to calculate a PPP solution using the ionospheric-free linear combination. By exerting this method, Deng et al. (2009) have reached an RMS of 3 millimeters of the ZTD estimates in comparison to ZTD estimates based on PPP solutions using real observations on two frequencies. The generated synthetic frequency data was derived from reference stations within a distance of 52 km to 75 km.

In this study, data of the four IGS (International GNSS services) stations GRAZ, MEDI, WTZR, and ZIMM were applied together with the SEID model to generate the synthetic second frequency for the case study stations from which only SF observations were used. Due to the fact that goGPS supports SEID only for GPS, no other GNSS were included in the analysis. For the PPP solution, CNES (Centre National d'Etudes Spatiales) final products available from CDDIS (Crustal Dynamics Data Information System) were used for satellite orbits and clock solutions. In this case study, the ZTD was estimated with an update rate of 30 seconds. Then, the estimated ZTD values were averaged over every 1 hour in order to provide better consistency with the processing of the tomography model.

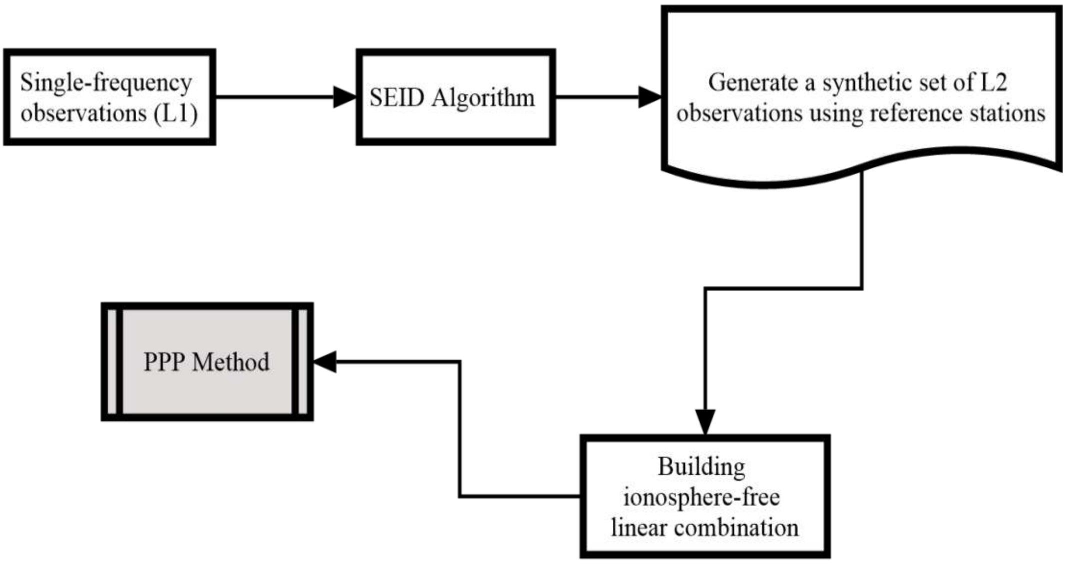

Fig 5. 2. Building L2 observations used in goGPS software (Scheme 1) (Adavi et al., 2022a)

5.1.2.2 Network Strategy

Generally, the process of ZTD determination by means of the Bernese GNSS software in baseline mode is illustrated by the flow diagram in Fig 5. 3 (Dach et al., 2015). According to this figure, phase and code observations are preprocessed, and single-difference observations are created. After a successful cycle slip detection and marking of outliers, station coordinates and ZTDs are calculated in the parameter estimation step (GPSEST).

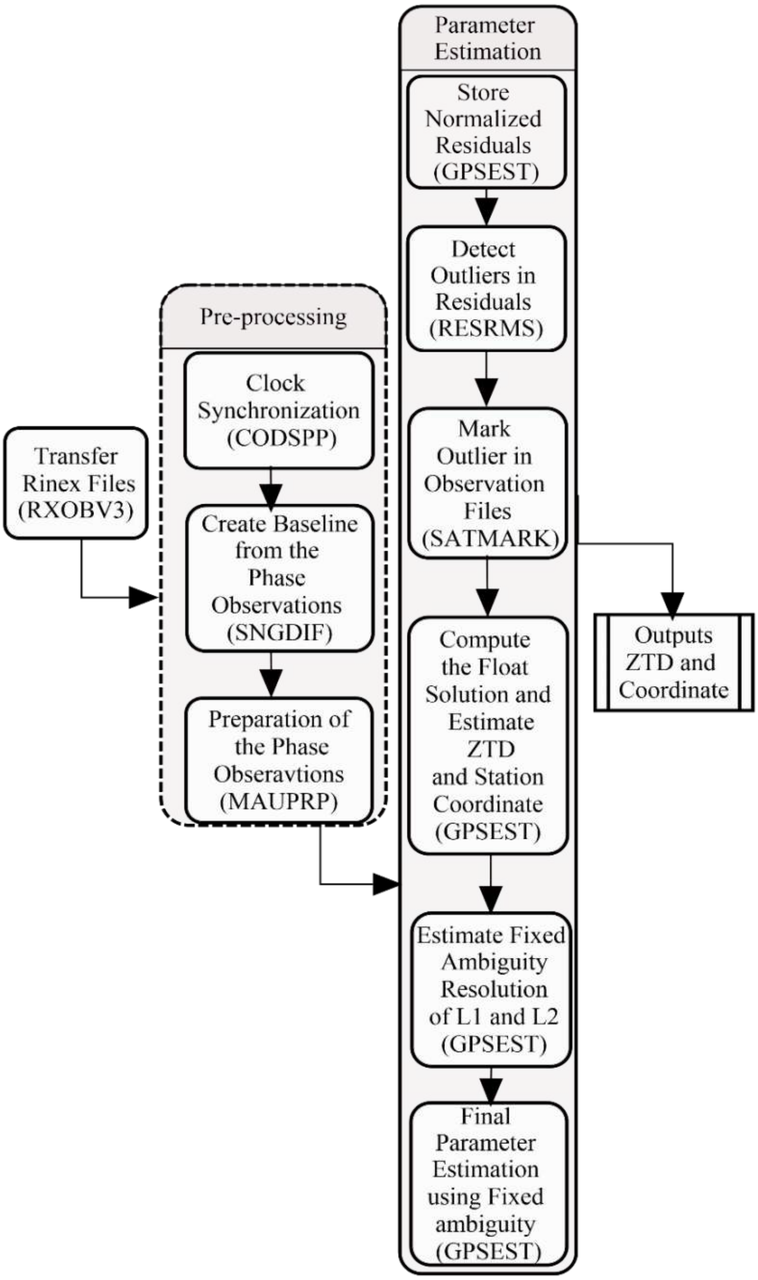

Fig 5. 3. Flowchart of tropospheric parameter estimation using the Bernese GNSS software (Scheme 2) (Adavi et al., 2022a)

Final precise orbits and earth rotation parameters provided from CNES are applied to achieve high precision. Ephemeris data is parametrized via the collocation method in module ORBGEN and interpolated to the desired GNSS observations epochs (here 30 sec). For datum definition, the coordinates of the IGS stations, GRAZ, MEDI, WTZR, and ZIMM, were tightly constrained. Besides, the relative and absolute a priori ZTD sigmas for all stations were set to 5 meters and 1 meter, respectively. In contrast to the float PPP scheme, the phase ambiguities were fixed in the DF scheme. In this strategy, ZTD was estimated every 15 minutes over the investigated period. Finally, hourly mean values of the estimated DF ZTDs were calculated to establish better consistency with the tomography model. Table 5. 1 summarizes the main inputs and settings applied to estimate ZTD in baseline mode.

Table 5. 1. Bernese GNSS processing settings

Parameters		Bernese Processing
Reference System		ITRF2014
Coordinate format		XYZ
Satellite Orbit and Clock		IGS Final Products (CDDIS) / 30 sec
Earth Rotation Parameters		IGS Final ERPS (CDDIS)
Tropospheric Model	Dry	Dry GMF
	Wet	Wet GMF
	Mapping Function	VMF1
	Gradient	CHENHER
Ionospheric Model		Global Ionospheric Models "GIMs" (CODE)
Ocean tidal loading		FES2004 model (Chalmers)
Atmospheric tidal loading		Ray and Ponte 2003 model based on ITRS 2010
Ambiguity Fixing Strategy		Quasi Ionosphere-Free (QIF)
GNSS System		GRE/GR/GE
Phase centre eccentricities and variations		PCV.I14
Observation type		Phase and Code
Elevation angle		5 degrees
Observation sampling rate		30 sec

5.1.3 Weather Condition in the Study Period

Observations on days 232-245 in August 2019 have been chosen due to the unstable weather conditions with high and low amounts of precipitation in the period of interest. Fig 5. 4 shows variations of total precipitation (accumulated water in the frozen and liquid states, including rain and snow (Muñoz Sabater, 2022)) revealed by the AROME model and the observed relative humidity calculated from radiosonde data.

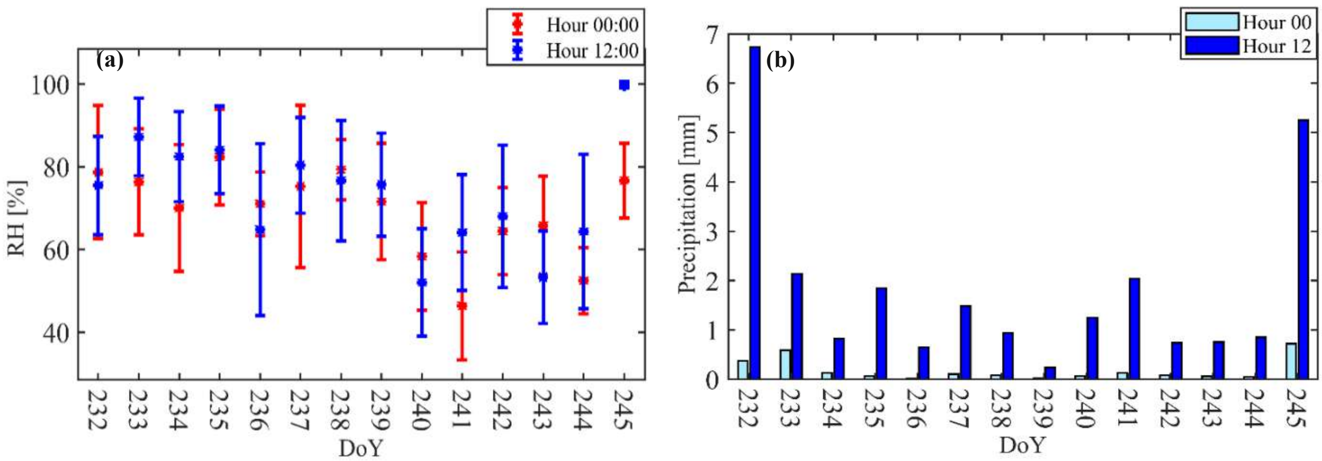

Fig 5. 4. Variations of relative humidity up to 4 km height (a) and average of total precipitation within the whole area (b) during the time of interest (Adavi et al., 2022a)

5.1.4 GNSS ZTD in Comparison to NWM ZTD

To illustrate the impact of schemes on the ZTD and SWD's accuracy, the estimated ZTD from SF and DF observations were compared to the ZTD derived by ray-tracing through the AROME model. As shown in Fig 5. 5, the consistency of the derived ZTDs by the DF algorithm is higher compared to ZTDs calculated from SF data both at midnight and noontime. However, the performance of both strategies with respect to AROME at noontime is slightly superior compared to midnight. In addition, the inconsistency between the SF ZTDs and AROME ZTDs is much more visible in comparison to DF ZTDs and AROME ZTDs. This could be explained by considering the float solution of the PPP ZTD estimation process. Moreover, remaining mis-modelling of ionopsheric variation by the SEID algorithm could affect the ZTD solution (Aichinger-Rosenberger, 2021). Nevertheless, the obtained results show the potential of the SF observations to estimate ZTD with an average RMSE of less than 7.5 cm with respect to AROME ZTD.

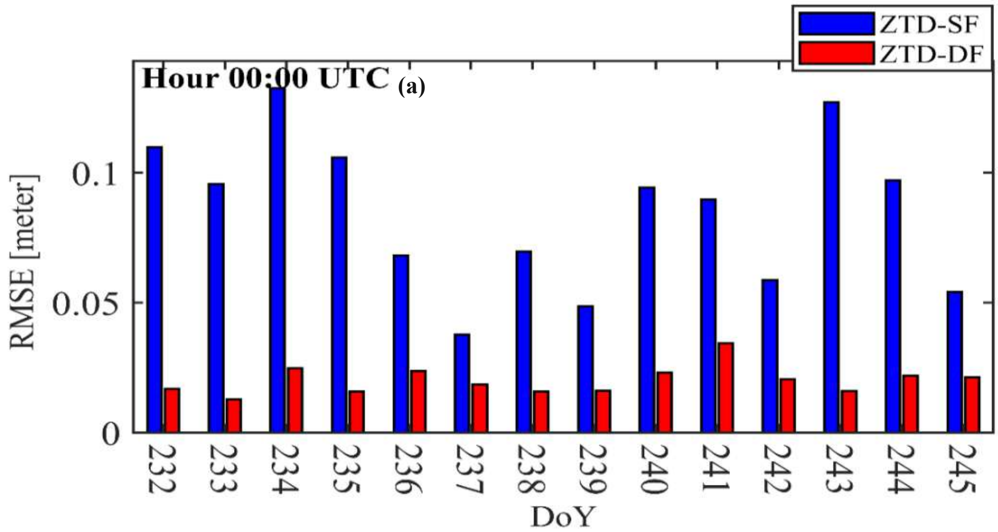

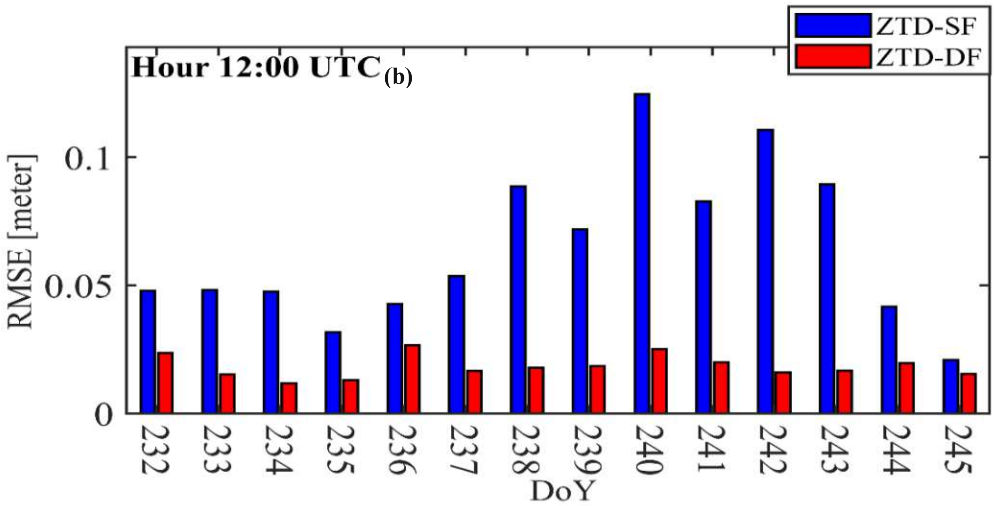

Fig 5. 5. Average RMSE of ZTD difference at 00:00 UTC (a) and 12:00 UTC (b) determined for days 232–245 for single-frequency and dual-frequency observations with respect to AROME (Adavi et al., 2022a)

Table 5. 2 summarizes the average RMSE for both SF and DF strategies at midnight and noontime during the period of interest. The numbers in brackets denote the minimum and maximum RMSE among all GNSS stations.

Table 5. 2. Mean RMSE over all stations with respect to AROME ZTDs for SF and DF schemes during the period of interest (Adavi et al., 2022a)

RMSE [meter]	Midnight	Noontime
SF Scheme	0.085 [0.038 0.130]	0.065 [0.021 0.125]
DF Scheme	0.020 [0.013 0.034]	0.018 [0.012 0.026]

Moreover, Table 5. 3 reports the mean Bias during the period of interest for SF and DF schemes at midnight and noontime. Again the numbers in brackets denote the minimum and maximum bias among all GNSS stations. According to this table, the range of Bias variations in the DF scheme is smaller than in the SF scheme. In addition, a considerable Bias of the SF ZTDs of about 0.23 meters shows up for station WEYE. This may return to insufficiently resolved ambiguities that have an impact on the ZTD estimation process.

Table 5. 3. Mean Bias over all stations for SF and DF schemes during the period of interest (Adavi et al., 2022a)

Bias [meter]	Midnight	Noontime
SF Scheme	0.021 [-0.017 0.230]	-0.022 [-0.085 0.078]
DF Scheme	-0.009 [-0.026 -0.002]	-0.006 [-0.019 0.001]

Fig 5. 6 represents the time series of SF ZTD and DF ZTD for two example stations, GRAZ (height approx. 538 m) and TRAI (height approx. 407 m), compared to AROME ZTD during the period of interest at midnight and noontime. As shown in this figure, the discrepancy between the GNSS ZTD for both SF and DF schemes against the AROME ZTD is relatively high at noontime. This difference most probably returns to the quality of the employed part of the AROME model for the GRAZ station since the estimated ZTDs are close to the computed tropospheric delays by IGS analysis centres. For instance, the difference between the ZTDs from IGS and the estimated DF ZTDs is less than 0.01 cm and 0.02 cm at noontime for DoYs 236 and 238, respectively. Nevertheless, the behaviour of DF ZTD generally shows considerable similarity with the AROME ZTD. The correlation between the time series of SF ZTD and AROME ZTD is also appreciable but not as high as for DF ZTD.

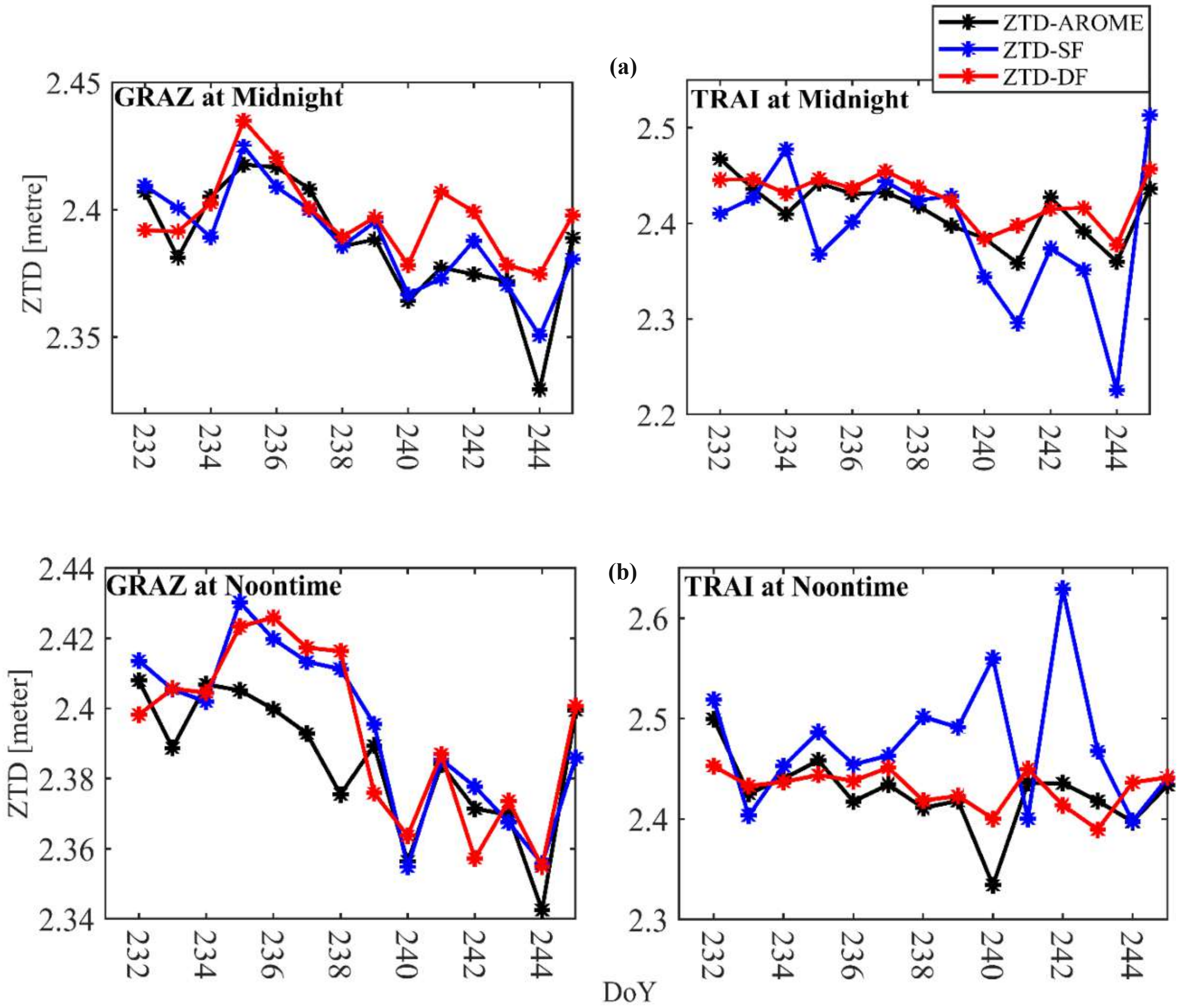

Fig 5. 6. Time series of average ZTD using SF and DF schemes for GRAZ and TRAI stations at midnight (a) and noontime (b) (Adavi et al., 2022a)

In order to gain a better representation of the consistency of GNSS ZTD in both schemes and AROME ZTD, the Pearson correlation was calculated during the period of interest at midnight and noontime for all GNSS stations. Indeed, the correlation was estimated per hour between the ZTD series of GNSS stations. Table 5. 4 summarizes the mean correlation over all investigated days. Similar to Table 5. 2 and Table 5. 3, the numbers in brackets show the minimum and maximum correlation among all studied GNSS stations. According to these results, DF ZTD is consistent with AROME ZTD for both midnight and noontime. For SF ZTD, the correlation drops significantly but remains still above 50%. Therefore, still a reasonable but limited consistency with AROME can be stated which is slightly higher at noontime in comparison to midnight. The lower correlation of the SF ZTD can be explained by complexity to describe the ionospheric delay with SEID. Moreover, there might also be artifacts from model deficiencies e.g., satellite clocks in PPP processing. As expected a successful integer fixing of the ambiguities improves the results and leads to a much more accurate estimation of the SF ZTD.

Table 5. 4. Mean Correlation over all stations for SF and DF schemes during the period of interest (Adavi et al., 2022a)

Correlation [%]	Midnight	Noontime
SF Scheme	66 [49 92]	79 [43 93]
DF Scheme	97 [89 99]	97 [94 99]

It has to be highlighted that not only the GNSS ZTDs but also deficiencies in the AROME model can cause inconsistency between ZTDs time series. Fig 5. 7 shows the differences between relative humidity (RH) and temperature (T) of the AROME model and RS measurements on DoY 235. As can be seen in Fig 5. 7, the difference between temperature profiles of AROME and RS are varying from -2 K to 4 K. For RH profiles, the difference range is changing between -40% and 60%.

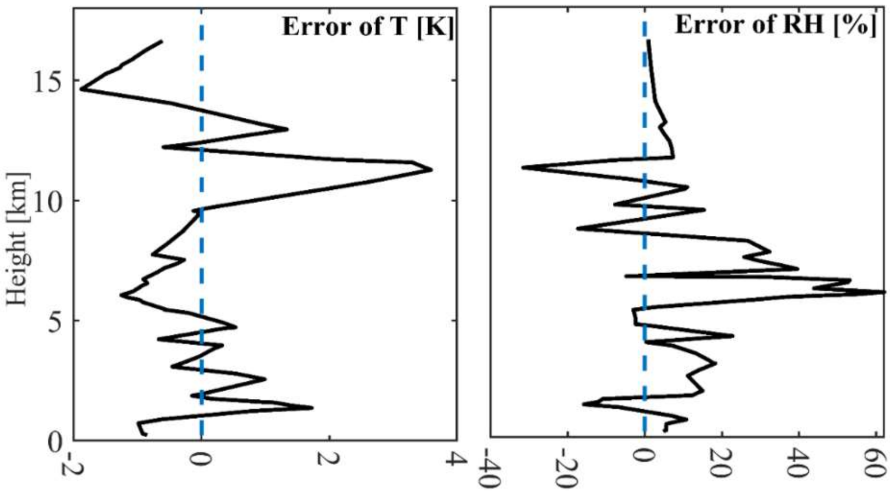

Fig 5. 7. Difference of T (left) and RH (right) of the AROME model in comparison to radiosonde (RS) observations on DoY 235 at midnight (hour 00:00 UTC) at RS11035 location (Adavi et al., 2022a)

Table 5. 5 summarizes mean RMSE of temperature and relative humidity in comparison to RS11035 profiles (red star in Fig 4.1) during the period of interest.

Table 5. 5. Daily RMSE of AROME meteorological profiles in comparison to RS measurements (Adavi et al., 2022a)

Parameter	Up to 5 Km	5 km to 18 km
T [K]	Max= 2.33 and Min= 0.35	Max= 2.23 and Min= 0.77
RH [%]	Max= 25.52 and Min= 7.07	Max= 32.81 and Min= 8.81

5.1.5 Iterative Regularization Techniques versus TV

In this section, the accuracy of the reconstructed profiles using different strategies is evaluated by reference radiosonde observations located at Vienna airport (RS11035) at midnight and noontime. Fig 5. 8 presents the studied schemes in this research. As shown in this figure, the wet refractivity field is reconstructed by considering

SF and DF datasets using the ART techniques and TV method. Overall, the wet refractivity outcome of seven different regularization methods are compared to the radiosonde wet refractivity on basis of SF and DF observations in this research, which are: (1) Landweber+ AROME, (2) MART+ AROME, (3) ART+ AROME, (4) TV, (5) Landweber+ TV, (6) MART+ TV, and (7) ART+ TV. Moreover, it should be highlighted that the time resolution of the tomography model is chosen to be 1 hour that means 24 epochs in each day.

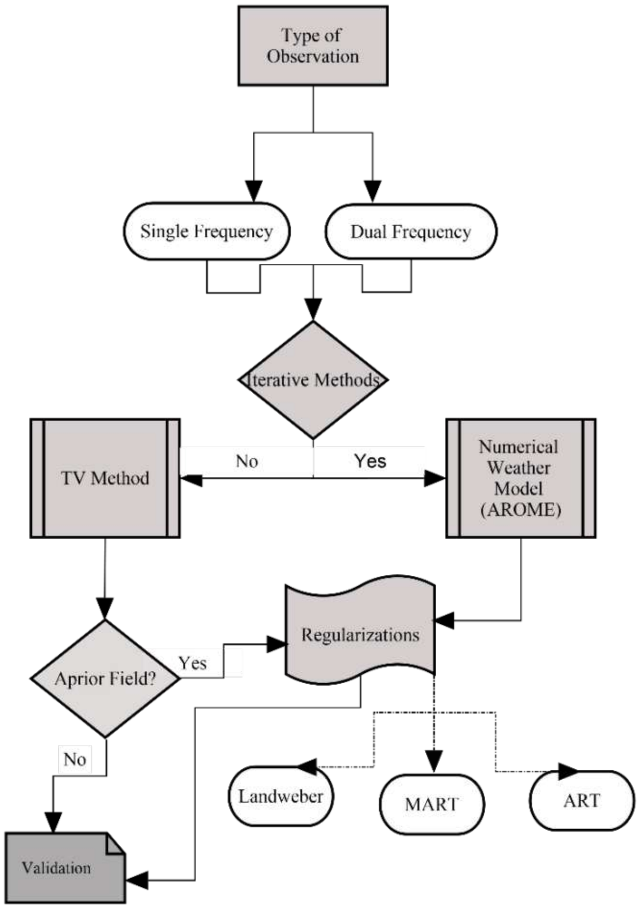

Fig 5. 8. Studied schemes on basis of SF and DF observations (Adavi et al., 2022a)

Fig 5. 9 demonstrates the average of MAE in the wet refractivity field over the period of interest for the SF and DF schemes that apply to different regularization methods in order to reconstruct the tomography solution. According to Fig 5. 9 (a,b), the performance of the SF scheme is comparable with the DF scheme especially when the AROME model is applied as an initial field at midnight. However, the differences between SF and DF schemes for the ART method were increased at noon, which may return to the sensitivity of the ART method to the existing noise in SF ZTD. Moreover, the TV regularization method provides promising results mainly for the DF scheme. Therefore, the TV algorithm could provide an acceptable reconstructed wet refractivity field without the existence of an initial field. In addition, the output of the TV method was applied in the ART techniques as an initial guess. ART+ TV is generally superior for the DF scheme based on Fig 5.9. Moreover, ART+ TV has minimum MAE for the SF scheme at midnight, but MART+TV provides better results compared to other ART techniques+ TV during noontime.

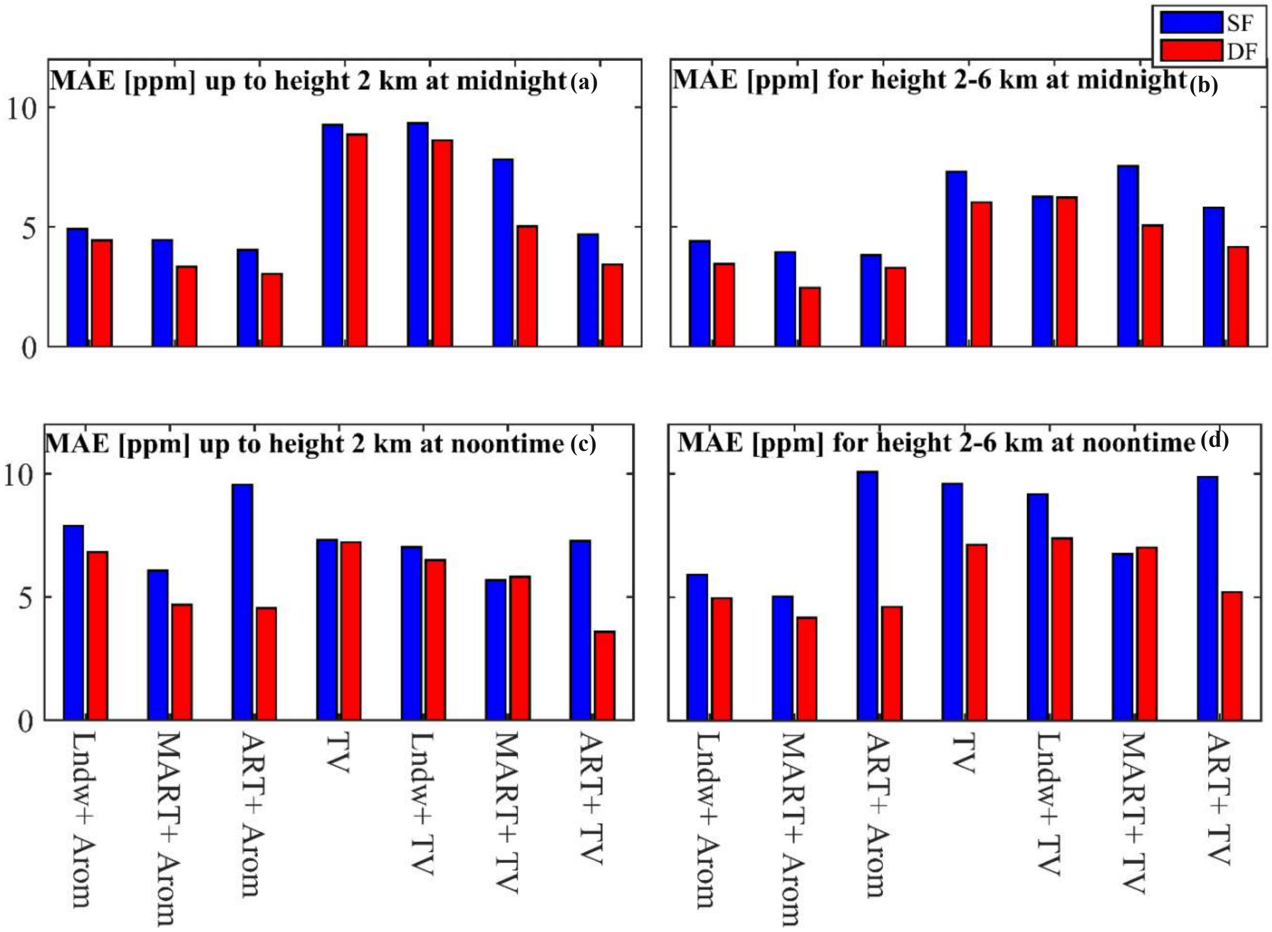

Fig 5. 9. MAE of the reconstructed wet refractivity profiles for heights up to 2 km at 00:00 UTC (a), 2 km to 6 km at 00:00 UTC (b), up to 2 km at 12:00 UTC (c), and 2 to 6 km at 12:00 UTC (d) at RS11035 location (Adavi et al., 2022a)

In order to discover the overall accuracy of the retrieved wet refractivity using the tomography method, the dispersion of the different schemes in comparison to the radiosonde profile at RS11035 was calculated for the period of interest. Fig 5. 10 shows the scatter-plot of wet refractivity for the DF scheme (left panel) and for the SF scheme (right panel). The y-axis denotes wet refractivity (in ppm) calculated from the RS measurements, while the x-axis shows wet refractivity of the tomographic approach. Each graphic covers 252 data points evaluated within the 14 days period investigated here times the 9 voxels (height layers) above the RS launch site times 2 launches per day (14×9×2=252). According to Fig 5. 10, the spreading of the reconstructed tomography field in the DF scheme is generally smaller than in the SF scheme. The TV algorithm for both, the DF and SF schemes, shows a comparable dispersion to the least-square line. The match between RS and reconstructed wet refractivity by applying the AROME model as a priori field is closer than for other schemes for both, the SF and DF strategies. Moreover, as shown in Fig 5. 10, applying TV output as an initial field for ART regularization techniques provides reasonable results in both schemes.

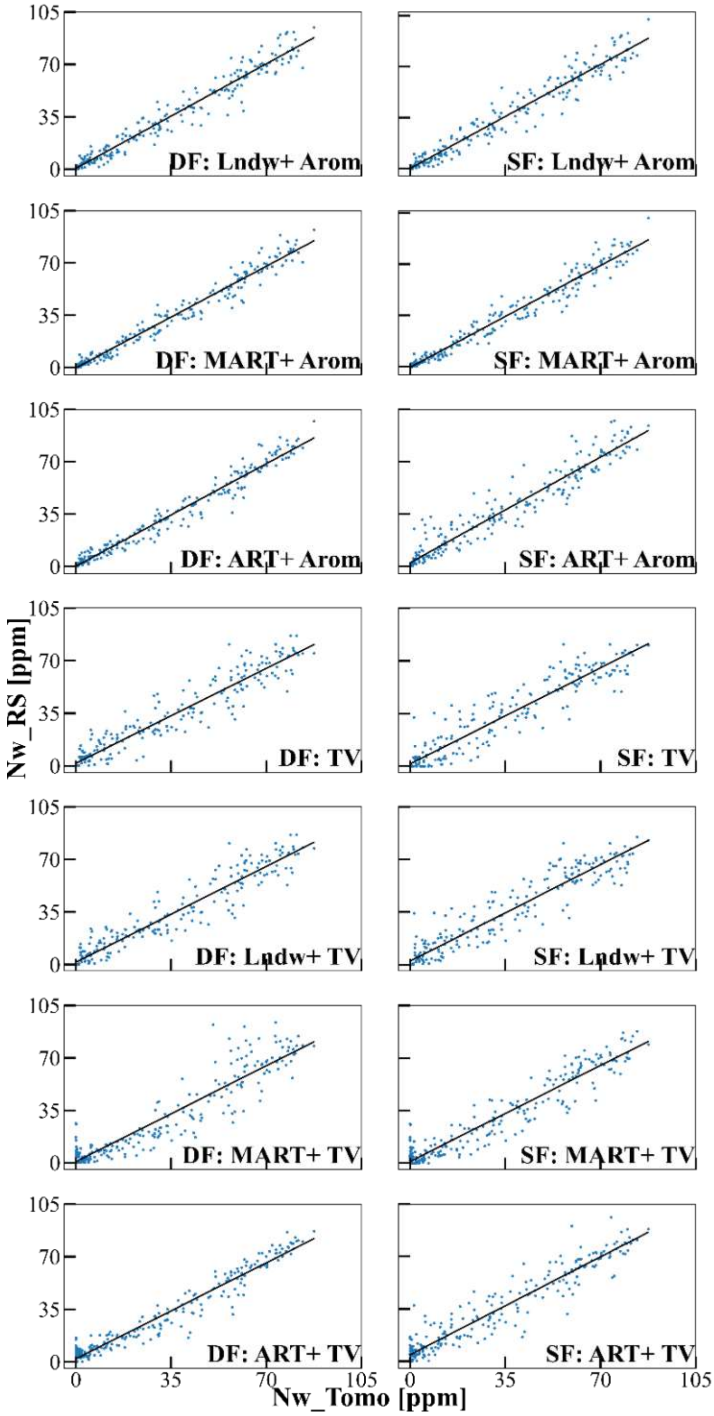

Fig 5. 10. Comparison of reconstructed wet refractivity of DF schemes (left panel) and SF schemes (right panel) to RS11035 wet refractivity during the period of interest (Adavi et al., 2022a)

To better interpret the obtained results, the slope of the least-square line is reported in Table 5. 6. According to this table and also Fig 5. 10, it could be concluded that the performance of all ART techniques (ART, MART, and Landweber) + AROME for the SF scheme is as good as for the DF scheme since the slope of the corresponding least-square lines is almost close to 1:1. The TV method and ART techniques+ TV for both schemes slightly underestimate the wet refractivity field. However, the obtained results from these methods are also reasonable.

Table 5. 6. The slope of the least-square line for all regularization methods in SF and DF schemes (Adavi et al., 2022a)

	Lndw +Arom	MART +Arom	ART +Arom	TV	Lndw +TV	MART +TV	ART +TV
SF	1.00	0.97	0.98	0.90	0.91	0.92	0.91
DF	1.02	0.99	1.01	0.91	0.92	0.91	0.94

According to the reported values in Table 5. 7, the correlation for different regularization techniques in SF and DF schemes are almost higher than 95% except for MART+TV in the SF scheme, which is about 93%. Therefore, the retrieved wet refractivity for SF and DF schemes using all regularization techniques correlates considerably with the RS profile.

Table 5. 7. Correlation Coefficient [%] between the reconstructed wet refractivity profile and RS profile using different regularization methods for SF and DF schemes during the period of interest (Adavi et al., 2022a)

	Lndw +Arom	MART +Arom	ART +Arom	TV	Lndw +TV	MART +TV	ART +TV
SF	97.98	98.65	98.56	95.77	96.06	93.21	97.63
DF	97.80	98.42	96.67	94.98	95.23	95.68	95.57

The average RMSE of wet refractivity for all days considered for the location of RS11035 are listed in Table 5. 8 (see Appendix B for daily RMSE results). It can be concluded that the differences of the reconstructed refractivity profiles by applying the AROME model as an initial field (obtained from both the SF and DF schemes) with respect to refractivity calculated from RS data are less than 4.6 ppm and 9.5 ppm at midnight and noontime, respectively. In addition, the accuracy of the TV method and TV+ ART techniques for SF and DF schemes is roughly comparable during the studied epochs. In general, as expected, the DF scheme shows a lower RMSE almost for all regularization techniques compared to the SF scheme. Nevertheless, even in the SF scheme, the TV method and TV+ ART techniques could provide reasonable results in tropospheric tomography.

Table 5. 8. Average RMSE [ppm] over 14 days for different schemes of SF and DF modes at the location of RS11035 (Adavi et al., 2022a)

	Lndw +Arom		MART +Arom		ART +Arom		TV		Lndw +TV		MART +TV		ART +TV	
	00 h	12 h	00 h	12 h	00 h	12 h	00 h	12 h	00 h	12 h	00 h	12 h	00 h	12 h
SF	4.51	6.76	4.02	5.37	4.01	9.37	8.52	8.23	7.89	8.24	8.94	6.33	6.11	8.99
DF	4.09	5.94	2.93	4.56	3.32	4.69	7.81	6.85	7.84	6.73	6.37	6.73	4.86	5.04

The average Bias was also calculated over the study period to assess further the accuracy of the reconstructed wet refractivity field, using different regularization methods in SF and DF schemes. Table 5. 9 summarizes the average bias for the location of RS11035 during the whole experimental period. According to that, the bias of the reconstructed tomography profile using different regularization techniques is almost the same for SF and DF schemes at midnight and noontime. Similar to the MAE, the bias for ART+ AROM and ART+ TV during noontime in the SF scheme is significant. Mis-modeling of the ionospheric delay by the SEID model might be a potential reason. In addition, this could be due to higher solar activities during the noontime, which causes noise in SF ZTD and consequently SWD observations, since the ART technique is especially sensitive to the existing noise in the observations. Moreover, it should be highlighted that the correlation between reconstructed profiles and RS profiles obtained by various regularization schemes in the SF scheme is almost higher than for the DF scheme, while bias and RMSE demonstrate different results. This may return to the fact that correlation is not sensitive to any shift in the reconstructed wet refractivity profile with respect to the RS profile. Nevertheless, all statistical results show promising results using TV and ART techniques + TV for DF and SF schemes to reconstruct wet refractivity in the troposphere.

Table 5. 9. Average Bias [ppm] over 14 days for different schemes of SF and DF modes at the location of RS11035(Adavi et al., 2022a)

	Lndw +Arom		**MART +Arom**		**ART +Arom**		**TV**		**Lndw +TV**		**MART +TV**		**ART +TV**	
	00 h	12 h	00 h	12 h	00 h	12 h	00 h	12 h	00 h	12 h	00 h	12 h	00 h	12 h
SF	0.20	1.14	-1.23	-0.16	-0.62	5.88	-1.52	-0.84	-1.34	1.02	-2.31	-0.73	-0.83	5.57
DF	0.38	0.54	0.05	-0.99	-0.23	-0.49	-1.02	-1.01	-1.15	-0.95	-0.27	-2.22	0.67	-0.40

5.1.6 Feasibility of Near-Real-Time Tomography using TV Method

One of the challenges that stand in GNSS tomography is the dependency of the accuracy of the retrieved wet refractivity structure on the quality of the a priori field using some of the solution strategies like ART methods. Therefore, the retrieved tomography field may be very similar to the a priori field instead to reflect the real physical conditions if the chosen regularization parameter was not suitable. Another challenging task in the GNSS tomography is to reconstruct a reasonable near-real-time solution, especially when the number of rays is low and the area covered by the voxel model is large.

In this part, the feasibility of the TV technique to reconstruct the wet refractivity in a short tomography window is investigated. The main strategy of this research is presented in Fig 5. 11. As shown in this figure, six different temporal resolutions (10 minutes to 60 minutes) with a time step of 10 minutes are defined and then the wet refractivity field is estimated using the TV method. Moreover, the Landweber method by considering the AROME model as an initial field is also applied to retrieve the wet refractivity solution to interpret the TV results better.

Finally, radiosonde measurements located at Vienna airport (RS11035) are utilized to compare the estimated wet refractivity field in order to obtain the accuracy of the proposed method.

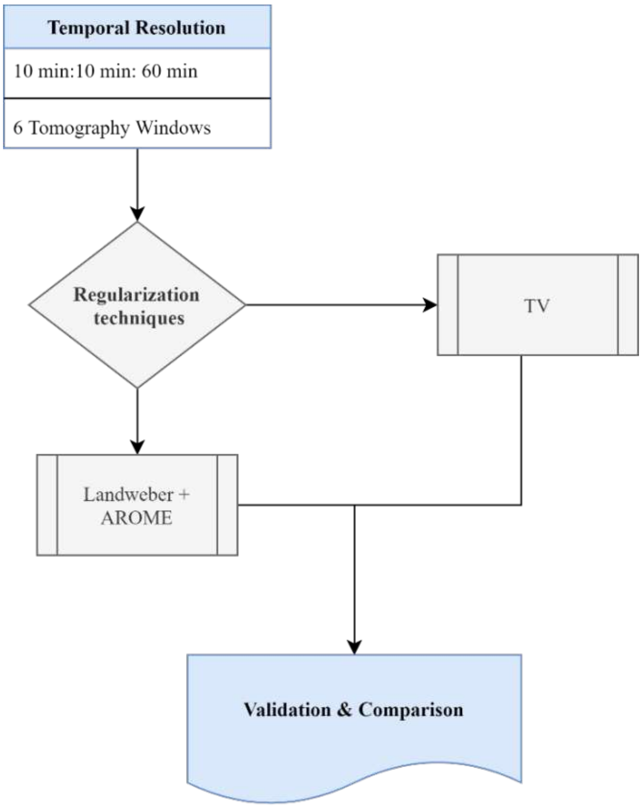

Fig 5. 11. Main strategy of studying the feasibility of the TV method for the near real-time reconstruction (Adavi and Weber, 2022)

Fig 5. 12 shows examples of the reconstructed wet refractivity profiles in comparison to the RS profiles for three days of the study period with different performances on DoYs 232, 237, and 244. Fig 5. 12 (a) and Fig 5. 12 (b) present the results for midnight and noontime, respectively. Even for shorter tomography windows of up to 40 minutes, the agreement between the reconstructed profiles and the RS profile at midnight is at the 5 ppm and 7.6 ppm level, for DoYs 232 and 237, respectively. However, on DoY 244, the performance of the TV method is poor at midnight and reaches 13.6 ppm for a temporal resolution of 10 minutes. During noontime, the RMSE of the retrieved model in comparison to the RS profile for the tomography windows of shorter than 40 minutes on DoYs 232, 237, and 244 are about 4.85 ppm, 7.3 ppm, and 4.4 ppm, respectively. For temporal windows of more than 40 minutes, the quality of the reconstructed profiles using the TV method is quite good for all sample days at midnight and noontime. In the following, the efficiency of the TV method is demonstrated by MAE, RMSE, and Std calculated over the whole period.

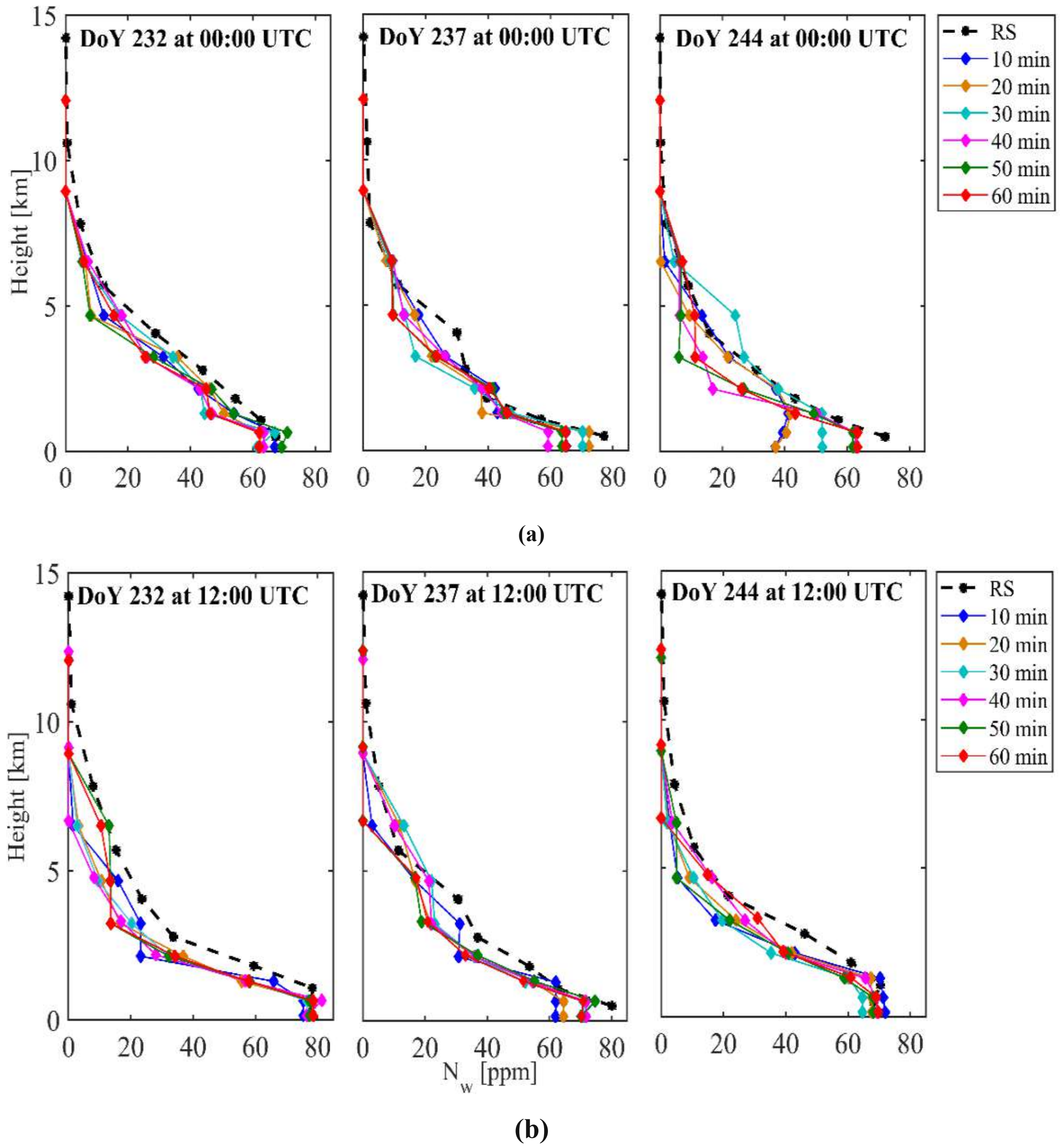

Fig 5. 12. Comparison of tomographic refractivity profiles of different tomography windows to the profile calculated from RS11035 data at midnight (a), and noontime (b) for DoYs 232, 237, and 244 (Adavi and Weber, 2022)

Fig 5. 13 presents the average MAE over the experimental period for the reconstructed wet refractivity in different temporal resolutions. According to the obtained results, for the lower layers, the inconsistency between the retrieved field and RS wet refractivity is mostly better at noontime in comparison to midnight. Moreover, the discrepancy between the tomography solution and the RS profile is almost decreasing with extending the tomography time window. However, for a temporal resolution of 20 minutes and 30 minutes at midnight, the inconsistencies are pretty high compared to other tomography windows due to the considerable condition number of the structure matrix on DoYs 242-244. For the upper layers from 2 km to 6 km, the obtained results for noontime and midnight are comparable. Additionally, the discrepancy of reconstructed wet refractivity with respect to the RS profile generally amounts to 7 ppm or less for spans longer than 40 minutes for both studied height layers.

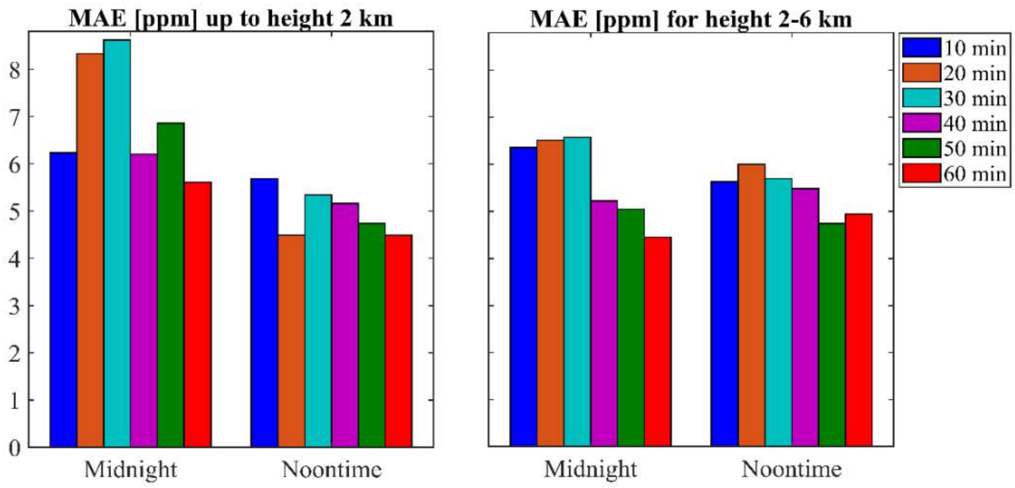

Fig 5. 13. Average MAE of the reconstructed wet refractivity field for heights up to 2 km, and 2 to 6 km at midnight and noontime at RS11035 location (Adavi and Weber, 2022)

In the next step, RMSE, Std, and Bias were calculated for the reconstructed wet refractivity field using the TV method during the entire study period at midnight and noontime. Table 5. 10 reports the average value over all 14 days of these statistical parameters for different temporal resolutions at midnight (see Appendix C for daily RMSE results). The numbers show that the performance of the tomography model, calculated with high temporal resolution, is comparable with longer time steps. As expected, the RMSE, Std and MAE of the tomography solution with 60 minutes temporal resolution are slightly better than for other schemes. By looking at Table 1, it becomes clear that the average Biases for the temporal resolutions of 20 minutes and 30 minutes are larger than for 10 minutes. As shown in Table C. 1 (see Appendix C), this is due to the three problematic days (DoYs 242-244) with the highest inconsistency with respect to the RS profiles, which most probably returns to the weak performance of the tomography model in the lower layers (see Fig 5.13). The main factors for this inconsistency could be related to the low amount of water vapour in the troposphere (see Fig 5.4 (b)) and the lack of proper definition of the regularization parameter for the TV technique. For the shown Bias values in Table 1, there is no general judgment due to the different behaviour of this quantity by extending temporal resolution. This could return to the varying signs of the Bias and the sensibility of this statistical parameter to the systematic errors in the GNSS data processing, meteorological measurements (here pressure), and the instability of the retrieved solution using the TV method. However, it is worth mentioning that a sensor Bias is usually removed by the meteorologists before assimilation in the NWM models based on test periods. So in case the parameter retrieval 'environment' is stable, also the bias should be kept stable and can be absorbed before assimilation. Furthermore, according to the reported Bias in Table 1, it turns out that the wet refractivity solutions calculated in tomography windows of more than 10 minutes are averagely underestimating RS wet refractivity over the experimental period.

Table 5. 10. Average RMSE, Std, and Bias over the experimental period for all different temporal resolutions (epoch 00:00 UTC, location: RS11035) (Adavi and Weber, 2022)

Midnight	RMSE [ppm]	Std [ppm]	Bias [ppm]	MAE [ppm]
10 min	6.77	6.46	0.33	1.70
20 min	7.72	7.26	-0.28	2.11
30 min	7.46	6.95	-0.61	1.93
40 min	5.80	5.30	-0.41	1.86
50 min	6.05	5.70	-0.97	1.58
60 min	5.26	5.02	-0.71	1.19

Table 5. 11 presents the statistical evaluation of retrieved wet refractivity using the TV method at noontime (see Appendix C for daily RMSE results). From this table, it becomes obvious that the performance of the TV technique at noontime enhanced up to 30 % compared to midnight. This is generally because of the low accuracy of the retrieved wet refractivity for DoYs 242-244. For other days, the accuracy of the tomography solution is comparable at midnight and noontime. Additionally, the amount of water vapour is higher at noontime in comparison to midnight. This variation of water vapour is a crucial factor for the TV performance. Furthermore, the estimated tomography profiles using the TV method are generally underestimating the wet refractivity of the reference RS profile similar to midnight according to the reported Bias values.

Table 5. 11. Average RMSE, Std, and Bias over the experimental period for all different temporal resolutions (epoch 12:00 UTC, location: RS11035) (Adavi and Weber, 2022)

Noontime	RMSE [ppm]	Std [ppm]	Bias [ppm]	MAE [ppm]
10 min	5.72	5.24	-0.46	1.91
20 min	5.47	5.05	-0.90	1.77
30 min	5.81	5.29	-0.74	1.98
40 min	5.50	5.04	-0.003	1.79
50 min	4.98	4.58	-0.07	1.58
60 min	4.82	4.54	-0.30	1.18

In the next step, the average correlation between the reconstructed wet refractivity with the RS profile was calculated over the experimental period at midnight and noontime. According to the reported correlations in Table 5. 12, it can be stated that the behaviour of the retrieved profiles is considerably close to the RS profile with a correlation of more than 95 % and 97 % for all tomography windows at midnight and noontime, respectively. In addition, the correlation between the tomography solutions and RS wet refractivity is slightly higher at noon than for midnight. As expected, the correlation of the tomography solution with the RS profile almost increases with extending the tomography time window.

Table 5. 12. Average correlation coefficient [%] over the entire study period between the retrieved wet refractivity profile and RS profile for different temporal resolution (Adavi and Weber, 2022)

	10 min	20 min	30 min	40 min	50 min	60 min
Midnight	96.40	95.12	95.61	97.38	97.23	97.98
Noontime	97.84	97.88	97.69	98.03	98.37	98.48

In order to gain a better interpretation of the obtained results, the wet refractivity field was also reconstructed using the Landweber technique by considering the AROME model as an a priori field. According to Fig 5. 14, the RMSE of the Landweber method at midnight is smaller than for the TV method in all temporal resolutions. The TV technique has provided a more reliable or at least comparable tomography solution with respect to the Landweber method for all temporal resolutions at noontime. Additionally, the quality of the reconstructed field using the Landweber method technique extremely depends on the initial field, and it does not change significantly with varying the tomography window. In comparison, the accuracy of the wet refractivity retrieved by the TV method is clearly increased by extending the temporal window up to 60 minutes especially at midnight. It should also be highlighted that the TV technique has provided a more reliable tomography solution than the Landweber method for all temporal resolutions at noontime.

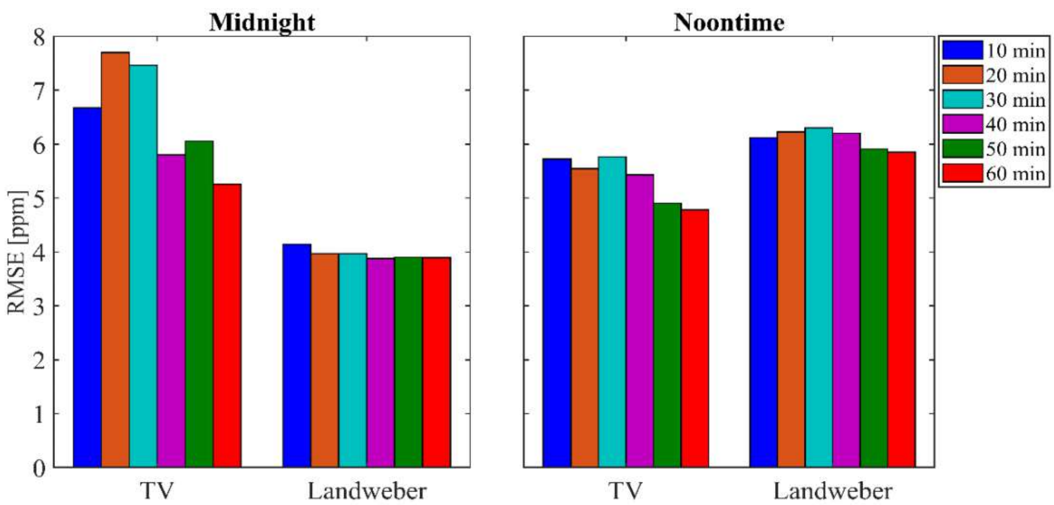

Fig 5. 14. Average RMSE over the entire study period for TV and Landweber methods at midnight and noontime (Adavi and Weber, 2022)

According to the obtained results, the TV technique reconstructed the wet refractivity field with an accuracy of less than 8 ppm and 6 ppm at midnight and noontime, respectively. In addition, the accuracy of this method was comparable with the accuracy of the Landwber method even in a short tomography window at noontime and windows of at least 40 minutes at midnight. Thereby, the TV method would be a good choice to estimate the tomography solution, especially when there is no access to the (reliable) initial field.

5.2. EVN Network: Impact of the GALILEO Constellation on the Tropospheric Tomography

To improve observation geometry compared to a sole GPS/ GLONASS system scenario, observations to further multi-GNSS might be applied. This advanced scenario has become an essential research point in the recent decade. Therefore, the aim of this part is to investigate the impact of different constellations to solve the ill-posed inverse problem to retrieve the wet refractivity field by focusing on GALILEO's effect on the accuracy of the estimated refractivity. Regarding this, the designed models were loosely constrained to the a priori field to provide an optimum situation for assessing the influence of the GALILEO constellation in the tomography solution. Therefore, as shown in Fig 5. 15, three different schemes, namely (1) GPS + GLONASS + GALILEO (GRE), (2) GPS+ GLONASS (GR), and (3) GPS+ GALILEO (GE), have been considered to analyse the impact of the GALILEO constellation on the accuracy of the reconstructed wet refractivity field.

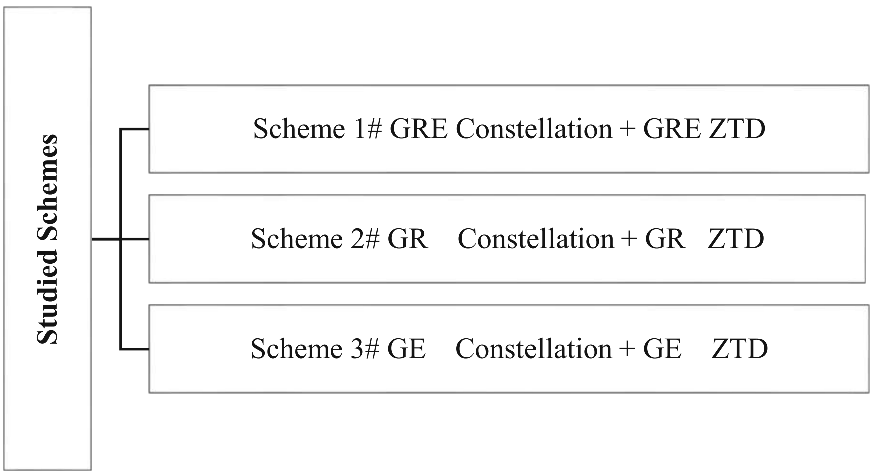

Fig 5. 15. Different Schemes to analyse the impact of GALILEO on the tomography solution

In this section, first, the configuration of the designed tomography model for the EVN network is described. Then, the weather conditions in the study period are described. After that, the ZTD estimated from different constellations (GRE, GR, and GE) is compared to the derived ZTD from the AROME model using ray-tracing for evaluating the precision of GNSS ZTDs. Finally, the Landweber method is applied to reconstruct the wet refractivity field in the GRE, GR, and GE schemes.

5.2.1 Tomography Model Configuration

Here, the model space resolution matrix has been again applied in order to select the optimum horizontal resolution for the tomography model covered by the EVN network (see Section 4.1.1.2 in Chapter 4).Therefore, five different horizontal resolutions from 30 km to 70 km with step size 10 km were considered. According to the obtained results, 60 km was picked out as an optimum resolution due to the minimum discrepancy with the identity matrix as well as reasonable size (not too large) to assume a constant value of wet refractivity per voxel. Fig 5. 16 shows the designed tomography model for the EVN network.

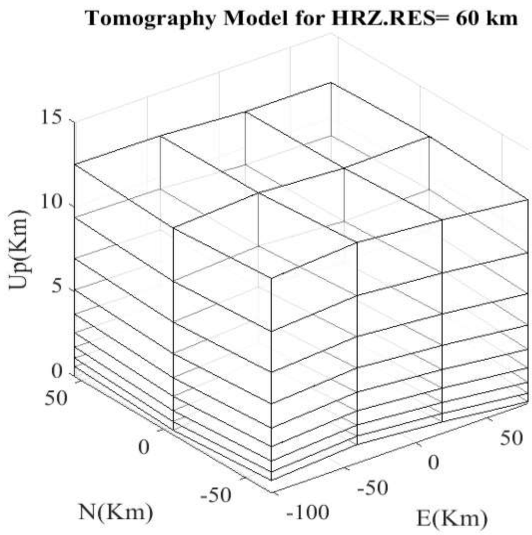

Fig 5. 16. Designed Tomography Model for the EVN network

Moreover, the exponential layer model was applied to define the vertical layer. Wet refractivity in each voxel was assumed to be stable for 1 hour and therefore, the temporal window is 1 hour in the designed tomography model. Fig 5. 17 illustrates the configuration of the designed tomography model in this case study.

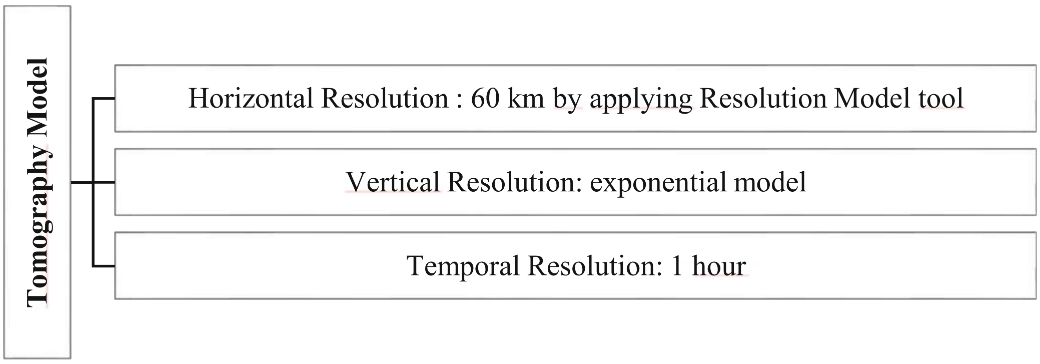

Fig 5. 17. Tomography configuration in the EVN network

5.2.2 Weather Condition in the Study Period

In order to investigate the impact of the GALILEO constellation on the GNSS tomography solution, two different time periods have been chosen. The first period covers 10 days in April 2019 from 100 to 109 (Fig 5. 18 (a-b)) and the second period covers DoYs 233-244 in August 2019 (Fig 5. 18 (c-d)). According to Fig 5. 18 (a-b), the atmospheric conditions in the second half of the April time window were mostly dry. Therefore, this period has been considered as the dry time of the tomography model. In contrast to April, the time period in August 2019 has been judged as the wet period due to considerable precipitation and humidity and also according to the report of the European Severe Weather Database (ESWD).

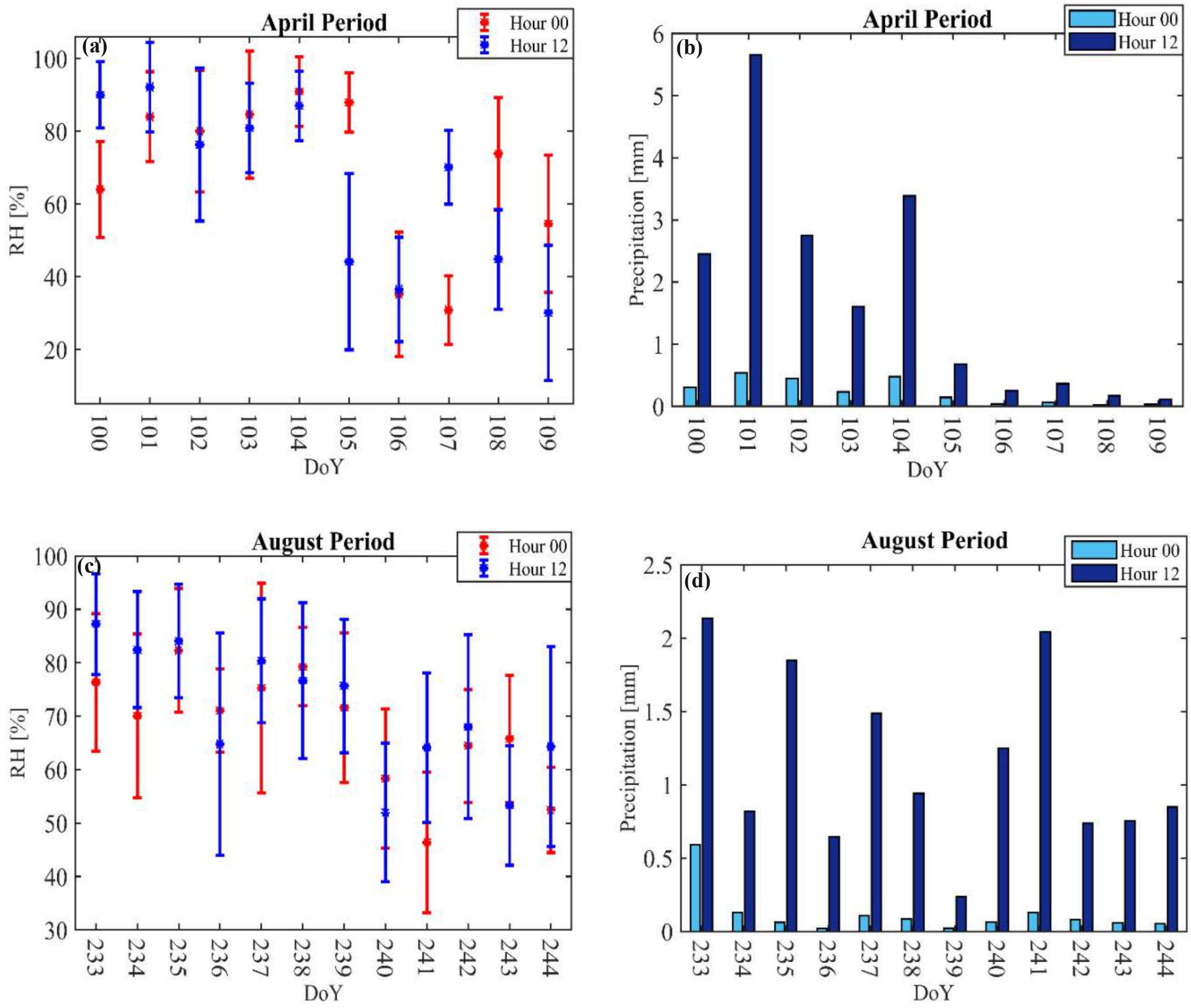

Fig 5. 18. Variations of relative humidity up to 4 km height (a, c) and average of total precipitation within the whole area (b, d) during the study period

5.2.3 GNSS ZTD in Comparison to NWM ZTD

GNSS ZTD (GRE, GR, and GE) was determined by means of the Bernese GNSS software in baseline mode for the EVN network (see Table 5. 1 and Fig 5. 3 for more details). Table 5. 13 summarizes the Std values for the different time periods and mentioned schemes using the Bernese software. Based on that, the estimated ZTDs using different constellations are on average less than 1.4 mm and 2 mm for the April and August periods, respectively.

Table 5. 13. Average Std for different Schemes in ZTD outputs (TRP file) of Bernese GNSS software

Std [mm] / Study Period	GRE	GR	GE
Apr (100-109)	1.3± 0.4 [mm]	1.3± 0.4 [mm]	1.4± 0.5 [mm]
Aug (233-244)	1.8 ± 0.6 [mm]	1.8± 0.6 [mm]	2.0± 0.7 [mm]

To evaluate the estimated ZTDs, the GNSS ZTD estimated using GRE, GR, and GE schemes has been compared to the derived ZTD by ray-tracing through the AROME numerical weather model. Fig 5. 19 shows the average

RMSE of the GNSS ZTD over all GNSS stations located in the EVN network with respect to derived ZTD from the AROME model for the April period. According to this figure, the consistency between derived ZTDs from different schemes and AROME ZTD is generally comparable during the experimental period. However, RMSE values are considerable on some days for various schemes. This may return to the quality of GNSS observations, and the number of created baselines which subsequently affect the ambiguity fixing rate (see Table 5. 1 and Fig 5. 3 for more details). Therefore, different results are expected by changing baseline sets. Moreover, the quality of the AROME model has also an impact on the obtained RMSE. Table 5. 14 details the average RMSE for the different GNSS schemes at midnight and noontime. As demonstrated in this table, RMSE values for all schemes during the noontime are slightly better than midnight. Nevertheless, the reported RMSEs are close for all schemes.

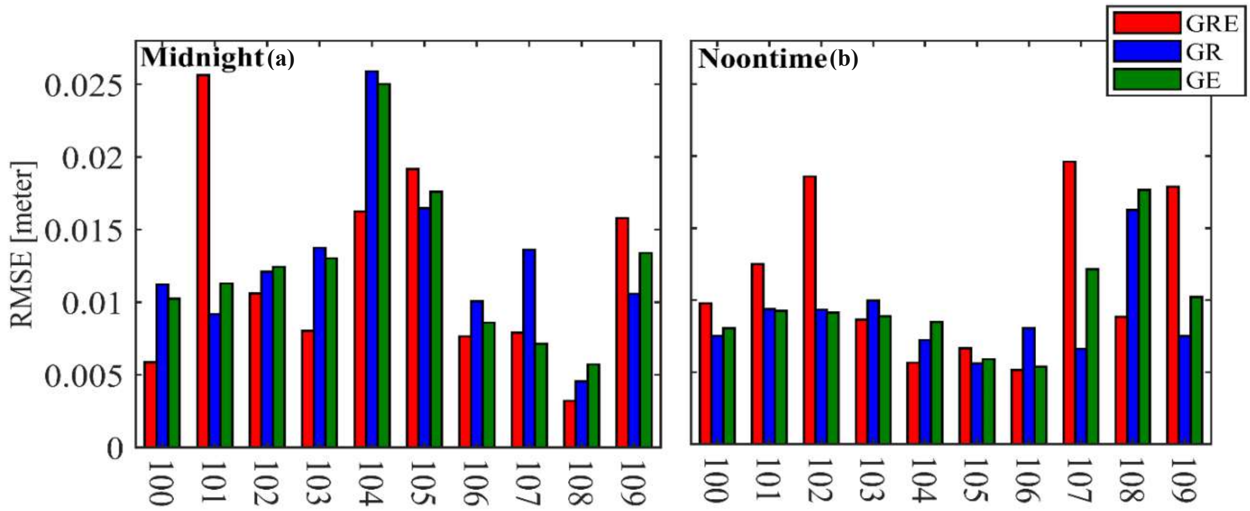

Fig 5. 19. Average RMSE of ZTD values determined for days 100-109 for GRE, GR, and GE schemes with respect to AROME at midnight (a), and noontime (b)

Table 5. 14. Mean RMSE over all stations for GRE, GR, and GE schemes during April, DoYs 100-109 of the year 2019

RMSE [meter]	GRE	GR	GE
Midnight	0.012 [0.003 0.026]	0.013 [0.005 0.026]	0.012 [0.006 0.025]
Noontime	0.011 [0.005 0.019]	0.009 [0.006 0.016]	0.010 [0.005 0.018]

The scatter plots of the different schemes (GRE, GR, and GE) relative to the AROME model have been provided in order to analyse the estimated ZTD. According to Fig 5. 20, the similarity between GNSS ZTD and AROME ZTD is higher than 99 percent for all schemes in April 2019.

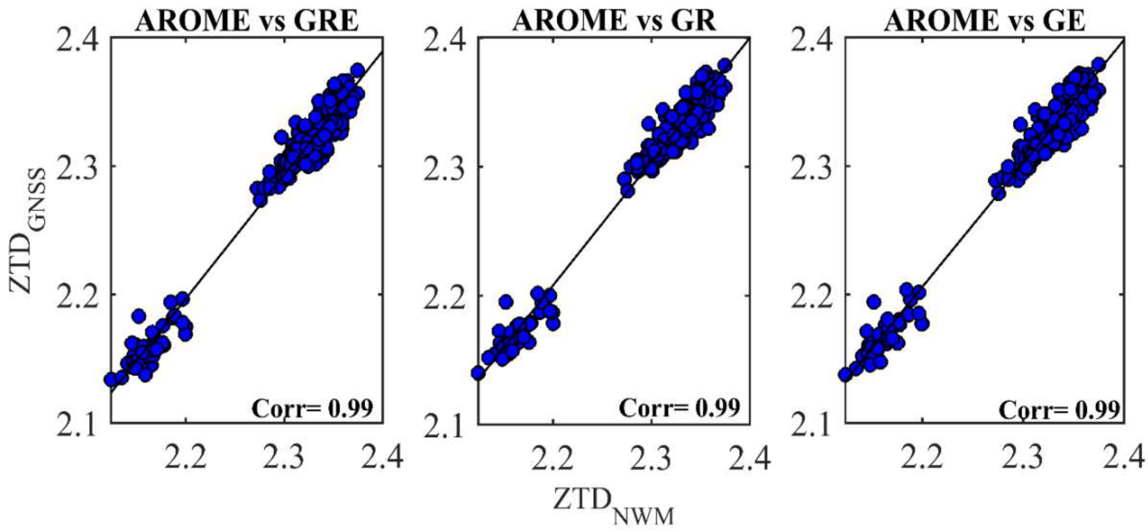

Fig 5. 20. Scatter plots of the GNSS-based ZTDs and AROME-based ZTD for DoYs 100-109 of the year 2019

The same verification was done for the wet period in August 2019. According to Fig 5. 21, the average RMSE for GRE and GR schemes are slightly smaller than for the GE scheme over the experimental period. Nevertheless, the estimated ZTDs for all schemes agreed with the AROME ZTD at a level of a few subcentimeter.

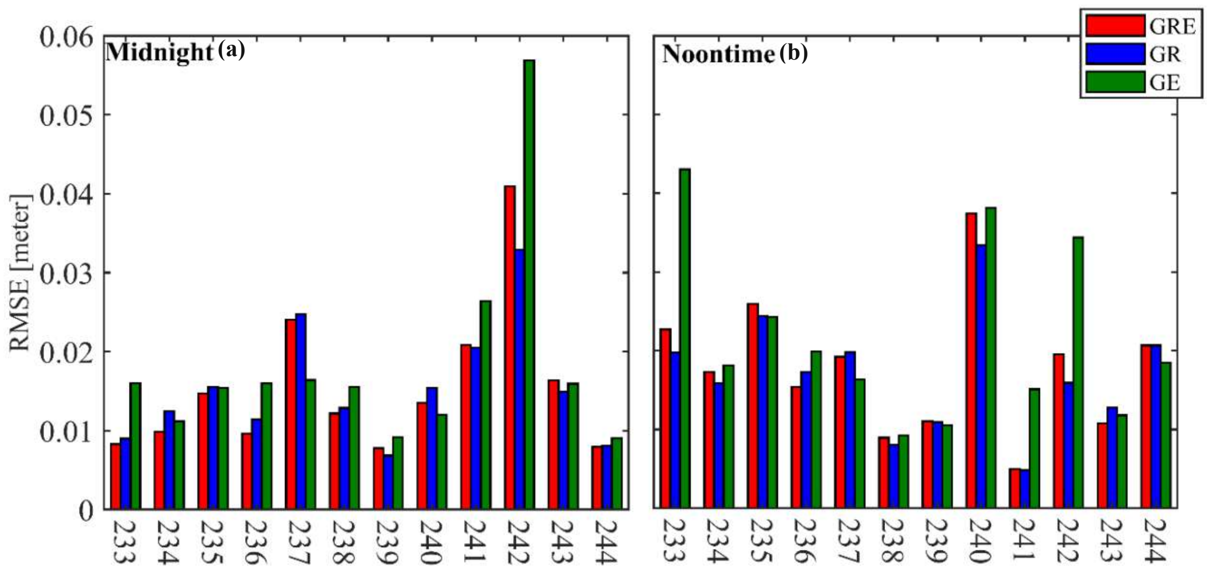

Fig 5. 21. Average RMSE of ZTD values determined for days 233-244 for GRE, GR, and GE schemes with respect to AROME at midnight (a), and noontime (b)

Table 5.15 summarizes the average RMSE for the different GNSS schemes at Midnight and noontime during the August period. By looking at Table 5. 14 and Table 5. 15, it becomes clear that the accuracy of the GNSS ZTD compared to the AROME ZTD is generally worse in the August period compared to the April period. This may return to the fact that the April period is less wet than the August period. Therefore, ZTD amounts are smaller in the April period and consequently less discrepancy with respect to the AROME ZTD. In addition, the quality of the GNSS measurements and the AROME model also influences the estimated inconsistency between the GNSS ZTD and AROME ZTD.

Table 5. 15. Mean RMSE over all stations for GRE, GR, and GE schemes during August, DoYs 233-244 of the year 2019

RMSE [meter]	GRE	GR	GE
Midnight	0.016 [0.008 0.041]	0.015 [0.007 0.033]	0.018 [0.009 0.057]
Noontime	0.018 [0.005 0.037]	0.017 [0.005 0.033]	0.022 [0.009 0.043]

As shown in Fig 5.22, the correlation between the GRE, GR, and GE schemes and AROME ZTD is higher than 96 percent in August 2019. This confirms that GNSS ZTD for all schemes provides also consistent ZTDs in the August period. Thereby, all estimated ZTDs using different schemes for both experimental periods, namely April and August, could be employed to compute SWD (see Section 2.4) and then tropospheric tomography modelling.

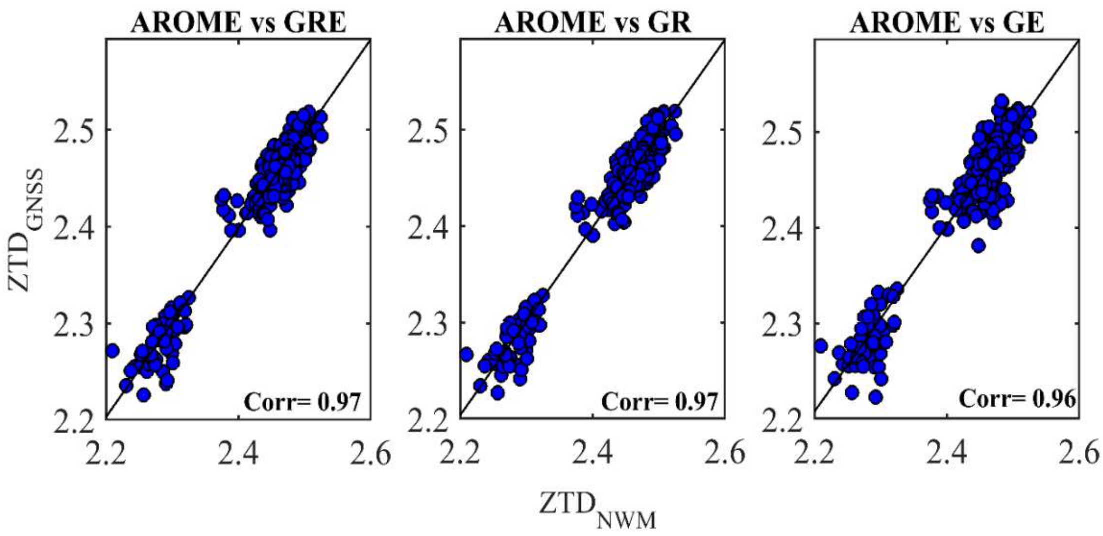

Fig 5. 22. Scatter plots of the GNSS-based ZTDs and AROME-based ZTD for DoYs 233-245 of the year 2019

5.2.4 Analysis of different GNSS Constellation by Focusing on GALILEO in GNSS Tomography

The accuracy of the reconstructed tomography profiles using different schemes was assessed by reference radiosonde observations taken at Vienna airport (RS11035) at midnight and noontime. According to Fig 5. 23 (a), the agreement between the GE scheme and the radiosonde profile in the April period is almost equivalent to the GRE scheme. Both schemes are slightly better than the GR scheme during midnight where the average RMSE for GRE, GE, and GR schemes are 3.15 ppm, 3.20 ppm, and 3.43 ppm, respectively. For noontime (see Fig 5. 23 (b)), the accuracy of the GR scheme (3.24 ppm) is approximately 5% better than the accuracy of GRE (3.43 ppm) and GE (3.30 ppm).

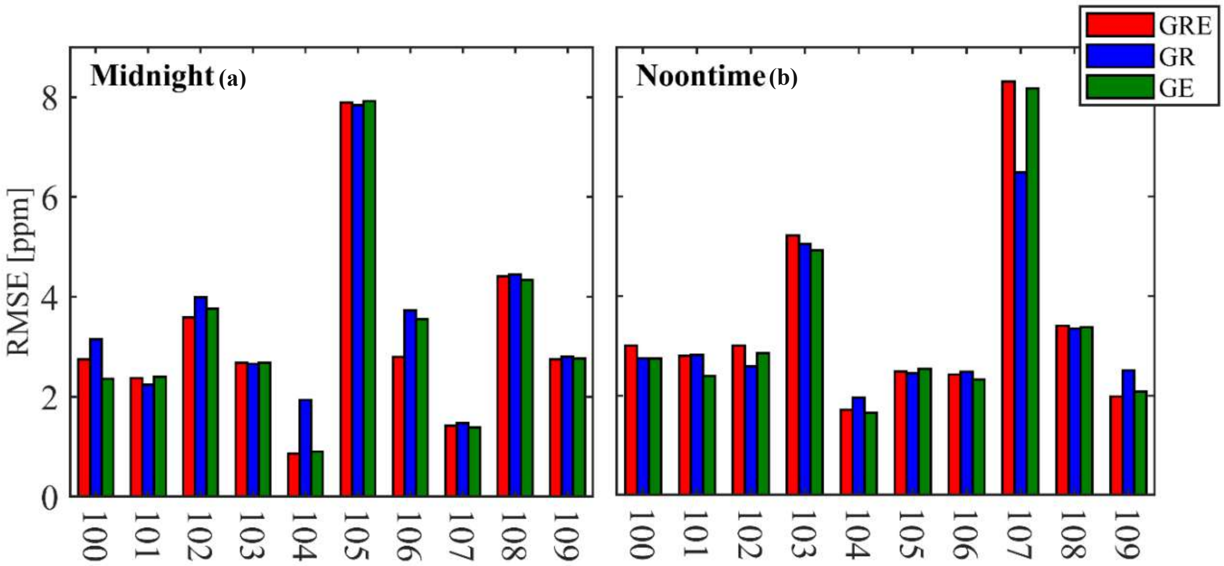

Fig 5. 23. RMSE of the reconstructed wet refractivity profile with respect to RS11035 in the April period for GRE, GR, and GE schemes at midnight (a), and noontime (b)

Additionally, the performance of all investigated schemes on DoY 105 at midnight and DoY 107 at noontime are weak. Since the number of observations is almost similar in all schemes during the experimental period (see Fig 5. 24), it could probably return to the accuracy of the SWDs, and the quality of the initial field (AROME model). Moreover, other factors like instability of the retrieved field and real differences in the sampled atmospheric conditions at different locations and times could be effective in this respect.

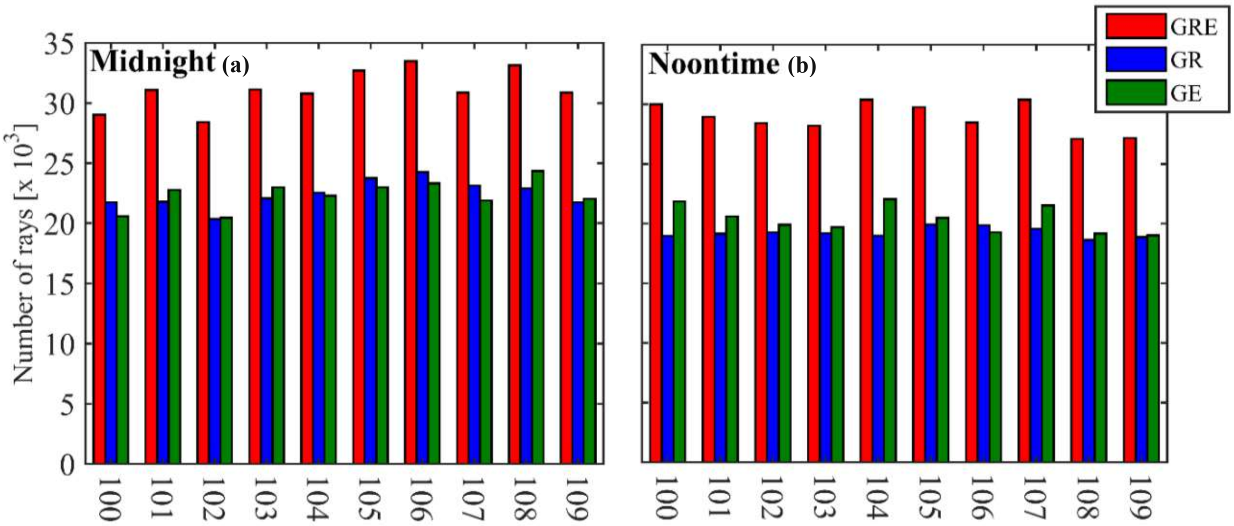

Fig 5. 24. The number of rays in the tomography model in the April period at midnight for GRE, GR, and GE schemes

In order to assess the quality of the initial field, the derived wet refractivity profiles from the AROME model and radiosonde measurements were compared. According to Fig 5. 25, the inconsistency between the AROME model and radiosonde in the target days, namely 105 and 107, are high, and consequently, it caused a large RMSE for these days. Therefore, the reconstructed tomography solution by means of the iterative techniques, here Landweber, is considerably affected by the initial field.

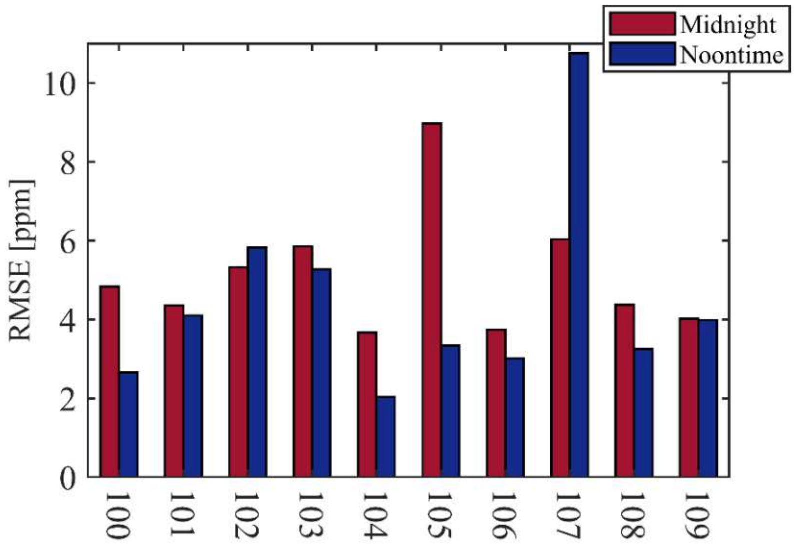

Fig 5. 25. RMSE of wet refractivity derived from AROME model compared to RS11035 over the April period

Table 5. 16 presents the average MAE for height 2 km in the April period. According to this table, the average MAE derived using the GR scheme, are generally better than for the GRE and GE schemes. This means the derived profile using the GR scheme is slightly closer to the RS profile in lower layers in comparison to GRE and GE schemes.

Table 5. 16. Average MAE [ppm] for height up to 2 km in GRE, GR, and GE schemes over the April period

April Period	GRE	GR	GE
Midnight	3.91	3.72	3.86
Noontime	4.20	3.97	4.14

The MAE for heights between 2 km to 6 km is summarized in Table 5. 17 during the experimental period. Based on the obtained results, the performance of GE is generally better for midnight and noontime in comparison to GRE and GR schemes. Nevertheless, there is no significant difference between various schemes to retrieve the tomography model.

Table 5. 17. Average MAE [ppm] for height between 2-6 km in GRE, GR, and GE schemes over the April period

April Period	GRE	GR	GE
Midnight	2.13	2.86	1.95
Noontime	2.65	2.52	2.34

The retrieved wet refractivity profiles from different schemes have been compared to RS11035 in the August period as well. Fig 5. 26 demonstrates the discrepancy between the RS and reconstructed wet refractivity profiles using various schemes during the experimental period. As displayed in Fig 5. 26 (a), the agreement between all schemes is comparable for midnight, and the average RMSE is 4.01 ppm, 4.04 ppm, and 4.01 ppm for GRE, GR, and GE schemes, respectively. For noontime, the average RMSE for the GE scheme (4.94 ppm) is partly better than for GRE (5.09 ppm) and GR (5.32 ppm) as shown in Fig 5. 26 (b). Based on the obtained results, all schemes could reconstruct the wet refractivity field using the tomography model with an average RMSE of about 6 ppm during the August period.

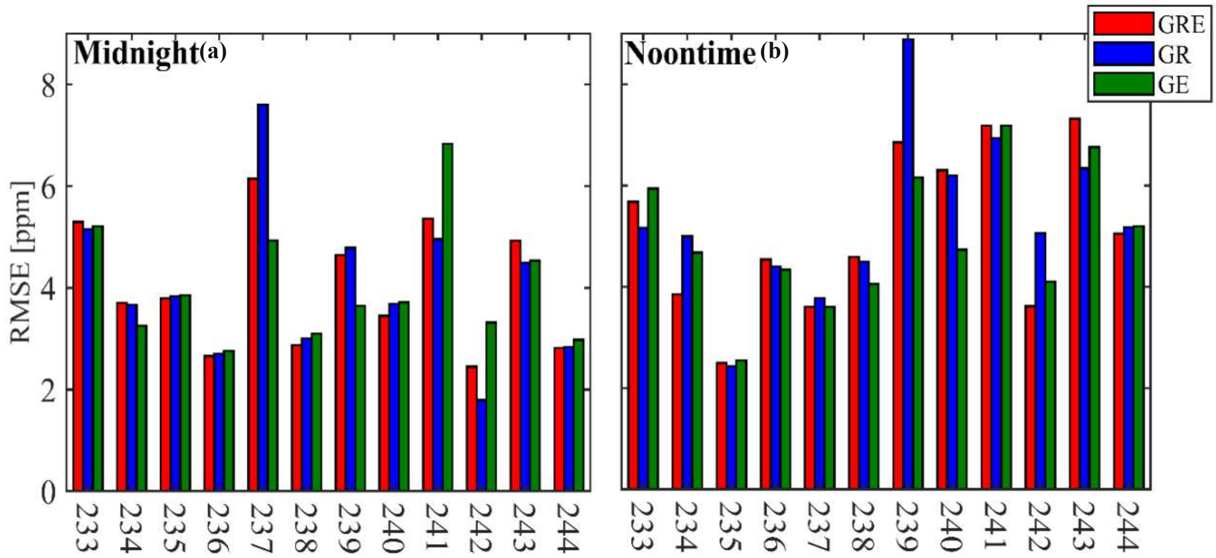

Fig 5. 26. RMSE of the reconstructed wet refractivity profile with respect to RS11035 in the August period for GRE, GR, and GE schemes at midnight (a), and noontime (b)

Table 5. 18 reports the average MAE in GRE, GR, and GE schemes for different periods. As stated in this table, the GE scheme shows slightly worse performance in comparison to GRE and GR schemes for lower layers during midnight. However, the MAE of the GE scheme is relatively better at noontime compared to the two other schemes.

Table 5. 18. Average MAE [ppm] for height up to 2 km in GRE, GR, and GE schemes over the August period

August Period (233-244)	GRE	GR	GE
Midnight	4.17	4.14	4.32
Noontime	5.33	5.79	4.96

For upper layers as shown in Table 5. 19, the average MAE of the GE scheme is comparable to the GR scheme and better than for the GRE scheme at midnight. Moreover, the performance of GRE and GR schemes is stronger compared to the GE scheme during noontime.

Table 5. 19. Average MAE [ppm] for height 2-6 km in GRE, GR, and GE schemes over the August period

August Period (233-244)	GRE	GR	GE
Midnight	4.06	3.89	3.76
Noontime	4.53	4.56	4.96

For the next step, the general impact of the investigated constellations on the retrieved wet refractivity field was assessed. To do so, the average correlation between the reconstructed wet refractivity with the RS profile was computed over the experimental periods, namely April and August. Based on the reported correlation in Table 5. 20, all schemes provide a comparable correlation for both study periods. However, the correlation between the RS wet refractivity profile and the tomography solution is slightly higher during the August period in comparison to the April period. This could return to the different sample length of study periods. Nevertheless, the reconstructed profiles using all constellation are considerably close to the RS profiles with a correlation of more than 95 %. Based on the obtained results, the third GNSS system had no significant impact on the accuracy of the tomography for this research because a sufficient number of rays could almost be provided using a combination of two GNSS constellations. However, having GNSS signals at different elevation angles should be considered as pre-requirements to achieve an acceptable quality for the retrieved wet refractivity field in the area of interest.

Table 5. 20. Average correlation coefficient [%] over two study periods between the retrieved wet refractivity profile and RS profile for GRE, GR, and GE schemes

Corr [%]	GRE	GR	GE
Apr Period (100-109)	95.2	95.3	95.1
Aug Period (233-244)	98.5	98.4	98.6

5.3. COST Action: Investigation on the Topography Effects and Ray-Tracing Methods on the GNSS Tomography, and Pre-analysis of Tomography results using Spread

In recent years, different ray-tracing methods have been developed in the GNSS or VLBI community to calculate slant tropospheric delays from NWM data (Hobiger et al., 2008;Hofmeister, 2016;Nafisi et al., 2012). In the GNSS tomography field, pioneering research by Haji Aghajany and Amerian (2017) applied 2D and 3D Eikonal ray-tracing methods in water vapour tomography with initial testing of its impact on the reconstructed field. Möller and Landskron (2019) developed a mixed linear ray-tracing method to reconstruct the bended path which can be used for near-real-time applications. However, in these studies, the effect of the different coordinate types used in the straight-line strategy compared to the ray-tracing method were not investigated. In addition, the impact of the topography of the area of interest to design a tomography model was not evaluated.

Furthermore, the quality of the reconstructed field is still one of the challenges in the GNSS tomography. Up to now, ground-based GNSS observations (e.g. (Möller, 2017)), radiosonde profiles (e.g. (Hanna et al., 2019)), and Numerical Weather Models (e.g. (Brenot et al., 2020)) have been used for assessing the accuracy of the reconstructed field.

To study the above mentioned topics, at first, the tomography model configuration is introduced. Then, the weather conditions during the period of interest are described. Next, the effect of a straight-line (in ENU and UTM coordinates) ray-tracing method versus a 2D Eikonal method will be analysed. Moreover, the topography impact on the tomography modelling using different ray-tracing schemes is compared to radiosonde data in this section, as well. After that, the relation between spread of the resolution matrix and Std and Bias is investigated in order to propose a new tool to evaluate the accuracy of the reconstructed wet refractivity field.

5.3.1 Tomography Model Configuration

As stated in Section 4.1.2, the investigated area covers the western part of the Czech Republic and south Germany with 72 GNSS stations. According to previous researches (Brenot et al., 2018;Hanna et al., 2019), the horizontal resolution of the tomography model is 50 km with an exponential model in the vertical direction (Manning, 2013;Möller, 2017;Perler, 2011). Moreover, a time resolution of 1 hour was applied for this research. This should be also highlighted that 16 GNSS stations are located outside of the designed tomography model (see Fig 4. 3).

5.3.2 Weather Conditions and Case Periods

DoYs149–176 (29 May to 25 Jun) of year 2013 were selected as the period of interest due to the atmospheric process that caused the central European floods in June 2013 (Douša et al., 2016). Fig 5. 27 shows the mean ZWD variation over Jun 2013 and the associated accumulated rain for Prague synoptic station. This period covers highly dynamic weather. The amount of precipitation for DoYs 149-151 is 0 mm, 29 mm, and 14 mm, respectively (see Douša et al. (2016) for more details). Moreover, no GNSS-based ZWDs exist between DoYs 149-151 in the COST action dataset, and only synthetic SWDs (ray-traced) are available for this period.

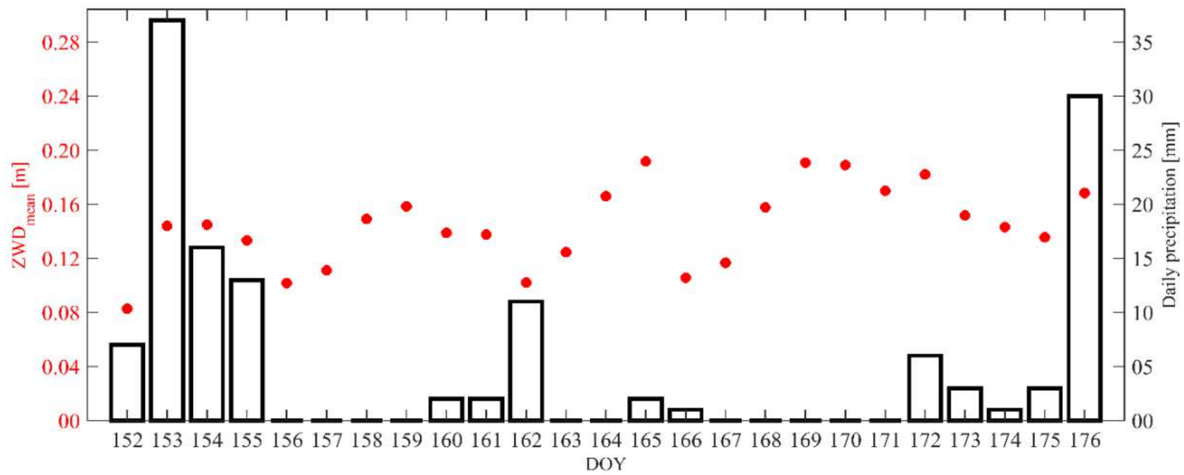

Fig 5. 27. Mean ZWD during the time of interest (red dots) plotted over daily precipitation (black bars) during the time of interest at Prague synoptic station (Douša et al., 2016;Adavi et al., 2020)

Table 5. 21 details the study period chosen for evaluation of the Eikonal ray tracing and application of the spread. For evaluating the Eikonal ray-tracing as well as the topography impact on the quality of the tomography solution, the overall period DoY 160-176 was considered in the year 2013. On top, three different case studies are applied in order to investigate the significance of the spread as follows:

1. Synthetic: DoY 149-165,
2. Synthetic: DoY 160-165,
3. GNSS: DoY 160-165.

Here, the 'synthetic dataset' (provided by COST Action ES1206) is composed of ray-traced slant delays passing through the reference NWP field (here ALADIN model). The use of synthetic data could provide a reasonable judgment in comparison to the GNSS based slant delays. Thereby, two different datasets have been considered here to assess the spread of the resolution matrix with and without GNSS data noises in the COST benchmark dataset to analyse the spread as discussed above. In addition, to provide the consistency between the 2nd and 3rd datasets, only GNSS observations have been selected which existed in the synthetic dataset as well.

Table 5. 21. Study periods and underlying datasets for Eikonal and spread evaluation

Goal of Analysis	GNSS data	Synthetic Data
Eikonal+ Topo	160-176	-
Spread	160-165	149-165 & 160-165

5.3.3 Impact of Topography on the GNSS Tomography

To analyse the effect of the topography in the area of tomographic modelling, two different schemes were used. In the first scheme, the tomography model was designed without topography information of the study region (black lines on the left and right panel in Fig 5. 28). In the second scheme, the tomography model was designed by considering topography information of the study area (Red dashed lines in the left and right panels in Fig 5. 28).

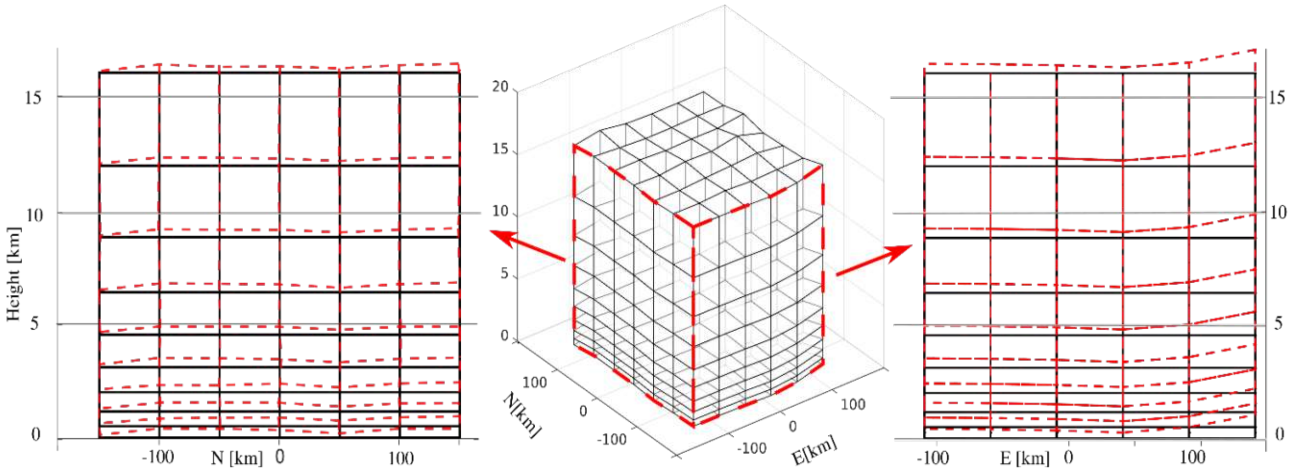

Fig 5. 28. Designed tomography model without topography (black solid lines) and with topography (red dashed lines). Left cross-section along S-N direction and right cross-section along E-W direction (Adavi et al., 2020)

The clear difference between the two models is depicted in Fig 5. 28. It influences the design matrix $\boldsymbol{A}$, as the location of intersection points between signal and model faces are shifted. Therefore, it changes the distance that each signal travelled through the tomography model. As seen in Fig 5. 28, the difference between using topography (red) and not using topography (black), especially in the North-East part, reaches up to 800 m in height, which corresponds to 2 layers at the bottom part of the model.

The consequence of the topography is visible also in Fig 5. 29, which shows that the number of rays passing through voxels in scheme#2 (with topography) is higher than in scheme#1 (without topography). Fig 5. 29 depicts a snapshot of one hour (23.30 h-00.30 h each investigated day). In general, the lowest layer is most affected, but satellite geometry can also cause a reasonable gain of intersected voxels in upper layers. Therefore, when the topography effect is accounted for, we can expect an increased number of d_{nm} elements in the matrix $\boldsymbol{A}$. In fact, increasing the redundancy of observations in each voxel can lead to a better reconstruction of the parameter of interest (due to lower condition number) in the desired voxel. The essential increase of rays in the topography scheme is caused by additional rays originating from GNSS stations outside the tomography volume. This affects especially voxels located in columns close to the borders of the tomography volume. Additionally, differences between the numbers of rays in the two schemes can also specifically relate to block stations located close to the model border.

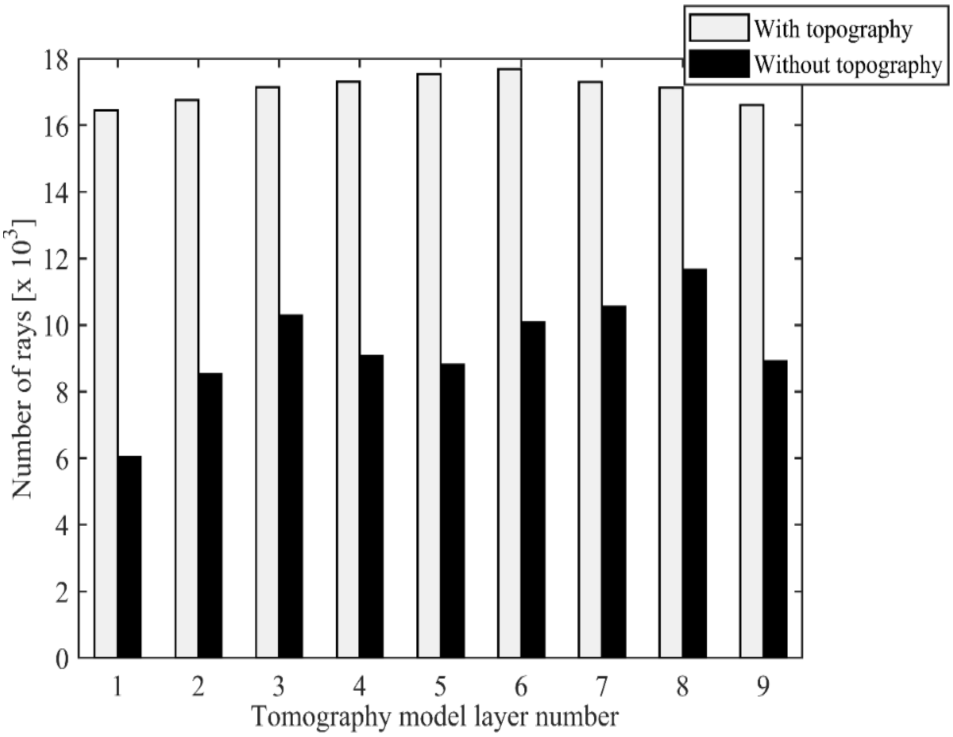

Fig 5. 29. The number of rays in each model layer (1 = bottom, 9 = top) within 1 hour (30 sec observation rate)

5.3.4 Eikonal Ray-Tracing Method vs. Straight-Line Geometry

Reference radiosonde observations were used to evaluate the effects of the topography and of the different ray-tracing methods on the accuracy of the reconstructed field. For this purpose, the estimated wet refractivity profiles have been verified above the locations of radiosonde stations Meiningen (RS10548) and Kummersbruk (RS10771) (red dots in Fig 5. 30) against the corresponding wet refractivity profiles derived from the radiosonde observations at midnight and noontime each day. Therefore, four reference profiles for each day are available. Due to the topography, the heights of the voxel model differ for the locations of RS10548 and RS10771 by 318 meters and 360 meters, respectively.

To compare radiosonde and tomography profiles, all 9 vertical layers from the reconstructed wet refractivity are considered. Moreover, the RS position is assumed to be in the same location at the centres of Voxels. Then, the reconstructed field is interpolated using IDW (Inverse distance weighting) on the RS location in each layer. Fig 5. 30 shows the agreement between the radiosonde profile and tomography wet refractivity profiles for one selected epoch over all profiles. In this figure, the model using topography is marked with red and the model without topography is marked with black. Each panel represents one processing approach: Fig 5. 30 (a)) Eikonal (see Section 3.2.3.2); Fig 5. 30 (b)) Eikonal ($N=1$) ; Fig 5. 30 (c)) Straight line with topocentric coordinates ; Fig 5. 30

(d)) Straight line with UTM projection. In order to focus on the selected day with the lowest accuracy in the set DoY 164 (00h:00m UTC) was considered. Clearly using topography in the most precise approach (Fig 5. 30 (a)) is required as the model without topography is producing biased fields (up to -7 mm/km) below 8km. The impact of topography on the straight geometry (Eikonal ($N=1$), NEU and UTM) is less definitive, however, Fig 5. 30 (b) and Fig 5. 30 (c) show a positive impact of topography for the middle levels (2–8km).

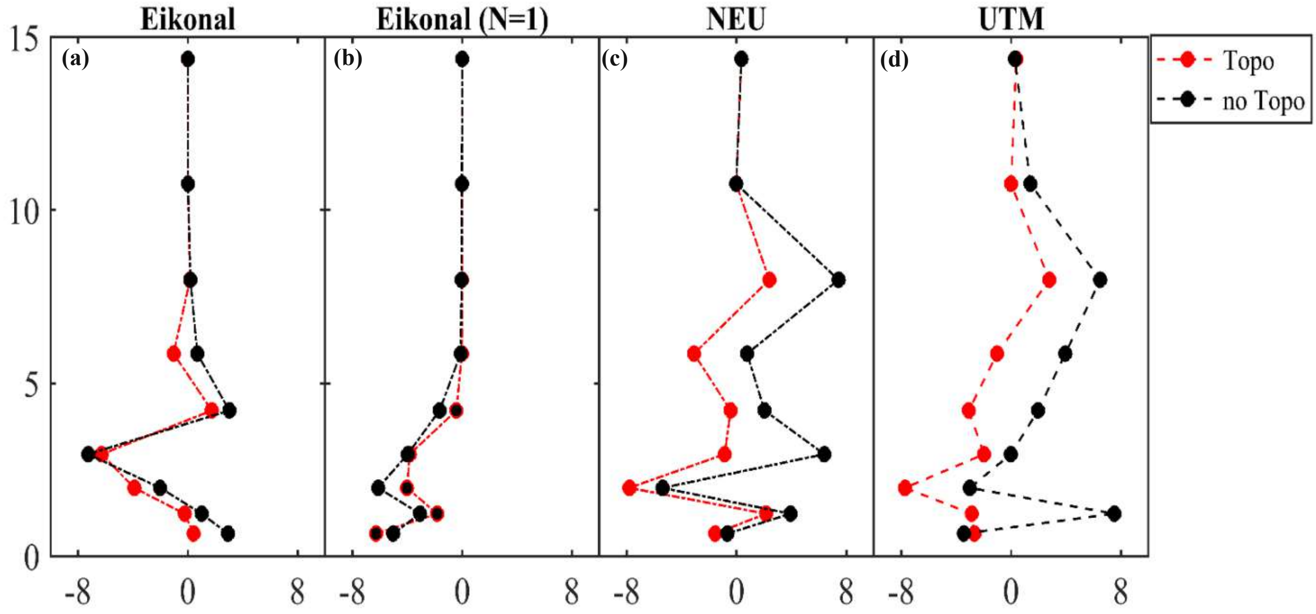

Fig 5. 30. Comparison of tomographic refractivity profiles (Nw_{tomo} [ppm]) of different schemes to the profile derived from radiosonde data (Nw_{base}) DoY 164, at 00h:00m in UTC. Four types of parameterization: Eikonal, Eikonal ($N=1$), NEU, and UTM by considering topography information and without topography (Adavi et al., 2020)

The overall RMSE for all days considered for station Meiningen (RS10548) at 00h00m in UTC (DoY 160 to DoY 176) is summarised in Table 5. 22. Results for the same station at 12h00m UTC and station Kummersbruk (RS10771) for both midnight and noon are presented in the Appendix D. Clearly, the best-performing algorithm is based on the Eikonal model with topography information included. The overall RMSE for all selected dates is 1.3 [mm/km], which is an improvement over the straight-line approach using UTM projection by 50%. The straight line solution produces results with errors 2.4 [mm/km] twice higher than the Eikonal approach with topography. A similar relation holds for the models without topography. The Eikonal solution is almost two times more accurate than the solution based on a straight line geometry (1.8 [mm/km] versus 3.4 [mm/km]). It is also worth to mention that using topography improves the Eikonal solution by 34%. A similar improvement is visible for other parametrisations (NEU and UTM). Moreover, by ignoring the bending effect in Eq. (3.23) ($N=1$), the impact of the spherical coordinate system on the tomography solution is visible. According to these results, choosing an appropriate coordinate system has a considerable effect on the reconstructed field, especially when considering large areas with some hundred quadratic kilometres.

Table 5. 22. RMSE [mm/km] of wet refractivity profiles for different schemes for all days at epoch (00h: 00m in UTC) for RS10548, black boxes mark the rainy days and the red box marks the worst day shown in Fig 5. 30 (Adavi et al., 2020)

DoY	Eikonal +Topo	Eikonal (N=1) + Topo	Straight line [UTM+Topo]	Straight line [NEU+Topo]	Eikonal	Eikonal (N=1)	Straight line [UTM]	Straight line [NEU]
160	1.380	2.018	2.172	2.628	1.990	2.354	2.741	3.271
161	0.993	1.922	2.088	3.216	1.433	2.363	3.093	4.616
162	0.837	1.893	2.287	2.686	1.498	2.371	2.986	3.109
163	1.570	2.089	2.128	2.690	2.064	2.419	2.842	3.728
164	2.563	2. 865	3.293	3.064	2.906	3.177	3.960	4.025
165	0.754	1.275	1.197	1.650	1.014	2.034	2.466	2.819
166	1.167	1.251	1.217	1.679	1.197	1.801	2.657	2.590
167	2.076	2.204	2.405	2.746	2.263	2.973	2.976	3.979
168	1.641	1.898	2.482	2.846	2.152	2.305	3.025	3.856
169	1.009	1.968	2.763	3.471	2.124	2.646	3.566	4.168
170	2.391	2.919	2.921	3.286	2.873	3.127	3.225	4.055
171	1.491	1.942	2.100	2.250	1.945	2.211	2.656	2.995
172	1.009	1.432	1.322	1.399	1.243	1.836	2.431	2.659
173	0.885	1.212	1.224	1.398	1.173	1.618	2.634	2.789
174	0.925	1.635	1.867	2.189	1.695	2.073	2.560	2.995
175	0.839	1.372	1.380	1.872	1.060	1.568	1.699	2.341
176	0.798	1.309	1.531	1.914	1.384	1.804	1.786	2.951
MEAN [mm/km]	**1.313**	**1.836**	**2.022**	**2.411**	**1.766**	**2.275**	**2.783**	**3.350**

To investigate the inconsistency between various parameterization methods with respect to the height, the relative error was applied (Zhao et al., 2019). According to Table 5. 23, below the height level of 3 km the relative errors of the Eikonal ray-tracing method with considering topography are smaller against the other parameterization methods. Nevertheless, using this parameterization method in the upper layers does not have any considerable effect compared to Eikonal (*N=1*). In addition, applying topography in tomography modelling provides more reasonable reconstructed wet refractivity fields both in the upper and lower layers.

Table 5. 23. Relative error regarding to the layers below and above 3 km for the four types of parameterization, Eikonal, Eikonal (*N=1*), NEU, and UTM (by considering topography information and without that) at hour 00h:00m UTC for RS10548 (Adavi et al., 2020)

Height	**Eikonal +Topo**	**Eikonal (*N=1*) + Topo**	**Straight line [UTM+Topo]**	**Straight line [NEU+Topo]**	**Eikonal**	**Eikonal (N=1)**	**Straight line [UTM]**	**Straight line [NEU]**
H<=3 km	0.044	0.073	0.076	0.093	0.071	0.091	0.104	0.138
H > 3 km	0.295	0.308	0.372	0.617	0.367	0.316	1.986	1.072

The statistical characteristics of the differences between the eight schemes and the radiosonde data are also presented by Fig 5. 31. Regarding the obtained box plots, the number of outliers in the Eikonal ray-tracing method is smaller than for other schemes. In this figure, IQR is defined as the difference between the first and third quartiles ($|Q_1 - Q_3|$) and shows the spread of data without outliers affect. Moreover, Q_2 approximately represents the bias of all errors. Therefore, according to the obtained IQR and Q_2 in Fig 5.30, it can be concluded that the Eikonal + Topo scheme refractivity estimates are more close and the NEU scheme shows an increased dispersion compared to other schemes.

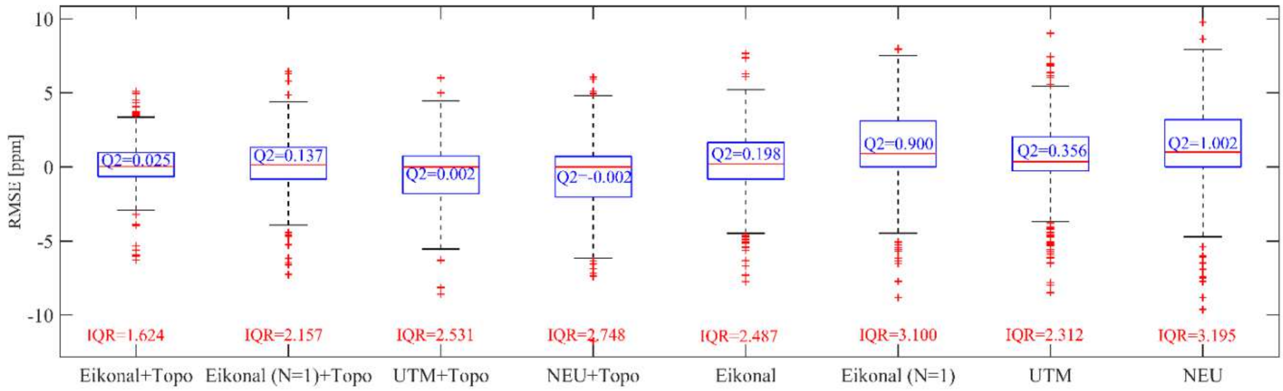

Fig 5. 31. Box plots of refractivity differences between the four types of parameterization, Eikonal, Eikonal (*N=1*), NEU, and UTM (by considering topography information and without) at location of RS10548 (00.00h UTC and 12.00h UTC) (Adavi et al., 2020)

Interestingly, Fig 5. 32 shows the dispersion of the reconstructed field (Tomo $\boldsymbol{N_w}$) relative to the radiosonde profile (RS $\boldsymbol{N_w}$) in different schemes at hour 00h:00m and hour 12h:00m in the investigated period. As shown in this figure, it becomes clear that the reconstructed wet refractivity field by Eikonal + Topo is more consistent with the RS wet refractivity in comparison to other parameterization methods.

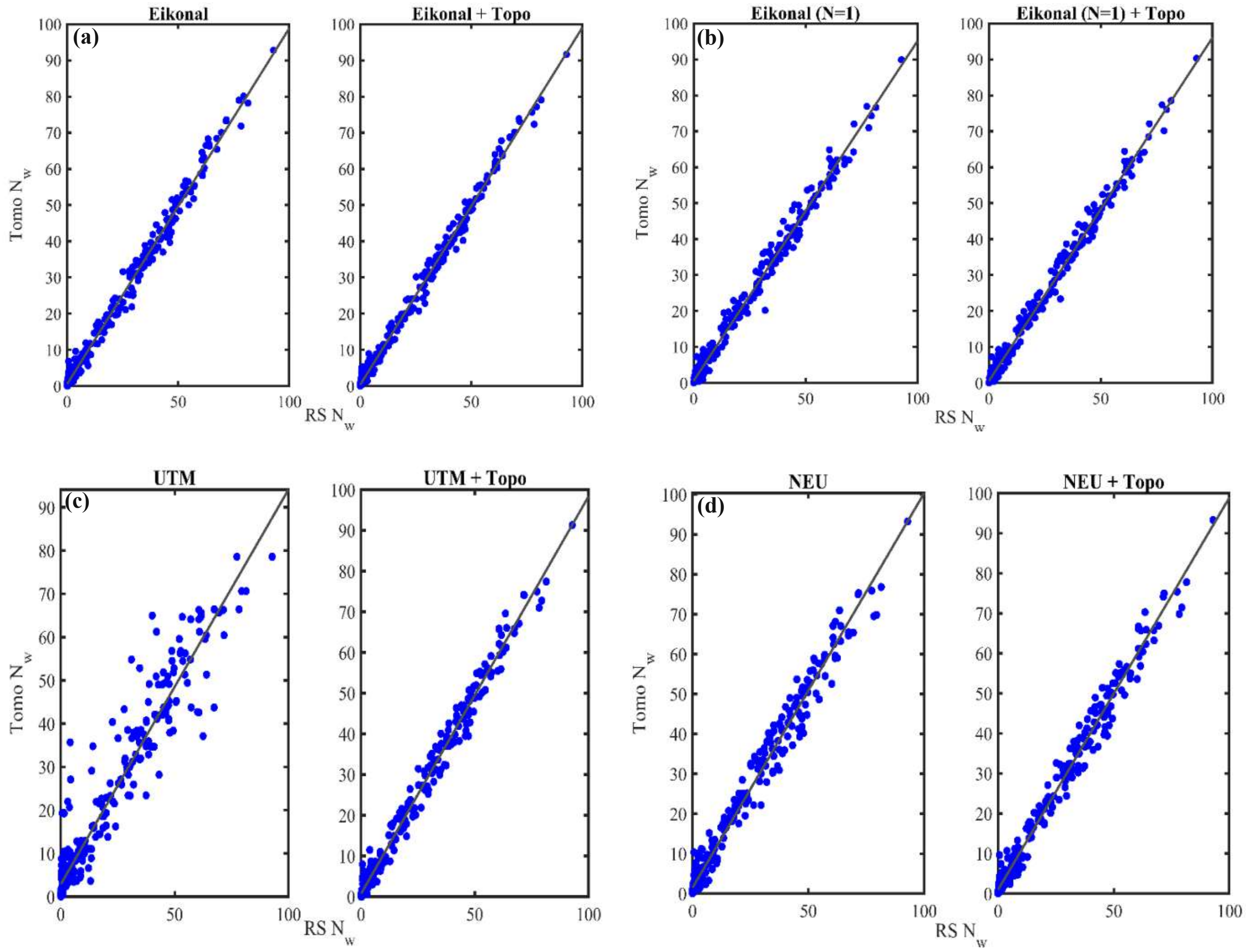

Fig 5. 32. Scatter plots of four types of parameterization, Eikonal, Eikonal (*N=1*), NEU, and UTM by considering topography information and without at location RS10548 (Adavi et al., 2020)

5.3.5 Spread as a Proxy for GNSS Tomography

As explained in Section 3.5.2, the spread of the resolution matrix can be employed to measure the quality of the estimated parameters, here wet refractivity. Therefore, to investigate the efficiency of the spread as an indicator for the model accuracy, the correlation between Std, Bias, and the spread were calculated for the tomography model designed for the COST Action network (see Section 4.1.2). For this purpose, two different schemes have been defined as follows:

- **Loose Constraints (LC):** Damping coefficient 0.1 ($\delta_m = 0.1$) refer to Eq. (3.57) and Eq. (3.59)
- **Tight Constraints (TC):** Damping coefficient 0.9 ($\delta_m = 0.9$) refer to Eq. (3.57) and Eq. (3.59)

Therefore, the correlation between the spread of the resolution matrix and the other statistical parameters could be calculated according to the following diagram (see Fig 5. 33).

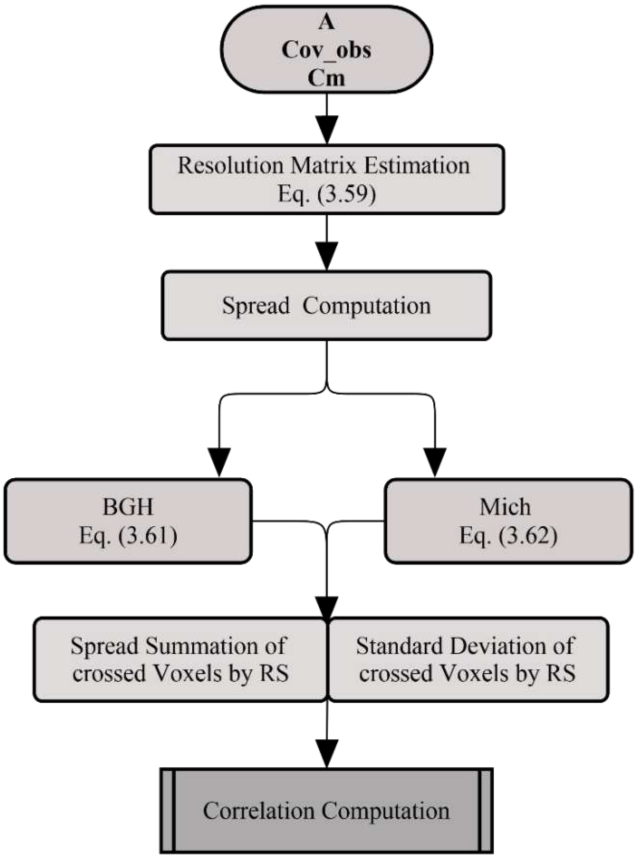

Fig 5. 33. The flow diagram of the correlation computation (Adavi et al., 2022b)

In the following, first, the accuracy of the reconstructed tomography profiles is investigated for both synthetic and GNSS datasets over the experimental periods. Next, the correlation between spreads (Mich and BGH) and statistical parameters (Std and Bias) are obtained to assess the spread as a quality indicator for GNSS tropospheric tomography.

5.3.5.1 Validation of Tomography Solution using NWM and RS data

In the GNSS dataset, the reference values for the tomography derived refractivity were calculated from the Kummersbruk (RS10771) and Meiningen (RS10548) radiosonde station meteo profiles gathered at hours 00:00 and 12:00 UTC each day. For the synthetic dataset, the reference wet refractivity profiles were computed from the NWM model at the radiosonde locations over the experimental periods. This returns to the fact that the SWDs derived from the NWM model and not GNSS measurements. Thereby, the retrieved wet refractivity field cannot reflect the real physical condition observed using the radiosonde. In consequence, an acceptable tomography solution by means of the synthetic dataset has a minimum discrepancy with the wet refractivity extracted from the NWM model. Fig 5. 34 shows the reconstructed wet refractivity profile, the wet refractivity derived from RS10771, and the NWM wet refractivity profile for two random days at midnight. According to this figure, the discrepancy between the synthetic tomography solution and the NWM profile is quite small. For the GNSS dataset, the inconsistency between the recovered tomography wet refractivity field and the RS profile is small but visible.

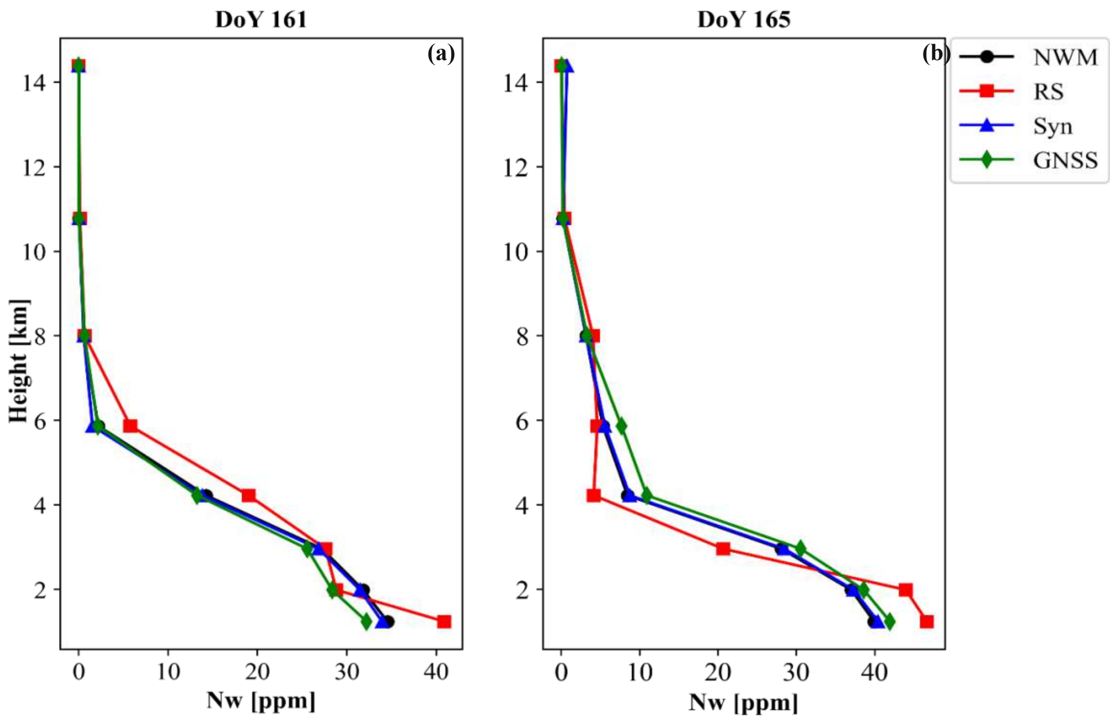

Fig 5. 34. Comparison of the retrieved wet refractivity profiles from the synthetic and GNSS dataset to the reference profiles derived from NWM and radiosonde data on DoYs (a) 161, (b) 165 at Midnight for RS10771 (Adavi et al., 2022b)

Table 5. 24 presents the average values of RMSE, Std, and Bias over all experimental periods. According to the obtained results, the retrieved tomography profiles using the synthetic dataset are generally underestimating the wet refractivity derived from the NWM model (ALADIN). In contrast, the reconstructed wet refractivity using the GNSS dataset is overestimated with respect to the wet refractivity obtained by the RS measurements. Moreover, due to the absence of GNSS observation errors, the quality of the reconstructed wet refractivity solution using the synthetic observations is better than for the GNSS observations.

Table 5. 24. Average RMSE, Std, and Bias with respect to the RS wet refractivity profiles for the real dataset and NWM wet refractivity profiles for the synthetic dataset over the experimental period at RS10771 location (Adavi et al., 2022b)

	RMSE [ppm]	Std [ppm]	Bias [ppm]
Synthetic_149_165 [Ref:NWM]	1.52	0.82	-1.15
Synthetic_160_165 [Ref:NWM]	1.75	1.07	-1.18
GNSS_160_165 [Ref:RS]	3.87	3.51	0.34

Following the same procedure for the location of RS10548, similar performance graphs can be obtained. Fig 5. 35 illustrates the retrieved wet refractivity profile performance compared to the reference profiles for two selected days (DoYs 162 and 164) at midnight. According to this figure, the agreement between the tomography solution using synthetic data and NWM data on DoY 162 is better than for DoY 164. However, in general, the estimated wet refractivity field using the synthetic dataset is behaving like the NWM profiles. For the GNSS dataset, the discrepancy between the tomography solution and the RS profile is smaller in the upper layers in comparison to the lower layers.

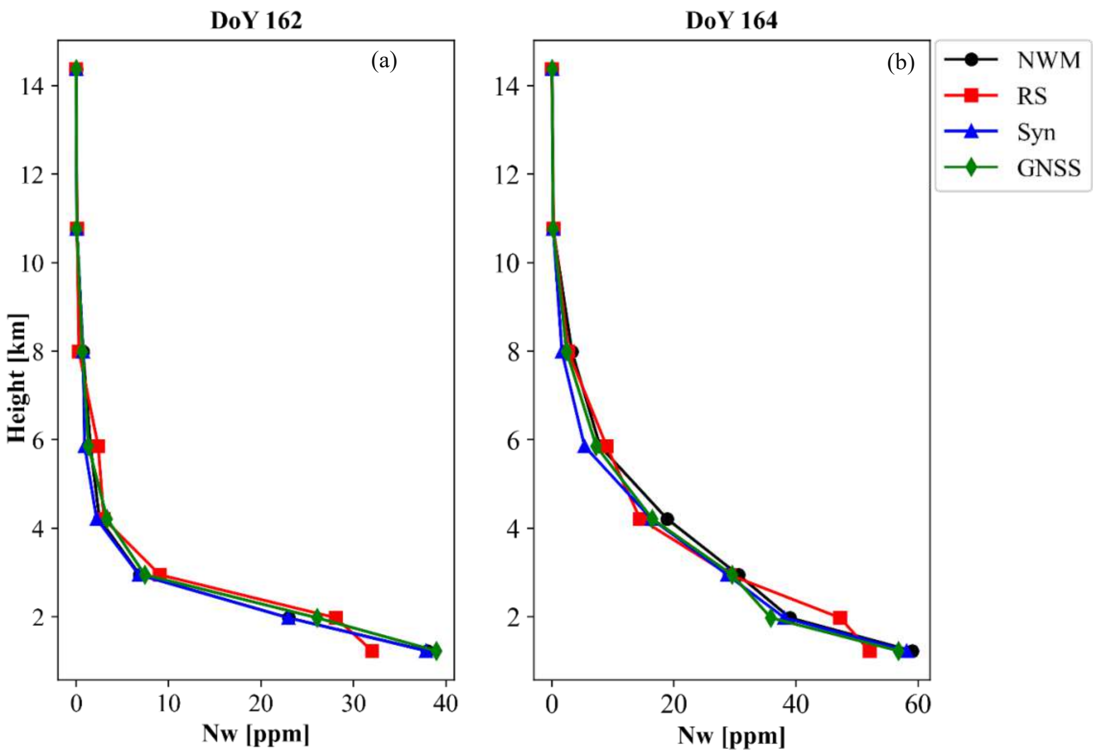

Fig 5. 35. Comparison of the retrieved wet refractivity profiles obtained from the synthetic and GNSS datasets with respect to the reference profiles derived from NWM and radiosonde data on DoYs (a) 162, (b) 164 at Midnight for RS10548 (Adavi et al., 2022b)

In addition, Table 5. 25 gives the statistical results when comparing the tomography solutions and the reference profiles over the experimental period for both synthetic and GNSS datasets. According to the obtained results, the reconstructed profiles underestimate wet refractivity in all datasets and periods with respect to the corresponding reference profiles. Moreover, similar to RS10771, the performance of the estimated tomography profiles based on the synthetic dataset is better than for the GNSS dataset.

Table 5. 25. Average RMSE, Std, and Bias with respect to the RS wet refractivity profiles for the real dataset and NWM wet refractivity profiles for the synthetic dataset over the experimental period at RS10548 location (Adavi et al., 2022b)

	RMSE [ppm]	Std [ppm]	Bias [ppm]
Synthetic_149_165 [Ref:NWM]	1.84	0.87	-1.19
Synthetic_160_165 [Ref:NWM]	1.89	1.17	-0.77
GNSS_160_165 [Ref:RS]	3.62	3.46	-0.27

5.3.5.2 Correlation Analysis of Spread of Resolution Matrix

In order to analyse the correlation between spread and two statistical parameters, namely Std and Bias, first, the summation of the spread of voxels crossed by the radiosonde profiles was computed. Then, to gain a better interpretation of the dependency between statistical parameters and the spread, all values were normalised by the following formula, and afterwards the differences between those values were considered.

$$X_n = (X - X_{min})/(X_{max} - X_{min}) \tag{5.1}$$

whereby X and X_n are the original value and the normalized value, respectively. Finally, Pearson correlation has been utilised to compute the correlation coefficient between statistical parameters (Std and Bias) and spread.

Fig 5. 36 shows the difference between spreads, namely BGH (Section 3.5.2, Eq. (3.61)) and Mich (Section 3.5.2, Eq. (3.62)), and Std for three different time spans of the synthetic and real dataset at RS10771. It can be seen from Fig 5. 36, that the difference between BGH spread and Std is smaller than for the Mich spread. Therefore, the time series of BGH spread follows more closely the Std variations compared to the Mich spread.

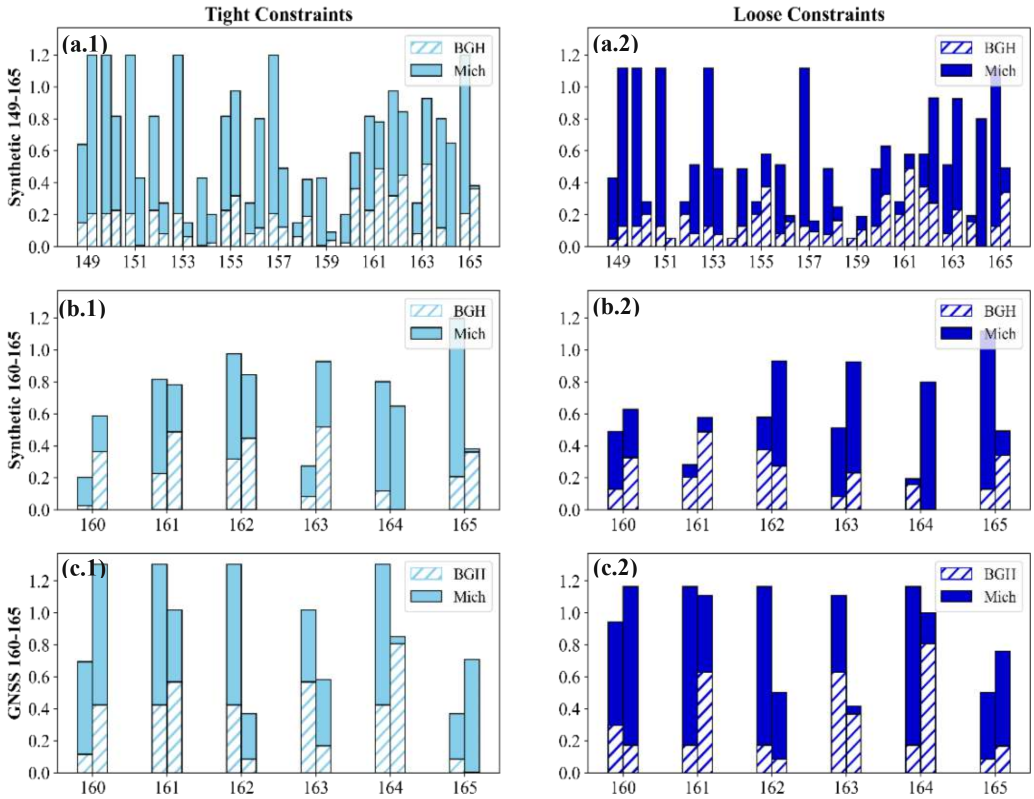

Fig 5. 36. Differences between spread and Std for RS10771. The left column shows the solution by applying tight constraints on the a priori field, whereas the right column shows loose constraints (Adavi et al., 2022b)

To better interpret Fig 5. 36, Table 5. 26 gives the correlation between spread and Std time series for the different schemes and datasets. We must consider that small BGH spread and large Mich spread point to a well-resolved wet refractivity field due to their specification (Section 3.5.2, Eq. (3.61) and Eq. (3.62)). Therefore, the computed correlation for BGH and Mich spreads are positive and negative, respectively. For the synthetic dataset, the negative correlation of the Mich spread in the long period is higher than for the short period. However, inspecting the results gained with the GNSS dataset, the correlation of the Mich spread is almost comparable to the synthetic dataset. According to the obtained results, the BGH spread shows a considerable positive correlation in all datasets. Altogether, both spread types show a promising correlation (about 0.5- 0.7) with the Std of the recovered wet refractivity for almost all investigated periods. However, applying LC on the a priori field results in a better match between spread and Std in comparison to TC. Consequently, the selection of $\boldsymbol{C_m}$ significantly affects the obtained results.

Table 5. 26. Correlation of spread and Std with respect to the radiosonde for the real dataset and NWM wet refractivity profiles for the synthetic dataset over the experimental period at RS10771 location (Adavi et al., 2022b)

	BGH_LC	BGH_ TC	Mich_ LC	Mich_ TC
Synthetic_149_165	0.69	0.54	-0.62	-0.41
Synthetic_160_165	0.67	0.51	-0.44	-0.14
GNSS_160_165	0.55	0.47	-0.63	-0.49

In Table 5. 27, the correlation between the Bias of the recovered refractivity field and the spread is given. According to these results, the correlation of BGH spread with the Bias (see Section 3.5.1, Eq. (3.50)) is highest in all datasets. However, as the Bias can be positive or negative, the correlation just reflects the tendency for a considerable absolute spread to a large bias. Moreover, the correlation of Mich spread shows reasonable large numbers between -0.6 to -0.4 for the GNSS dataset and synthetic dataset (149-165). In addition, compared to TC, LC provides higher coherency with the spread based on the obtained correlation.

Table 5. 27. Correlation of spread and Bias with respect to the radiosonde for the real dataset and NWM wet refractivity profiles for the synthetic dataset over the experimental period at RS10771 location (Adavi et al., 2022b)

	BGH_LC	BGH_ TC	Mich_ LC	Mich_ TC
Synthetic_149_165	0.71	0.57	-0.61	-0.63
Synthetic_160_165	0.73	0.44	-0.41	-0.37
GNSS_160_165	-0.53	-0.50	0.49	0.26

The same analysis has been performed for radiosonde location RS10548. Fig 5. 37 shows the differences between spread and the corresponding Std. According to that, the overall match between BGH spread and Std in the synthetic schemes is slightly better in comparison to Mich spread, which is consistent with the results obtained for radiosonde location RS10771 results.

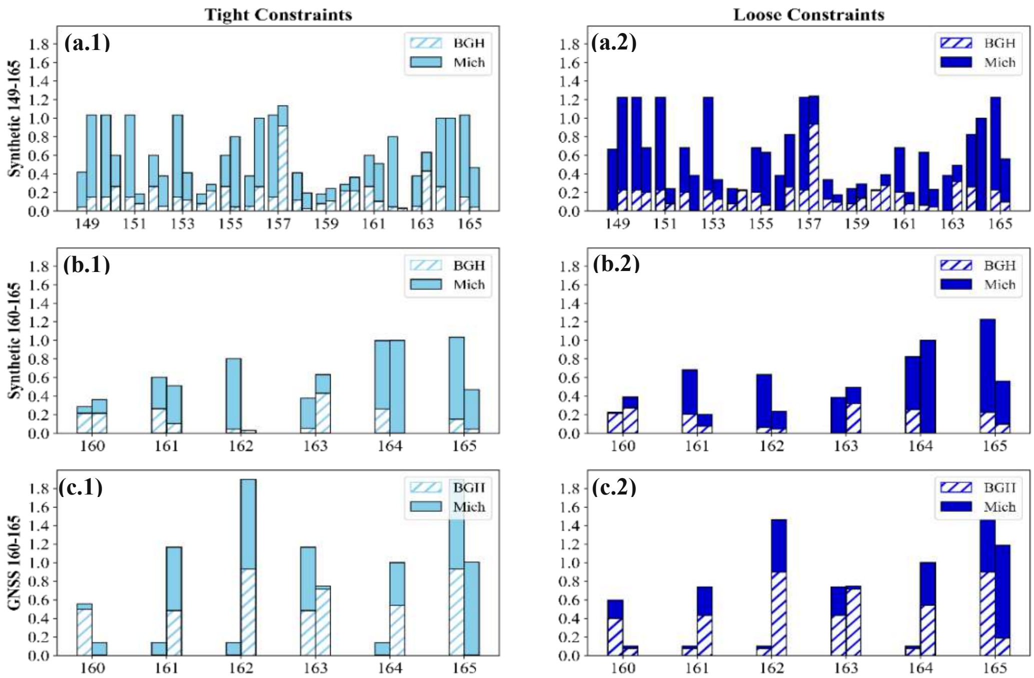

Fig 5. 37. Differences between spread and Std for RS10548. The left column of graphs shows the solution by applying tight constraints on the a priori field, whereas the right column shows loose constraints (Adavi et al., 2022b)

Table 5. 28 presents the correlation between Std and the spread. Based on the obtained correlations, the general performance of the BGH spread is almost similar to Mich spread. Both spreads have a correlation of up to 0.8 with respect to the Std for the synthetic dataset (Ref: NMW wet refractivity). TC schemes show similar performance in comparison to LC schemes. For the GNSS data set (Ref: RS wet refractivity), the correlation between the Mich spread and the Std reaches to -0.70. However, the smallest correlation is obtained with the BGH spread and the Std of this dataset. The improved coherence of Mich spread with Std at this RS location is caused by the fact that the investigated model column pertains to boundary voxels of the model area.

Table 5. 28. Correlation of spread and Std with respect to the radiosonde for the real dataset and NWM wet refractivity profiles for the synthetic dataset over the experimental period at RS10548 location (Adavi et al., 2022b)

	BGH_LC	BGH_ TC	Mich_ LC	Mich_ TC
Synthetic_149_165	0.49	0.54	-0.56	-0.51
Synthetic_160_165	0.81	0.79	-0.68	-0.77
GNSS_160_165	-0.28	-0.17	-0.43	-0.70

As shown in Table 5. 29, the correlation between refractivity biases and BGH spread is not considerable for the RS10548 location. Nevertheless, Mich spread shows a reasonable correlation with the Bias. Nonetheless, it cannot demonstrate a clear judgment about the behaviour of the Bias against the spread. This is due to the fact that the Bias of the tomography model depends on the different factors such as systematic errors in the GNSS dataset, meteorological measurements and NWM model.

Table 5. 29. Correlation of spread and Bias with respect to the radiosonde for the real dataset and NWM wet refractivity profiles for the synthetic dataset over the experimental period at RS10548 location (Adavi et al., 2022b)

	BGH_LC	BGH_ TC	Mich_ LC	Mich_ TC
Synthetic_149_165	0.07	0.15	-0.57	-0.45
Synthetic_160_165	0.27	0.26	-0.28	-0.37
GNSS_160_165	-0.15	-0.16	0.72	0.73

In order to achieve a better interpretation of the obtained results, the absolute differences between Spread and Std of the studied time series could be compared. The smaller difference shows high similarity, whereas the larger difference indicates low similarity between time series. Therefore, the average of accumulated differences between spread and Std were computed. Fig 5. 38 presents the comparison of the average accumulated differences during the periods of interest for the locations of RS10771 (hatched bars) and RS10548 (non-hatched bars). According to this figure, by applying loose constraints, spread provides an acceptable characterisation of the accuracy of the tomography model in most cases. In addition, BGH spread has a higher consistency with the variations of Std in comparison to Mich spread. Consequently, BGH spread calculated with loose constraints on the a priori refractivity field is the recommended quantity to predict the accuracy of the retrieved tomography field.

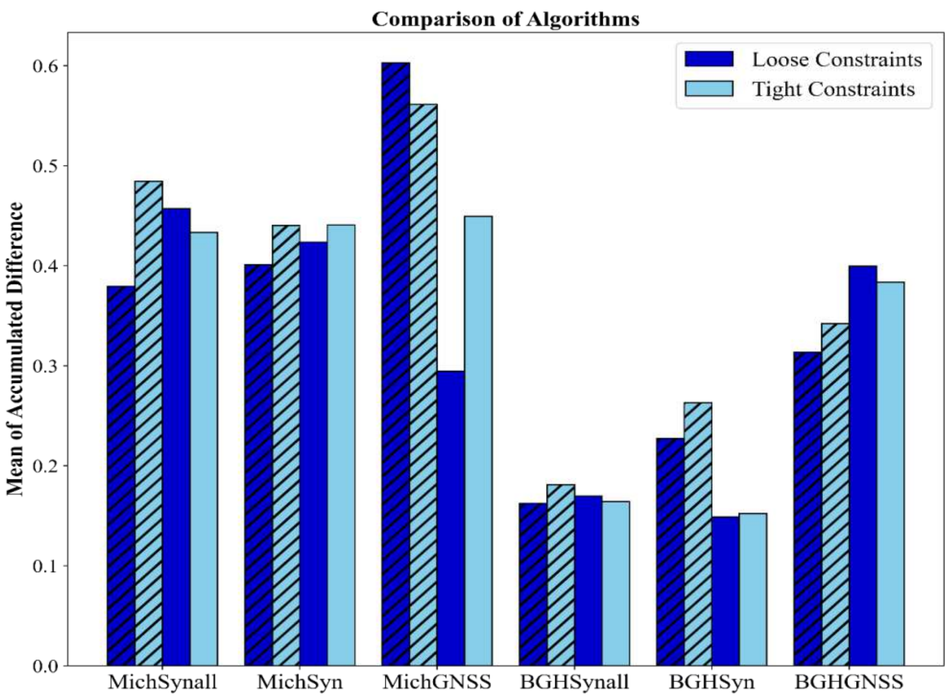

Fig 5. 38. The accumulated absolute difference between spread and Std for RS10771 (hatched bars) and RS 10548 (non-hatched bars), for Michelini spread (Mich) and Backus-Gilbert (BGH) for GNSS (GNSS) and synthetic datasets for all experimental periods from DoYs 149 to DoY 165 (syn) and DoYs 160-165 (syn, GNSS) (Adavi et al., 2022b)

According to the obtained results, the spread of the resolution matrix showed a strong correlation (up to 0.81 for synthetic and 0.70 for real observations) with the Std of the reconstructed wet refractivity. However, there was no clear picture depending on the applied spread computation models with the Bias of the retrieved tomography solution which can return to the systematic effects in the GNSS dataset such as pressure meteorological measurements or the quality of the NWM model over the experimental period.

5.4. CORS Network: GOES-R as an Initial Field for GNSS tomography

The tomography model suffers in terms of solution uniqueness as propagated signals do not pass through some of the model elements. Therefore, horizontal and/or vertical constraints and additional data sources should be used to avoid the singularity of the estimated wet refractivity field. In this section, the combination of the wet refractivity map computed from the GOES-16 sounder with the GNSS tomography is investigated to attain a unique solution. Therefore, a 3D tomography model has been defined over a regional area covered by the CORS Network (see Section 4.1.3 in Chapter 4) to analyse the efficiency of the proposed dataset. For this purpose, two different schemes have been considered to achieve the feasibility of the estimated 3D wet refractivity images using GOES-16 (see Fig 5. 39).

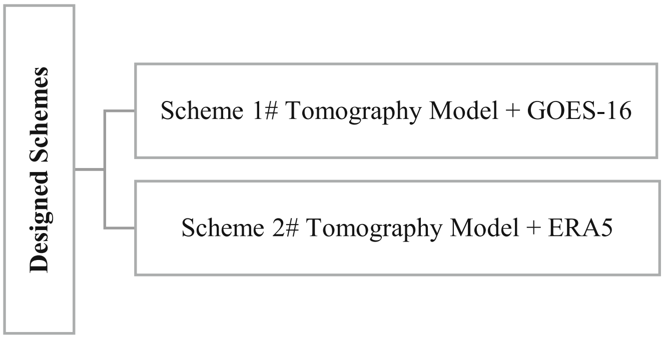

Fig 5. 39. Two Schemes to analyse the impact of GOES-16 as an initial field on the tomography solution

In this part, first, the configuration of the tomography model for the CORS network is identified. Then, the weather condition and GOES-R events during the period of interest are described. Finally, the tomography solution is reconstructed using the Landweber method by applying GOES-16 and ERA5 schemes.

5.4.1 Tomography Model Configuration

The model space resolution matrix ($\boldsymbol{R_m}$) has been applied in order to select the optimum size for the horizontal dimension of the model elements (see Section 3.2.2 for more details). For this purpose, six different horizontal resolution matrices have been analysed from 20 km to 70 with the step size 10 km above the area of interest. Fig 5. 40 shows the schematic view of the designed voxels with a horizontal resolution of 20 km. The shaded elements in this figure indicate voxels, which are not crossed by GNSS signals. According to Fig 5. 40, the number of empty voxels, especially in the first layers, is huge. Therefore the tomography model should be tightly constrained to achieve a unique solution. Hence, the reconstructed wet refractivity mostly captures the constraints rather than the real condition of the troposphere.

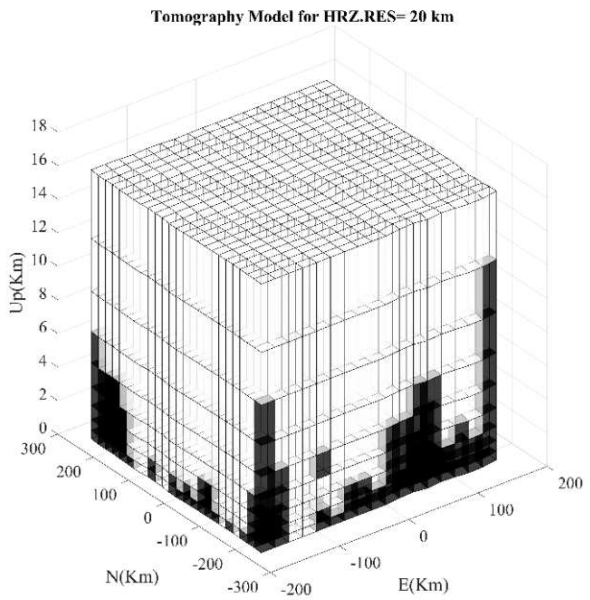

Fig 5. 40. Designed tomography model with the step size of 20 km above the CORS GNSS network

In addition, voxels should not be too large due to the constant amount of wet refractivity in each element for the intended tomography window. Therefore, 60 km has been selected as an optimum horizontal voxel size. This is due to the resolution matrix of the tomography model with 60 km horizontal resolution is more close to the identity in comparison to other options. Fig 5. 41 illustrates the designed tomography model over the CORS GNSS network.

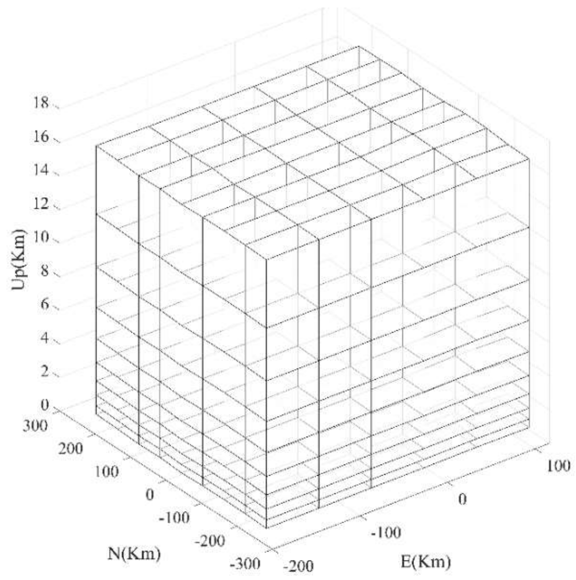

Fig 5. 41. Designed Tomography Model above the CORS GNSS network

Moreover, the exponential model has been applied to design the vertical layers of the tomography model. In addition, a temporal resolution of 1 hour has been chosen to assure that the wet refractivity amount can be assumed as constant. Fig 5. 42 demonstrates the configuration of the designed tomography model in the CORS network.

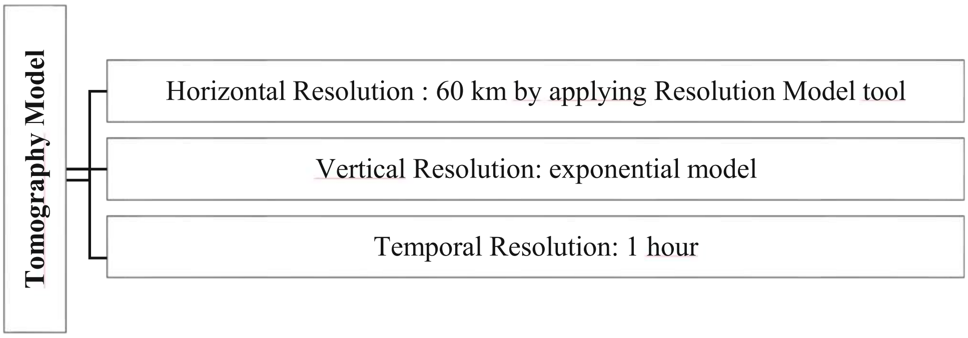

Fig 5. 42. Tomography model configuration in the CORS network

5.4.2 GOES-R events and Weather Condition on the Study Period

In order to achieve a better judgment about the performance of GOES-16 data in the tomography solution, four different months from July to October 2019 have been considered. Table 5. 25 summarizes the studied months with their days of interest in the CORS case study (see Section 4.1.3).

Table 5. 30. The studied months with their intended days in the CORS network

Month	DoY
July	193-194
August	214-217
September	259-260
October	281-283

The weather condition during the experimental period are displayed in Fig 5. 43 where the variation of relative humidity was measured by the radiosonde station and total precipitation was derived using the ERA5 model. According to the variation of these parameters, the period of interest contains both, wet and dry days, which is beneficial for the tomography study.

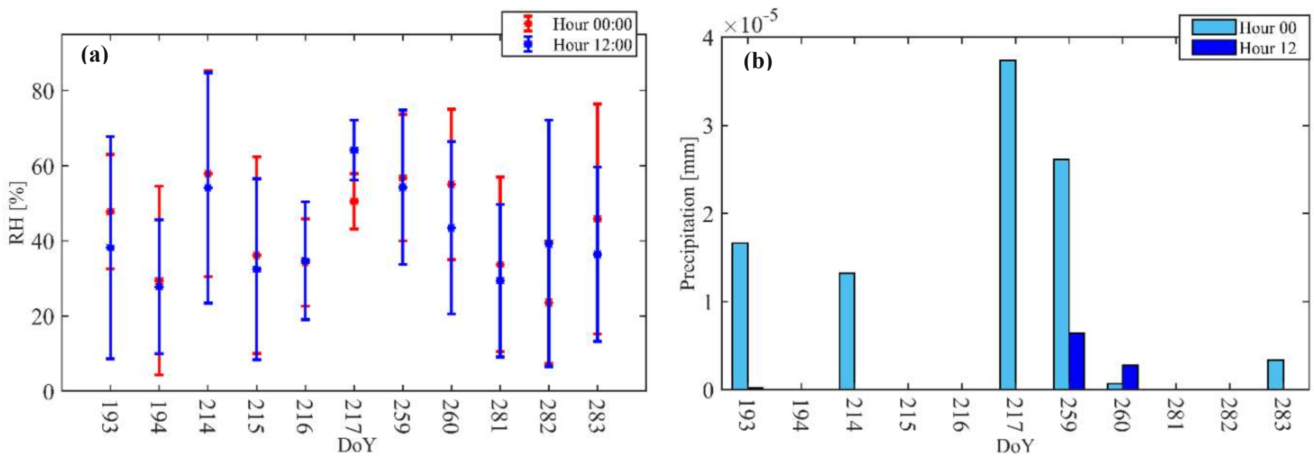

Fig 5. 43. Variations of relative humidity up to 4 km height (a) and average of total precipitation within the whole area (b) during the time of interest

To achieve a reasonable initial field, the density of the GOES-16 events, which report temperature and relative humidity products, should be looked upon. Fig 5. 44 presents the distribution of the GOES-16 events within the area of interest for two different days at midnight and noontime. According to this figure, the density of the GOES-16 profiles is acceptable. However, interpolation and extrapolation should be applied since there are some gaps in the dataset. Here, the natural neighbour interpolation method has been employed to produce missing humidity and temperature values in the area of interest (Ledoux and Gold, 2005).

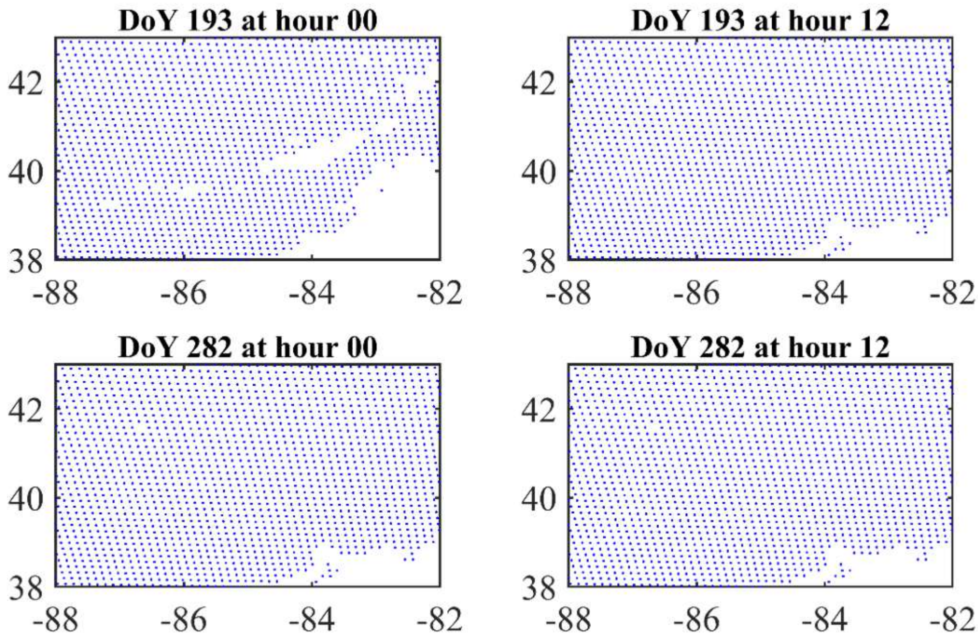

Fig 5. 44. GOES-16 events in the area of interest

5.4.3 Analysis of GOES-R as an a priori Field on the Tropospheric Tomography

To analyse the accuracy of the reconstructed wet refractivity by applying GOES-16 as an a priori field, data of the radiosonde station located at Wilmington (RS72426) has been used at midnight and noontime. Fig 5. 45 shows the reconstructed wet refractivity profile derived from scheme#1 and scheme#2 in comparison to the radiosonde profiles at midnight for two different days. Based on this figure, the performance of GOES-16 on DoY 259 is superior to the ERA5 scheme almost in all vertical levels. However, the behaviour of the retrieved profiles using GOES-16 as a priori field on DoY 193 is almost the same as for the ERA5 scheme in the lower layers, but for upper layers, this scheme shows a better agreement with the RS profile.

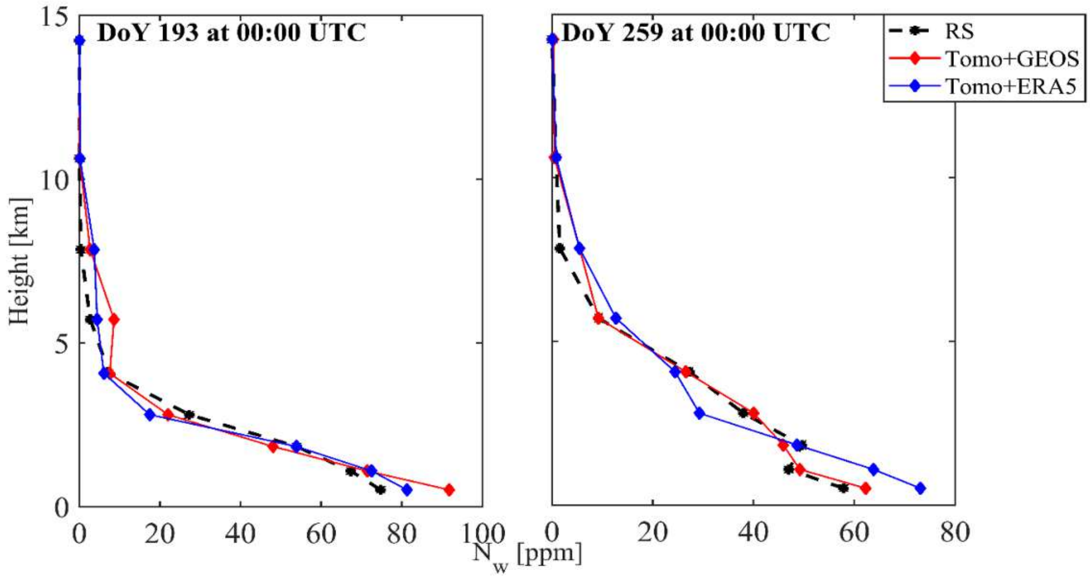

Fig 5. 45. The comparison of reconstructed tomography profiles by GEOS-16 and ERA5 to the RS72426 profiles at midnight for DoYs 193 and 259

Fig 5. 46 displays the RMSE of the retrieved tomography solution using different schemes on 11 days for midnight. The average RMSE for the GOES and ERA schemes is about 5.58 ppm and 6.81 ppm at midnight. Therefore, the consistency between the GOES scheme and RS profile is generally better than for the ERA5 scheme. However, the performance of the GOES scheme is not the same on all days, and this may return to the accuracy of the GOES's products for different hours and weather conditions.

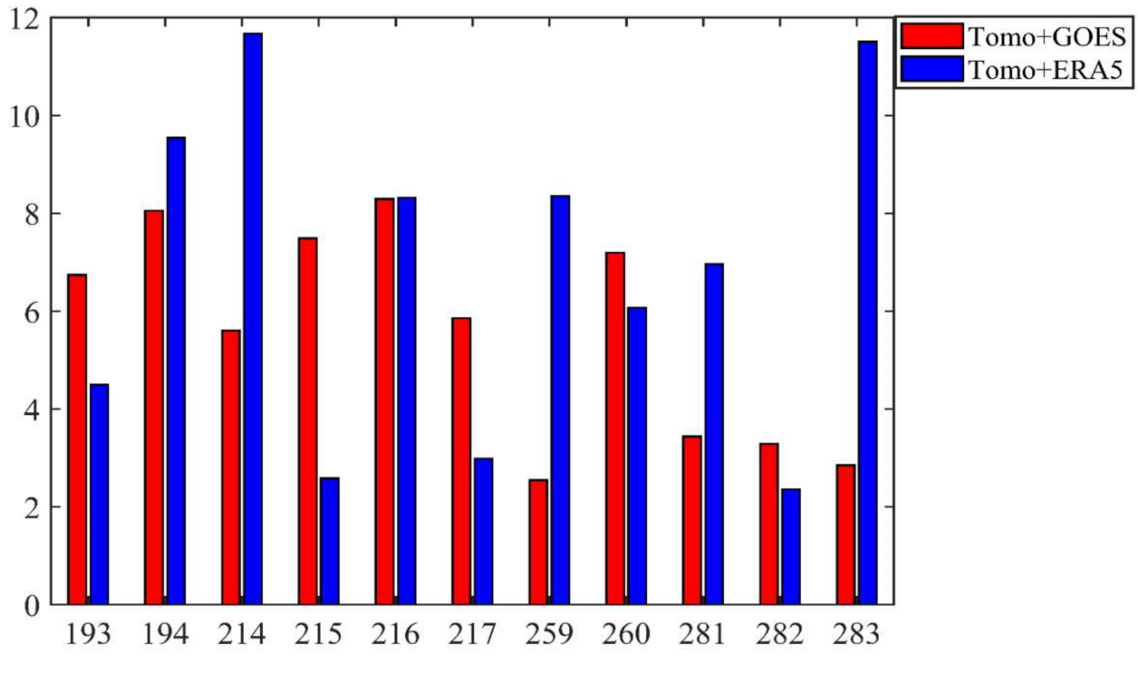

Fig 5. 46. RMSE of the reconstructed wet refractivity profile with respect to RS72426 in the period of interest at midnight

Moreover, the dispersion of the two different schemes relative to the RS72426 profiles during the study period at midnight is presented in Fig 5. 47. As illustrated in this figure, the GOES scheme is slightly better than the ERA5 scheme because the slope of the corresponding least-squares line is nearly close to 1:1. This demonstrates the positive impact of GOES-16 as an initial field on the tomography solution.

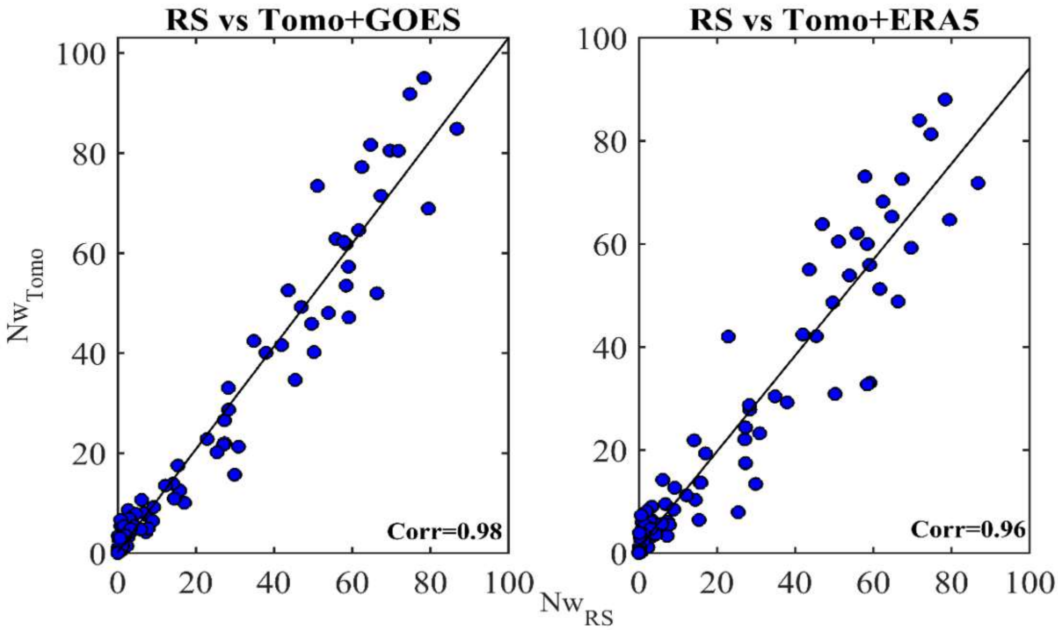

Fig 5. 47. Scatter plots of two schemes, GOES-16 and ERA5 at midnight for RS72426

The same analysis has been performed for noontime. Fig 5. 48 represents the RMSE of schemes with respect to RS72426. According to the obtained results, the average RMSE for the GOES scheme is about 3.64 ppm and about 6.26 ppm for the ERA5 scheme. Therefore, the accuracy of the tomography solution has been increased by about 58% when applying the GOES dataset as an initial field.

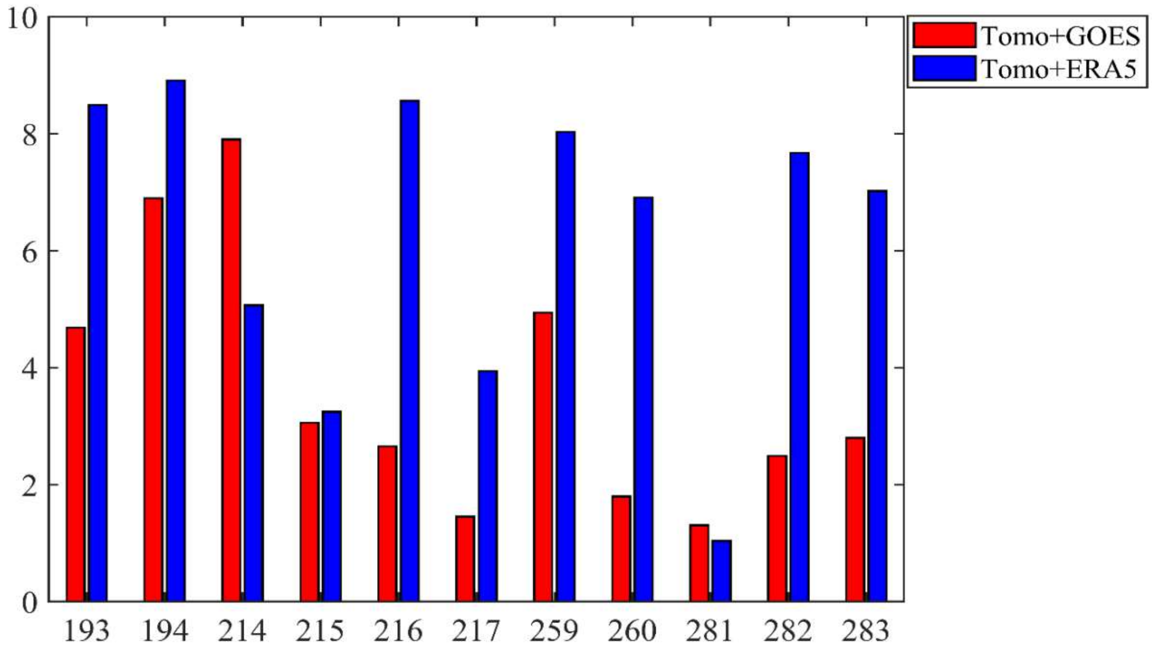

Fig 5. 48. RMSE of the reconstructed wet refractivity profile with respect to RS72426 in the period of interest at noontime

Fig 5. 49 shows the dispersion of GOES and ERA5 schemes relative to the RS72426 profiles during the study period at noontime. As shown in this figure, the spreading of the GOES scheme is generally smaller than for the ERA5 scheme in noontime as well. This proves the positive effect of GOES-16 on the quality of the retrieved field.

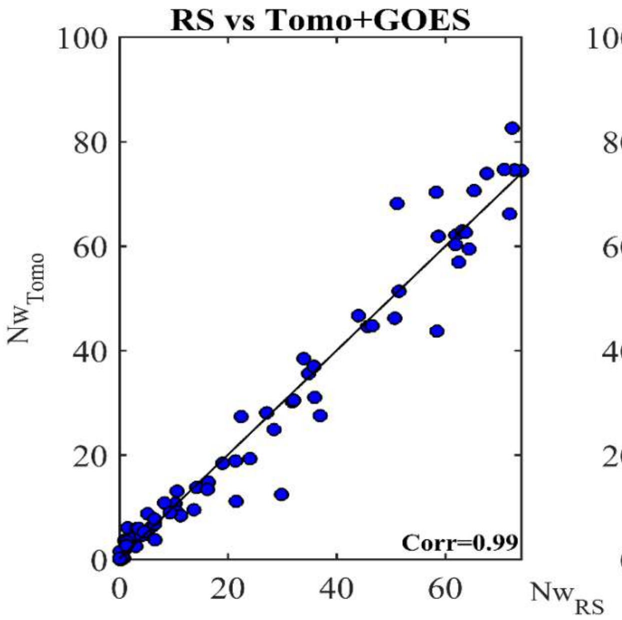

Fig 5. 49. Scatter plots of two schemes, GOES-16 and ERA5 at noontime for RS72426

In addition, the MAE of the reconstructed profiles in respect to RS72426 have been calculated in order to see the impact of GOES-16 on different vertical layers. As reported in Table 5. 31, the GOES scheme has superior performance for the lower layers, especially in the noontime. For upper layers, the discrepancy between the retrieved tomography profiles from GOES and ERA5 schemes and the RS profile is almost identical at both epochs.

Table 5. 31. Average MAE regarding the height of the layers below and above 6 km for different temporal resolution at midnight and noontime

Time / Height	Midnight		Noontime	
	GOES-16	ERA5	GOES-16	ERA5
Up to 2 km	7.58	9.54	4.51	8.13
Height 2 km to 6 km	2.58	3.43	2.08	3.29

Chapter 6

6 Conclusion and Outlook

GNSS tropospheric tomography is one of the applications of GNSS, which attracts more and more interest in the field of meteorology. This method can reconstruct the water vapour of the atmosphere, which considerably affects weather forecasting and early warning systems of severe weather. GNSS tomography is an all-weather remote sensing technique to capture the spatiotemporal behaviour of atmospheric water vapour using the standing infrastructure of GNSS satellites and networks. In this method, traditionally, a regular spaced 3D grid stretches from the GNSS network to the effective height of the troposphere in the area of interest. Then, the wet refractivity in these voxels is reconstructed using the SWD observations in the desired tomography domain by means of the discrete inverse concept. Nevertheless, the quality of the reconstructed profile highly depends on different factors like observation distribution, inversion technique, regularization methods, initial field, and used constraints in the model. In consequence, the main focus in this dissertation was committed to some of these factors to retrieve an appropriate wet refractivity field. In the following, the key findings from this analysis, which have been investigated throughout the various experiment, will be summarized.

Two different strategy schemes as well as different iterative regularization methods and the TV technique have been employed in order to analyse the potential of using the single frequency (SF) observations in comparison of the dual frequency (DF) observations. The results showed that the NWM AROME ZTD correlate with GNSS DF ZTD and SF ZTD on average at 97% and 66%, correspondingly. Analyzing RMSE of the estimated ZTDs using SF and DF observations showed that the DF scheme provides better results (avg. RMSE 0.019 meter) in comparison to the SF scheme (avg. RMSE 0.075 meter). Furthermore, the Bias of SF ZTD was slightly larger during noontime which can be explained by the daily solar radiation and consequential complexity to describe the ionospheric delay with SEID. Moreover, there might also be artifacts from model deficiencies e.g., satellite clocks in PPP processing. As expected a successful integer fixing of the ambiguities improves the results and leads to a much more accurate estimation of the ZTD. The accuracy of retrieved refractivity fields using various regularization methods in SF and DF schemes were assessed by RS observations. According to the obtained results, the performance of ART techniques (ART, MART, and Landweber) by applying the AROME model as an initial field was comparable for both SF and DF schemes. In addition, the accuracy of the reconstructed wet refractivity field using the TV method and ART techniques + TV for SF schemes was almost as good as for the DF scheme. Moreover, the correlation between retrieved wet refractivity and RS wet refractivity for all regularization techniques in SF and DF schemes was almost higher than 95%. However, a considerable MAE and Bias for ART+ AROM and ART+ TV in the SF scheme has been detected during noontime. This study showed that entering ZTDs calculated from SF data instead of DF data yields to a degradation of the RMSE of the reconstructed profiles between 10%-40% over all investigated regularization techniques. In the presence of a reasonable initial field, an acceptable reconstruction of the wet refractivity at the level of 4-7 ppm with respect to radiosonde profiles could be achieved, but also TV+ Landweber and TV+ MART techniques can retrieve wet refractivity profiles at the 6-8 ppm-level. In future studies, PPP AR (Ambiguity Resolution) techniques have to be further investigated to improve ZTD estimates derived from

DF or even SF data. Moreover, the tomography approach based on the TV regularization method should be investigated in more extended periods and under different weather conditions to prove the potential of this method for reconstructing the wet refractivity field without using any initial field.

In the further step, the application of the TV method in different temporal resolutions was investigated in order to assess the near-real tomography solution without any initial field. According to the gained results, the accuracy of the retrieved wet refractivity field in all tomography windows using the TV method at noontime improved almost 30% compared to midnight. In addition, the correlation between the tomography solution and RS profiles for all temporal resolutions was higher than 95%. Moreover, the inconsistency between the reconstructed wet refractivity field and the reference profile was less than 8.5 ppm at midnight and 5.6 ppm at noontime for lower layers. For upper layers, the discrepancy between the tomography solution and the reference solution was maximally about 7 ppm and 6 ppm at midnight and noontime, respectively. Further investigations were also performed to compare the estimated tomography solutions using the TV method with the Landweber technique. Based on the obtained results, the accuracy of the retrieved field using the Landweber method was generally better than for the TV technique at midnight. At noontime, the performance of retrieving wet refractivity by the TV method, especially for spans longer than 40 minutes, was comparable to the Landweber technique or even better. Therefore, reconstructing the tomography model using the TV method is advantageous in case of no access to a reliable initial field even for a short tomography window if the condition number of the design matrix is not very large and also the amount of water vapour in the troposphere is considerable high. However, it should be noted that considering the short tomography window is not always applicable due to various weather conditions during a day. Therefore, further investigations are encouraged to assess the plausibility of the TV method in other case studies located in different climate zones and over further time periods. Furthermore, assessing the TV method in comparison to other regularization techniques, which are independent of an initial field, may provide a better judgment about the quality of the retrieved wet refractivity field using this method.

The next important study was to investigate the effect of straight-line methods versus ray tracing methods for computing the length of a ray within a model element. To the author' best knowledge, this is a first attempt to reconstruct the wet refractivity field using 2D Eikonal raytracing method, which is a balance between accuracy of 3D Eikonal raytracing and simplicity and processing speed of straight-line. Moreover, the accuracy of the ray-tracing method when neglecting the bending effect was investigated. In addition, the effect of accounting the topography in the tomography model was investigated. The results showed that defining topography in the tomography model had a considerable impact in the lower layers on the reconstructed wet refractivity field. Moreover, applying the Eikonal ray-tracing method led to an improved accuracy of the estimated wet refractivity field compared to straight-line schemes (up to 84%). In the shown test case (volume of about 250 km × 320 km ×10 km) the straight-line strategy performs much better in a UTM coordinate system than in a NEU coordinate system. Nevertheless, further investigation encompassing areas different in size are encouraged to achieve a general interpretation of the studied parameterization method.

Further attention was then given to the validation of the tomography solution as well as to predict a model accuracy. For this purpose, the spread of the resolution matrix was investigated as a new approach. Two spread definitions, denoted Michelini (Mich) and Backus-Gilbert (BGH), were used in order to analyse the correlation with posterior calculated stochastic quantities like Std and Bias. Due to the impact of the observation covariance matrix as well as the quality of the initial field, the damped least-squares method was applied to calculate a reasonable resolution matrix. This is due to the key responsibility of the resolution matrix in spread computations. For the first implementation, only $\boldsymbol{C_{obs}}$ was considered as a diagonal matrix because calculating the full-populated measurements covariance matrix is quite challenging. However, this could be improved in the future by applying the turbulence theory to estimate off-diagonal elements of the covariance observation matrix. Besides, the a priori covariance matrix of the unknown parameters was defined by considering low and high damping coefficients, called LC and TC, respectively. Nevertheless, introducing the 'real accuracy' of the wet refractivity model extracted from the NWM would lead to more realistic results. This can be achieved if the standard deviation of temperature, pressure, and water vapour pressure fields of the NWM is accessible. To investigate the success percentage of spread as a proxy for the GNSS tomography, the correlation coefficient between these values and statistical measures, Std and Bias, were calculated over the experimental period for the synthetic and real datasets. According to the obtained results, the correlation between spread and Std was considerable. However, the Bias showed different behaviour with respect to spread which can return to the systematic errors in the GNSS dataset, meteorological measurements and the quality of the NWM model over the experimental period. In addition, LC shows a generally higher correlation in comparison to TC. Moreover, the absolute differences of BGH spread with respect to Std are generally smaller than for Mich spread. Hence, it can be concluded that applying BGH spread with LC weighting is the promising method to investigate the accuracy of a tomography model. Nevertheless, it should be noted that to achieve acceptable results, calculating a realistic prior covariance matrix of unknowns is required. In consequence, this work confirms the high correlation of the spread (up to 0.81 for synthetic and 0.70 for GNSS data) with the Std of the retrieved refractivity field. Therefore, this parameter could be used in future as an a priori quality index for the tomography solution to analyse the performance of the tomography model before the reconstruction process, especially for the Near Real-Time (NRT) applications. In addition, this factor can be employed to recheck the reconstructed tomography solution to assure the quality of all parts of the model, which is essential for now-casting and forecasting applications. Nevertheless, further case studies are encouraged to assess the performance of spread.

Further, the impact of the GALILEO constellation on GNSS tomography was investigated in two different periods covering April (dry period) and August (wet period) 2019. According to the obtained results, the RMSE of GE ZTD compared to AROME ZTD was about 0.012 meters in the dry period. However, this number increased to 0.020 meters in the wet period which may return to the larger amount of ZTD in this period or the quality of the AROME model. In addition, there was a high correlation, more than 96%, between AROME ZTD and GNSS ZTD for all schemes (GRE, GR, and GE). The accuracy of the reconstructed wet refractivity profile using different constellation schemes with respect to RS11035 for both experimental periods was almost comparable. Based on the obtained results, all schemes could reconstruct the wet refractivity field with an accuracy between 1.8-8.9 ppm and 0.8-8.3 during the April and August periods. The computed correlation between various schemes (GRE, GR, GE) and the RS profile was also more than 95% which confirmed all combinations of satellite constellations could provide a wet refractivity profile close to the RS profile. Thereby, the third GNSS system had no significant impact on the accuracy of the tomography for this research, because a sufficient number of rays was almost provided using a combination of two GNSS satellites. However, having GNSS signals at different elevation angles should be considered as pre-requirements to achieve an acceptable quality for the retrieved wet refractivity field in the area of interest. Nevertheless, the current study only certified in a small area, and therefore further research in different area is encouraged to evaluate the obtained results. In addition, the estimated ZTD using different constellations completely depends on the ambiguity fixing resolution step and a high ambiguity fixing rate leads us to more accurate tropospheric delays. Finally, defining the vertical constraint like radio occultation and radiosonde in future studies could be helpful in terms of enhancing the accuracy of the results, specifically in the lower layers of the model.

Finally, the impact of derived wet refractivity maps from GOES-R as an initial field in the retrieved tomography solution was examined. Based on the attained results, the RMSE of the reconstructed wet refractivity with respect to the radiosonde measurements was about 5.58 ppm at midnight and 3.64 ppm at noontime. On average GOES-R data could improve the RMSE of the tomography model by 15-43 % during the period of interest in comparison to using ERA5 as an initial field. Moreover, according to the obtained MAE, applying GOES-R as an initial field could enhance the tomography MAE for lower layers by 15-35 % compared to ERA5 model as an a priori field. Nevertheless, further studies to apply the collocation technique to interpolate the meteorological measurements of GOES-R to a denser grid could increase the impact of this geostationary satellite for the reconstructed tomography field.

First and foremost, the idea of using the spread of the resolution matrix as an a priori quality index for the tomography solution can hopefully be used to evaluate the reconstructed field or to recheck the quality of the retrieved tomography solution. In terms of the parameterization method, considering the orography of the study area for designing the tomography model can lead to a better quality for the retrieved wet refractivity field. In addition, 2D Eikonal raytracing, the fast and simplified version of the 3D Eikonal, can expectantly estimate an accurate tomography solution. Moreover, the SF observations can be successfully used as an acceptable input for the GNSS tropospheric tomography in the presence of a reliable a priori field. According to the finding of this work, the TV method is recommended to the GNSS tomography community in case of no reliable initial field, especially during noontime. The TV method estimates the tomography solution, which is comparable with other regularization techniques associated with an a priori field.

Last but not least, there are still some open questions that undoubtedly throw light on the author to enhance the quality of the obtained results and, in consequence, GNSS tropospheric tomography. Therefore, the further research plan include as follows:

- Assessing the quality of the tomography solution using the covariance matrix
- Defining a formula for the spread which can directly estimate Std of the retrieved solution
- Applying GEOS-R profiles as direct observations to the tomography model
- Finding a method to define a dynamic tomography temporal resolution, perhaps by utilizing tropospheric horizontal gradients.

Appendices

Appendix A

Gradient Components of the Refractivity in a Spherical Coordinate System

In order to derive the gradients of the refractivity field with respect to a spherical coordinate system, it is necessary to define an osculating sphere of radius as follows (Millman and Parker, 1979):

$$R = \frac{a\,\sqrt{1-e}}{1-e^2\ \sin\varphi^2} \tag{A.1}$$

Then, the refractivity $n_k(r,\lambda,\theta)$ at layer k can be computed through the NWM grid by applying the bilinear interpolation method (Hobiger et al., 2008):

$$n_k = (1-\xi)\,(1-\eta)\,n_{i,j,k} + \xi\,(1-\eta)\,n_{i+1,j,k} + \xi\,\eta\,n_{i+1,j+1,k} + (1-\xi)\,\eta\,n_{i,j+1,k} \tag{A.2}$$

where

$$\xi = \frac{(\lambda-\lambda_i)}{(\lambda_{i+1}-\lambda_i)} \tag{A.3}$$

$$\eta = \frac{(\theta-\theta_i)}{(\theta_{i+1}-\theta_i)} \tag{A.4}$$

In order to compute the refractivity between layers k and $k+1$ and by the assumption of exponentially decreasing of refractivity, we have (Hobiger et al., 2008):

$$n(r,\lambda,\theta) = 1 + (n_k(\lambda,\theta)-1)\,exp\big(C(r-R_k)\big) \tag{A.5}$$

with $C = \log\left(\frac{n_{k+1}(\lambda,\theta)-1}{n_k(\lambda,\theta)-1}\right)/R_{k+1} - R_k$.

Now, the partial derivatives of refractivity could be computed as follows (Hobiger et al., 2008):

$$\frac{\partial n(r,\lambda,\theta)}{\partial r} = (n_k(\lambda,\theta)-1)\,C\,exp\big(C(r-R_k)\big) \tag{A.6}$$

$$\frac{\partial n_k}{\partial \lambda} = \frac{(1-\xi)\,(n_{i+1,j,k}-n_{i,j,k}) + \xi\,(n_{i+1,j+1,k}-n_{i,j+1,k})}{\lambda_{i+1}-\lambda_i} \tag{A.7}$$

$$\frac{\partial n_k}{\partial \theta} = \frac{(1-\eta)\,(n_{i,j+1,k}-n_{i,j,k}) + \eta\,(n_{i+1,j+1,k}-n_{i+1,j,k})}{\theta_{i+1}-\theta_i} \tag{A.8}$$

By defining $M_k(r,\lambda,\theta) = (r-R_k/R_{k+1}-R_k)\ \big(exp\big(C\,(r-R_k)\big)/n_k(\lambda,\theta)-1\big)$, Eq. (A.7) and Eq. (A.8) could be given as below:

$$\frac{\partial n(r,\lambda,\theta)}{\partial \lambda} = \frac{\partial n_k}{\partial \lambda}\,exp\big(C\,(r-R_k)\big) + M_k(r,\lambda,\theta)\left((n_k(\lambda,\theta)-1)\,\frac{\partial n_{k+1}}{\partial \lambda} - (n_{k+1}(\lambda,\theta)-1)\,\frac{\partial n_k}{\partial \lambda}\right) \tag{A.9}$$

$$\frac{\partial n(r,\lambda,\theta)}{\partial \theta} = \frac{\partial n_k}{\partial \theta}\,exp\big(C\,(r-R_k)\big) + M_k(r,\lambda,\theta)\left((n_k(\lambda,\theta)-1)\,\frac{\partial n_{k+1}}{\partial \theta} - (n_{k+1}(\lambda,\theta)-1)\,\frac{\partial n_k}{\partial \theta}\right) \tag{A.10}$$

Appendix B

Supplementing Tables denoting the Accuracy of the reconstructed Wet refractivity Profiles using different Regularization Techniques on Basis of Single and dual frequency observations

Table B. 1. RMSE [ppm] of reconstructed wet refractivity profiles for different regularization schemes (SF scheme, epoch 00:00 UTC, location: profile of RS11035 launch)

DoY	Lndw+Arom	MART+ Arom	ART+ Arom	TV	Lndw+TV	MART+TV	ART+TV
232	4.92	3.14	2.97	7.05	6.37	8.45	4.54
233	4.30	4.86	4.97	7.76	4.01	7.53	7.86
234	4.53	3.30	2.58	6.19	4.75	9.99	3.72
235	3.86	5.27	7.11	8.64	8.52	16.35	13.48
236	2.41	3.77	5.95	9.73	9.89	11.86	8.24
237	7.09	3.60	4.24	6.42	6.59	11.40	4.88
238	3.94	2.87	3.74	9.67	7.86	11.19	10.13
239	7.90	3.49	3.69	13.63	13.94	9.31	5.80
240	2.13	6.57	2.98	9.93	9.84	8.35	3.01
241	4.62	2.89	2.52	10.05	11.23	2.39	2.37
242	3.93	2.88	3.60	9.21	6.40	8.33	6.79
243	3.47	3.67	3.29	8.13	8.12	7.52	5.29
244	2.62	4.21	1.95	5.18	5.19	5.78	3.51
245	7.35	5.79	6.60	7.62	7.79	6.73	5.90
Mean	**4.51**	**4.02**	**4.01**	**8.52**	**7.89**	**8.94**	**6.11**

Table B. 2. RMSE [ppm] of reconstructed wet refractivity profiles for different regularization schemes (DF scheme, epoch 00:00 UTC, location: profile of RS11035 launch)

DoY	Lndw+Arom	MART+ Arom	ART+ Arom	TV	Lndw+TV	MART+TV	ART+TV
232	3.18	1.90	2.05	3.37	3.42	4.04	2.78
233	4.43	2.32	2.66	6.54	6.44	4.50	4.00
234	3.96	2.54	2.12	4.82	4.35	2.66	2.11
235	2.92	2.26	2.19	8.64	8.72	6.48	4.46
236	2.23	2.86	2.96	7.19	6.99	4.39	3.21
237	7.37	4.57	4.77	6.92	6.91	7.75	5.11
238	3.84	2.96	3.68	9.74	9.22	7.66	7.48
239	7.74	3.81	3.75	8.64	8.43	9.74	6.07
240	2.56	1.33	2.66	11.84	11.87	9.20	4.69
241	4.75	4.46	4.87	10.87	10.87	8.02	6.80
242	3.65	3.73	5.00	8.46	10.23	8.95	7.08
243	3.46	1.51	3.03	9.66	9.57	4.50	4.70
244	2.64	2.39	1.83	7.29	7.31	5.16	4.41
245	4.54	4.37	4.93	5.39	5.41	6.05	5.15
Mean	**4.09**	**2.93**	**3.32**	**7.81**	**7.84**	**6.37**	**4.86**

Table B. 3. RMSE [ppm] of reconstructed wet refractivity profiles for different regularization schemes (SF scheme, epoch 12:00 UTC, location: profile of RS11035 launch)

DoY	Lndw+Arom	MART+ Arom	ART+ Arom	TV	Lndw+TV	MART+TV	ART+TV
232	9.36	6.20	7.01	10.44	9.61	6.40	5.67
233	9.07	6.33	6.68	7.40	6.10	8.95	4.91
234	9.00	8.12	6.58	6.69	7.39	6.74	7.59
235	4.08	5.98	9.12	5.79	5.62	7.68	7.68
236	4.51	2.74	11.22	8.38	8.24	2.05	12.38
237	5.10	2.76	8.37	7.01	7.55	4.70	8.78
238	8.80	6.15	8.08	10.87	11.25	7.10	10.59
239	8.35	6.23	4.43	8.60	7.39	3.66	4.43
240	7.93	5.37	18.17	14.75	15.66	9.26	18.77
241	6.40	7.32	5.49	6.24	6.23	6.61	3.21
242	3.76	1.95	9.66	6.36	7.01	8.47	8.85
243	4.52	3.41	19.38	7.08	6.87	5.91	17.78
244	9.35	7.93	8.60	5.54	6.72	4.52	7.04
245	4.41	4.71	8.33	10.03	9.27	6.59	8.25
Mean	**6.76**	**5.37**	**9.37**	**8.23**	**8.24**	**6.33**	**8.99**

Table B. 4. RMSE [ppm] of reconstructed wet refractivity profiles for different regularization schemes (DF scheme, epoch 12:00 UTC, location: profile of RS11035 launch)

DoY	Lndw+ Arom	MART+ Arom	ART+ Arom	TV	Lndw+TV	MART+TV	ART+TV
232	4.13	3.95	2.93	5.87	5.86	5.09	3.71
233	6.90	5.77	6.88	9.67	9.48	8.26	6.23
234	8.74	4.58	3.73	9.32	8.08	6.01	4.84
235	4.09	6.56	8.25	11.28	11.31	10.17	9.16
236	4.76	2.20	3.18	7.87	8.00	4.61	3.94
237	4.35	2.45	3.64	8.15	8.30	8.10	6.51
238	7.83	5.56	6.91	6.94	6.89	8.60	7.73
239	10.46	8.42	7.46	10.02	9.93	11.60	6.68
240	5.30	2.65	2.50	5.71	5.49	4.48	3.42
241	6.13	6.72	4.93	2.57	2.18	4.15	4.60
242	3.48	1.71	2.95	3.70	3.78	5.09	3.51
243	3.61	1.58	2.45	6.68	6.61	5.71	2.26
244	9.56	8.24	6.41	4.51	4.59	6.24	4.59
245	3.87	3.49	3.52	3.64	3.74	6.13	3.39
Mean	**5.94**	**4.56**	**4.69**	**6.85**	**6.73**	**6.73**	**5.04**

Appendix C

Supplementing Tables denoting the Accuracy of the reconstructed Wet refractivity Profiles in different temporal resolutions using TV and Landweber techniques

Table C. 1. RMSE of the wet refractivity field for different temporal resolutions during the entire study period using TV technique at hour 00:00 UTC for RS11035

Time-Res / DOY	10	20	30	40	50	60
232	1.94	3.52	4.88	3.67	3.40	3.62
233	6.88	6.65	7.83	6.04	7.78	6.00
234	6.41	5.51	4.55	4.30	3.48	3.61
235	5.57	7.19	7.79	7.48	5.06	3.31
236	7.02	7.83	5.00	4.27	5.24	4.40
237	6.68	6.76	7.57	7.12	6.98	6.75
238	5.95	5.19	5.30	4.28	4.99	5.21
239	5.39	9.32	6.96	6.06	6.05	4.76
240	5.65	5.52	5.71	5.81	5.84	6.48
241	5.53	4.50	5.22	4.73	6.18	6.09
242	7.28	12.39	13.31	12.54	12.30	9.56
243	8.98	14.10	15.07	6.84	7.03	4.96
244	13.57	13.30	10.06	6.64	5.84	4.64
245	8.02	7.44	7.60	5.91	5.13	4.80
Mean	**6.78**	**7.80**	**7.63**	**6.12**	**6.09**	**5.30**

Table C. 2. RMSE of the wet refractivity field for different temporal resolutions during the entire study period using Landweber technique at hour 00:00 UTC for RS11035

Time-Res / DOY	10	20	30	40	50	60
232	2.92	2.67	3.07	2.78	2.96	3.02
233	4.18	4.15	4.39	3.76	3.68	3.49
234	4.21	4.05	3.57	3.17	3.60	4.02
235	3.04	3.49	3.33	3.12	2.89	2.87
236	2.00	2.57	2.53	2.44	2.40	2.30
237	7.11	5.99	6.41	6.90	6.76	6.71
238	3.50	3.70	3.74	3.78	3.82	3.84
239	7.74	7.82	7.76	7.74	7.73	7.74
240	2.96	2.27	2.12	2.14	2.21	2.28
241	5.36	4.35	4.06	4.12	4.37	4.72
242	3.42	3.62	3.66	3.63	3.62	3.57
243	3.46	3.47	3.44	3.38	3.18	2.88
244	2.62	2.61	2.59	2.59	2.58	2.61
245	5.46	4.81	4.89	4.66	4.77	4.52
Mean	**4.14**	**3.97**	**3.97**	**3.87**	**3.90**	**3.90**

Table C. 3.RMSE of the wet refractivity field for different temporal resolutions during the entire study period using TV technique at hour 12:00 UTC for RS11035

Time-Res / DOY	10	20	30	40	50	60
232	4.82	3.64	3.00	4.83	3.90	3.57
233	2.84	2.62	5.52	6.18	4.77	4.45
234	4.11	4.10	6.62	6.95	6.25	5.37
235	7.39	8.93	11.31	7.93	5.52	5.08
236	5.60	8.02	4.53	4.09	3.77	3.45
237	7.25	6.67	6.58	6.21	6.97	6.12
238	6.47	7.92	6.07	6.38	6.61	6.64
239	6.79	7.66	7.06	6.48	5.64	5.83
240	7.85	5.91	7.94	7.08	7.03	6.86
241	7.26	3.39	4.30	3.85	3.29	3.08
242	3.93	4.51	4.23	3.81	3.42	3.28
243	6.85	5.44	5.48	5.30	5.50	5.63
244	4.19	2.96	4.39	3.70	2.81	4.43
245	4.79	4.83	4.27	4.26	4.20	3.65
Mean	**5.72**	**5.47**	**5.81**	**5.50**	**4.98**	**4.82**

Table C. 4. RMSE of the wet refractivity field for different temporal resolutions during the entire study period using Landweber technique at hour 12:00 UTC for RS11035

Time-Res / DOY	10	20	30	40	50	60
232	5.19	5.38	6.00	5.83	4.28	5.13
233	4.10	4.67	4.87	4.82	4.77	4.69
234	6.87	7.52	8.46	8.58	7.40	7.24
235	5.67	5.66	5.63	5.60	5.57	5.56
236	3.33	3.38	3.33	3.31	3.48	3.30
237	11.40	11.72	11.70	11.04	10.49	10.37
238	9.17	9.18	9.10	8.67	8.76	8.73
239	10.15	9.97	9.43	8.97	8.66	8.01
240	3.08	3.14	4.19	4.30	4.17	4.01
241	7.50	7.12	7.29	7.20	6.45	6.34
242	3.40	4.33	3.46	3.84	4.31	4.50
243	4.49	3.93	4.15	4.50	4.46	4.21
244	7.95	7.72	7.39	7.02	6.86	6.79
245	3.38	3.47	3.24	3.14	3.03	2.99
Mean	**6.12**	**6.23**	**6.30**	**6.20**	**5.91**	**5.85**

Appendix D

Supplementing Tables denoting the Accuracy of the reconstructed Wet refractivity Profiles using different ray-tracing methods with and without Considering Topography in the Tomography Model

Table D. 1. RMSE [mm/km] of wet refractivity profile for different schemes during the time of interest at epoch (12H: 00M in UTC) for RS10548

DoY	Eikonal +Topo	Eikonal (N=1) + Topo	Straight line [UTM+Topo]	Straight line [NEU+Topo]	Eikonal	Eikonal (N=1)	Straight line [UTM]	Straight line [NEU]
160	1.045	1.996	2.009	2.585	1.658	2.017	2.780	3.282
161	1.097	1.728	2.127	2.364	1.648	2.034	2.672	2.658
162	0.952	1.874	1.969	2.317	1.358	1.894	2.505	2.948
163	1.610	2.066	2.616	2.812	1.975	2.619	2.978	3.113
164	2.075	2.409	2.767	3.185	2.489	2.784	3.156	3.528
165	1.604	2.097	2.158	2.529	2.045	2.185	2.507	2.936
166	1.206	1.957	2.001	2.353	1.598	2.237	2.580	2.709
167	2.439	2.865	3.268	3.821	2.620	2.808	3.750	3.908
168	2.478	2.638	2.993	3.301	2.868	3.254	3.442	3.595
169	2.796	3.140	3.292	3.750	3.196	3.433	3.778	3.999
170	2.697	2.885	3.504	3.643	3.177	3.578	3.834	4.109
171	1.924	2.302	2.749	3.135	2.219	2.886	3.020	3.467
172	1.674	1.984	2.065	2.108	1.826	2.011	2.149	2.308
173	1.096	1.731	1.916	2.291	1.483	2.219	2.440	2.664
174	2.540	2.957	3.943	4.646	3.137	3.984	4.385	4.996
175	1.971	2.512	2.550	2.769	2.305	2.504	2.724	3.008
176	1.765	2.004	2.096	2.101	2.089	2.186	2.303	2.527
MEAN [ppm]	**1.822**	**2.302**	**2.589**	**2.924**	**2.217**	**2.626**	**3.000**	**3.279**

Table D. 2.RMSE [mm/km] of wet refractivity profile for different schemes during the time of interest at epoch (00H: 00M in UTC) for RS10771

DoY	Eikonal +Topo	Eikonal (N=1) + Topo	Straight line [UTM+Topo]	Straight line [NEU+Topo]	Eikonal	Eikonal (N=1)	Straight line [UTM]	Straight line [NEU]
160	1.722	1.822	2.232	2.435	2.080	2.380	2.712	2.939
161	1.960	2.413	2.599	2.990	2.333	2.816	3.039	3.272
162	1.148	1.696	1.934	2.222	1.685	1.852	2.355	2.858
163	2.539	2.812	3.186	3.200	2.975	3.090	3.363	3.696
164	2.131	2.839	3.222	3.595	2.586	2.928	3.672	3.904
165	1.439	2.007	2.093	2.648	1.700	2.193	2.892	2.920
166	2.307	2.692	3.180	3.240	2.518	2.812	3.743	3.887
167	2.378	2.847	3.691	3.990	2.767	2.974	3.809	4.321
168	2.366	2.646	3.307	3.544	2.679	2.902	3.539	3.845
169	2.578	2.828	3.016	3.108	2.973	3.073	3.328	3.659
170	1.442	2.002	2.122	2.459	1.864	2.307	2.658	2.744
171	2.464	2.763	3.194	3.659	2.976	3.468	3.520	4.503
172	1.138	1.950	1.996	2.037	1.803	2.132	2.189	2.604
173	1.417	1.765	1.824	1.953	1.693	2.011	2.417	2.562
174	1.481	1.820	1.959	2.153	1.715	2.104	2.233	2.567
175	1.273	1.726	1.803	1.903	1.757	2.079	2.224	2.321
176	1.333	1.688	1.933	2.131	1.798	1.822	2.374	2.548
MEAN [ppm]	**1.830**	**2.254**	**2.546**	**2.780**	**2.229**	**2.526**	**2.945**	**3.244**

Table D. 3. RMSE [mm/km] of wet refractivity profile for different schemes during the time of interest at epoch (12H: 00M in UTC) for RS10771

DoY	Eikonal +Topo	Eikonal (N=1) + Topo	Straight line [UTM+Topo]	Straight line [NEU+Topo]	Eikonal	Eikonal (N=1)	Straight line [UTM]	Straight line [NEU]
160	1.504	1.819	2.031	2.517	1.962	2.282	2.410	2.969
161	1.410	1.598	2.121	2.227	1.975	2.212	2.670	2.808
162	1.590	1.801	1.960	2.163	1.790	2.136	2.522	2.671
163	1.985	2.360	2.497	2.814	2.313	2.524	2.729	3.056
164	1.985	2.467	2.760	3.134	2.561	3.158	3.343	3.525
165	1.299	2.260	2.505	2.691	1.956	2.553	2.774	2.995
166	2.596	2.740	3.062	3.567	2.951	3.017	3.756	3.888
167	2.680	3.066	3.427	3.694	3.226	3.408	4.292	4.504
168	2.874	3.217	3.495	3.853	3.472	3.625	3.922	4.339
169	1.645	1.942	2.266	2.531	2.146	2.333	2.569	2.904
170	2.102	2.413	2.740	2.882	2.663	2.887	3.026	3.206
171	2.913	3.438	3.864	3.987	3.562	3.823	4.149	4.223
172	1.648	1.908	2.004	2.145	1.723	1.946	2.374	2.576
173	1.787	2.255	2.340	2.522	2.280	2.970	3.003	3.095
174	2.015	2.664	2.706	3.323	2.639	2.826	3.031	3.700
175	1.561	2.035	2.416	2.495	2.061	2.697	2.717	2.773
176	2.264	2.680	2.927	2.953	2.754	2.972	3.445	3.773
MEAN [ppm]	**1.992**	**2.392**	**2.654**	**2.912**	**2.473**	**2.786**	**3.102**	**3.353**

Acronyms

ART Algebraic Reconstruction Technique

CDDIS Crustal Dynamics Data Information System

CNES Centre National d'Etudes Spatiales

DD Double Difference

DF Dual Frequency

DOY Day of Year

ECEF Earth-Centered, Earth-Fixed

ECMWF European Centre for Medium-Range Forecast

EPOSA Echzeit Positionierung Austria

ERA5 ECMWF Re-Analysis Version 5

ERA-Interim ECMWF Re-Analysis product

EVN Energie Versorgung Niederösterreich

GIM Global Ionosphere Model

GMF Global Mapping Function

GNSS Global Navigation Satellite Systems

GPT3 Global Pressure Temperature 3

GLONASS Globalnaya Navigatsionnaya Sputnikovaya Sistema

GPS Global Positioning System

GEOS-R Geostationary Operational Environmental Satellite-R Series

IDW Inverse Distance Weighting

GID Gaussian Inverse Distance

IF LC Ionosphere-Free Linear Combination

IFK Fredholm integral of the first kind

IGS International GNSS Service

ITRF International Terrestrial Reference Frame

MAE Mean Absolute Error

MART Multiplicative ART

MRI Magnetic Resonance Imaging

NRT Near-Real Time

NWM Numerical Weather Model

PPP Precise Pointe Positioning

RINEX Receiver Independent Exchange Format

RMSE Root Mean Square

RE Relative Error

RO Radio Occultation

RTK Real-Time Kinematic

SEID Satellite-Specific Epoch-Differenced Ionospheric Delay Model

SF Single-Frequency

SHD Slant Hydrostatic Delay

STD Slant Total Delay

Std Standard deviation

SWD Slant Wet Delay

TV Total Variation

VMF Vienna Mapping Function

ZHD Zenith Hydrostatic Delay

ZTD Zenith Total Delay

ZWD Zenith Wet Delay

List of Tables

Table 2. 1. Key characteristics of different techniques and instrument to measure the water vapour (table adapted from (Champollion et al., 2005;Heublein, 2019;Sá, 2018) 8

Table 2. 2. Input parameters for NMF, IMF and VMF mapping functions 15

Table of Figures

Bibliography

Adavi, Z., and Mashhadi-Hossainali, M.: 4D-Tomographic Reconstruction of the Tropospheric Wet Refractivity Using the Concept of Virtual Reference Station, Case Study: North West of Iran, Meteoroloy and Atmospheric Physics, 125, 10.1007/s00703-014-0342-4, 2014.

Adavi, Z., and Mashhadi-Hossainali, M.: 4D-tomographic reconstruction of water vapor using the hybrid regularization technique with application to the North West of Iran, Advances in Space Research, 55, 1845–1854, 10.1016/j.asr.2015.01.025, 2015.

Adavi, Z., and Weber, R.: Evaluation of Virtual Reference Station Constraints for GNSS Tropospheric Tomography in Austria Region, Advances in Geosciences, 50, 39-48, 10.5194/adgeo-50-39-2019, 2019.

Adavi, Z., Rohm, W., and Weber, R.: Analyzing Different Parameterization Methods in GNSS Tomography Using the COST Benchmark Dataset, IEEE Journal of Selected Topics in Applied Earth Observations and Remote Sensing, 13, 6155-6163, 0.1109/JSTARS.2020.3027909, 2020.

Adavi, Z., and Weber, R.: Application of the Total Variation Method in near real-time GNSS Tropospheric Tomography [under review], International Association of Geodesy Symposia, 2022.

Adavi, Z., Weber, R., and Glaner, M. F.: Assessment of regularization techniques in GNSS tropospheric tomography based on single- and dual-frequency observations, GPS Solutions, 26, https://doi.org/10.1007/s10291-021-01202-2, 2022a.

Adavi, Z., Weber, R., and Rohm, W.: Pre-analysis of GNSS tomography Solution using the concept of Spread of Model Resolution Matrix, Journal of Geodesy, 10.1007/s00190-022-01620-1, 2022b.

Aichinger-Rosenberger, M.: Tropospheric delay parameters derived from GNSS-tracking data of a fast-moving fleet of trains, PhD. Dissertation, Department of Geodesy and Geoinformation, TU Wien, 187 pp., 2021.

Al-Shaery, A., Lim, S., and Rizos, C.: Investigation of Different Interpolation Models Used in Network-RTK for the Virtual Reference Station Technique, Journal of Global Positioning Systems, 10, 136-148, 10.5081/jgps.10.2.136, 2011.

Alkhalifah, T., and Fomel, S.: Implementing the fast marching Eikonal solver: Spherical versus Cartesian coordinates, Geophys. Prospect., 49, 165–178, 2001.

Alves, D. B. M., Sapucci, L. F., Marques, H. A., de Souza, E. M., Gouveia, T. A. F., and Magário, J. A.: Using a regional numerical weather prediction model for GNSS positioning over Brazil, GPS Solutions, 20, 677–685 https://doi.org/10.1007/s10291-015-0477-x, 2016.

Andrisaniand, A., and Francesco, V.: Humidity Profiles Retrieved From GNSS Radio Occultations by a Non-negative Residual Constrained Least Square Error Method Frontiers in Earth Science 8, 10.3389/feart.2020.00320 2020.

Aster, R., Borchers, B., and Thurber, C.: Parameter Estimation and Inverse Problems, International Geophysics Series, edited by: DMOWSKA, R., HOLTON, J. R., and ROSSBY, H. T., Elsevier Academic Press., 316 pp., 2005.

Bai, Z.: Near-Real-Time GPS Sensing of Atmospheric Water Vapour, PhD. Dissertation, Built Environment and Engineering, Queensland University of Technology, 169 pp., 2004.

Bastin, S., Champollion, C., Bock, O., Drobinski, P., and Masson, F.: Diurnal cycle of water vapor as documented by a dense GPS network in a coastal area during ESCOMPTE IOP2, Journal of Applied Meteorology and Climatology, 46, 167-182, 2007.

Bender, M., and Raabe, A.: Preconditions to ground based GPS water vapour tomography, Ann. Geophys, 25, 1727-1734, 2007.

Bender, M., Dick, G., Ge, M., Deng, Z., Wickert, J., Kahle, H.-G., Raabe, A., and Tetzlaff, G.: Development of a GNSS water vapour tomography system using algebraic reconstruction techniques, Advances in Space Research, 47, 1704-1720, 10.1016/j.asr.2010.05.034, 2011.

Benevides, P., Nico, G., Catalão, J., and Miranda, P. M. A.: Inclusion of high resolution MODIS maps on a 3D tropospheric water vapor GPS tomography model, SPIE 9640, Remote Sensing of Clouds and the Atmosphere XX, 96400R, Toulouse, France, 2015a.

Benevides, P., Nico, G., Catalão, J., and Miranda, P. M. A.: Merging SAR interferometry and GPS tomography for high-resolution mapping of 3D tropospheric water vapour, IEEE International Geoscience and Remote Sensing Symposium (IGARSS), Milan, 2015b.

Bevis, M., Businger, S., Herring, T., Rocken, C., R.A., A., and Ware, R. H.: GPS meteorology: remote sensing of atmospheric water vapor using the Global Positioning System, Journal of Geophysical Research, 97 (D14), 15787–15801, 1992.

Bi, Y., Mao, J., and Li, C.: Preliminary Results of 4-D Water Vapor Tomography in the Troposphere Using GPS, Advances in Atmospheric Sciences, 23, 551-560, 2006.

Bock, O., Tarniewicz, J., Thom, C., and Pelon, J.: Effect of small-scale atmospheric inhomogeneity on positioning accuracy with GPS, Geophysical Research Letters, 28, 2289-2292, 10.1029/2000GL011985, 2001.

Böhm, J., and Schuh, H.: Vienna Mapping Functions in VLBI analyses, Geophysical Research Letters, 10.1029/2003GL018984, 2004a.

Böhm, J., and Schuh, H.: Vienna Mapping Functions in VLBI analyses, Geophys Res Lett, 10.1029/2003GL018984, 2004b.

Böhm, J., Niell, A. E., Tregoning, P., and Schuh, H.: Global Mapping Function (GMF): A new empirical mapping function based on numerical weather model data, Geophysical Research Letters, 33, 10.1029/2005GL02554, 2006a.

Böhm, J., Werl, B., and Schuh, H.: Troposphere mapping functions for GPS and VLBI from ECMWF operational analysis data, Geophysical Research Letters, 111, 10.1029/2005JB003629, 2006b.

Born, M., and Wolf, E.: Principles of Optics, edited by: 7th, Cambridge Univ. Press, New York., 1999.

Braun, J. J., and Rocken, C.: Water vapor tomography within the planetary boundary layer using GPS, International Workshop on GPS Meteorology, Tsukuba, Japan, 2003, 3-09-01-04,

Braun, J. J., Rocken, C., and Liljegren, J.: Comparisons of line-of-sight water vapor observations using the global positioning system and a pointing microwave radiometer, Journal of Atmospheric and Oceanic Technology, 20, 606-612, 2003.

Braun, J. J.: Remote Sensing of Atmospheric Water Vapor with the Global Positioning System, PhD. Dissertation, Department of Aerospace Engineering Sciences, University of Colorado, 137 pp., 2004.

Brenot, H., Walpersdorf, A., Reverdy, M., van Baelen, J., Ducrocq, V., Champollion, C., Masson, F., Doerflinger, E., Collard, P., and Giroux, P.: A GPS network for tropospheric tomography in the framework of the Mediterranean hydrometeorological observatory Cévennes-Vivarais (southeastern France), Atmospheric Measurement Techniques, 7, 553-578, 10.5194/amt-7-553-2014, 2014.

Brenot, H., Rohm, W., Kačmařík, M., Möller, G., Sá, A., Tondaś, D., Rapant, L., Biondi, R., Manning, T., and Champollion, C.: Cross-validation of GPS tomography models and methodological improvements using CORS network, Atmospheric Measurement Techniques Discussions, 2018, 1-42, 10.5194/amt-2018-292, 2018.

Brenot, H., Rohm, W., Kačmařík, M. M., G., Sá, A., Tondaś, D., Rapant, L., Biondi, R., Manning, T., and Champollion, C.: Cross-Comparison and Methodological Improvement in GPS Tomography, Remote Sensing, 12, 2020.

Cai, G., Chen, B. M., and Lee, T. H.: Unmanned Rotorcraft Systems, Springer, 2011.

Carlomusto, M.: GOES-R Series Product Definition and User's Guide (PUG), Volume 5: Level 2 + Products, GOES-R/Code 416, 726, 2019.

Cerveny, V.: Seismic Ray Theory, Cambridge Univ. Press,New York., 713 pp., 2005.

Champollion, C.: GPS Tomography of Tropospheric Water Vapour Measurements - Application to Intense Precipitations Quantification de la vapeur d'eau troposphérique par GPS (modèles 2D et tomographies GPS) - Application aux précipitations intenses, PhD. Dissertation, Université Montpellier II - Sciences et Techniques du Languedoc, 2005.

Champollion, C., Masson, F., Bouin, M. N., Walpersdorf, A., Doerflinger, E., Bock, O., and van Baelen, J.: GPS water vapour tomography: preliminary results from the ESCOMPTE field experiment, Atmospheric Research, 74, 253-274, 10.1016/j.atmosres.2004.04.003, 2005.

Champollion, C., Flamant, C., Bock, O., Masson, F., Turner, D. D., and Weckwerth, T.: Mesoscale GPS tomography applied to the 12 June 2002 convective initiation event of IHOP_2002, Quarterly of the Royal Meteorology Society 135, 645-662, 10.1002/qj.386, 2009, 2009.

Chen, B., and Liu, Z.: Voxel-optimized regional water vapor tomography and comparison with radiosonde and numerical weather model, Journal of Geodesy, 88, 691–703, 10.1007/s00190-014-0715-y, 2014.

Chen, G., and Herring, T. A.: Effects of atmospheric azimuthal asymmetry on the analysis of space geodetic data, Geophysical Research, 102, 20489-20502, 10.1029/97JB01739 1997.

Collins, S., James, R., Ray, P., Chen, K., Angie Lassman, A., & Brownlee, J.: Grids in Numerical Weather and Climate Models, Climate Change and Regional/Local Responses, edited by: Zhang, Y., and Ray, P., IntechOpen, London, 2013.

CORS https://geodesy.noaa.gov/CORS/standard1.shtml, access: 2022-01-24, 2022.

Cros, B., Durand, P., Cachier, H., Drobinsk, P., Fréjafon, E., Kottmeier, C., Perros, P. E., Peuch, V.-H., Ponche, J.-L., Robin, D., Saïd, F., Toupance, G., and Wortham, H.: The ESCOMPTE program: an Overview., Atmospheric Research, 69, 241-279, 2004.

Dach, R., Lutz, S., Walser, P., and Fridez, P.: Bernese GNSS Software Version 5.2, Astronomical Institute, University of Bern, 2015.

Davis, J. L., Herring, T. A., Shapiro, I. I., Rogers, E. E., and Elgered, G.: Geodesy by radio interferometry: effects of atmospheric modeling errors on estimates of baseline length, Radio Science, 20, 1593–1607, 1985.

Davis, J. L., Elgered, G., Niell, A. E., and Kuehn, C. E.: Ground-based measurements of the gradients in the 'wet' radio refractivity of air, Radio Science, 28, 1003-1018, 1993.

Defrise, M., Vanhove, C., and Liu, X.: An algorithm for total variation regularization in high-dimensional linear problems, Inverse Problems, 27, 065002, 10.1088/0266-5611/27/6/065002, 2011.

Deng, Z., Bender, M., Dick, G., Ge, M., Wickert, J., Ramatschi, M., and Zou, X.: Retrieving tropospheric delays from GPS networks densified with single frequency receivers, Geophysical Research Letters, 36, 10.1029/2009gl040018., 2009.

Dick, G., Gendt, G., and Reigber, C.: First experience with near real-time water vapor estimation in a German GPS network, Journal of Atmospheric and Solar-Terrestrial Physics, 63, 1295-1304, 2001.

Ding, N., Zhang, S., and Zhang, Q.: New parameterized model for GPS water vapor tomography, Annales Geophysicae, 35, 311-323, 10.5194/angeo-35-311-2017, 2017.

Dodson, A. H., Shardlow, P. J., Hubbard, L. C. M., Elgered, G., and Jarlemark, P. O. J.: Wet tropospheric effects on precise relative GPS height determination, Journal of Geodesy, 70, 188-202, 10.1007/bf00873700, 1996.

Douša, J.: Evaluation of tropospheric parameters estimated in various routine GPS analysis, Physics and Chemistry of the Earth, 29, 167-175, 2004.

Douša, J., Dick, G., Kačmařík, M., Brožková, R., Zus, F., Brenot, H., Stoycheva, A., Möller, G., and Kaplon, J.: Benchmark campaign and case study episode in central Europe for development and assessment of advanced GNSS tropospheric models and products, Atmospheric Measurement Techniques, 9, 2989-3008, 2016.

Dowling, T. E., and Showman, A. P.: CHAPTER 9 - Earth as a Planet: Atmosphere and Oceans, in: Encyclopedia of the Solar System (Second Edition), edited by: McFadden, L.-A., Weissman, P. R., and Johnson, T. V., Academic Press, San Diego, 169-188, 2007.

Elfving, T., Nikazad, T., and Hansen, P. C.: Semi- Convergence and Relaxation Parameters for a Class of SIRT Alogorithms, Electronic Transactions on Numerical Analysis, 37, 321-336, 2010.

Elfving, T., Hansen, P. C., and Nikazad, T.: Semi-Convergence and relaxation parameters for projected SIRT algorithms, Journal on Scientific Computing, 34, A2000-A2017, 2012.

Elgered, G., Davis, J. L., Herring, T. A., and Shapiro, I. I.: Geodesy by Radio Interferometry: Water Vapour Radiometry for Estimation of the Wet Delay, Journal of Geophysical Research, 10.1029/90JB00834, 1991, 1991.

Elósegui, P., Ruis, A., Davis, J. L., Ruffini, G., Keihm, S. J., Bürki, B., and Kruse, L. P.: An experiment for estimation of the spatial and temporal variations of water vapor using GPS data, Physics and Chemistry of the Earth, 23, 125-130, https://doi.org/10.1016/S0079-1946(97)00254-1, 1998.

eo Sharing Earth Observation Resources: https://directory.eoportal.org/web/eoportal/satellite-missions/g/goes-r, access: 2022-01-24, 2022.

Fleagle, R. G., and Businger, J. A.: An Introduction to Atmospheric Physics, edited by: ed., n., Academic Press, 1980.

Flores, A.: Atmospheric Tomography Using Satellite Radio Signals, PhD. Dissertation, de Teoria del Senyal i Comunicacions, Politècnica de Catalunya, Barcelona, 1999.

Flores, A., Gradinarsky, L. P., El´osegui, P., Elgered, G., Davis, J. L., and Rius, A.: Sensing atmospheric structure: Tropospheric tomographic results of the small-scale GPS campaign at the Onsala Space Observatory, Earth Planets Space, 52, 941-945, 2000a.

Flores, A., Ruffini, G., and Rius, A.: 4D Tropospheric Tomography using GPS Slant Wet Delays, Annales Geophysicae, 18, 223-234, 10.1007/s00585-000-0223-7, 2000b.

Gegout, P., Oberlé, P., Desjardins, C., Moyard, J., and Brunet, P.-M.: Ray-Tracing of GNSS Signal Through the Atmosphere Powered by CUDA, HMPP and GPUs Technologies, IEEE Journal of Selected Topics in Applied Earth Observations and Remote Sensing, 7, 1592-1602, 10.1109/JSTARS.2013.2272600, 2014.

Ghafari Razin, M.-R., and Voosoghi, B.: Estimation of tropospheric wet refractivity using tomography method and artifcial neural networks in Iranian case study, GPS Solutions, 24, https://doi.org/10.1007/s10291-020-00979-y, 2020.

Ghoddousi-Fard, R.: Modelling tropospheric gradients and parameters from NWP models, PhD. Dissertation, Department of Geodesy and Geomatics Engineering, University of New Brunswick, 244 pp., 2009.

Golub, G. H., and Matt, U.: Generalized Cross-Validation for Large Scale Problems, 1996.

Gordon, R., Bender, R., and Herman, G. T.: Algebraic Reconstruction Techniques (ART) for Three-dimensional Electron microscopy and X-ray Photography, Journal of Theoretical Biology 29, 471-481, 1970.

Gordon, R.: A Tutorial on ART (Algebraic Reconstruction Techniques), IEEE Transactions on Nuclean Science, NS-21, 1974.

Gradinarsky, L., and Jarlemark, P.: Ground-based GPS tomography of water vapour: Analysis of simulated and real data, Journal of the Meteorological Society of Japan, 82, 551-560, 2004.

Grewal, M. S., Weill, R. L., and Andrews, A. P.: Global Positioning Systems, Inertial Navigation, and Integration, edited by: 2nd, Wiley, 2007.

Guerova, G.: Application of GPS derived water vapour for Numerical Weather Prediction in Switzerland, PhD. Dissertation, Institute of Applied Physics, University of Bern, 2003.

Guo, J., Yang, F., Shi, J., and Xu, C.: An Optimal Weighting Method of Global Positioning System (GPS) Troposphere Tomography, IEEE Journal of Selected Topics in Applied Earth Observations and Remote Sensing, PP, 1 - 8, 10.1109/JSTARS.2016.2546316, 2016.

Haase, J., Ge, M., Vedel, H., and Calais, E.: Accuracy and Variability of GPS Tropospheric Dealy Measurements of Water Vapor in the Western Mediterranean, Journal of Applied Meteorology, 42, 1547-1568, 2003.

Haji Aghajany, S., and Amerian, Y.: Three dimensional ray tracing technique for tropospheric water vapor tomography using GPS measurements, Journal of Atmospheric and Solar-Terrestrial Physics 164, 81-88, https://doi.org/10.1016/j.jastp.2017.08.003, 2017.

Haji Aghajany, S., Amerian, Y., and Verhagen, S.: B-spline function-based approach for GPS tropospheric tomography, GPS Solutions, 24, 2020.

Hall, C. M., Hansen, G., Sigernes, F., and Kuyeng Ruiz, K. M.: Tropopause height at 78° N 16° E: average seasonal variation 2007–2010, Atmospheric Chemistry and Physics, 11, 5485-5490, 10.5194/acp-11-5485-2011, 2011.

Hanna, N., Trzcina, E., Möller, G., Rohm, W., and Weber, R.: Assimilation of GNSS tomography products into WRF using radio occultation data assimilation operator, Atmospheric Measurement Techniques Discussions, 2019, 1-32, 10.5194/amt-2018-419, 2019.

Hansen, P. C.: Rank-Deficient and Discrete ILL-Posed Problems:Numerical Aspect of Linear Inversion., edited by: SIAM, Philadelphia, 264 pp., 1998.

Herrera, A. M., Suhandri, H. F., Realini, E., Reguzzoni, M., and De Lacy, M. C.: goGPS: Open-Source MATLAB Software, GPS Solutions, 20, 595–603, https://doi.org/10.1007/s10291-015-0469-x, 2016.

Herring, T. A.: Modeling atmospheric delays in the analysis of space geodetic data, Refraction of transatmospheric signals in geodesy, 157-164, 1992.

Herschke, P. M.: Modeling and extrapolation of path delays in GPS signals, MSc. Dissertation, Department of Physics, ETH,Swiss Federal Institute of Technology, 2002.

Heublein, M.: GNSS and InSAR based water vapor tomography: A Compressive Sensing solution, PhD. Dissertation, Institute of Photogrammetry and Remote Sensing, Karlsruhe Institute of Technology, Germany., 134 pp., 2019.

Hirahara, K.: Local GPS tropospheric tomography, Earth Planets Space, 52, 935-939, 2000.

Hobiger, T., Ichikawa, R., Koyama, Y., and Kondo, T.: Fast and accurate ray-tracing algorithms for real-time space geodetic applications using numerical weather models, Journal of Geophysical Research, 113, 10.1029/2008JD010503, 2008.

Hofmeister, A.: Determination of path delays in the atmosphere for geodetic VLBI by means of ray-tracing, PhD. Dissertation, Department of Geodesy and Geoinformation, Technical university of Vienna Vienna, 309 pp., 2016.

Hopfield, H. S.: Two-quartic tropospheric refi·activity profile for correcting satellite data, Journal of Geophysical Research, 74, 4487-4499, 1969.

Hopfield, H. S.: Tropospheric effect on electromagnetically measured range: Prediction from surface weather data, Radio Science, 6, 357-367, 1971.

Hopfield, H. S.: Tropospheric refraction effects on satellite range measurements, APL Technical Digest, 11, 11-21, 1972.

Hoyle, V. A.: Data Assimilation for 4-D Wet Refractivity Modelling in a Regional GPS Network, MSc. Dissertation, Department of Geomatics Engineering, Calgary,Alberta,Canada., 190 pp., 2005.

Hurter, F., Geiger, A., Perler, D., and Rothacher, M.: GNSS water vapor monitoring in the Swiss Alps, IEEE International Geoscience and Remote Sensing Symposium, 2012, 1972-1975,

Ifadis, I. M.: The excess propagation path of radio waves: Study of the influence of the atmospheric parameters on its elevation dependence, Survey Review, 31, 289-298, 1992.

Jaberi Shafei, M., and Mashhadi-Hossainali, M.: Application of the GPS reflected signals in tomographic reconstruction of the wet refractivity in Italy, Journal of Atmospheric and Solar-Terrestrial Physics, 207, https://doi.org/10.1016/j.jastp.2020.105348, 2020.

Jang, J., and Hong, S. Y.: Comparison of nonhydrostatic and hydrostatic dynamical cores in two regional models using the spectral and finite difference methods: dry atmosphere simulation, Meteorol. Atmos.Phys., 128, 229–245, https://doi.org/10.1007/s00703-015-0412-2, 2016.

Jensen, T. L., Jørgensen, J. H., Hansen, P. C., and Jensen, S. H.: Implementation of an optimal first-order method for strongly convex total variation regularization, BIT Numerical Mathematics, 52, 329-356, https://doi.org/10.1007/s10543-011-0359-8, 2012.

Jia, R., Yu, X., Xing, J., Ning , Y., and Sun, H.: An improved method using adaptive smoothing for GNSS tomographic imaging of ionosphere, PLoS ONE, 15, https://doi.org/10.1371/journal.pone.0250613, 2021.

Jones, J., Guerova, G., Dousa, J., Dick, G., de Haan, S., Pottiaux, E., Bock, O., and Pacione, R.: COST Action ES1206: GNSS4SWEC-Advanced GNSS Tropospheric Products for Severe Weather Events and Climate, in: EGU General Assembly Conference Abstracts, 2018.

Kačmařík, M., and Rapant, L.: New GNSS tomography of the atmosphere method – proposal and testing, Geoinformatics FCE CTU, 12, 63-76, https://doi.org/10.14311/gi.9.6, 2012.

Kak, A. C., and Slaney, M.: Principles of Computerized Tomographic Imaging, The Institute of Electrical and Electronics Engineers, New York., 1999.

Kaltenbacher, B., Neubauer, A., and Scherzer, O.: Iterative Regularization Methods for Nonlinear Ill-Posed Problems, 2008.

Karl, W. C.: Regularization in Image Restoration and Reconstruction, in: Handbook of Image and Video Processing, 2nd ed., edited by: Bovik, A. L., New York, NY, USA: Elsevier, 183-202, 2005.

Kleijer, F.: Troposphere Modeling and Filtering for Precise GPS Leveling, PhD. Dissertation, TU Delft, 278 pp., 2004.

Krietemeyer, A., Ten Veldhuis, M.-c., Van der Marel, H., Realini, E., and Van de Giesen, N.: Potential of Cost-Efficient Single Frequency GNSS Receivers for Water Vapor Monitoring, Remote Sensing, 10, 10.3390/rs10091493, 2018.

Kunitsyn, V. E., and Tereshchenko, E. D.: Ionospheric Tomography, Springer, Berlin, 2003.

Landskron, D.: Modeling tropospheric delays for space geodetic techniques, PhD. Dissertation, Department of Geodesy and Geoinformation, TU Wien, 188 pp., 2017.

Landskron, D., and Böhm, J.: VMF3/GPT3: refined discrete and empirical troposphere mapping functions, Journal of Geodesy, 92, 349-360, 10.1007/s00190-017-1066-2, 2018.

Landweber, L.: An iteration formula for Fredholm integral equations of the first kind, American Journal of Mathematics, 73, 615–624, 1951.

Ledoux, H., and Gold, C.: An Efficient Natural Neighbour Interpolation Algorithm for Geoscientific Modelling, in: Developments in Spatial Data Handling, Springer, Berlin/Heidelberg, Germany, 97-108, 2005.

Lee, J. K., Kamalabadi, F., and Makela, J. J.: Localized three-dimensional ionospheric tomography with GPS ground receiver measurements, Radio Science, 42, 10.1029/2006RS003543, 2007.

Li, C.: An Efficient Algorithm For Total Variation Regularization with Applications to the Single Pixel Camera and Compressive Sensing, MSc. Dissertation, Rice University, 2009.

Lohvithee, M.: Iterative Reconstruction Technique for Cone-beam Computed Tomography with Limited Data, Ph.D. Dissertation, Department of Electrical and Electronic Engineering, University of Bath, 2019.

Lutgens, F. K., Tarbuck , E. J., and Herman, R. L.: The Atmosphere – An Introduction to Meteorology, Prentice-Hall, Englewood Cliffs, New Jersey, edited by: Edition, F., Pearson, New York, 1912 pp., 2018.

Lutz, S. M.: High-resolution GPS tomography in view of hydrological hazard assessment, PhD. Dissertation, ETH Zurich, 219 pp., 2008.

Maercklin, N.: Seismic structure of the Arava Fault, Dead Sea Transform, PhD, Potsdam : Deutsches GeoForschungsZentrum GFZ, 142 pp., 2004.

Manning, T., Zhang, K., Rohm, W., Choy, S., and Hurter, F.: Detecting Severe Weather using GPS Tomography: An Australian Case Study, Journal of Global Positioning Systems, 11, 58-70, 10.5081/jgps.11.1.58, 2012.

Manning, T.: Sensing the dynamics of severe weather using 4D GPS Tomography in the Australian region, PhD. Dissertation, School of Mathematical and Geospatial Sciences College of Science, Engineering and Health, Royal Melbourne Institute of Technology (RMIT) University, 2013.

Marini, J. W.: Correction of satellite tracking data for an arbitrary tropospheric profile, Radio Science, 7, 223-231, 1972.

Meindl, M., Schaer, S., Hugentobler, U., and Beutler, G.: Tropospheric gradient estimation at code: Results from global solutions, Journal of the Meteorological Society of Japan, 82, 331–338, 2004.

Mendes, V. B.: Modeling the Neutral Atmosphere Propagation Delay in Radiometric Space Techniques, PhD. Dissertation, Department of Geodesy and Geomatics Engineering, University of New Brunswick, 1999.

Michelini, A., and McEvilly, T.: Seismological studies at Parkfield. I. Simultaneous inversion for velocity structure and hypocenters using cubic B-splines parameterization, Bulletin of the Seismological Society of America, 81, 524-552, 1991.

Miller, C. R., and Routh, P. S.: Resolution analysis of geophysical images: Comparison between point spread function and region of data influence measures, Geophys. Prospect., 55, 835–852, 10.1111/j.1365-2478.2007.00640.x, 2007.

Millman, R. S., and Parker, G. D.: Elements of Differential Geome-try, Prentice-Hall, Upper Saddle River, N. J, 1979.

Möller, G.: Reconstruction of 3D wet refractivity fields in the lower atmosphere along bended GNSS signal paths, PhD. Dissertation, TU Wien, 2017.

Möller, G., and Landskron, D.: Atmospheric bending effects in GNSS tomography, Atmospheric Measurement Techniques, 12, 23-34, 10.5194/amt-12-23-2019, 2019.

Moore, D. S., Notz, W. I., and Fligner, M. A.: The Basic Practice of Statistics, edited by: Edition, t., 2013.

ERA5-Land hourly data from 1981 to present. Copernicus Climate Change Service (C3S) Climate Data Store (CDS): https://cds.climate.copernicus.eu/cdsapp#!/dataset/reanalysis-era5-land?tab=overview, access: 2022-02-09 2022.

Nafisi, V., Madzak, M., Böhm, J., Ardalan, A. A., and Schuh, H.: Ray-traced tropospheric delays in VLBI analysis, Radio Science, 47, 1-17, 10.1029/2011RS004918, 2012.

Natterer, F.: The Mathematics of Computerized Tomography, Wiley, New York, 245 pp., 1986.

Niell, A. E.: Global mapping functions for the atmosphere delay at radio wavelengths, Geophysical Research, 101, 3227-3246, 1996.

Niell, A. E.: Preliminary evaluation of atmospheric mapping functions based on numerical weather models, Phys. Chem. Earth, 26, 475-480, 2001.

Niell, A. E.: The IMF mapping functions, International Workshop on GPS Meteorology, Tsukuba, Japan, January 14–17, 2003.

Nikazad, T.: The Use of Landweber Algorithm in Image Reconstruction, PhD. Dissertation, Department of Mathematics, Linköpings University, Sweden, 2007.

Nilsson, T., Gradinarsky, L., and Elgered, G.: GPS Tomography Using Phase Observations. In Geoscience and Remote Sensing Symposium, IGARSS'04, 2004.

Nilsson, T., and Gradinarsky, L.: Water vapor tomography using GPS phase observations: simulation results, IEEE Transactions on Geoscience and Remote Sensing, 44, 2927–2941, 10.1109/TGRS.2006.877755, 2006.

Nilsson, T., Gradinarsky, L. P., and Elgered, G.: Water vapour tomography using GPS phase observations: Results from the ESCOMPTE experiment, TELLUS, 59A, 674-682, 10.1111/j.1600-0870.2007.00247.x 2007.

Nilsson, T., Böhm, J., Wijaya, D. D., Tresch, A., Nafisi, V., and Schuh, H.: Path Delays in the Neutral Atmosphere, in: Atmospheric Effects in Space Geodesy, edited by: Böhm, J., and Schuh, H., Springer Berlin Heidelberg, Berlin, Heidelberg, 73-136, 2013.

NOAA/ESRL Radiosonde Database: https://ruc.noaa.gov/raobs/, access: 2022-01-24, 2022.

Noguchi, W., Yoshihara, T., Tsuda, T., and Hirahara, K.: Time-Height Distribution of Water Vapor Derived by Moving Cell Tomography During Tsukuba GPS Campaigns, Journal of the Meteorological Society of Japan, 82, 561-568, 2004.

Norquist, D. C., and Chang, S. S.: Diagnosis and Correction of Systematic Humidity Error in a Global Numerical Weather Prediction Model, Monthly Weather Review, 122, 2442-2460, 1994.

Notarpietro, R., Cucca, M., Gabella, M., Venuti, G., and Perona , G.: Tomographic reconstruction of wet and total refractivity fields from GNSS receiver networks, Advanced in Space Research, 47, 898–912, 2011.

National Weather Service, Radiosondes: https://www.weather.gov/jetstream/radiosondes, access: 2022-01-24, 2022.

Park, K.-D., Lee, H.-C., Kim, M.-S., Kim, Y.-G., Seo, S. W., and Park, J.: Accuracy Comparison of GPT and SBAS Troposphere Models for GNSS Data Processing, Journal of Positioning, Navigation, and Timing, 7, 183-188, https://doi.org/10.11003/JPNT.2018.7.3.183, 2018.

Perler, D.: Water vapour tomography using global navigation satellite systems, PhD. Dissertation, ETH Zurich, Switzerland, 2011.

Perler, D., Geiger, A., and Hurter, F.: 4D GPS water vapor tomography: new parameterized approaches, Journal of Geodesy, 85, 539-550, 10.1007/s00190-011-0454-2, 2011.

Persson, M., Bone, D., and Elmqvist, H.: Total variation norm for three-dimensional iterative reconstruction in limited view angle tomography, Physics in Medicine and Biology 46, 53 - 866, 2001.

Priego, E., Jones, J., Porres, M., and Seco, A.: Monitoring water vapour with GNSS during a heavy rainfall event in the Spanish Mediterranean area, Geomatics, Natural Hazards and Risk, 8, 282-294, 10.1080/19475705.2016.1201150, 2017.

Pu, Z., and Kalnay, E.: Numerical Weather Prediction Basics: Models, Numerical Methods, and Data Assimilation, in: Handbook of Hydrometeorological Ensemble Forecasting, edited by: Duan, Q., Pappenberger, F., Wood, A., Cloke, H., and Schaake, J., Springer, Berlin, Heidelberg. , 2019.

Radon, J.: On the determination of functions from their integral values along certain manifolds, IEEE Transactions on Medical Imaging, 5, 170-176, 1986.

Rius, A., Ruffini, G., and Cucurull, L.: Improving the vertical resolution of ionospheric tomography with GPS occultations, Geophys Res Lett, 24, 2291–2294, 1997.

Rocken, C., van Hove, T., Johnson, J., Solheim, F., Ware, R., Bevis, M., Chiswell, T., and Businger, S.: GPS/STORM: GPS sensing of atmospheric water vapor for meteorology, Journal of Atmospheric and Oceanic Technology (12, 468–478, 1995.

Rohm, W., and Bosy, J.: Local tomography troposphere model over mountains area, Atmospheric Research, 93, 777-783, 10.1016/j.atmosres.2009.03.013, 2009.

Rohm, W., and Bosy, J.: The verification of GNSS tropospheric tomography model in a mountainous area, Advances in Space Research, 47, 1721-1730, 10.1016/j.asr.2010.04.017, 2011.

Rohm, W., Zhang, K., and Bosy, J.: Unconstrained, robust Kalman filtering for GNSS troposphere tomography, Atmos. Meas. Tech. , 6, 9133-9162, 10.5194/amtd-6-9133-2013, 2013.

Rothacher, M., Schaer, S., Beutler, G., Schlüter, W., and Hase, H. O.: Phase Center Variations of GPS Antennas Derived From GPS Observations of Specially Designed Calibration Campaigns, Supplement to EOS, American Geophysical Union,1996 Spring Meeting,May 20-24, 77, G11A-16, 1996.

Rudin, L. I., Osher, S., and Fatemi, E.: Nonlinear total variation based noise removal algorithms, Physica D: Nonlinear Phenomena, 60, 259-268, https://doi.org/10.1016/0167-2789(92)90242-F, 1992.

Rüeger, J.: Refractive index formulae for electronic distance measurements with radio and millimetre waves, Unisurv Report, 109, 758-766, 2002.

Sá, A.: Tomographic determination of the spatial distribution of Water Vapour using GNSS observations for real-time applications, PhD. Dissertation, Geodesy and Cartography, Wroclaw University of Environmental and Life Sciences, 174 pp., 2018.

Saastamoinen, J.: Contributions to the theory of atmospheric refraction.Part II: refraction corrections in satellite geodesy, Bulletin Géodésique, 107, 13-34, 1973.

Schmit, T. J., Gunshor, M. M., Paul Menzel, W., Gurka, J., Li, J., and Bachmeier, S.: Introducing the next-generation advanced baseline imager (ABI) on GOES-R, Bulletin of the American Meteorological Society, 86, 1079–1096, https://doi.org/10.1175/BAMS-86-8-1079, 2005.

Schmit, T. J., Griffith, P., Gunshor, M. M., Daniels, J. M., Goodman, S. J., and Lebair, W. J.: A closer look at the ABI on the GOES-R series, Bulletin of the American Meteorological Society, 98, 681-968, https://doi.org/10.1175/BAMS-D-15-00230.1, 2017.

Schmit, T. J., Lindstrom, S. S., Gerth, J. J., and Gunshor, M. M.: Applications of the 16 spectral bands on the Advanced Baseline Imager (ABI), Journal of Operational Meteorology, 6, 33-46, https://doi.org/10.15191/nwajom.2018.0604, 2018.

Schmit, T. J., Li, J., Lee, S. J., Li, Z., Dworak, R., Lee, Y. K., Bowlan, M., Gerth, J., Martin, G. D., Straka, W., Baggett, K. C., and Cronce, L.: Legacy atmospheric profiles and derived products from GOES-16: Validation and applications, Earth and Space Science, 6, 1730– 1748, https://doi.org/10.1029/2019EA000729, 2019.

Schüler, T.: On Ground-Based GPS Tropospheric Delay Estimation, Ph.D. Dissertation, Bauingenieur-und Vermessungswesen, Studiengang Geodäsie und Geoinformation, der Bundeswehr München, 2001.

Schüler, T., Posfay, A., Hein, G. W., and Biberger, R.: A global analysis of the mean atmospheric temperature for GPS water vapor estimation. C5: atmospheric effects,IONGPS., 14th International Technical Meeting of Satellite Division of the Institute of Navigation, Salt Lake City, Utah, 2001,

Seeber, G.: Satellite Geodesy, de Gruyter, Berlin., 1993.

Seko, H., Shimada, S., Nakamura , H., and Kato, T.: Three-dimensional distribution of water vapor estimated from tropospheric delay of GPS data in a mesoscale precipitation system of the baiu front, Earth Planets Space, 52, 927–933, 2000.

Shangguan, M., Bender, M., Wickert, J., and Raabe, A.: Validation of GNSS Water Vapour Tomography with Radiosonde Data, Geodätische Woche Nürnberg, 2011,

Shangguan, M.: Analysis and derivation of the spatial and temporal distribution of water vapor from GNSS observations, Ph.D. Dissertation, TU Berlin, 121 pp., 2014.

Sibson, R.: A vector identity for the Dirichlet tesselation, in: MathematicalProceedings of the Cambridge Philosophical Society, 151-155, 1980.

Sidky, E. Y., Kao, C. M., and Pan, X.: Accurate image reconstruction from few-views and limited-angle data in divergent-beam CT, Journal of X-Ray Science and Technology, 14, 119-139, 2006.

Siegfried, M. R.: Inversion of Extremely Ill-Conditioned Matrices in Floating-Point, Japan Journal of Industrial and Applied Mathematics, 26, 249-277, 10.1007/BF03186534, 2009.

Skone, S. H.: ENGO 633 Atmospheric Effects on Satellite Navigation Systems, Winter term course notes, Geomatics Engineering Department, University of Calgary, 2003.

Snay, R. A.-., and Soler, T.: Continuously Operating Reference Station (CORS): History, Applications, and Future Enhancements, Journal of Surveying Engineering 134, 95-104, 10.1061/(ASCE)0733-9453(2008)134:4(95), 2008.

Song, S., Zhu, W., Ding, J., and Peng, J.: 3D water-vapor tomography with Shanghai GPS network to improve forecasted moisture field, Chinese Science Bulletin, 51, 607-614, 2006.

Scripps Orbit and Permanent Array Center / California Spatial Reference Center: http://sopac-csrc.ucsd.edu/index.php/data-download/, access: 2022-01-24, 2022.

Stahel, K., Moore, R. D., Floyer, J. A., Asplin, M. G., and McKendry, I. G.: Comparison of approaches for spatial interpolation of daily air temperature in a large region with complex topography and highly variable station density, Agricultural and Forest Meteorology, 13, 10.1016/j.agrformet, 2006.

Stensrud, D. J.: Parameterization schemes: Keys to understanding numerical weather prediction models, Cambridge University Press, 2009.

Stolle, C., Schluter, S., and Heise, M.: A GPS based three-dimensional ionospheric imaging tool: process and assessment, Advanced in Space Research, 38, 2313–2317, 10.1016/j.asr.2006.05.016, 2006.

Subbarao, P. M. V., Munshi, P., and Muralidhar, K.: Performance of iterative tomographic algorithms applied to non-destructive evaluation with limited data, NDT&E international, 30, 359-370, 10.1016/S0963-8695(97)00005-4, 1997.

The so called 'Effective Height of Emission' vs the Actual Height of Emission – which is more informative?: https://tallbloke.wordpress.com/2014/07/13/the-so-called-effective-height-of-emission-vs-the-actual-height-of-emission-which-is-more-informative/comment-page-1/, access: 2021-10-20, 2014.

Tang, J., Nett, B. E., and Chen, G.-H.: Performance comparison between total variation (TV)-based compressed sensing and statistical iterative reconstruction algorithms, Physics in medicine and biology, 54, 5781-5804, 10.1088/0031-9155/54/19/008, 2009.

Tarantola, A.: Inverse Problem Theory and Methods for Model Parameter Estimation, SIAM, ix + 339 pp., 2005.

Tarniewicz, J., Bock, O., Pelon, J., and Thom, C.: Raman lidar for external GPS path delay calibration devoted to high accuracy height determination, Physics and Chemistry of the Earth, Parts A/B/C, 27, 329-333, http://dx.doi.org/10.1016/S1474-7065(02)00008-6, 2002.

Toomey, D. R., and Foulger, G. R.: TomographiIcn versiono f LocalE arthquakDe ata Fromt he Hengill-GrensdaluCr entralV olcano Complex,I celand, Journal of Geophysical Research, 9, 17,497-417,510, 1989.

Treuhaft, R. N., and Lanyi, G. E.: The effect of the dynamic wet troposphere on radio interferometric measurements, Radio Science, 22, 251-265, 1987.

Troller, M.: GPS based determination of the integrated and spatially distributed water vapor in the troposphere, PhD. Dissertation, Geodätisch-geophysikalische Arbeiten in der Schweiz.Swiss Geodetic Commission, ETH Zurich, 2004.

Turk, F. J., Padullés, R., Ao, C. O., Juárez, M. d. l. T., Wang, K.-N., Franklin, G. W., Lowe, S. T., Hristova-Veleva, S. M., Fetzer, E. J., Cardellach, E., Kuo, Y.-H., and Neelin, J. D.: Benefits of a Closely-Spaced Satellite Constellation of Atmospheric Polarimetric Radio Occultation Measurements, Remote Sensing, 11, https://doi.org/10.3390/rs11202399, 2019.

Turonova, B.: Simultaneous Algebraic Reconstruction Technique for Electron Tomography using OpenCL, MSc. Dissertation, Saarland University, 78 pp., 2011.

14-Tage Wettervorhersage: https://14-tage-wettervorhersage.de/news/thema/140926/, 2022.

Upper Air Observations: http://weather.uwyo.edu/upperair/, access: 2022-01-24, 2022.

Van Baelen, J., Reverdy, M., Tridon, F., Labbouz, L., Dick, G., Bender, M., and Hagen, M.: On the relationship between water vapour field evolution and precipitation systems lifecycle, Quarterly of the Royal Meteorology Society, 137, 204-223, 10.1002/qj.785, 2011, 2011.

Vienna Mapping Functions Open Access Data: https://vmf.geo.tuwien.ac.at/, access: 2022-01-24, 2022.

Vogel, C. R., and Oman, M. E.: Iterative methods for total variation denoising, SIAM J. Sci. Comput., 17, 227–238, 10.1137/0917016, 1996.

Wallace, J. M., and Hobbs, P. V.: Atmospheric science: an introductory survey, Academic Press, 2006.

Wang, Y., Ding, N., Zhang, Y., Li, L., Yang, X., and Zhao, Q.: A New Approach of the Global Navigation Satellite System Tomography for Any Size of GNSS Network, Remote Sensing, 12, 617, 2020.

Wickert, J., Beyerle, G., Hajj, G. A., Schwieger, V., and Reigber, C.: GPS radio occultation with CHAMP: Atmospheric profiling utilizing the space-based single difference technique, Geophys. Res. Lett., 29, 28.21_28.24, https://doi.org/10.1029/2001GL013982, 2002.

Wickert, J., Arras, C., Brack, A., Dick, G., Kepkar, A., Männel, B., Nguyen Thai, C., Oluwadare, T. S., Schmidt, T., Zus, F., and Schuh, H.: Ground and Space based GNSS for Space Weather Monitoring at GFZ: Overview and Recent Results, Abstract Book, IAG 2021 - Scientific Assembly of the International Association (Online from Beijing, China 2021), 2021.

Wong, D. W. S.: Interpolation: Inverse-Distance Weighting, in: International Encyclopedia of Geography: People, the Earth, Environment and Technology, 2017.

Wu, L.: A Parameter Choice Method for Tikhonov Regularization ENTA Kent State University, 6, 22, 2003.

Xia, P., Cai, C., and Liu, Z.: GNSS troposphere tomography based on two-step reconstructions using GPS observations and COSMIC profiles, Annales Geophysicae, 31, 1805-1815, 10.5194/angeo-31-1805-2013, 2013.

Xiaoying, W., Ziqiang, D., Enhong, Z., Fuyang, K. E., Yunchang, C., and Lianchun, S.: Tropospheric wet refractivity tomography using multiplicative algebraic reconstruction technique, Advances in Geosciences, 53, 156–162, 2014a.

Xiaoying, W., Ziqiang, D., Enhong, Z., Fuyang, K. E., Yunchang, C., and Lianchun, S.: Tropospheric wet refractivity tomography using multiplicative algebraic reconstruction technique, Advances in Space Research, 53, 156–162, 2014b.

Yang, F., Guo, J., Shi, J., Zhou, L., Xu, Y., and Chen, M.: A Method to Improve the Distribution of Observations in GNSS Water Vapor Tomography, Sensors (Basel), 18, 2526, 10.3390/s18082526, 2018.

Yang, L., Hill, C., and Moore, T.: Numerical weather modeling-based slant tropospheric delay estimation and its enhancement by GNSS data, Geo-spatial Information Science 16, https://doi.org/10.1080/10095020.2013.817107, 2013.

Yao, Y., and Zhao, Q.: A novel, optimized approach of voxel division for water vapor tomography, Meteorology and Atmospheric Physics, 1-14, 10.1007/s00703-016-0450-4, 2016.

Yao, Y., Zhao, Q. Z., and Zhang, B.: A method to improve the utilization of GNSS observation for water vapor tomography, Annales Geophysicae, 34, 143–152, 10.5194/angeo-34-143-2016, 2016.

Yao, Y., Xiin, L., and Zhao, Q.: A new tropospheric tomography model combining the pixel-based and function-based models, Annales Geophysicae, 37, 89-100, 10.5194/angeo-2018-34, 2019.

Yu, F., and Wu, X.: Radiometric Calibration Accuracy of GOES Sounder Infrared Channels, IEEE Transactions on Geoscience and Remote Sensing, 1187 - 1199, 10.1109/TGRS.2012.2219625, 2012.

Yuan, P., Yin, X., Möller, G., and Hansjörg, K.: A global uncertainty model for GNSS integrated water vapor derived from ERA5, GPT3 and co-located meteorological sensors, Remote Sensing of Environment, 2020.

Zhang, B., Fan, Q., Yao, Y., Xu, C., and Li, X.: An Improved Tomography Approach Based on Adaptive Smoothing and Ground Meteorological Observations, Remote Sens., 9, 2017.

Zhang, D., Guo, J., Fang, T., Wei, N., Mei, W., Zhou, L., Yang, F., and Zhao, Y.: TMF: A GNSS Tropospheric Mapping Function for the Asymmetrical Neutral Atmosphere, Remote Sens., 13, https://doi.org/10.3390/rs13132568, 2021.

Zhang, J.: Investigations into the Estimation of Residual Tropospheric Delays in a GPS Network, Msc. Dissertation, Department of Geomatics Engineering, Calgary, 185 pp., 1999.

Zhao, Q., Yao, Y., Cao, X., Zhou, F., and Xia, P.: An Optimal Tropospheric Tomography Method Based on the Multi-GNSS Observations, Remote Sens., 10, 2018.

Zhao, Q., Zhang, K., Yao, Y., and Li, X.: A new troposphere tomography algorithm with a truncation factor model (TFM) for GNSS networks, GPS Solutions, 23, 64, 10.1007/s10291-019-0855-x, 2019.

Zhao, Q., Yao, W., Yao, Y., and Li, X.: An improved GNSS tropospheric tomography method with the GPT2w model, GPS Solutions, 24, https://doi.org/10.1007/s10291-020-0974-4, 2020.

Zus, F., Douša, J., Kačmařík, M., Václavovic, P., Balidakis, K., Dick, G., and Wickert, J.: Improving GNSS Zenith Wet Delay Interpolation by Utilizing Tropospheric Gradients: Experiments with a Dense Station Network in Central Europe in the Warm Season, Remote Sensing, 11, 674, 2019.

Curriculum Vitae

Zohreh Adavi

Email zohreh.adavi@tuwien.ac.at, zohre.adavi@gmail.com

Sex *Female* **Nationality** *Iranian*

ORCID: 0000-0003-3059-8456

ACADEMIC EDUCATION

10/2019-Present

PhD Student

TU Wien, Department of Geodesy and Geoinformation

10/2012-10/2014

Master of Science in Geodesy (Score: A+)

Khajeh Nasir Toosi University of Technology, Tehran (Iran)

The title of Thesis: Local 4D Tomographic Modelling of Water Vapour in North-West of Iran

09/2008-09/2012

Bachelor of Science in Geoinformatics Engineering (Score: A+)

Khajeh Nasir Toosi University of Technology, Tehran (Iran)

WORK EXPERIENCE

05/2018-Present

Project Assistant

TU Wien, Department of Geodesy and Geoinformation

01/2015-12/2017

Lecturer of Least Square, Physical Geodesy, Micro Geodesy, Geodetic, Geodesy

Islamic Azad University (South Tehran Branch)

09/2016-05/2017

Lecturer of Surveying Engineering

K. N. Toosi University of Technology, Faculty of Civil Engineering

10/2014-05/2015

Teacher Assistant of Geodesy, Least square and Surveying Engineering.

K. N. Toosi University of Technology, Faculty of Geodesy and Geomatics

MEMBERSHIP

09/2016-Present

Member of IAG Working Group- GNSS Tomography